



National Library
of Canada

Canadian Theses Service

Ottawa, Canada
K1A 0N4

Bibliothèque nationale
du Canada

Service des thèses canadiennes

NOTICE

The quality of this microform is heavily dependent upon the quality of the original thesis submitted for microfilming. Every effort has been made to ensure the highest quality of reproduction possible.

If pages are missing, contact the university which granted the degree.

Some pages may have indistinct print especially if the original pages were typed with a poor typewriter ribbon or if the university sent us an inferior photocopy.

Previously copyrighted materials (journal articles, published tests, etc.) are not filmed.

Reproduction in full or in part of this microform is governed by the Canadian Copyright Act, R.S.C. 1970, c. C-30.

AVIS

La qualité de cette microforme dépend grandement de la qualité de la thèse soumise au microfilmage. Nous avons tout fait pour assurer une qualité supérieure de reproduction.

S'il manque des pages, veuillez communiquer avec l'université qui a conféré le grade.

La qualité d'impression de certaines pages peut laisser à désirer, surtout si les pages originales ont été dactylographiées à l'aide d'un ruban usé ou si l'université nous a fait parvenir une photocopie de qualité inférieure.

Les documents qui font déjà l'objet d'un droit d'auteur (articles de revue, tests publiés, etc.) ne sont pas microfilmés.

La reproduction, même partielle, de cette microforme est soumise à la Loi canadienne sur le droit d'auteur, SRC 1970, c. C-30.

THE UNIVERSITY OF ALBERTA

DESIGN AND MODELING OF TE CW CO₂ LASER

(S)

by

MOHAMED SALEM ELGWAILY

A THESIS

SUBMITTED TO THE FACULTY OF GRADUATE STUDIES AND RESEARCH
IN PARTIAL FULFILMENT OF THE REQUIREMENTS FOR THE DEGREE OF
DOCTOR OF PHILOSOPHY

DEPARTMENT OF ELECTRICAL ENGINEERING

EDMONTON, ALBERTA

SPRING 1988

Permission has been granted
to the National Library of
Canada to microfilm this
thesis and to lend or sell
copies of the film.

The author (copyright owner)
has reserved other
publication rights, and
neither the thesis nor
extensive extracts from it
may be printed or otherwise
reproduced without his/her
written permission.

L'autorisation a été accordée
à la Bibliothèque nationale
du Canada de microfilmer
cette thèse et de prêter ou
de vendre des exemplaires du
film.

L'auteur (titulaire du droit
d'auteur) se réserve les
autres droits de publication;
ni la thèse ni de longs
extraits de celle-ci ne
doivent être imprimés ou
autrement reproduits sans son
autorisation écrite.

ISBN 0-315-42754-X

THE UNIVERSITY OF ALBERTA

RELEASE FORM

NAME OF AUTHOR: MOHAMED SALEM ELGWAILY

TITLE OF THESIS: DESIGN AND MODELING OF TE CW CO₂ LASER

DEGREE: DOCTOR OF PHILOSOPHY

YEAR THIS DEGREE GRANTED: 1988

Permission is hereby granted to THE UNIVERSITY OF ALBERTA LIBRARY to lend or sell such copies for private, scholarly or scientific research purposes only.

The author reserves other publication rights, and neither the thesis nor extensive extracts from it may be printed or otherwise reproduced without the author's written permission.

(SIGNED) *MSC*

ADDRESS: 317 Queen's Court,

Edmonton, Alberta

T6J 2E5

DATE April 25, 1988

THE UNIVERSITY OF ALBERTA
FACULTY OF GRADUATE STUDIES AND RESEARCH

The undersigned certify that they have read, and
recommend to the Faculty of Graduate Studies and Research,
for acceptance, a thesis entitled DESIGN AND MODELING OF TE
CW CO₂ LASER submitted by MOHAMED SALEM ELGWAILEY in partial
fulfilment of the requirements for the degree of DOCTOR OF
PHILOSOPHY.

(Supervisor)

(Supervisor)

(External Examiner)

DEDICATION

To my wife Mahassen and my sons

Amr, Khalid, Tariq and Hazim

for providing purpose for this work.

ABSTRACT

The open channel flow laser gas discharge is successfully modeled and presented. The mass flow structure and the heat flow in a TE CW CO₂ laser gas discharge system have been investigated in detail, both theoretically and experimentally, in order to advance the state of the art for these devices.

The design and construction of a self-sustained TE CW CO₂ laser gas discharge system, used in this study are described. In this particular system, two anode arrays are located at the top and bottom of the discharge section, while the cathode is located in the middle of the channel. Experimental measurements indicated the effect of a stagnation region, caused by cathode, on gas flow profiles and heat flow. Convective cooling proved to be responsible for heat disposal from the discharge region. A 17% increase in the gas velocity was achieved, when the input power increased to 5.01 kW.

A computational analysis, using a single-fluid gasdynamic model was performed. A computer code, "IGCP" has been developed to provide a detailed simulation of the open channel flow laser gas discharge. The time-dependent Navier-Stokes equations were solved numerically in two dimensional cartesian coordinates, in order to give a steady-state solution. These include the equations of

conservation of mass, momentum and energy. The algorithm is based upon an iterative, alternating direction implicit (ADI) temporal advancement technique. The IGCP computer code is capable of utilizing very large time-steps, thereby substantially reducing computational cost.

Results of this computer simulation confirmed the measurements which were performed to investigate the effect of a stagnation region, caused by the cathode, on the gas flow profiles and the heat flow in our device. Also, a flow separation phenomenon was observed downstream of the cathode. Finally, including the energy equation in our computer code allowed the prediction of the gas temperature within the discharge region and downstream of the cathode. This, together with the prediction of velocity profiles, elucidated the role played and the characteristics of the process of convective cooling in our system.

ACKNOWLEDGEMENTS

The author wishes to thank Dr. J. Tulip who supervised the experimental work of this project, and provided the financial support through NSERC research grants. The author also wishes to express his deep gratitude to Dr. C.E. Capjack who supervised the computer simulation work of this project. His guidance, encouragement and fruitful discussions during the course of this study are greatly appreciated.

The author wishes to thank Dr. D.J. Marsden of the Mechanical Engineering Department for many useful discussions. Helpful discussions with Dr. H.J.J. Seguin and Dr. D.H. Kelly of the Electrical Engineering Department are greatly acknowledged.

Many thanks go to the many individuals in the laser laboratory for their assistance. Special thanks are due to Mr. H. Gans and his staff for the excellent service provided in the machine shop.

Finally, the deepest appreciation is expressed to the author's entire family, especially his wife, for her patience, understanding and encouragement during this work.

Table of Contents

Chapter		Page
1.	INTRODUCTION	1
1.1	CO ₂ LASERS AND HISTORICAL REVIEW	1
1.2	PROBLEMS ASSOCIATED WITH CO ₂ LASERS	6
1.3	TYPES OF GLOW DISCHARGE INSTABILITIES	7
1.3.1	CHARGED-PARTICLE PRODUCTION INSTABILITIES (STRIATIONS)	7
1.3.2	THERMAL INSTABILITIES (PLASMA CONSTRICKTION)	15
1.4	SCOPE OF THE THESIS	25
2.	STABILIZATION OF THE DISCHARGE AND COMPUTER SIMULATION IN CO ₂ LASERS	28
2.1	IONIZATION-ASSISTED CO ₂ LASERS	30
2.2	DISCHARGE STABILIZATION BY TURBULENCE	40
2.3	MAGNETIC FIELD STABILIZATION	50
2.4	OTHER STABILIZATION TECHNIQUES	56
2.5	COMPUTER SIMULATION IN CO ₂ LASERS	57
3.	EXPERIMENTAL SYSTEM DESIGN	61
3.1	INTRODUCTION	61
3.2	GAS TRANSPORT LASER SYSTEM	61
3.2.1	FLOW SYSTEM	61
3.2.2	LASER CHAMBER	66
3.2.3	CATHODE ELECTRODE	67
3.2.4	ANODE ELECTRODE	67
3.3	HIGH VOLTAGE POWER SUPPLY	69
3.3.1	HIGH VOLTAGE VARIAC	70
3.3.2	HIGH VOLTAGE TRANSFORMER	70
3.3.3	HIGH VOLTAGE RECTIFIER	70
3.4	ELECTRICAL CHARGE SYSTEM	71

3.5 TESTING THE FLOW SYSTEM	73
4. GAS DYNAMIC MODEL AND THE COMPRESSIBLE NAVIER-STOKES EQUATIONS	82
4.1 INTRODUCTION	82
4.2 EQUATIONS OF MOTION	86
4.3 GAS DYNAMIC EQUATIONS IN CARTESIAN COORDINATES ..	89
4.4 BASIC NUMERICAL CONSIDERATIONS	91
4.5 THE COMPUTATIONAL MESH	95
4.6 SPATIAL FINITE DIFFERENCING	98
4.6.1 FLUX TERM DIFFERENCING	99
4.6.2 FORCE TERM DIFFERENCING	102
4.7 TEMPORAL FINITE DIFFERENCING	103
5. LINEARIZATION AND SOLUTION OF THE FINITE DIFFERENCE EQUATIONS	106
5.1 INTRODUCTION	106
5.2 LINEARIZATION OF THE FINITE DIFFERENCE EQUATIONS	106
5.3 SOLUTION OF THE FINITE DIFFERENCE EQUATIONS	112
5.4 NUMERICAL BOUNDARY CONDITIONS	118
5.4.1 INTRODUCTION	118
5.4.2 BOUNDARY CONDITIONS OF THE OPEN CHANNEL FLOW LASER GAS DISCHARGE	120
5.5 CODE VERIFICATION	141
5.6 ITERATION CONTROLS	146
5.7 DYNAMIC TIME STEP CONTROLS	147
6. NUMERICAL AND EXPERIMENTAL RESULTS OF THE OPEN CHANNEL FLOW (ISOTHERMAL CASE)	148
6.1 INTRODUCTION	148
6.2 NUMERICAL RESULTS OF THE OPEN CHANNEL FLOW	148

6.2.1 NUMERICAL RESULTS OF THE TWO-ELECTRODE SYSTEM	148
6.2.2 NUMERICAL RESULTS OF THE THREE-ELECTRODE SYSTEM	153
6.3 EXPERIMENTAL RESULTS OF THE OPEN CHANNEL FLOW ..	163
6.3.1 EXPERIMENTAL RESULTS OF THE TWO-ELECTRODE SYSTEM	163
6.3.2 EXPERIMENTAL RESULTS OF THE THREE-ELECTRODE SYSTEM	164
7. NUMERICAL AND EXPERIMENTAL RESULTS OF THE OPEN CHANNEL FLOW LASER GAS DISCHARGE	170
7.1 INTRODUCTION	170
7.2 NUMERICAL RESULTS OF THE OPEN CHANNEL FLOW LASER GAS DISCHARGE	170
7.2.1 VELOCITY VECTOR DISTRIBUTION	171
7.2.2 VELOCITY PROFILES (COMPUTATIONAL)	176
7.2.3 TEMPERATURE DISTRIBUTION	182
7.2.4 PRESSURE DISTRIBUTION	189
7.2.5 MASS FLOW DISTRIBUTION AND SIMULATION MATCH TO EXPERIMENTS	195
7.3 EXPERIMENTAL RESULTS OF THE OPEN CHANNEL FLOW LASER GAS DISCHARGE	203
7.3.1 SYSTEM OPERATION	203
7.3.2 VELOCITY PROFILE MEASUREMENTS	205
7.3.3 TEMPERATURE DISTRIBUTION MEASUREMENTS	233
7.4 COMPARISON OF EXPERIMENTAL AND SIMULATION RESULTS	252
8. CONCLUDING REMARKS	262
8.1 CONCLUSIONS	262
8.2 FUTURE CONSIDERATIONS	266
REFERENCES	268
APPENDIX A	290

APPENDIX B 298

VITA 301

List of Figures

Fig.		Page
1.1	Ionization instability mechanisms [27].	10
1.2	Oscillogram of the discharge current and the moving domain [29].	14
1.3	Thermal instability mechanisms [36].	18
1.4	Thermal instability growth times [36].	20
2.1	Sketch of electron-beam-controlled discharge [12].	33
2.2	Discharge configuration of the photoinitiated and photosustained system [11].	35
2.3	Schematic of the uv preionization laser [55].	37
2.4	Application of r.f. to gas discharge [58].	38
2.5	Sketch of high power laser which uses aerodynamic stabilization [67].	42
2.6	Schematic drawing of the EDCL laser [73].	45
2.7	Schematic of baffle-electrode geometry [74].	46
2.8	Illustration of the discharge channel and turbulence generators [75].	48
2.9	Schematic of a cross-field laser showing the stabilizing magnetic field B [79].	51
2.10	Schematic of magnetically stabilized transverse gas discharge [81].	53
2.11	Schematic of magnetically stabilized coaxial gas discharge [83].	55
3.1	General view of the TE CW CO_2 high power laser.	62
3.2	Schematic diagram of the TE CW CO_2 laser.	63
3.3	Close view and the inside of the discharge chamber.	68
3.4	The electric discharge circuit.	72

Fig.	Page
3.5 Arrangement for velocity measurements.	74
3.6 Locations of measurement points.	75
3.7 Measured velocity profiles along the x-axis, with no cathode.	76
3.8 Measured velocity profiles along the x-axis, with cathode in place.	77
3.9 Velocity distribution along the discharge length z.	79
3.10 Variation of gas velocity with gas pressure.	80
4.1 The finite difference computational mesh.	96
4.2 Mesh points used in mixed derivative calculations.	101
5.1 Simulation mesh configuration for the two-electrode system.	121
5.2 Simulation mesh configuration for half the structure of the three-electrode system.	122
5.3 Basic geometry of the three-electrode system.	123
5.4 Boundaries of the single step configuration.	124
5.5 Staggered (hybrid) mesh system.	131
5.6 Sharp corner cell treatment.	135
5.7 Basic geometry of the two-electrode system.	143
5.8 Boundaries of the double step configuration.	145
6.1 Initial and final velocity profiles, number of iterations are NC4=1 and NC4=500.	150
6.2 Mass flow distribution along the x-axis.	152
6.3 Velocity vector distribution in the single step structure scheme.	155

Fig.	Page
6.4 Mass flow distribution along the x-direction in the single step case	156
6.5 Velocity profiles at different points on the x-axis, for the single step structure.	158
6.6 Velocity vector distribution in the double step structure scheme.	160
6.7 Mass flow distribution along the x-direction in the double step case.	161
6.8 Velocity profiles at different points on the x-axis, for the double step structure.	162
6.9 Measured velocity distribution across the channel for the two-electrode system.	165
6.10 Comparison of computed and measured velocity profiles for the two-electrode system.	166
6.11 Measured gas velocity distribution across the channel for the three-electrode system.	167
6.12 Comparison of computed and measured velocity profiles for the three-electrode system.	168
7.1 Velocity vector distribution for 1.56 kW input power and a cathode temperature of 420 °k.	173
7.2 Velocity vector distribution for 3.16 kW input power and a cathode temperature of 500 °k.	175
7.3 Velocity vector distribution for 5.01 kW input power and a cathode temperature of 600 °k.	177
7.4 Velocity profiles at different axial distances downstream, $P_{inp} = 1.56$ kW.	178
7.5 Velocity profiles at different axial distances downstream, $P_{inp} = 3.16$ kW.	180
7.6 Velocity profiles at different axial distances downstream, $P_{inp} = 5.01$ kW.	181

7.7	Velocity profiles for different levels of input power at $x=11.5$ cm downstream.	183
7.8	Gas temperature profiles at different axial distances, $P_{inp} = 1.56$ kW.	184
7.9	Gas temperature profiles at different axial distances, $P_{inp} = 3.16$ kW.	186
7.10	Gas temperature profiles at different axial distances, $P_{inp} = 5.01$ kW.	187
7.11	Temperature profiles for different input powers at $x=11.5$ cm downstream from the cathode.	188
7.12	Pressure profiles at $x=1.5$ and 5.5 cm from the entrance, $P_{inp} = 1.56$ kW.	191
7.13	Pressure profiles at different axial distances, $P_{inp} = 1.56$ kW.	192
7.14	Pressure profiles for different input power values at $x=2.5$ cm downstream from the cathode.	194
7.15	Pressure profiles for different input power values at $x=6.5$ cm downstream from the cathode.	196
7.16	Pressure profiles for different input power values at $x=11.5$ cm downstream from the cathode.	197
7.17	Pressure profile along the flow direction (x), at $y=24.5$ mm from the center of the cathode.	198
7.18	Pressure profile along the flow direction (x), at $y=33.0$ mm from the center of the cathode.	199
7.19	Mass flow distribution along the flow direction for input power of 1.56 kW.	201
7.20	Mass flow rate as a function of the pressure difference percentage.	202
7.21	Transverse-electric CW CO_2 glow discharge.	204

Fig.	Page
7.22 V-I characteristic, laser gas mixture is CO ₂ /N ₂ /He in the proportion 1:6:12 and p=20 torr.	206
7.23 Velocity profiles at different gas pressures, P _{inp} = 1.56 kW.	207
7.24 Velocity profiles at different gas pressures, P _{inp} = 3.16 kW.	209
7.25 Velocity profiles at different gas pressures, P _{inp} = 5.01 kW.	210
7.26 Velocity profiles at different laser gas mixtures.	211
7.27 Velocity profiles at z=z1, z2, z3 and z4.	213
7.28 Velocity distribution along the discharge length (z) at p=20 torr.	214
7.29 Velocity profile dependence on the input power at z=z1 and x=11.5 cm.	216
7.30 Velocity profile dependence on the input power at z=z2 and x=11.5 cm.	217
7.31 Velocity profile dependence on the input power at z=z3 and x=11.5 cm.	218
7.32 Velocity profile dependence on the input power at z=z4 and x=11.5 cm.	219
7.33 Velocity profile dependence on axial distance (x), for P _{inp} = 1.56 kW.	220
7.34 Velocity profile dependence on axial distance (x), for P _{inp} = 3.16 kW.	222
7.35 Velocity profile dependence on axial distance (x), for P _{inp} = 5.01 kW.	223
7.36 Velocity profile dependence on the input power at x=31.5 cm and z=z4.	224
7.37 Velocity profile dependence on the input power at x=26.5 cm and z=z4.	226
7.38 Velocity profile dependence on the input power at x=21.5 cm and z=z4.	227
7.39 Velocity profile dependence on the input power at x=16.5 cm and z=z4.	228

Fig.	Page
7.40 Velocity profile dependence on the input power at $x=11.5$ cm and $z=z_4$.	229
7.41 Velocity profile dependence on the input power at $x=7.5$ cm and $z=z_4$.	230
7.42 Gas velocity distribution along the centerline (A-A), as a function of the input power.	232
7.43 Gas velocity dependence on input power at $x=2.5$ cm and $y=Y/2$.	234
7.44 Temperature profile dependence on gas pressure at $x=11.5$ cm and $z=z_4$.	239
7.45 Gas temperature dependence on input power for different gas pressures.	240
7.46 Temperature profile dependence on laser gas mixture at $x=11.5$ cm and $z=z_4$.	242
7.47 Gas temperature dependence on input power for different laser gas mixtures.	243
7.48 Temperature profile dependence on input power at $x=16.5$ cm and $z=z_4$.	245
7.49 Temperature profile dependence on input power at $x=31.5$ cm and $z=z_4$.	246
7.50 Temperature profiles along the direction of flow (x) at $z=z_4$.	248
7.51 Temperature profile at $z=z_1$ for input power of 5.01 kW.	249
7.52 Temperature profile at $z=z_4$ for input power of 5.01 kW.	250
7.53 Temperature profile dependence on the input power at $z=z_2$.	251
7.54 Gas temperature dependence on the input power at $z=z_2$ and $y=7.0$ cm.	253
7.55 Temperature profile dependence on the input power at $z=z_3$.	254
7.56 Gas temperature dependence on the input power at $z=z_3$ and $y=7.0$ cm.	255

Fig.	Page
7.57 Maximum and minimum temperatures along the z-axis, at $x=11.5$ cm.	256
7.58 Comparison of computed and measured velocity profiles for the TE CW CO ₂ laser.	258
7.59 Comparison of computed and measured gas temperature profiles for the TE CW CO ₂ laser.	259

LIST OF SYMBOLS

A	surface area
c'	thermal molecular velocity
C	capacitance
C_s	adiabatic sound speed
C_p	heat capacity
C_v	specific heat at constant volume
CFL	Courant-Friedrichs-Lowy
CW	continuous wave
d	diameter
dv	unit volume
D	diode
D.C.	direct current
e	electronic charge
eV	electron volt
f_i	fractional percentage of the i th gas
GD	gasdynamic
h_i	scale factor for the x_i -coordinate
I	discharge current
Q_h	convective heat transfer per unit volume
Q	external heat source per unit mass
R	resistance
R	universal gas constant
R.F.	radio frequency
t	time
T	neutral gas temperature

\mathbf{u}	state vector
U.V.	ultra-violet
\mathbf{v}	velocity
\mathbf{V}	voltage
\mathbf{i}	unit tensor
\mathbf{j}	Jacobian tensor
K_B	Boltzmann's constant
ℓ	iteration index
L	length
L	inductance
m	average molecular mass
m_{mix}	average molecular mass of a gas mixture
M_i	molecular weight
\mathbf{n}	normal vector
n_e	electron density
n_n	neutral gas density
N_A	Avogadro's number
p	gas pressure
P_o	output power
Δ	incremental change
ϵ	convergence criterion
γ	ratio of specific heat capacities
λ	mean free path
η	shear viscosity coefficient
ζ	bulk viscosity coefficient
Π	pressure tensor
ρ	neutral mass density

τ viscous stress tensor

∇ gradient

\wedge denotes a tensor quantity

CHAPTER 1

INTRODUCTION

1.1 CO₂ LASERS AND HISTORICAL REVIEW

In recent years there has been a significant demand of high power carbon dioxide lasers. From the standpoint of potential industrial applications, the carbon dioxide laser unquestionably ranks first. The CO₂ laser offers both high power and high efficiency, at an infrared wavelength. Carbon dioxide lasers have been used to weld metals, cut ceramics, and perform many other material-processing tasks.

The first discovery of cw laser action in a CO₂ gas discharge was reported by Patel in 1964 [1,2]. An average power output of approximately 1 mW at 10.4 μm and 9.4 μm was obtained. An important advancement for the CO₂ laser was the use of a mixture of CO₂, N₂ and He, as the active medium [3-5]. This mixture allowed an increase in power output and efficiency. N₂ excites the CO₂ molecules to the upper laser level, via collisions between vibrationally excited N₂ molecules and ground state CO₂ molecules. The role of He, is to cool the gas, by aiding in the depopulation of the lower CO₂ vibrational energy level; thereby maintaining a large population inversion.

The early experiments were performed with slow gas flow. Using a $\text{CO}_2\text{-N}_2\text{-He}$ gas mixture in a 7.7 cm inside diameter by 230 cm long water cooled discharge tube with slow gas flow, Patel et. al. [5] obtained 106 W of average power at 6.2 percent efficiency. In 1969, the utilization of fast-flowing-gas techniques for CO_2 lasers was reported. These techniques increased the output power obtainable per unit length of discharge by several orders of magnitude and made possible multikilowatt electrically excited lasers in reasonable sizes[6-9].

Deutsch et. al. [6] reported a 140 W power output produced by using a 10 cm long, 13.5 mm i.d. discharge tube at a pressure range of 10-120 torr. The cooling of the system was provided by rapid removal of hot gas from the discharge region. Tiffany et. al. [7], and Targ and Tiffany [8] used closed-cycle gas cooling techniques and succeeded in obtaining a self-contained CW KW CO_2 laser having a 1 m active length. The $\text{CO}_2\text{-N}_2\text{-He}$ gas mixture is recirculated through a heat exchanger following forced convection transverse to the optical cavity and the electrical discharge. The transverse geometry permits efficient cooling, even at moderate flow velocities (about 30 m/sec).

In CO_2 lasers employing slow-flow velocities, and at high drive power, the walls are not effective in cooling the gas in the large-diameter tubes required for high power. On the other hand if the gas-flow transit time is much faster

than the characteristic time for diffusion to the walls of the laser channel, the excess heat absorbed by the gas from the discharge is swept away by the flowing gas. In this case, the laser medium is cooled efficiently by convection, rather than by diffusion to the walls.

For high-power compact low-weight CO₂ lasers convection cooling of the gas medium is desirable. Heating of the gas causes degradation of the population inversion; primarily because of population of the lower states. In the case of cooling by diffusion, the maximum power output per unit volume (P_o) scales as [7]:

$$P_o \propto \rho \lambda c / d^2 \quad (1.1)$$

where c is the thermal molecular velocity, d is the diameter of the discharge tube, ρ is the gas density and λ is the mean free path of the CO₂ molecules in the gas mixture. It is obvious from Eqn. 1.1 that the available power output per unit volume decreases with increasing diameter, at the same rate at which the volume itself is increasing, leaving the power per unit length unchanged. Also, the mean free path is inversely proportional to gas density, so that these two factors effectively cancel each other. Hence, no net improvement in the available power output results from changing the gas density. The only alternative option for increasing power output in diffusion-cooled lasers is to increase the tube length. Such tube scaling has led to 73 m

4

long CO₂ lasers, used for radar transmitters; having output powers in the few kilowatt range [10].

However, when forced convection is the dominant cooling mechanism, the maximum available power output per unit volume is proportional to $v_{\text{flow}}/d_{\text{flow}}$ [7], where v_{flow} is the flow velocity and d_{flow} is the distance through the active laser region in the direction of the flow. In this case the mean free path is no longer important to the cooling of the active region. Therefore, it is possible to consider increasing the density of the gas mixture, with a corresponding increase in the available power output per unit volume. The attractive features of this fast flow concept has led to the use of aerodynamic techniques by Hill [9], whereby continuous electric discharges were produced uniformly over large volumes in near-sonic CO₂-N₂-He flow systems. A laser power in excess of 20 kW has been achieved in this manner.

The desirable features obtained with a high-volume flowing gas laser are: (1) convective cooling reduces the thermal population of the lower laser level, (2) laser pump power can be increased because of more effective cooling, and (3) the flow of new material into the laser active region increases the potential laser power that can be obtained from the device (ie. increases the device's saturation parameter).

To obtain higher energies in higher pressure lasers, the idea of reducing the electrode spacing was used. However, as the pressure is increased, a plasma glow-to-arc transition becomes more probable. Such a transition is marked by a sudden increase in plasma current, the appearance of a bright white arc in the discharge, and a decrease in the voltage drop across the gas. When an arc discharge occurs, it will terminate laser action by a combination of (i) dropping the electron temperature and (ii) heating the gas. In the development of the TEA lasers, short excitation times less than the glow-to-arc transition time are necessary. The utilization of preionization techniques in high pressure lasers was beneficial, such as the use of UV by Seguin and Tulip [11], and the use of electron beam by Fenstermacher et. al. [12].

A major research interest in the high-power CO₂ laser field in the last several years has been to devise techniques that will permit the operation of electrical-discharge CO₂ lasers in the atmospheric pressure range. Plasma instabilities are the major problems to be overcome at these higher pressures. The techniques discussed e.g. in [11] and [12] are directed toward the solution of these problems. Under high-discharge power and/or high-pressure conditions, the performance characteristics of high-power CO₂ laser discharges are seriously affected by the development of gross plasma nonuniformities; which manifest themselves in the form of pulsating arc-like

current filaments. These plasma instabilities lead to a reduction in laser power and efficiency, and significantly complicate the development of effective and useful laser scaling criteria.

1.2 PROBLEMS ASSOCIATED WITH CO₂ LASERS

The development of convection cooling techniques for molecular lasers represented a major advance in the state-of-the-art. Moreover, with the surface of the containment vessel no longer serving as a heat sink, much greater flexibility in discharge configuration and operating conditions became possible. As a consequence, the scaling of convection-cooled molecular lasers to large volumes and high pressures has become a reality. However, it has been found that for many conditions of interest large-volume convection lasers are subject to the occurrence of plasma instabilities, that may prevent attaining high electrical power density levels. This represents a serious problem which challenges further advances in the high power laser industry.

The most common manifestations of plasma instability in glow discharges are the occurrence of ionization waves (striations) as reported by Pekarek [13], and thermal constriction (glow collapse) as studied by Ecker et. al. [14]. Occasionally both the striations and the glow collapse are observed simultaneously, as reported by Garscadden [15].

These two basic types of instability are the ones commonly observed in electrically excited molecular lasers; whether or not an external source of ionization is used to sustain the plasma.

1.3 TYPES OF GLOW DISCHARGE INSTABILITIES

Ionization waves (striations) and thermal constriction (glow collapse) are the most important instability types observed in electrically excited molecular lasers. Moving striations were first observed in an Argon positive column by Gentle [16]. Moving striations in CO₂ laser mixtures were observed in a self-sustained convection discharge by Nighan et. al. [17]; and in an electron-beam sustained discharge by Douglas-Hamilton and Mani [18,19], and by Vitshes et. al. [20]. The striation mode of instability in CO₂ laser discharges occurs as a consequence of negative-ion production, and is referred to as electron attachment-induced ionization instability. The glow collapse instability [21-26] has the most serious consequences for high-power laser applications, since its occurrence usually establishes the maximum electrical power density that can be achieved. A detailed review of these two types of instabilities follows.

1.3.1 CHARGED-PARTICLE PRODUCTION INSTABILITIES (STRIATIONS)

The striations (also called an ionization instability) results from temporal amplification of an imbalance between

charged particle production and loss processes, during a disturbance in plasma properties. Nighan et. al. [17] established a criteria for calculation of plasma conditions, leading to ionization instability in plasmas generally employed in high-power molecular laser applications. It was found from their study, that negative ion formation plays an important role in causing this instability. For conditions typical of electrically excited CO₂ laser mixtures, appearance of an ionization instability requires a negative ion concentration greater than one-tenth that of the electrons, combined with an electron temperature value below approximately 1.5 eV.

Theoretical and experimental studies of negative-ion processes in weakly ionized glow discharges have been described by Nighan and Wiegand [27]. The objective of that work was to determine and explain the initial causes of instabilities in charged-particle production and loss processes in molecular discharges, in which negative ions are present and produced by dissociative electron attachment of CO₂, CO or O₂. It was shown, that when the electron and negative-ion densities are comparable, an attachment rate which increases strongly with electron temperature can cause a mode of ionization instability; even when the plasma is sustained by an external source of ionization. Further, the growth rate of this attachment induced ionization instability is strongly peaked in the direction of the steady electric field. The ultimate manifestation of this

mode of ionization instability is in the form of a striated plasma.

For the ionization instability to occur, a positive feedback mechanism is required. Such a mechanism can lead to an electron attachment-induced ionization instability, if the effect of the electron temperature disturbance is sufficient to overcome the damping influence of recombination and detachment processes. This is illustrated by the sequence diagram shown in Fig. 1.1, where comparison is made with the situation encountered when negative ions are not present (case A). In case (A), ionization and recombination are dominant because of the absence of negative ions. In this case, an initial local fluctuation in the electron density is accompanied by a local decrease in the electron temperature. In a self-sustained discharge, where the rate of recombination is much greater than the ionization rate, a decrease in the electron density occurs. This results in a negative feedback mode which has a stabilizing effect.

In case (B) where negative ions are present, attachment and detachment become the dominant processes. If the electron attachment rate is an increasing function of the electron temperature, and comparable to the ionization rate, then the loss of electrons resulting from electron-molecule attachment dominates over electron production from ionization during a positive fluctuation in electron

The contents of this page has been removed because of the unavailability of copyright permission.

Contents:

Fig. 1.1 Ionization instability mechanisms.

Source:

W.L. Nighan and W.J. Wiegand, Phys. Rev. A, Vol. 10, No. 3, p. 922 (1974).

temperature. The dominance of attachment over ionization during a disturbance favors an inverse relationship between disturbances in electron temperature and electron density and a positive feedback mechanism is then established; thus causing an instability.

Douglas-Hamilton and Mani [18, 19] described the plasma instability in an electron-beam ionized discharge. This instability occurs in the form of current oscillations in gas mixtures, in which the dissociative attachment rate increases strongly with electric field. The principle of external ionization provides a stable discharge even in high-pressure (>760 torr) gases where a steady state is set up between production of secondary electrons by the external source and loss of secondary electrons by recombination and attachment processes. Under steady-state conditions, a local increase in the electric field results in the lowering of the electron density, and hence the conductivity. To maintain a constant current density, the electric field increases further, resulting in an enhanced attachment rate. Thus an instability occurs which is almost the inverse of the ionization instability; since increasing the electric field results in a reduction rather than an increase of the electron density. This attachment instability has been identified experimentally in a high-pressure externally ionized discharge. The instability manifests itself in the form of oscillations in the discharge current.

The hydrodynamic stability of a plasma with negative ions in a constant electric field was studied theoretically by Oraevskii et. al., [28], with the assumption that the negative ions are formed through the dissociative attachment of electrons to molecules. The mechanism for formation of negative ions is given by $e+XY=X+Y^-$. Calculations were carried out for two cases; those in which the charged particles recombine at the walls, and those recombining in the interior region. It was found that if the rate of dissociative attachment exceeds the growth of the ionization rate as the electron temperature is raised, the plasma is unstable. This instability is of a periodic nature.

An important study of the self-excited current oscillations of a glow discharge in a gas flowing transverse to the discharge axis was described by Myl'nikov and Napartovich [29]. Bright layers (domains) were detected at pressures of 10 to 100 torr in CO_2-N_2 gas mixtures. These layers are generated periodically near the cathode; they travel to the anode and vanish there. It was found that when the discharge current reaches a critical value J_{cr} , oscillations in the current and voltage across the discharge gap appear. These oscillations in the discharge current are due to the appearance of the domain in the cathode region and its motion toward the anode.

The period of current oscillations consists of two parts, during which the current decreases from J_{cr} to J_{min} .

and then increase to J_{ct} . The decrease in the current corresponds to the formation and motion of a domain from the cathode toward the anode, while the increase in the current corresponds to the absence of domains from the gap to the establishment of the state of the discharge preceding the appearance of the domain. This is shown in Fig. 1.2, where (K) is the cathode, (A) is the anode, (D) is the domain, and v is the gas flow velocity.

An experimental study was described by Akishev et. al. [30] for the conditions of an attachment instability in a self-sustained discharge in flowing air, for a broad range of experimental conditions. This instability leads to current oscillations and the formation of domains which move from the cathode toward the anode. It was reported that there is a real possibility of controlling the threshold for the attachment instability; by adjusting the local conditions (those near the cathode) in the discharge plasma. For example, in experiments in a transverse discharge they found that it is possible to suppress the attachment instability by creating a turbulent flow near the cathode. The use of turbulence in stabilizing a discharge will be presented in more detail in chapter 2.

Galaktionov and Pivovar [31] reported an experimental and theoretical study of the mechanism responsible for the decrease in the electron density caused by increasing CO concentration. They were concerned with the formation of the

The contents of this page has been removed because of the unavailability of copyright permission.

Contents:

Fig. 1.2 Oscillogram of the discharge current and the moving domain.

Source:

G.D. Myl'nikov and A.P. Napartovich, Sov. J. Plasma Phys., Vol. 1, No. 6, p. 486 (1975).

ions O^- and CO_3^- and related ion-ion recombination. In experiments on a volume discharge with external ionization of the medium which contains CO_2 , it was shown that at certain values of E/N the electron density is governed by ionizational amplification, the formation of O^- ions due to dissociative attachment to CO_2 , and the formation of a CO_3^- ions due to the highly effective reaction $O^- + CO_2 + M \rightarrow CO_3^- + M$. Because of the collision destruction of CO_3^- ions, the steady-state electron density is controlled by the loss of CO_3^- ions in ion-ion recombination, with CO_2 as a third body.

Aleksandrov [32] studied the case of three-body attachment of electrons to O_2 in a gas discharge with CO_2 , N_2 , He or O_2 as the third body. The process follows the reaction $e + O_2 + M \rightarrow O_2^- + M$, where M is the third body. It was found that this reaction is the primary mechanism by which electrons are consumed in an atmospheric pressure gas discharge, in which technical grade gases with $\approx 1\%$ O_2 are used. It is also believed that the three-body attachment of electrons to O_2 can lead to a superheating instability of a gas discharge [33] as will be described in the next section.

1.3.2 THERMAL INSTABILITIES (PLASMA CONSTRICTION)

The occurrence of a glow discharge collapse (also referred to in the literature as plasma constriction, contracion, and glow-to-arc transition) manifests itself in all types of gas discharges, and can occur gradually or

appear with a sudden onset. The occurrence of this contraction usually accompanies an increase in pressure, electric power density, or both. It will be shown in the following review that local overheating or superheating of the gas is primarily responsible for the occurrence of this kind of instability.

Because of this problem, large-volume glow discharges have in the past been limited to low pressures (≤ 50 torr) [34]. However, in molecular laser applications, it is important to operate the discharge in the glow mode at high pressures (1 atm. or more). In fact plasma constriction and related phenomena in CO_2 lasers provide a significant obstacle to scaling of these lasers to higher powers; even when the plasma is sustained by an external source of ionization [33]. However, recent progress has been made in developing an understanding of the basic causes of this thermal-type instability, for conditions typical of high-power density molecular lasers. This aspect will be described later.

Haas [35] studied the thermal mode of instability, which can occur individually or simultaneously with the vibrational relaxation mode. Because of the coupling between vibrational and translational energy, thermal and/or vibrational instability modes are considered as part of a group of thermal instabilities. In the thermal mode, a necessary condition for instability is that the V-T

relaxation time must decrease rapidly with increasing gas temperature. The instability in this case is driven by local thermal heating due to vibrational relaxation.

As the gas temperature rises the V-T relaxation time τ_{VT} decreases, increasing the energy release within the gas due to vibrational relaxation. If thermal conduction is unable to transport this energy away, and back pumping of vibration is inefficient in reabsorbing this energy, the gas temperature will continue to rise; producing a runaway condition. The characteristic time for evolution of the instability is τ_t , generally $10^{-3}-10^{-2}$ sec. Since the pressure remains nearly constant during the linear stage of this instability, the conductivity rises sharply; producing a local concentration in the current flow, and thus a glow contraction.

Nighan and Wiegand [36] analyzed the factors causing a glow-to-arc transition in volume-dominated molecular gas discharges, in terms of the collisional processes taking place in the plasma. It has been shown that arcing can be initiated by the growth of disturbances, in either vibrational or translational temperatures. Their calculations indicated that thermal and/or vibrational instabilities will occur for most conditions of importance to high-power CW CO₂ convection lasers, and that the growth time for these instabilities is typically on the order of 1 msec. The instability mechanism is illustrated in Fig. 1.3,

The contents of this page has been removed because of the unavailability of copyright permission.

Contents:

Fig. 1.3 Thermal instability mechanism.

Source:

W.L. Nighan and W.J. Wiegand, Appl. Phys. Lett., Vol. 25, No. 11, p. 633 (1974).

in which a local decrease in gas density leads to an effectively instantaneous response in electron temperature. The resulting large increase in electron density, strongly affects vibrational excitation of the molecule; which is also influenced by the changing gas density and temperature. Further there are two primary feedback mechanisms resulting in enhanced gas heating, vibrational relaxation and electron-molecule collisions.

The characteristic growth times of an instability, τ_g , were computed by Nighan and Wiegand, for a plasma at pressures of 20 and 200 torr and a gas temperature of 300 k. These are shown in Fig. 1.4. Consideration of this figure reveals some important points: (i) The fact that the computed growth times are everywhere positive indicates that vibrational instability occurs for all values of electric power density considered. (ii) For the 20 torr case, the growth time of an instability τ_g is always greater than about 10^{-3} sec; which is comparable with the gas residence time in convectively cooled CO₂ lasers. Such discharges can be stably maintained for pressures of about 20 torr. (iii) For 200 torr pressures and at increased power density, the instability growth time is reduced significantly, e.g. τ_g is less than 10^{-3} sec. Since fluid residence time in convection lasers is almost always greater than 1 msec, this result may serve to explain the difficulty of maintaining a diffuse volume-dominated discharge as the pressure is increased. Results of Fig. 1.4 show that stable laser discharge

The contents of this page has been removed because of the unavailability of copyright permission.

Contents:

Fig. 1.4 Thermal instability growth times.

Source:

W.L. Nighan and W.J. Wiegand, Appl. Phys. Lett., Vol. 25, No. 11, p. 633 (1974).

operation for pressures above 100 torr and steady power densities above about 10 W/cm^3 requires reduction in the gas residence time in convection lasers to values well below 1 msec.

The basic causes of glow collapse and/or glow-to-arc transition have been studied by Nighan [33] for convection cooled, externally sustained molecular-discharges. It was found that the growth rate of a thermal instability is sensitive to the electron loss process. In the thermal mode of instability, temporal changes in neutral particle properties play an important role in the initial growth of these disturbances. The evolution of the thermal instability was shown to be significantly affected by the nature of the electron loss process, e.g., recombination, attachment, three-body attachment, and by subsequent reactions involving negative ions. It was concluded that there are two distinct mechanisms which can be the driving force for thermal instability in molecular discharges: (i) electron vibrational excitation leading to an increase in vibrational temperature; and (ii) vibrational reservoir collapse, caused by a surge in vibrational-translation relaxation leading to a decrease in vibrational temperature. The conditions required for the occurrence of these thermal instabilities were discussed in detail by Nighan.

Eletskii and Samirnov [37] studied the contraction of the positive column of an axial glow discharge and explained

the mechanism as follows: The charged particles produced mainly in a narrow region along the tube axis recombine before they reach the tube wall, so that they are concentrated in a narrow region, thus the discharge contracts. They showed also that the ionization can fall off abruptly with distance from the discharge axis. Evolution of heat in the gas leads to a temperature drop over the tube cross section. Since the pressure in the tube is constant, the gas density near the axis is lower than that near the walls. It follows that an electron at the tube axis acquires a greater energy from the field between collisions than one moving near the wall. Accordingly, the average electron energy falls off with distance from the axis. Since the rate at which electrons are produced depends sharply on the average electron energy, a slight temperature drop in the gas is sufficient for electron formation in a narrow region near the axis.

Eletskii and Starostin [38] analyzed the mechanisms and conditions for the occurrence of an instability of a nonequilibrium state of a molecular gas, in which there is a large difference between the vibrational and translational temperatures. They reported that this instability is of the "thermal-explosion" nature, which is due, not to an activation energy, but to a strong temperature dependence of the rate constant for vibrational relaxation. The onset of this instability occurs if the heat evolved as a result of vibrational relaxation of molecules is not rapidly removed.

from the volume in which the vibrationally excited molecules are formed most rapidly. The resulting gas heating leads to a rapid increase in the rate of vibrational relaxation, because of the strong temperature dependence of the corresponding rate constant.

Eletskii and Starostin [39] reported that when a certain current (or pressure) is exceeded, the discharge contracts into a narrow region near the axis of the discharge tube. As a result only a small part of the gas in the tube is useful. As the current or pressure is raised further, the contraction usually becomes even more pronounced. The onset conditions for the mechanism of contraction of the discharge in molecular gases were studied. The particular conditions under which the contraction mechanism operates are governed by the sensitivity of the radial profile of the ionization frequency to the thermal inhomogeneity of the positive column.

Jacob and Mani [22] investigated the thermal and acoustic instabilities that could possibly cause arcing in high power pulsed and CW gas lasers. The physical mechanism for a thermal instability was described as follows: If the gas density drops locally, the heating at that point increases because of an increase in the electrical conductivity. This increases the pressure locally, and the gas expands so that the density drops further. This process

continues and eventually may lead to the constriction of the discharge and subsequent arcing. They also reported that the growth rate of the instability is proportional to the power density for low input powers; while it goes as the cube root of the power density for high input powers.

The ionization-thermal (superheating) instability was analyzed by Soroka and Shapiro [40] for the plasma of a self-maintained glow discharge. In this plasma, the electrons not only produce the population inversion in the level system of the heavy particles but also replenish the loss of charged particles due to ambipolar diffusion, attachment, and recombination. The discharge is assumed to be a convectively cooled volume discharge. The threshold conditions were found for the onset of the instability, which causes the discharge to break up into filaments. The dimensions of the inhomogeneity of the medium, the pressure, and the mixture composition affect the maximum power which can be supplied.

It was shown that, depending on the propagation direction of the perturbations, there can be two different types of instabilities (longitudinal and transverse). In the case of longitudinal perturbations, we have the purely ionization instability, which is due to a strong positive feedback. The scale time for the onset of this instability is $\approx 10^{-5}$ sec. In the case of transverse perturbations, there can be an ionization-thermal (superheating)

instability, due to the existence of a weaker feedback. The scale time for this instability is approximately 10^{-3} sec. The ionization-thermal instability occurs if the energy loss from the perturbation region does not balance the energy pumping by volume processes.

1.4 SCOPE OF THE THESIS

The main objective of this thesis is to advance the understanding of the behavior of the open channel flow laser gas discharge. In particular, the flow structure and heat flow in a TE CW CO₂ laser gas discharge system will be studied, in order to advance the state-of-the-art for these devices. A review of CO₂ lasers and the problems associated with them, including the different kinds of instabilities which usually occur in these lasers, was presented in this chapter. In chapter 2, some of the efforts which have been expended to enhance the understanding of basic discharge processes and to stabilize the glow discharge in high power CO₂ lasers will be reviewed.

To carry on our project, a TE CW CO₂ laser gas discharge system which uses a Mo spiral wire cathode and graphite anodes was built. The electrode structure was carefully designed and the proper materials for the different components in this system were used. After the system had been assembled, tests on the vacuum system, as well as preliminary measurements of the gas flow were done.

This will be described and discussed in chapter 3.

A computer code IGCP (Implicit Gasdynamic Computer Program) has been developed in order to analyze the open channel flow laser gas discharge. In this code, the time dependent Navier-Stokes equations were solved numerically in two dimensional cartesian coordinates in order to give a steady state solution. The solution was obtained using an alternating direction implicit (ADI) technique on a variable Eulerian mesh. The equations solved, and the finite difference technique used to approximate the nonlinear partial differential equations to a set of finite difference equations will be presented in chapter 4.

In chapter 5, the linearization of the nonlinear difference equations, which resulted from application of spatial and temporal finite difference techniques to the gas dynamic (GD) equations will be presented. Also, solution of the resulting set of algebraic equations using a Newton-Raphson iterative method will be described. In this chapter, the numerical boundary conditions will be given in the form which can be implemented in our implicit computer code (IGCP).

The numerical results for code verification and preliminary measurements will be described in chapter 6. The computer-simulation and experimental results of the open channel flow laser gas discharge, as well as a comparison between both results are presented in chapter 7. The

numerical results, including the velocity vector distribution, velocity profile, temperature distribution, pressure and mass flow, and their dependence on the discharge parameters will be described. The velocity profile and temperature distribution measurements, as a function of gas pressure, laser gas mixture, input power and discharge chamber dimensions will be presented.

Finally in chapter 8, a conclusion of both the numerical and experimental results will be presented. Furthermore, extended work for future consideration will be described.

CHAPTER 2

STABILIZATION OF THE DISCHARGE AND COMPUTER SIMULATION IN CO₂ LASERS

In this chapter, we review some of the efforts which have been done to enhance the understanding of the basic discharge processes and to stabilize the glow discharge in high power CO₂ lasers; in order to obtain a sufficient output power at high pressure and/or high power loading. An in-depth analysis has been reported by Haas [35]; who studied in detail the theoretical formulations of molecular discharge stability, in order to develop an understanding of the fundamental physical mechanisms influencing this stability. His analysis indicated that small-amplitude fluctuations present within these discharges excite several different wave modes identified as a space-charge relaxation mode, an electron thermal mode, an ionization mode, a negative-ion-production mode, an electronically-excited species production mode, a sound mode, a vibrational-energy relaxation mode, a heavy-particle thermal mode, and a vorticity mode. The stability of these modes was treated in detail and the different characteristic times were established.

Nighan [41] treated the fundamental plasma and collision processes of importance in high power electric

discharge lasers, with particular emphasis on CO₂ and CO laser media. He emphasized those aspects of the subject (such as electrical-optical conversion efficiency, discharge power density, and maintenance of a population inversion in molecular laser discharges). His work constituted a new and expanded understanding and appreciation of basic discharge processes. Also, plasma processes, of importance in convection laser discharges, discharges sustained by auxiliary sources of ionization, and pulsed high pressure laser discharges were given special attention. In addition, the effects on discharge behavior of negative ions and plasma chemical phenomena were explained. Such processes were shown to play an important role, with regards to plasma stability, as was reported by Nighan.

In another study by Wiegand and Nighan [42], analysis of plasma-chemical phenomena occurring in electrically excited mixtures of CO₂, N₂ and He, has shown that the principal dissociation products CO and O accumulate to significant levels in approximately 10⁻⁴ sec. This time is less than typical fluid residence times in convection lasers. In addition, numerous secondary minority species are produced on the same time scale; reaching concentrations significantly in excess of the charge particle densities. Furthermore, the dominant ionic species were found to be directly related to these discharges-generated minority species. They also reported that these investigations have shown that negative ion concentrations can become comparable

to the electron concentration for typical laser discharge conditions. In view of the importance of charged particle production and loss processes, as regards gas discharge stability, their findings provide valuable insight concerning mechanisms influencing the stability of electrically excited laser discharges.

Many other researchers [43-49] concentrated their efforts in the same direction; towards the basic understanding of gas discharge processes and the mechanisms which affect the stability of a discharge in CO₂-N₂-He lasers. Understanding the basic processes in the gas discharge enabled researchers to develop different techniques to overcome plasma instabilities, and made possible the production of stable discharge in CO₂ lasers at higher power loading. Different methods have been used to achieve this goal; such as the use of external source of ionization, turbulence, magnetic fields, and the proper choice of material and shape of the electrodes. This will be reviewed in the next sections.

2.1 IONIZATION-ASSISTED CO₂ LASERS

The use of external, independently controlled ionization sources such as high-energy electron beams [12,50-54], UV radiation [11,55-57] and RF excitation [58-60], as a means of producing relatively uniform, large volume glow discharges at high pressure, has resulted in

significant advances in gas-discharge technology. With this method of plasma production glow discharges have been produced for molecular laser applications over ranges of pressure and electrical power density which were previously inaccessible; as a consequence of the early onset of a glow-to-arc transition.

In the extensive theoretical study by Haas [35] of the stability of an electric discharge in molecular lasers, it was pointed out that the application of an external source of ionization significantly reduces the sensitivity of electron-density fluctuations to electron temperature, gas-density, and gas-temperature fluctuations; and thereby has a stabilizing influence on the ionization, negative-ion, and vibrational relaxation modes.

An electron-beam-controlled discharge has been used by Fenstermacher et. al. [12] to pump a variety of CO₂ laser gas mixtures, at atmospheric pressure in substantial volumes. This technique is characterized by fast (approximately 1-2μs) discharges between overvolted electrode structures, which deposit electrical energy into the laser gas mixture in a time short compared with the "arc" formation time. The distribution of electrical energy over an extended volume is accomplished by the use of multielectrode arrays; in which each electrode has its own capacitor feed or has a ballast resistor to limit the current. The apparatus used to produce such an

electron-beam-controlled plasma is shown in Fig. 2.1.

The electrons were produced by a 5 cm hot-cathode electrode gun and accelerated through a 0.003 cm Al vacuum window foil, by application of a high-voltage pulse (150 kV) for 10 μ sec. An electron current of 5 A was thus injected into the gas mixture, over an area of about 150 cm^2 . Fields of up to 4 kV/cm over 10 cm distances were applied from the main capacitor bank during the electron-injection pulse. With the use of electron-beam ionization, charged production in the plasma is decoupled from the applied electric field through the external electron-beam ionization source. This decoupling removes a major source of instabilities in the discharge. The major loss mechanism is volume recombination of the electron-ion pairs. The purpose of the electron beam is thus not to initiate the discharge, but rather to maintain the discharge against this loss.

A non-self-sustained gas discharge in $\text{N}_2\text{-CO}_2$ mixtures at atmospheric pressure was investigated by Velikhov et. al. [50]. An electron beam with an energy of approximately 10^5 eV and current of approximately 50 μ A was used as an external ionizer. A practical advantage of combined pumping is the possibility of exciting large volumes of gas at high pressure; because the external ionization source prevents an inhomogeneous pattern from developing in the initial stages of the discharge. This theoretical and experimental study presented a clarification of the feasibility to produce a

The contents of this page has been removed because of the unavailability of copyright permission.

Contents:

Fig. 2.1 Sketch of electron-beam-controlled discharge.

Source:

C.A. Fenstermacher, M.J. Nutter, W.T. Leland, and K. Boyer, *Appl. Phys. Lett.*, Vol. 20, No. 2, p. 56 (1972).

stationary non-self-sustaining gaseous discharge, whose current is due to the transfer of electrons generated by weak-current beams of charged particles. The reduced power of the external ionizer offers the promise of a CW CO₂ laser with combined pumping that could operate at high gas pressure.

A photoinitiated and photosustained TEA CO₂ laser was reported by Seguin and Tulip [11] in which the gases and the cathode are simultaneously irradiated by uv radiation from a high-field arc or spark. Such sparks are capable of producing hard uv radiation and have strong blackbody emission at wavelengths short enough to ionize the gases. The resulting photoionization and photoemission initiate and assist in sustaining a high energy low-field-strength discharge. The system is shown schematically in Fig. 2.2. The spark is formed in series with the main discharge between two tungsten pins separated by 2 mm. The plane mesh anode permits radiation from the spark to pass through the gases to the cathode. The doorknob capacitor (3600 pf) delays the rise of the main discharge voltage and imposes the full voltage across the spark for an initial small period. Uniform high-input-energy low-field-strength discharges were obtained in this structure, and the input energy was found to be linearly dependent on the electrode separation.

The contents of this page has been removed because of the unavailability of copyright permission.

Contents:

Fig. 2.2 Discharge configuration of the photoinitiated and photosustained system.

Source:

H. Seguin and J. Tulip, Appl. Phys. Lett., Vol. 21, p. 414
1972).

A large-volume high-pressure pulsed electrical CO₂ laser that employs volumetric photopreionization of the gas by ultraviolet radiation was demonstrated by Judd [55]. The independently controlled preionization discharge is initiated at some position remote from the main laser discharge volume, such as that shown in Fig. 2.3. The preionization discharge serves as a strong source of hard uv photon radiation, which propagates into the main discharge volume and photoionizes a fixed number of neutral gas molecules in this region. The resulting preionization background of electrons ensures a spatially uniform avalanche development in the main discharge plasma. The main discharge is also independently controlled and is initiated after a fixed time delay τ_d with respect to the preionizer discharge. High conversion efficiency and volumetric optical energy extraction have been obtained by Judd from this laser.

The application of auxiliary r.f. electric fields to complement and alter the distribution of ionization throughout the discharge volume was investigated by Eckbreth and Blaszuk [58] as a means of discharge stabilization. The r.f. was capacitatively coupled into the discharge through electrodes which sandwiched the channel, as shown in Fig. 2.4. The r.f. electrodes consisted of thin copper plates, slightly shorter in length than the discharge, and located on the outside of the top and bottom channel walls; so that the r.f. field was aligned transverse to the colinear d.c.

The contents of this page has been removed because of the unavailability of copyright permission.

Contents:

Fig. 2.3 Schematic of the uv preionization laser.

Source:

O.P. Judd, Appl. Phys. Lett., Vol. 22, No. 3, p. 95 (1973).

The contents of this page has been removed because of the
unavailability of copyright permission.

Contents:

Fig. 2.4 Application of r.f. to gas discharge.

Source:

A.C. Eckbreth and P.R. Blaszuk, AIAA 5th Fluid and Plasma
Dynamics Conference, Boston, Massachusetts, June 26-28 (1972),

field and gas flow. This study, and also the work by Eckbreth and Davis [59] demonstrated that application of r.f. auxiliary power, capacitively coupled into the discharge zone transverse to the d.c. field, is an effective means of enhancing closed-cycle discharge stability in CO₂ lasers; enabling stable operation at high power levels.

Ionization assisted discharges were also achieved by implementing other techniques such as using plasma injection [61]; where an ionized gas was injected into the main discharge region to obtain uniform continuous discharges in CO₂ laser gas mixtures at atmospheric pressure. In another experiment by Reilly [62] a pulser/sustainer concept, which produces pressure-and volume-scalable plasmas by essentially applying two successive discharges to the gas, was realized.

In another experiment by Bauman et. al. [63] a CW glow discharge exciting a subsonic, transverse flow CO₂ laser was stabilized by means of a CW auxiliary discharge. The stabilizing discharge was maintained between an array of individually ballasted anodes and the cathode of the main discharge. With this simple electrode configuration, the extension of stable glow operation to higher gas pressures than without stabilization was possible. The concept of auxiliary discharge was also used recently by WU [64] to improve the uniformity and stability of the main discharge in a TE CW CO₂ laser.

2.2 DISCHARGE STABILIZATION BY TURBULENCE

Turbulence is known to affect discharges because in addition to convection, a great deal of mixing takes place. This mixing is controllable and may offer distinct advantages in the design of discharges. Turbulence has the ability to disperse the discharge, allowing higher currents to exist in a pre-arcing mode. The early work of investigating the effect of turbulence on gas discharge properties is best described by the effort of Garosi et. al. [65,66]. They studied the gas discharge in flowing argon as the flow is increased from the laminar regime to the regime of fully developed pipe turbulence, with Reynolds numbers (Re) ranging from zero to 6300. The properties of the discharge, such as the density and density fluctuations, temperature, and electric field, were measured with Langmuir-type probes. The discharge was found to respond strongly to turbulent fluctuations of the un-ionized background gas. With increasing Reynolds number, plasma density fluctuations increase, the plasma column expands, and certain transport coefficients of the discharge rise well above their classical values.

One of the pioneering work, in which turbulence was implemented in CO_2 lasers, was reported by Brown and Davis [67]. They used a combined dc and rf excitation field and aerodynamic stabilization techniques to obtain a stable and homogeneous discharge. Four individually adjustable flow

conditioners were located upstream of the cathodes, in order to ensure that uniform-flow conditions were established downstream of the cathodes; thus inhibiting the onset of discharge instabilities. The high power laser investigated had an active volume 244 cm wide, by 6.3 cm high, by 53 cm long. A sketch showing the essential features of the discharge region is shown in Fig. 2.5. Continuous-output power levels greater than 20 kW have been achieved in their experiment for extended periods of time, with a maximum optical power of 27.2 kW, at an efficiency of 17.2 %.

Another effort by Shirahata and Fujisawa [68] to use turbulence to stabilize the discharge was reported. The system they used was a coaxial type cw CO₂ laser, in which the gas was aerodynamically mixed with the aid of oblique shock waves introduced into the discharge region. A homogeneous and stable discharge was attained in the transonic gas flow region. Improved small-signal gain and enhanced input power density were obtained.

Biblarz and Nelson [69] generated turbulence by using a screen (grid), and succeeded in obtaining homogeneous and stable discharges at higher discharge power. Their work was then extended by Biblarz et. al. [70]; to investigate in more detail the effect of grid-generated turbulence on the stability of the laser gas discharge. They reported that turbulent flows have the ability to stabilize a discharge and delay the occurrence of thermal instabilities, and that

The contents of this page has been removed because of the unavailability of copyright permission.

Contents:

Fig. 2.5 Sketch of high power laser which uses aerodynamic stabilization.

Source:

C.O. Brown and J.W. Davis, Appl. Phys. Lett., Vol. 21, No. 10, p. 480 (1972).

this effect is a fundamental one.

Shwartz and Lavie [71] studied the effects of turbulence on a weakly ionized plasma column. They developed a theoretical model for predicting the effects of turbulent flow on properties of the positive column. The model assumes that ions, which are imbeded in the turbulent neutral gas flow, acquire the motion of, and are completely correlated with, the neutral gas. The effect of turbulence on ambipolar diffusion, rate of ionization, electric field, electron temperature, and charge distribution was studied. The model predicts that an increase in the Reynolds number of the flow will increase the ionization rate, the electron temperature, and the electric field, and will flatten out the charge-concentration profiles. This is in agreement with past observations and with their own experimental results as they reported.

Some important effects that gas flow and turbulence can have on glow discharges and electrical lasers were considered by Shwartz and Wasserstrom [72]. A model for a discharge in a flowing gas, in which elementary principles of gas dynamics were combined with basic properties of discharges, was presented. By convecting the heat, the flow can have a significant influence on the gas temperature. In addition, if the flow is turbulent, it can change the rate of charged-particle diffusion and the effective thermal conductivity; and thus change the intrinsic properties of

the discharge (such as the electric field and the electron temperature). It was also concluded that, if turbulent flow is established in the tube, the current density becomes more uniform. The vigorous mixing due to turbulence spreads the electrons more uniformly, and also enhances heat conduction from hot spots. Therefore turbulence may be used to delay the formation of an arc.

Eckbreth and Davis [73] described the cross-beam electric-discharge convection laser (EDCL), in which a turbulent gas flow was used. Figure 2.6 shows a schematic drawing of the EDCL laser. It was found that input power to the discharge can be greatly enhanced (on the order of 30-40 %) by the introduction of small-scale turbulence just upstream of the cathode; by means of vortex generators arranged about the cross-section periphery or by means of a thin baffle which trips the flow. It was also predicted that in the presence of convection and turbulent diffusion, efficient power extraction can be achieved even when the optical beam volume is not well matched to the active discharge volume.

Eckbreth and Owen [74] presented a technique to condition the flow in rectangular EDCL channels, in which the flow and discharge are aligned. They discussed the importance of introducing turbulence and controlling the velocity profile in the system, which is shown schematically in Fig. 2.7. The discharge occurs between a distributed

The contents of this page has been removed because of the
unavailability of copyright permission.

Contents:

Fig. 2.6 Schematic drawing of the EDCL laser.

Source:

A.C. Eckbreth and J.W. Davis, Appl. Phys. Lett., Vol. 19, No. 4,
p. 101 (1971).

The contents of this page has been removed because of the unavailability of copyright permission.

Contents:

Fig. 2.7 Schematic of baffle-electrode geometry.

Source:

A.C. Eckbreth and F.S. Owen, Rev. Sci. Instrum., Vol. 43, No. 7,
p. 995 (1972).

cathode, in the upstream side, and an anode in a downstream location. The technique, they developed, consists of placing an array of individually adjustable baffles, spanned normal to the flow upstream of the cathode as shown in Fig. 2.7. The rotating baffles introduce the turbulence and control the velocity profile at the same time. The inlet flow to the laser channel was made approximately uniform, by passing the flow through a section of porous foam located several channel heights upstream of the baffle location. This study indicated the importance of obtaining a uniform velocity profile in the discharge region, in order to prevent the premature onset of discharge instabilities. It indicated also, that the turbulence level is also important in delaying the onset of discharge instabilities.

Wiegand and Nighan [75] investigated the influence of turbulence on the electrical power density threshold for glow constriction, for conditions typical of high-power CW convection cooled molecular lasers. The experimental arrangement used is shown in Fig. 2.8. The chamber is a rectangular Pyrex channel with a $5 \times 14 \text{ cm}^2$ cross-section. The cathode is located upstream and consists of an array of tantalum pins positioned 8.3 mm apart. A movable anode is used to vary the discharge length up to 1 meter. A 5-cm thickness of flow-conditioning foam with an average cell size of a few mm is used to eliminate fluid non-uniformities and large-scale eddies, while establishing a uniform velocity profile at the discharge channel inlet. A variety

The contents of this page has been removed because of the unavailability of copyright permission.

Contents:

Fig. 2.8. Illustration of the discharge channel and turbulence generators.

Source:

W.J. Wiegand and W.L. Nighan, Appl. Phys. Lett., Vol. 26, No. 10, p. 554 (1975).

of turbulence-generating grids and perforated plates were used to produce turbulence of different intensities and scale size. Stable and uniform glow discharges at pressures above 150 torr were maintained continuously in a recirculating gas cycle, due to turbulent effects.

Other research efforts were also reported, for example, Wasserstrom et al. [76] studied the interaction between electrical discharges and highly swirled and turbulent gas flow. They concluded that the limitations of high-power electrical lasers, due to heating of the gas and the instability of the glow discharge, can be alleviated by turbulent flow within the laser medium. Myshenkov and Makhvilaadze [77] investigated the possibility of suppression of an ionization instability in a glow discharge by turbulent transport. While Bondarenko et al. [78] studied the effect of turbulence on the stability of a self-sustained discharge in an air flow. They reported that, since the plasma electrons are coupled to the ions by electrostatic forces, while the ions are coupled-by collisions-to the neutral gas molecules, it can be expected that the controllable changes in the gas-dynamic properties of the flow (in particular, the turbulence intensity) can affect the course of instabilities; and thus the maximum power per unit volume which can be pumped into the discharge.

2.3 MAGNETIC FIELD STABILIZATION

The study of stabilized electrical discharges in a transverse flow by means of crossed magnetic field has been of considerable engineering and physical interest. The application of the cross-field magnetic stabilization technique to flowing molecular lasers is of great importance. In convectively cooled CO₂ laser discharges, the crossed magnetic field was used by Buczak et. al. [79,80] to stabilize the positive column against the transverse gas flow. An unstabilized plasma column is bowed strongly downstream under the force of the transverse gas flow. In order to achieve efficient laser operation, it is necessary to straighten and align the axis of the discharge collinear with the optical axis of the laser resonator. This is accomplished by employing a tapered transverse magnetic field, mutually perpendicular to the axial electric field of the discharge and the gas flow velocity as shown in Fig. 2.9.

Discharge stabilization is achieved via the interaction between the transverse magnetic field B and charged particle drift velocity v_d , along the electrical discharge axis. A $v_d \times B$ velocity component is established, which counteracts the gas flow velocity v . In this device, the magnetic pole piece is located downstream from the desired axis of the discharge, such that the discharge occurs in the fringing field of the pole piece. The tapered magnetic field results

The contents of this page has been removed because of the unavailability of copyright permission.

Contents:

Fig. 2.9 Schematic of a cross-field laser showing the stabilizing magnetic field B .

Source:

C.J. Buczek, R.J. Wayne, P. Chenausky, and R.J. Freiberg, Appl. Phys. Lett., Vol. 16, No. 8, p. 321 (1970).

in a transverse force on the axially drifting electrons which increases in the downstream direction. As a result, the magnetic force on the axially drifting electrons is increased downstream and decreased upstream from the laser optic axis. As the discharge tends to bow downstream, the increased magnetic field force pushes the discharge back toward the optical axis. If the discharge bends upstream, the decreased magnetic field allows the discharge to flow back along the desired axis.

In 1980, Seguin et. al. [81] described a new discharge stabilization technique for high-powered gas lasers. Profiled magnetic fields interacting with electron and ion sheaths at or near the electrode surface inhibit growth of electrothermal plasma instabilities and increase power loading by an order of magnitude. Figure 2.10 shows a schematic diagram of the initial "magnetic electrode" discharge stabilization structure. They predicted that this technique can be scalable for very large-volume devices.

The in-depth work by Capjack et. al. [82], enhanced the basic understanding of the role of magnetic fields in stabilizing the discharge in high power lasers. They examined the dynamics of a rotating plasma in a transverse electrode geometry, appropriate to high power CO₂ laser discharge pumping. The magneto-gas-dynamic fluid model, they developed, reveals that the spatially nonuniform electric and magnetic fields within the discharge cause the plasma

The contents of this page has been removed because of the unavailability of copyright permission.

Contents:

Fig. 2.10 Schematic of magnetically stabilized transverse gas discharge.

Source:

H.J.J. Seguin, C.E. Capjack, D. Antoniuk, and K.A. Nam, Appl. Phys. Lett., Vol. 37, No. 2, p. 130 (1980).

and neutral gas rotational velocities to be strongly sheared within the cathode fall and the positive column regions. This sheared rotation serves to both stabilize the discharge against glow to arc transitions and to drive a centrifugal neutral flow within the volume. This stabilization effect is important to high power lasers. An order of magnitude increase in discharge power loading has been achieved utilizing a simple "magnetic electrode" discharge configuration, such as the one shown in Fig. 2.10.

The magnetic field stabilization concept developed by Seguin et. al. [81] was also applied to a radial discharge [83], where a new magnetically stabilized coaxial electrode system supporting a radial discharge geometry was reported. A schematic diagram for this system is shown in Fig. 2.11. Performance was found to be largely independent of gas mixture and pressure such that high-power cw discharges were easily obtained in all the gases they tested. This stabilizing technique was found to be simple and scalable to provide a very large active volume in a compact system, as they reported. A cw power loading in excess of 40 kW/l was obtained in this system without experiencing any glow-to-arc transitions. This magnetically stabilized coaxial system was combined with a multi-element, fluid-ballasted cathode and external pulser preionization to produce a coaxial MAGPIE laser [84], which is a recognized achievement towards the production of efficient and compact CO₂ high power laser.

The contents of this page has been removed because of the unavailability of copyright permission.

Contents:

Fig. 2.11 Schematic of magnetically stabilized coaxial gas discharge.

Source:

H.J.J. Seguin, C.E. Capjack, D. Antoniuk, and V.A. Seguin, Appl. Phys. lett., Vol. 39, No. 3, p. 203 (1981).

2.4 OTHER STABILIZATION TECHNIQUES

Although the use of external source of ionization, turbulence, and magnetic fields to stabilize the discharge in CO₂ lasers was beneficial, some research efforts were directed toward improving the discharge using different discharge configurations and even different electrodes materials. For example Tiffany et. al. [7,8] proposed a cross gas flow laser in which the discharge and gas flow are orthogonal to the optical axis. This type of laser yields high small-signal gain at low gas flow rate (several ten m/s) and produces an output as high as 1 kW [79]. Also, the cross-beam laser in which the discharge and gas flow are orthogonal to the multipath optical axis can realize the largest active media and generates output as high as several tens of kWs [9,59,74].

Other research efforts were concerned with the shape of electrodes. For example Zheen et. al. [85] used a water cooled copper pipe for the cathode and an anode which consists of 45 cu pads. With a 86 mm length active region they obtained 2.5 kW output power from this laser. However, Kasamatsu et. al. [86,87] used the same idea but in this case, the cathode pipe was replaced by a spiral wire, and the anode cu pads were replaced by graphite segments. In this system, the cathode is cooled by the flowing gas and even the anode does not need water cooling because of the graphite's heat resistant qualities. With this simple system

they succeeded in obtaining a 6 kW output power using a discharge length of 137 cm.

2.5 COMPUTER SIMULATION IN CO₂ LASERS

Substantial increase in the output power of cw CO₂ lasers were achieved with the recognition of the advantages that forced convection cooling of the discharge offered over the earlier wall-cooled devices [6-9]. The output power of wall-cooled lasers is limited by the cooling rate to typically 100 W per meter length. With forced convection of the gas through the discharge, the power dissipation and thus output power may be increased by more than an order of magnitude. Such increases were rapidly realized, both by flowing the gas in an axial direction along the discharge tube, and by flowing the gas transversely across the discharge [88]. Typically, axial flow devices operate in the 0.5 to 5. kW range. Transverse-flow lasers utilize a relatively large area, low velocity gas flow and are scalable to rather higher powers; with devices having cw outputs of 1-15 kW being commercially available, and with higher powers being reported in the literature [9,67].

Despite these advances in CO₂ high power laser technology, convective cooling and the complexity of the novel electrode structures developed to stabilize the discharge, complicated the process and made it difficult to understand. For this reason, computer simulation was

necessary to enhance the understanding of the basic processes of gas discharges and kinetics in these lasers. The modeling of CO₂ laser kinetics has received much attention over the last decade. For example, Manes and Seguin [89] employed a model to predict the output power pulse shape from a TEA laser. The model they used, was reported to be useful in the evaluation of alternative pumping schemes and in the understanding of CO₂ TEA laser dynamics when nonlinear media are placed in the optical cavity.

In another example, where a gas-dynamic CO₂ laser was pumped by combustion of hydrocarbons, Tulip and Seguin [90] analyzed the expansion of a hot mixture of CO₂, N₂ and H₂O through a laval nozzle. Their calculations indicated that the expansion will result in a population inversion on the CO₂ laser transition for the used fuels. Other authors have considered the simulation of cw-discharge convectively cooled lasers; where Yoder et. al. [91] developed a computer code to predict small signal gain, optical quality (medium refraction), and output power for cw CO₂ electric lasers. They solved the fluid mechanics, plasma dynamics and kinetic rate equations simultaneously for two cavity configurations: flow parallel and flow transverse to the electric field. Their simulation proved useful in interpreting the results they obtained from experiments.

Another effort by Armandillo and Kaye [92] was reported, as they modeled a transverse-flow cw CO₂ laser. In that work, one-dimensional conservation equations describing the gas transport, coupled with multi-temperature model rate equations describing the molecular kinetics, were solved numerically, for the case of transverse flow, transverse-discharge carbon dioxide laser. The influence on gain distribution and output power of the discharge input power, as a function of variables such as flow velocity, cavity position, output coupling and carbon dioxide content was investigated. They reported that the computer model proved a useful tool for optimizing performance of the laser, in terms of power output, efficiency and beam quality.

The extensive work by Quartieri et. al., which was reported in their three-part paper [93-95], focused on modeling a high-power electron beam preionized CO₂ CW laser. The theoretical-numerical model they developed takes into account the effects of the mixture temperature, density and flow velocity variation on the laser's small-signal gain, as it relates to high power lasers. The laser chamber space profiles of all these quantities were obtained. Furthermore, they calculated the output radiation flux intensity and space distribution, using a simplified model for the optical cavity. The calculated numerical results from their detailed kinetic and fluid-dynamic model were compared with

experimental values relative to a four-component ($\text{CO}_2:\text{N}_2:\text{CO}:\text{He}$) cw CO_2 gas laser (model AVCO HPL 15) and were found very useful.

Monte Carlo simulation technique was used by Ngoc An et. al. [96] to analyze the electron behavior in the cathode fall region of a glow discharge in helium. The same technique was used by Razdan et. al. [97, 98] to model the cathode fall region of a glow discharge under the influence of a nonuniform electric field and a transverse magnetic field. Their simulation analysis were made for a helium gas discharge [97], and then extended to other gases of interest in CO_2 lasers; principally N_2 and CO_2 , and also for laser gas mixture of He, N_2 , and CO_2 in a 20:8:2 torr ratio [98].

It can be shown from the above review, that most of the computer simulation efforts were related to the molecular kinetics of the laser gas discharges; with little or no concern about gas transport processes and flow structures in CO_2 gas lasers. In 1984, Antoniuk et. al. [99] analyzed the gas flow in a magnetically stabilized glow discharge, by using a single fluid magnetogasdynamic model. The resulting system of time dependent, nonlinear, coupled partial differential equations was solved numerically on an Eulerian mesh, by using an iterative alternating direction implicit finite difference method. Their computer simulation results provided further insight for the design of magnetically stabilized glow discharges for laser applications.

CHAPTER 3

EXPERIMENTAL SYSTEM DESIGN

3.1 INTRODUCTION

The experimental apparatus used in this project consists mainly of a gas transport system and an excitation system. The gas transport system includes the laser chamber and electrodes, a gas blower, heat exchangers, ducts, and the laser tank. Figure 3.1 shows a general view of the system. A brief description for the different components is to follow.

3.2 GAS TRANSPORT LASER SYSTEM

The gas transport system is made of aluminum. It consists mainly of a flow system, laser chamber and electrodes.

3.2.1 FLOW SYSTEM

The main components of this system are the gas blower, the heat exchangers and the ducts. Figure 3.2 shows a schematic diagram of the gas flow system.

THE QUALITY OF THIS MICROFICHE
IS HEAVILY DEPENDENT UPON THE
QUALITY OF THE THESIS SUBMITTED
FOR MICROFILMING.

UNFORTUNATELY THE COLOURED
ILLUSTRATIONS OF THIS THESIS
CAN ONLY YIELD DIFFERENT TONES
OF GREY.

LA QUALITE DE CETTE MICROFICHE
DEPEND GRANDEMENT DE LA QUALITE DE LA
THESE SOUMISE AU MICROFILMAGE.

MALHEUREUSEMENT, LES DIFFERENTES
ILLUSTRATIONS EN COULEURS DE CETTE
THESE NE PEUVENT DONNER QUE DES
TEINTES DE GRIS.



Fig. 3.1. General view of the TS CW CO₂ high power laser.

Schematic of the TE CW CARBON DIOXIDE LASER

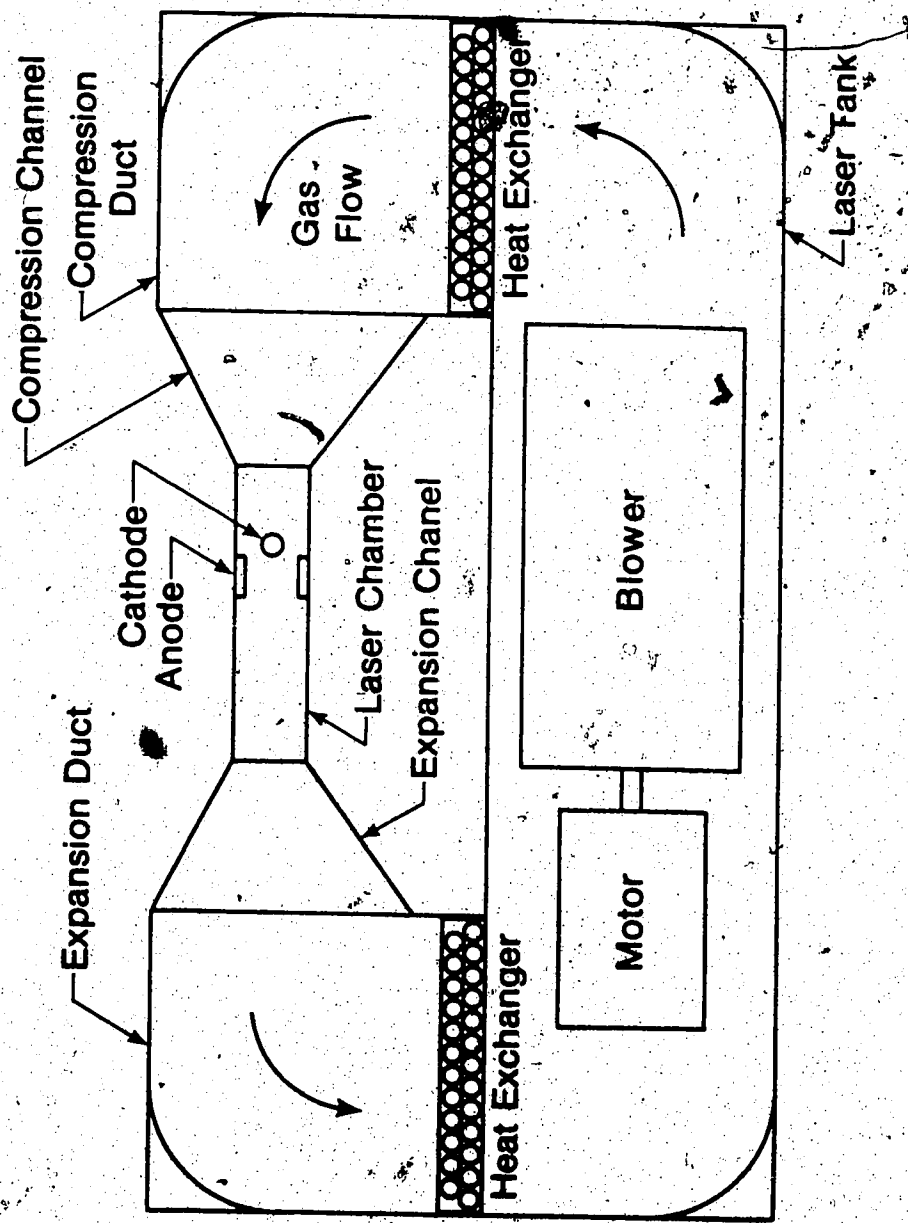


Fig. 3.2 Schematic diagram of the TE CW CO₂ laser.

A. GAS BLOWER

Gas circulation through the system is provided by a double stage blower some 61 cm in diameter. The blower's rotor is made from polyamid glass multiwing blades [100] of 20.32 cm length and 45° pitch, while the stator is made from polypropolyn blades of the same size. The blower has a capacity of 6.2 m³/s or about 13,284 CFM, and is capable of providing a flow velocity of 45 m/s. It is driven by a 15 HP 3-phase electric motor, which is located inside the laser tank close to the blower.

B. HEAT EXCHANGERS

Two heat exchangers are used. One is located downstream of the discharge region and helps to cool the heated gas before it is recirculated by the blower. The second heat exchanger, which is installed upstream of the discharge chamber, quenches the heat produced by the blower and the remaining heat carried by the circulation gas and allows fresh cool gas to enter the discharge region. The two heat exchangers are geometrically similar and each one is made of copper tubes 16 mm in diameter and circular Aluminum fins of 36 mm outside diameter and 0.2 mm thickness. The tubes are arranged in an eccentric double layer, as shown in Fig. 3.2. This geometry forces the circulated gas to pass through the entire surface of the heat exchanger, and to be efficiently cooled. The heat exchangers are 80 cm by 60 cm and fit on

the top of the laser tank at upstream and downstream locations. Adequate cooling is provided by flowing 15 lit/min of tap water through the heat exchangers.

C. DUCTS AND LASER TANK

The laser tank and ducts are made of aluminum alloy and are shown schematically in Fig. 3.2. The laser tank has a length of 245 cm, a width of 85 cm, and a depth of 50 cm. It accommodates the gas blower and the driving motor. It is separated from the ducts at the top by the heat exchangers on both sides. Curved aluminum sheets were installed at the corners in the laser tank. A compression duct and an expansion duct allow efficient and smooth gas circulation in the system.

The compression channel, which connects the compression duct to the laser chamber, was carefully designed; to match a window of 36 cm by 89 cm on the compression duct to a cross sectional area of 10 cm by 135 cm on the upstream side of the laser chamber. The compression channel has a conical shape and the slopes were chosen to maximize uniformity in the flow distribution across the channel height. The compression duct forces the circulated gas into the laser chamber through the compression channel, with a 5:3 compression ratio.

Metal fins were installed across the compression channel to ensure that the gas flow is equally distributed.

along the width of the channel (135 cm in the z-direction) upon entering the laser chamber [101]. On the other side, the expansion channel and expansion duct allow the circulated gas to flow through the heat exchanger. It is then drawn in by the blower.

3.2.2 LASER CHAMBER

The laser chamber, which has a rectangular cross section, is designed to accommodate the discharge electrodes. The dimensions of the discharge chamber are, 75 cm in the direction of the gas flow, 135 cm perpendicular to the gas flow direction, and 10 cm in height. Rectangular windows on the front side and the back end of the discharge chamber are installed for visual observation of the discharge. Also, optical mirrors can be attached to these windows, to form a laser cavity; whenever the operation of the system as a laser is desired. There are four ports on the top plate of the laser chamber for the purpose of diagnostic measurements.

According to the design of our system, the direction of gas circulation is as illustrated in Fig. 3.2. This allows a cool fresh laser gas mixture to be compressed into the discharge chamber and the hot gases to be removed from the discharge region. The laser gas mixture, which consists of $\text{CO}_2/\text{N}_2/\text{He}$, serves as the medium for the electric discharge and as the lasing medium.

3.2.3 CATHODE ELECTRODE

The cathode electrode is made of a 1 mm. diameter molybdenum (Mo) spiral wire. The spiral has a length of 135 cm, an outside diameter of 2.5 cm and a pitch of 5 turns per cm. The Mo wire is chosen because it has good heat resistance (melting point at 2600°C) and is suitable for hot cathodes. Also, it has a light weight since its density (10.2 gm/cu cm) is almost half that of tungsten (19.3 g/cu cm).

The Mo wire cathode is mechanically supported by a ceramic strip. It is located at the center of the channel just upstream of the anode sections and is cooled by the flowing gas mixture. Therefore no water cooling is necessary, this allows simplicity of construction. This Mo wire cathode also works like a large diameter electrode, thus making the gain distribution more uniform [87]. Figure 3.3 shows the discharge section, the inside of the discharge chamber and the cathode electrode.

3.2.4 ANODE ELECTRODE

The anode consists of 110 electrodes which are made of commercial graphite [86]. Each has a length of 50 mm, a width of 16 mm and a height of 12 mm. The anode is split into two sections, each section consists of 55 components. One section is mounted on the top plate of the laser chamber and the other section is mounted on the bottom plate, as

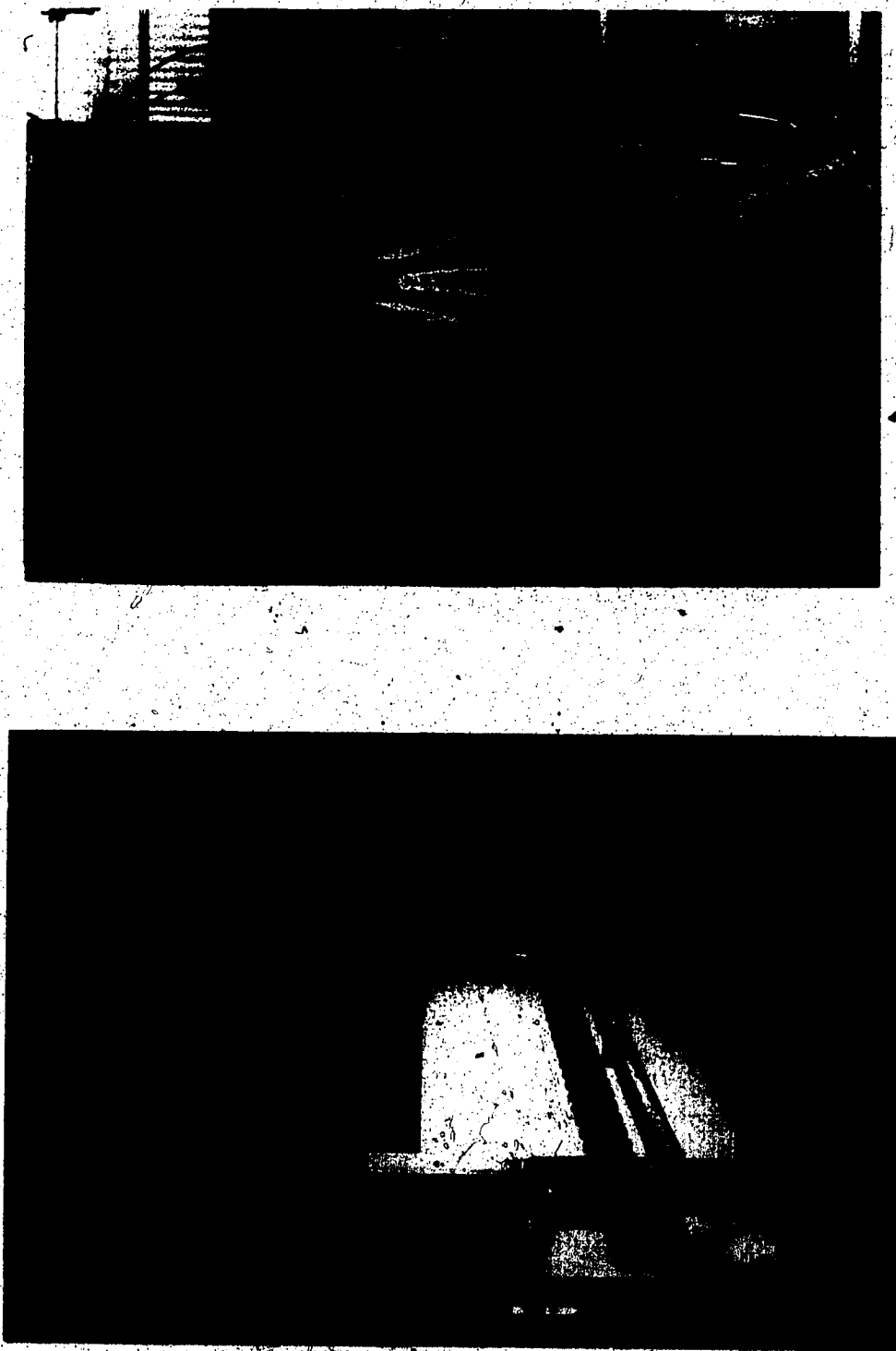


Fig. 3.3 Close view and the inside of the discharge chamber

shown on Fig. 3.3.

This anode electrode has two main advantages. First, because of the volume resistivity of the graphite, this anode can inhibit spark formation and can be discharged uniformly allowing a uniform glow discharge. Second, water cooling of the electrode sections is not necessary because of the graphite's heat resistant qualities. Each electrode component is connected to the feeding power supply through a ballast resistor to ensure uniform current distribution across the discharge length.

3.3 HIGH VOLTAGE POWER SUPPLY

To provide the required excitation power for the laser system, a high voltage power supply, which is capable of providing 45 KVA at a maximum current of 15 A was constructed. It consists of three main components:

1. High voltage variac to regulate the required power setting.
2. High voltage transformer to step up the 3-phase line voltage to the high voltage required.
3. High voltage rectifier to rectify the ac voltage and deliver the dc power to the laser electrodes.

The three circuits are described briefly in the next sections and will be shown in Fig. 3.4 of the electric discharge circuit in Section 3.4.

3.3.1 HIGH VOLTAGE VARIAC

To control the power in this system, a VARIAC autotransformer with paralleling choke is used. The three-phase parallel circuit consists of six autotransformers and three W50-P1 inductors. The presence of the inductor is important since it prevents the flow of potentially damaging currents from one unit to another.

3.3.2 HIGH VOLTAGE TRANSFORMER

The high voltage transformer used consists of three transformers each rated at 15 KVA. The three transformers are hooked up as a Delta on the primary side (low voltage side) and connected in a star (wye) circuit on the secondary side (high voltage side). The combination provides 45 KVA at 15 A maximum current.

3.3.3 HIGH VOLTAGE RECTIFIER

The high voltage-rectifier circuit used for this purpose operates from three-phase alternating current and makes use of power silicon rectifier diodes. The circuit consists of 126 rectifier cells arranged in six branches with 21 cells in each branch. Each rectifier cell has a rectifier diode of the type IR2138R shunted with a resistor R (280 K Ω) and a capacitor C (0.01 μ f, 1.6 KV). The function of the shunt resistors is to ensure a uniform voltage distribution amongst the series diodes. Otherwise, it is

probable that the reverse voltage across one or more diodes could exceed the breakdown limit (typically between 1000 to 2000 volts). The shunting capacitors are also used to provide similar protection and act as a filter for possible superimposed noise.

The rectifier assembly is contained in an oil media of sufficient volume to completely cover the assembly. The oil provides an electrical insulating medium which also carries heat away from the diodes. This oil must be of high dielectric strength, low viscosity and free of impurities such as inorganic acid, alkali and corrosive sulphur. The rectifier circuit will be shown among the components of the electric discharge circuit in Fig. 3.4, Section 3.4.

3.4 ELECTRICAL DISCHARGE SYSTEM

The output of the high voltage power supply is coupled to the cathode via a ballast resistor R1. This ballast resistor limits the discharge current flowing through the system. A fuse circuit is inserted in the line to protect the system in the event of a current surge. Figure 3.4 shows the electric discharge circuit. Each of the anode segments are connected to the power supply through identical ballast resistors R2. The role of ballast resistors R2 is to provide a uniform discharge current through the anode sections; thus giving a uniform discharge along the laser axis.

THE ELECTRIC DISCHARGE CIRCUIT

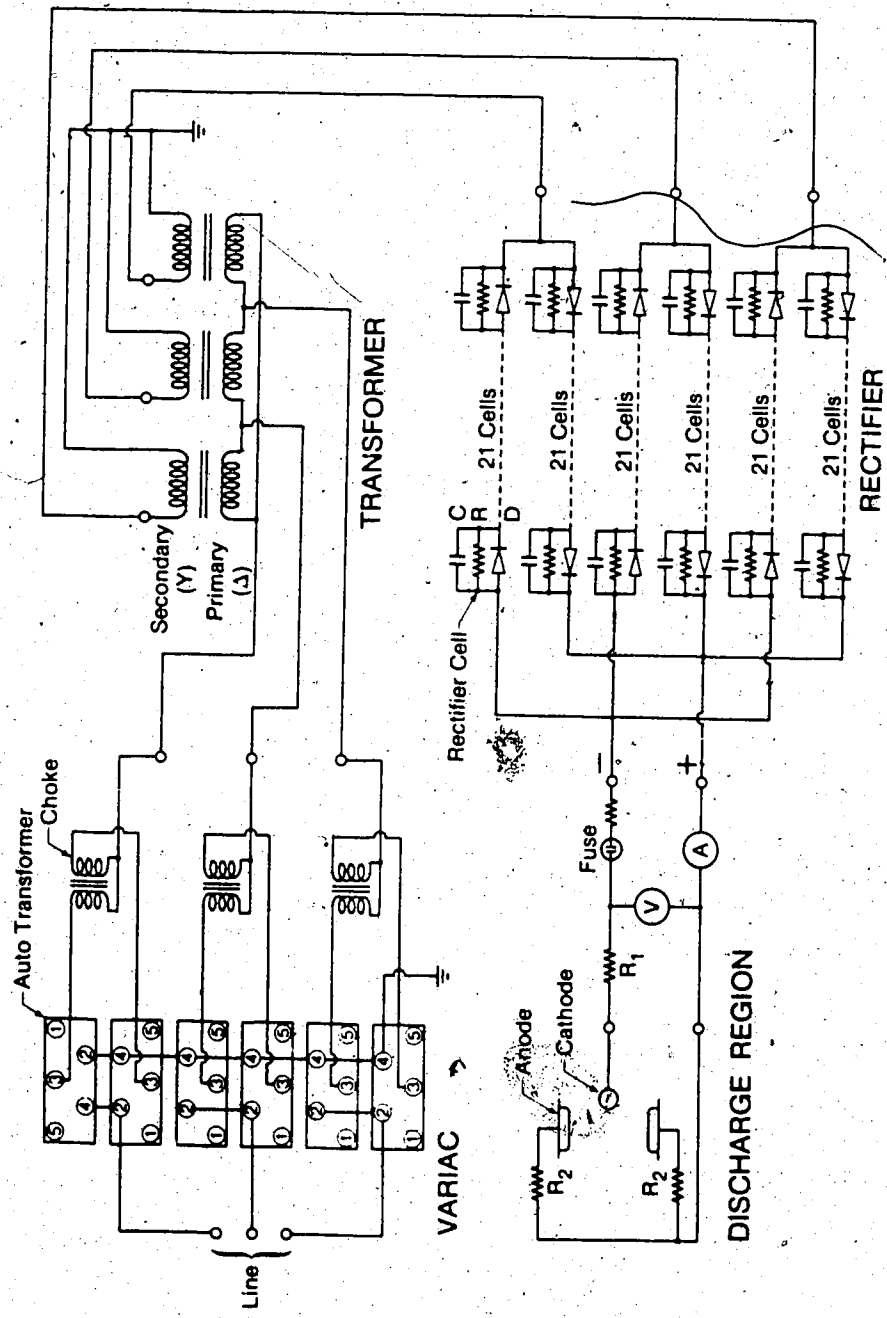


Fig. 3.4 The electric discharge circuit.

3.5 TESTING THE FLOW SYSTEM

The gas velocity distribution across the channel, downstream of the discharge section, was monitored using a pitot tube attached to a capacitance manometer. The pitot tube was inserted into the channel so that its tip was located at position $x=11.5$ cm downstream from the cathode, as shown in Fig. 3.5. The pitot tube was moved along the y -axis to scan the channel height y_{ch} . Measurements were performed at four different points on the z -axis, and at different locations on the x -axis, at $z=z_4$ as shown in Fig. 3.6. The pitot tube, which measures the static and total pressures [102,103], is connected to an electronic pressure meter (capacitance manometer). The pressure difference is measured, and from calibration curves the velocity can be obtained for different laser gas mixtures.

The velocity distribution at points z_1 , z_2 , z_3 and z_4 was obtained for different laser gas mixtures and pressures. With the cathode removed from its place, the velocity distribution was monitored at two locations on the x -axis at $z=z_4$. A total gas pressure of 50 torr, using a mixture of $\text{CO}_2/\text{N}_2/\text{He}$ with the proportions 1:1:18 was used. The results are shown in Fig. 3.7. With the cathode located in its place in the channel, the velocity distribution was monitored at the same previous positions. The results obtained are shown in Fig. 3.8. A stagnation point formed downstream of the cathode, in the middle of the channel, causes the velocity

Experimental Arrangement for Velocity Measurements

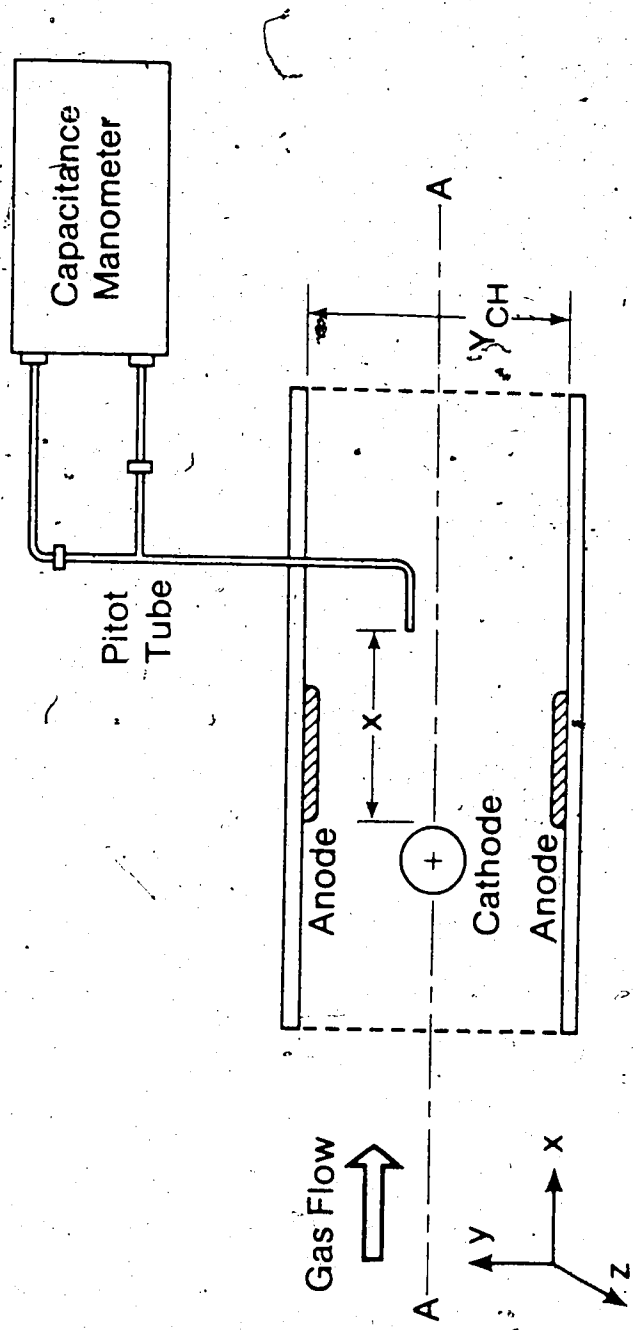


Fig. 3.5 Arrangement for velocity measurements.

Locations Of Measurement Points

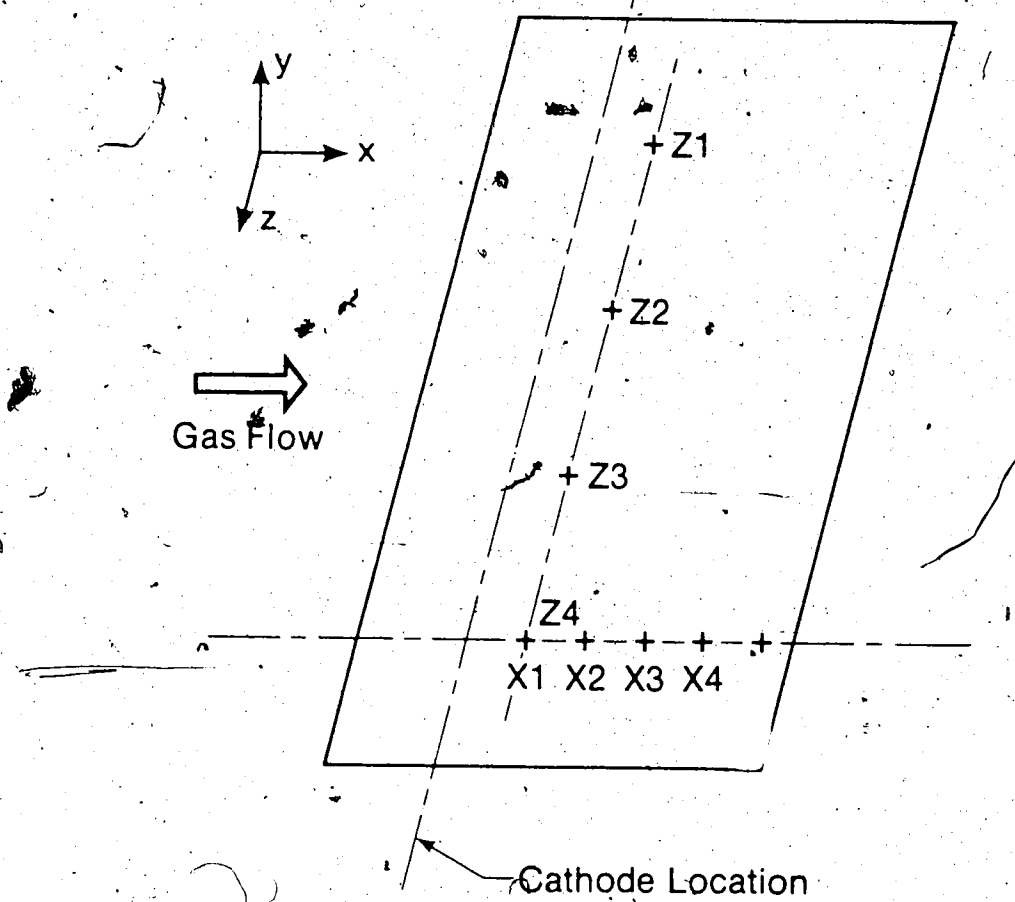


Fig. 3.6 Locations of measurement points.

Measured Velocity Profiles At Z=Z4

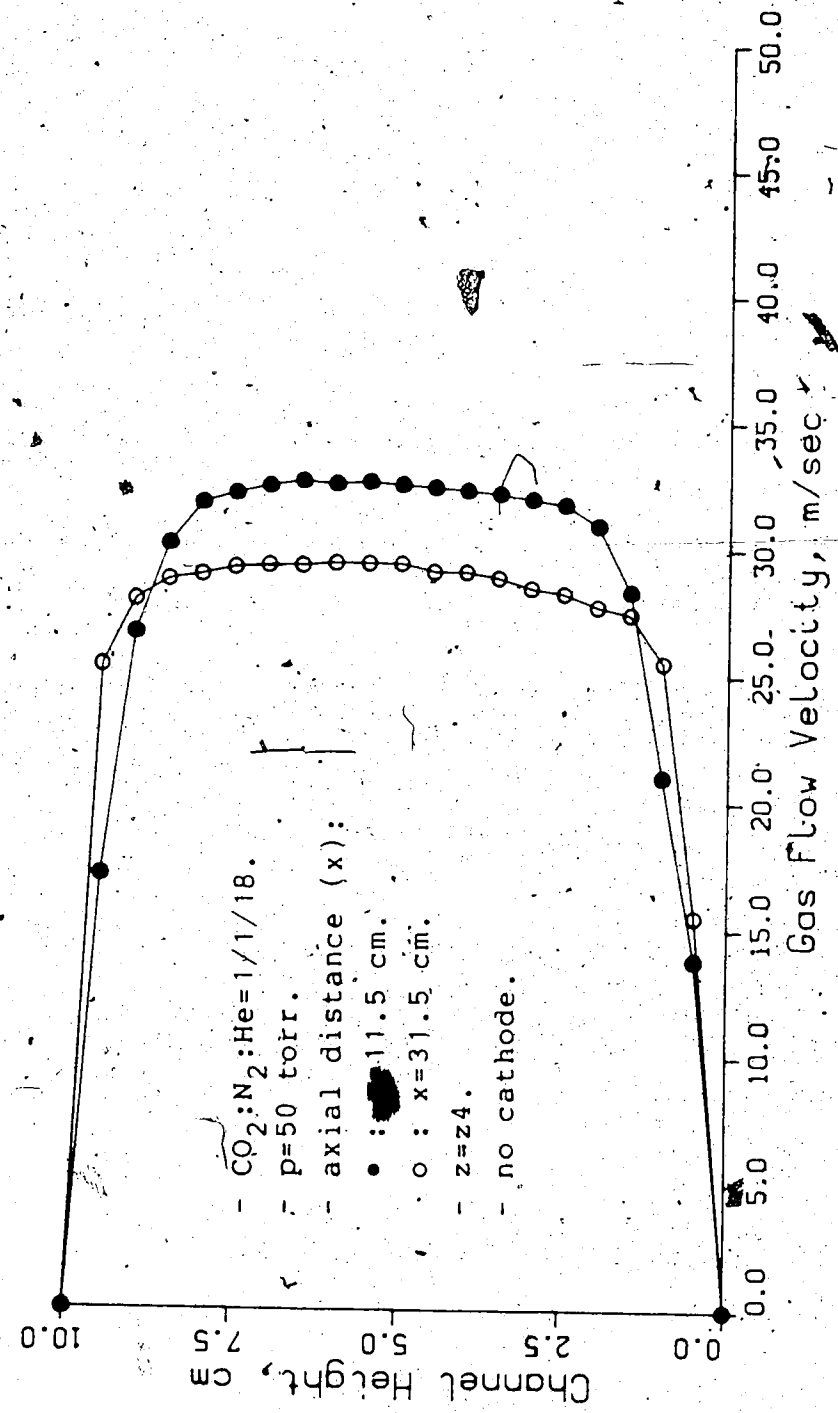


Fig. 3.7 Measured velocity profiles along the x-axis, with no cathode.

Measured Velocity Profiles At $Z=Z_4$

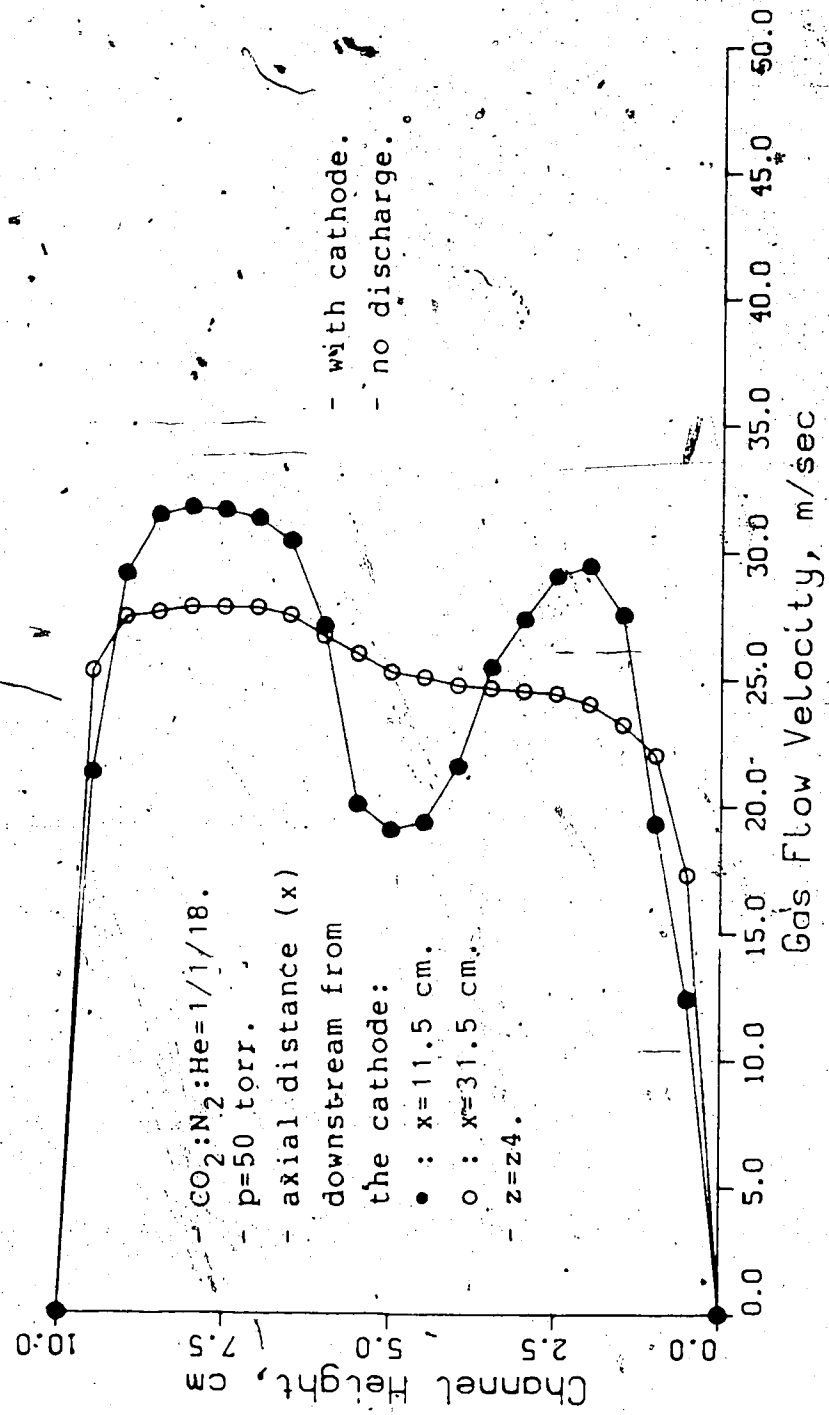


Fig. 3.8 Measured velocity profiles along the x-axis, with cathode in place.

to drop to about 65% of its maximum value. However, the velocity distribution across the channel tends to flatten as the flow advances downstream.

Figure 3.9 shows the gas velocity distribution projected across the z-direction, and measured at $y=7.5$ cm at several points on the z-axis. The flow velocity is seen to have uniform distribution across most of the channel region, with the exception of the edges, where the velocity drops off significantly due to the boundary layer effects [104,105]. Figure 3.10 shows the variation of the gas velocity with gas pressure at $x=11.5$ cm, $y=7.5$ cm and $z=z_2$. The pitot tube was used for these measurements with the experimental setup illustrated in Fig. 3.5. As can be seen from Fig. 3.10, the velocity increases with an increase in pressure of the laser gas mixture.

In conclusion, a Transverse Electric CW Carbon Dioxide Laser Gas Discharge System was designed and constructed. The geometry of the system together with an efficient gas blower allowed a gas velocity which is close to our design estimates. The use of a Mo spiral wire cathode and multiple graphite anodes proved useful in obtaining a uniform glow discharge. The system performed satisfactorily during the course of experimental measurements.

Velocity Distribution
Along The Discharge Length Z

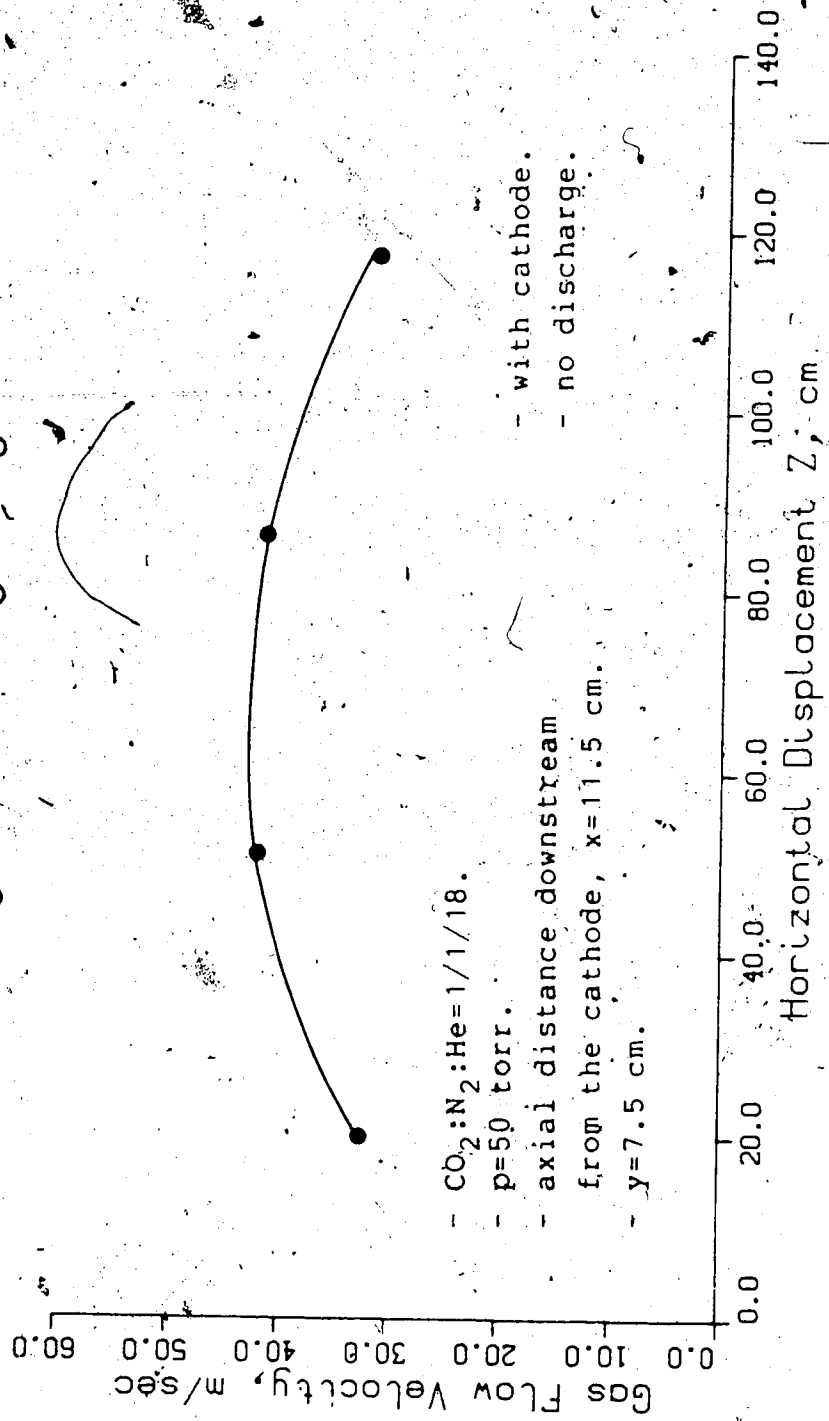


Fig. 3.9 Velocity distribution along the discharge length z.

Gas Velocity vs. Gas Pressure, $Z=Z_2$

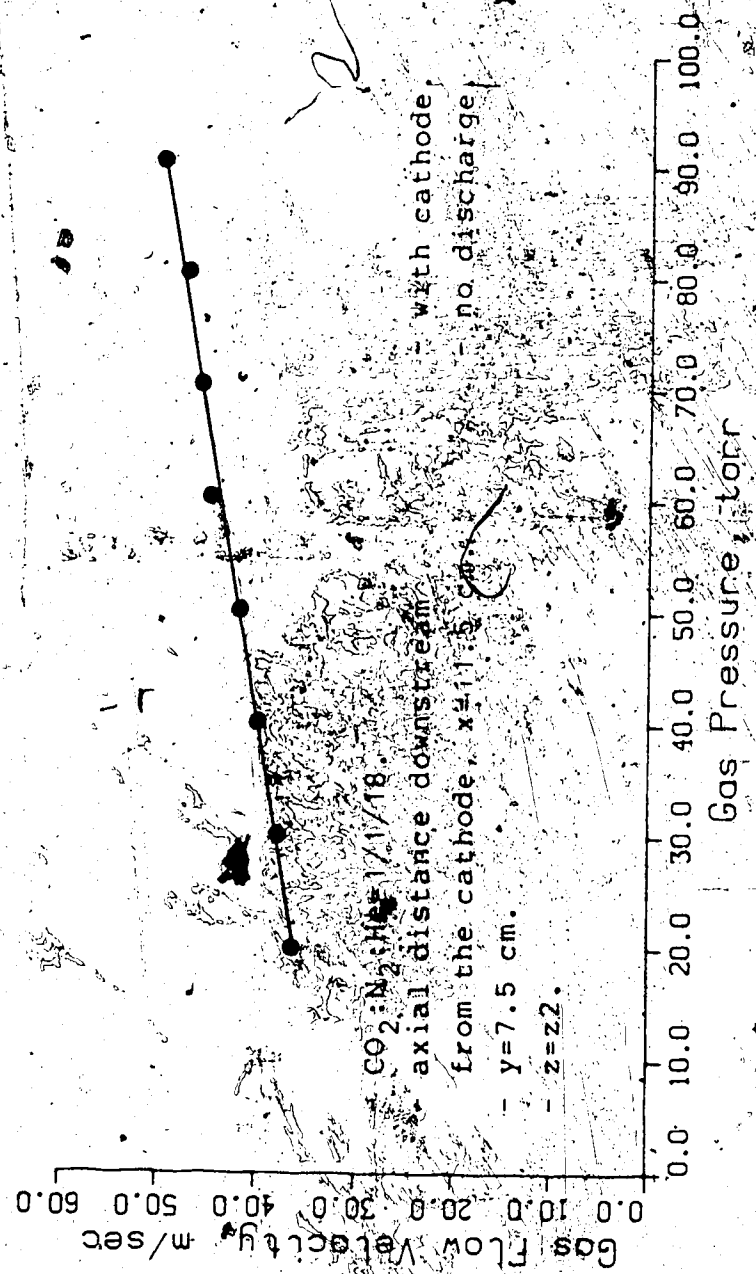


Fig. 3.10 Variation of gas velocity with gas pressure.

Experimental measurements were performed to investigate the behavior of the gas flow discharge in this system and to validate the computer algorithm. Parametric measurements were done to monitor the gas flow velocity and the temperature distribution in the discharge region. The operation of the system and the experimental results will be presented in Chapter 7.

CHAPTER 4

GAS DYNAMIC MODEL AND THE COMPRESSIBLE NAVIER-STOKES EQUATIONS

4.1 INTRODUCTION

In high power carbon dioxide lasers, the pumping mechanism is provided by a gas discharge. As a result, the performance of these electric discharge lasers is highly dependent upon the quality of the glow produced within the laser. To produce a large and efficient laser for useful industrial application, one must increase the discharge volume, the gas pressure and the input power. In doing so, it is necessary to satisfy two conditions: (i) the gas temperature should remain below about 600°K, since otherwise the lower laser level is filled and the population inversion destroyed [88], (ii) the electron temperature should be around 1 eV, in order to obtain high efficiency in transferring energy from the discharge to the upper vibrational levels of the CO₂ and N₂ molecules [88,106].

An interesting way to meet these constraints is to dispose of waste heat by convecting it out of the discharge [6,7,9]. Consequently the output radiation power does not scale with the length of the discharge tube, but rather with the mass flow rate of the lasing medium [107]. To satisfy

condition (ii), it is necessary to maintain a stable glow discharge. However, when the gas pressure or the input power is increased, the glow discharge becomes unstable and tends to collapse into arclike filaments [108]. The presence of various instabilities, such as ionization waves [47] and thermal constriction [36] place serious limitations on the performance of these lasers.

One approach that may be used in preventing the various instabilities from becoming a problem, is to cool the discharge gas efficiently; by rapidly circulating the gas mixture in the system. This should be done rapidly enough to keep the gas residence time well below 1 msec; which is the typical instability threshold time [36] in low pressure devices ($P \leq 100$ Torr). Also different stabilization techniques have been developed to stabilize the discharge. This could be either by ionization assistance [55], or by magnetic fields [82], or by turbulence [71], or by appropriately choosing the material and shape of the discharge electrodes [87]. However, these procedures have still been unable to overcome the scaling problems associated with the development of large volume high power lasers. A better understanding of the kinetic and heat transport processes in these laser gas discharge systems is still needed in order to advance the state of the art for these devices.

The main objective of the present work is to advance the understanding of the behavior of open channel flow laser gas discharges. In particular, the flow structure and heat flow within such devices will be elucidated.

The flow structure within the gas discharge system [109] is described by the Navier-Stokes equations. Unfortunately, the analytical solution of these GD equations, which form a set of nonlinear partial differential equations is, in general, impossible. Thus, a numerical solution is the only recourse.

The time dependent Navier-Stokes equations will be solved numerically in two dimensional cartesian coordinates, in order to give a steady state solution. This particular approach is used to yield a steady state solution because [110]:

1. some steady-state methods are strictly equivalent to time-dependent methods,
2. steady-state iterative methods cannot be presumed to be stable and should be analyzed for stability,
3. a computer program written for the time-dependent approach can be easily modified to achieve the steady-state solution,
4. the time-dependent methods are less susceptible to nonlinear instabilities and are thereby less sensitive to initial conditions, finally,
5. a time-dependent formulation offers the flexibility of

obtaining the transient solution, if it should be desired; more importantly, it does not presume the existence of a steady-state solution, which indeed may not exist.

The medium within the device being studied is a partially ionized gas composed of three fluids. These are: (1) a positively charged ion fluid, (2) a negatively charged electron fluid and (3) a neutral particle fluid. The simultaneous determination of the individual behavior of each of the fluids is complex, and in our case is not necessary. In the analysis that follows a single-fluid model is assumed because: (i) the fluid is actually dominated by the neutral particle fluid since the degree of ionization is very low ($\frac{n_e}{n_n} \approx 10^{-7}$) [130], (ii) there is a strong collisional coupling between the various species [111] thus making a single fluid model a reasonable approximation, and (iii) we are interested in the neutral flow and gas transport processes, rather than dealing with the charged particles. Charged particle behavior is often not well described using a fluid model and often other techniques must be used. For example, a Monte Carlo simulation code was used by Razdan et. al. [97,98] to describe the behavior of electrons and ions as they traverse the cathode fall region under the influence of magnetic fields.

In this chapter, the single fluid/gas-dynamic equations implemented in our computer code IGCP (Implicit Gasdynamic

Computer Program will be presented. These equations will be expressed in vector form and then expanded in orthogonal curvilinear coordinates. The solution of the resulting set of equations will be used to describe gas flow behavior in our laser device.

The nonlinear partial differential equations will be approximated by suitable finite-difference equations. This procedure leads to a set of algebraic equations which can be solved on a computational grid. By making the grid spacings sufficiently small, it is hoped that the solution obtained will give a good approximation to the solution of the original partial differential equations [112].

4.2 EQUATIONS OF MOTION

The motion of a compressible viscous fluid is governed by a set of differential equations [113-115] which represent the conservation of mass, momentum and energy. The first fluid equation (continuity equation) expresses conservation of mass and is given by:

$$\frac{\partial \rho}{\partial t} + \nabla \cdot (\rho \vec{v}) = 0 \quad (4.1)$$

where ρ and \vec{v} are the neutral gas density and velocity respectively.

The conservation of momentum is represented by the equation of motion as:

$$\frac{\partial}{\partial t} (\rho \vec{v}) + \nabla \cdot (\rho \vec{v} \vec{v}) + \nabla \cdot \Pi = 0 \quad (4.2)$$

where Π is the pressure tensor which is given by:

$$\Pi = \tau + pI \quad (4.3)$$

where τ is the viscous stress tensor, p is the hydrostatic pressure and I is the unit tensor.

τ can be described in subscript notation [116] as follows:

$$\tau_{ik} = -\eta \left(\frac{\partial v_i}{\partial x_k} + \frac{\partial v_k}{\partial x_i} - \frac{2}{3} \delta_{ik} \frac{\partial v_j}{\partial x_j} \right) + \xi \delta_{ik} \frac{\partial v_j}{\partial x_j}, \quad (4.4)$$

where η is the shear viscosity and ξ is the bulk viscosity.

This enables us to write Eqn 4.2 in vector form as:

$$\frac{\partial}{\partial t} (\rho \vec{v}) + \nabla \cdot (\rho \vec{v} \vec{v}) - \eta \nabla \cdot \nabla \vec{v} - (\xi + \frac{1}{3} \eta) \nabla (\nabla \cdot \vec{v}) = - \frac{KT}{m} \frac{1}{h} \frac{\partial \rho}{\partial x}. \quad (4.5)$$

Finally, the conservation of energy equation including a heat source term (Ohmic heating) is given by:

$$T \frac{DS}{Dt} = \frac{K \Delta^2}{\rho} + \Phi + \frac{1}{\rho} \frac{\partial}{\partial x^1} (K \frac{\delta T}{\partial x^1}) + Q. \quad (4.6)$$

In this equation, the term on the left-hand side represents the rate of change in the internal energy and is given by:

$$T \frac{DS}{Dt} = C_p \frac{dT}{dt} - \frac{\alpha T}{\rho} \frac{dP}{dt}, \quad (4.7)$$

where

$$\alpha = \frac{1}{V} \left(\frac{\partial V}{\partial T} \right)_P. \quad (4.8)$$

The first three terms on the right-hand side of Eqn. 4.6 represent molecular transport effects. The first term accounts for the dissipation of mechanical energy. The second term represents the rate of work from viscous stresses. The third term describes the internal conduction of heat. The fourth term (Q) is the external heat source per unit mass (Ohmic heating). Also we have

$$\Delta = e^{11} = \frac{\partial u^1}{\partial x^1} \quad (4.9)$$

and

$$\Phi = \frac{2\eta}{\rho} (e^{10} e^{11} - \frac{1}{3} \Delta^2) \quad (4.10)$$

where

$$e^{10} = \frac{1}{2} \left(\frac{\partial u^1}{\partial x^0} + \frac{\partial u^0}{\partial x^1} \right) \quad (4.11)$$

Using Eqn. 4.6 and Eqn. 4.7 we can write:

$$C_p \frac{dT}{dt} - \frac{\alpha T}{\rho} \frac{dP}{dt} = \frac{K \Delta^2}{\rho} + \Phi + \frac{1}{\rho} \frac{\partial}{\partial x^1} (K \frac{\partial T}{\partial x^1}) + Q. \quad (4.12)$$

In Eqn. 4.12, the second term on the left-hand side is small and can be neglected [1,17] for parameters of interest in our experiment. Also, the first term on the right-hand side is very small and can be neglected [114]. Thus Eqn. 4.12 can be simplified to:

$$C_p \frac{dT}{dt} = \Phi + \frac{1}{\rho} \frac{\partial}{\partial x^1} (K \frac{\partial T}{\partial x^1}) + Q. \quad (4.13)$$

Substituting Eqns. 4.9-4.11 into Eqn. 4.13, and arranging the derivative terms, we can write the conservation of

energy equation in vector form as:

$$\frac{\partial T}{\partial t} + C_p \nabla \cdot (\vec{v} T) - \frac{2\eta}{\rho} (\nabla \vec{v})^2 + \frac{2\eta}{3\rho} (\nabla \cdot \vec{v})^2 - \frac{K}{\rho} \nabla \cdot (\nabla T) = Q . \quad (4.14)$$

Thus Eqn. 4.1, Eqn. 4.5 and Eqn. 4.14 can be arranged in vector form as:

$$\frac{\partial \rho}{\partial t} + \nabla \cdot (\rho \vec{v}) = 0 . \quad (4.15a)$$

$$\frac{\partial}{\partial t} (\rho \vec{v}) + \nabla \cdot (\rho \vec{v} \vec{v}) - \eta \nabla \cdot \nabla \vec{v} - \eta (\nabla \cdot \vec{v}) (\nabla \cdot \vec{v}) + \frac{KT}{m} \frac{1}{h} \frac{\partial \rho}{\partial x} = 0 . \quad (4.15b)$$

$$\frac{\partial T}{\partial t} + \nabla \cdot (\vec{v} T) - \frac{2\eta}{\rho C_p} (\nabla \vec{v})^2 + \frac{2\eta}{3\rho C_p} (\nabla \cdot \vec{v})^2 - \frac{K}{\rho C_p} \nabla \cdot (\nabla T) - Q = 0 , \quad (4.15c)$$

where $Q'' = Q/C_p$

Equations 4.15 represent a set of nonlinear equations in the four unknowns ρ , $\rho \vec{v}$ and T , and constitute the basis of our two dimensional model.

4.3 GAS DYNAMIC EQUATIONS IN CARTESIAN COORDINATES

The set of Equations 4.15 must be expanded in a chosen coordinate system. The finite-difference technique can then be applied to the resulting equations. In our case, Eqns. 4.15 were first expanded in orthogonal curvilinear coordinates [118] to keep them as general as possible, so they can be used for different coordinate systems as required. This procedure is explained in detail in Appendix A.

Equations A.14 are the resulting equations in a general coordinate system. Reducing these equations to two dimensional cartesian coordinate results in a set of equations A.16 that are used in IGCP to simulate the gas flow behavior. Equations A.16 can then be represented in the following vector form:

$$\frac{\partial}{\partial t} \vec{M}(\vec{u}) + \vec{F}(\vec{u}) + \vec{G}(\vec{u}) = 0, \quad (4.16)$$

where $\vec{M}(\vec{u}) = \{\rho \vec{v}, \rho, T\}$ are the quantities advanced in time and $\vec{u} = \{v_1, v_2, \rho, T\}$ is the state vector of the system. The function $\vec{F}(\vec{u})$ contains all terms in Eqns. A.16 that have leading derivatives with respect to x_1 . These leading derivatives can take any of the following forms:

$$(1) \alpha \frac{\partial \phi}{\partial x_1} \quad (4.17a)$$

$$(2) \frac{\partial}{\partial x_1} (\alpha \phi) \quad (4.17b)$$

$$(3) \alpha \frac{\partial \phi}{\partial x_1} \frac{\partial \psi}{\partial x_2} \quad (4.17c)$$

$$(4) \frac{\partial}{\partial x_1} \left[\alpha \frac{\partial \phi}{\partial x_1} \right] \quad (4.17d)$$

$$(5) \frac{\partial}{\partial x_1} \left[\alpha \frac{\partial \phi}{\partial x_2} \right]. \quad (4.17e)$$

Similarly, the function $\vec{G}(\vec{u})$ contains all terms in Eqns. A.16 that have leading derivatives with respect to x_2 .

Comparing Eqns. A.16 and 4.16, the terms \vec{F} and \vec{G} can be inferred. Spatial and temporal finite differencing can then be applied to these terms as will be shown in the following

sections.

4.4 BASIC NUMERICAL CONSIDERATIONS

To solve a system of differential equations numerically, the continuous space-time domain must be replaced by a discrete space-time mesh. Also, the differential equations must be approximated at each mesh point by using algebraic finite difference equations. These relate the dependent variables at time t^{n+1} to the known variables at time t^n . If the finite difference equations are uncoupled in the unknowns between time levels, the difference equations are said to be explicit. In this case, the solution of a set of m difference equations valid over a two-dimensional lattice containing $N \times M$ points, involves a set of $m \times N \times M$ algebraic equations in the same number of unknowns.

The numerical solution of multi-dimensional compressible Navier-Stokes equations requires considerable computing resources. Therefore efficient computational techniques are a must. In the past, standard explicit methods [119, 120], were used to solve this problem. The requirement for numerical stability of an explicit scheme requires that an upper bound on the time step Δt given by the CFL (Courant-Friedrichs-Lowy) condition be respected. The CFL condition requires that the difference solution, which can propagate information across the mesh at a maximum

rate of one space step Δx during each time step Δt , must exceed all propagation speeds of the physical system being modelled. This includes effects as wave propagation, fluid motion and diffusion [121]. For our problem, the CFL condition is given by:

$$\Delta t \leq \Delta x / [v_a + \frac{\eta}{\rho \Delta x} + C_s] \quad (4.18)$$

In Eqn. 4.18, v_a is the advective velocity, η is the viscosity and C_s is the adiabatic sound speed given by:

$$C_s = \sqrt{\frac{\gamma p}{\rho}} \quad (4.19)$$

The restrictions are, of course, conditions which must be satisfied throughout the entire grid. With an upper bound on the time step, the explicit method although stable, it is not efficient particularly in dealing with multidimensional problems.

On the other hand, if the finite difference equations are coupled in the unknowns then the equations are said to be implicit, and in this case a simultaneous solution of the $m \times N \times M$ equations is required. Here, the number of multiplications involved in solving N simultaneous linear algebraic equations [122] is approximately $\frac{2}{3} N^3$. Therefore, the computing time per time step in a two-dimensional fully implicit calculation [123] can potentially be excessive. However, in contrast to the explicit techniques, the implicit method is stable regardless of the time step size.

used in the solution of the linear differential equations. When implicit differencing is used, the lattice speed or velocity of transmital on the mesh is infinite and the CFL limitation is always satisfied. Moreover, the time step limitation is relaxed from the CFL condition for nonlinear PDE's as well. [124]

In order to avoid the restrictions imposed on the time step when using an explicit differencing technique and the excessive computer time required in the implicit method, several authors [125-128] have incorporated the alternating direction implicit (ADI) technique first described by Peaceman and Rachford [129]. In this technique, the time advancement of the equations is divided into two steps. In the first half time step, the variables are advanced implicitly in one dimension and explicitly in the other dimension. The procedure is then reversed during the second half time step. Therefore, during one half time step there are M uncoupled set of $m \times N$ coupled simultaneous equations, and during the second half time step there are N uncoupled sets of $m \times M$ coupled simultaneous equations. These two sets are solved alternately during one full time step. Thus the ADI technique effectively reduces the required computer time and consequently the computational costs, while at the same time allowing large time steps to be used.

In the present work, we are using the ADI technique to solve the two-dimensional compressible Navier-Stokes equations. The numerical solution of a system of nonlinear

differential equations requires that these equations be replaced by a system of algebraic finite difference equations.

To define a continuous function $u(x,t)$ on the domain (x_1, x_2) , it is necessary that this domain be represented as a set of discrete points \bar{x}_i , $1 \leq i \leq I$, i.e., the domain is divided into a set of $N-1$ elements of width Δx such that:

$$\bar{x}_m = x_1 + \sum_{m=1}^{I-1} \Delta x_m \quad (4.20)$$

where

$$\Delta x_m = \bar{x}_m - \bar{x}_{m-1} \quad (4.21)$$

It is important to notice that the scale length Δx must be smaller than the wavelength of the rapidly varying function so that the phenomena can be observed. The points \bar{x}_i form a mesh or grid. The mesh points may move with a certain velocity with respect to a stationary observer in the laboratory frame. If this velocity equals the velocity of the fluid at all points on the mesh, the mesh is called Lagrangian. If this velocity is zero, then the mesh is called Eulerian.

Time can also be discretized and divided into small finite intervals which separate levels or moments in time so that:

$$t^n = t^0 + \sum_{m=1}^n \Delta t^m \quad (4.22)$$

where t^0 is an initial time and

$$\Delta t^m = t^m - t^{m-1} \quad (4.23)$$

Note also that Δt^m must be very small so that significant time dependent information is not lost. Now, the continuous function $\vec{u}(x,t)$ can be represented in a discrete form as:

$$\vec{u}_i^n = \vec{u}(\bar{x}_i, t^n) \quad (4.24)$$

which is defined over a temporal and spatial mesh or grid.

4.5 THE COMPUTATIONAL MESH

In the ICP an Eulerian mesh is used in which mesh points are kept fixed in the laboratory frame. The values of the discrete function $\vec{u}(\bar{x}_i, t^n)$ which are specified on mesh points, are defined as cell-centered quantities. In this case, the value of $\vec{u}_{i,j}$ is the average value of \vec{u} in the two-dimensional cell centered at $(\bar{x}_{i_1}, \bar{x}_{j_2})$. Figure 4.1 illustrates a mesh on a single plane where the dots represent the points at which the values of the state vector \vec{u} are stored. The interface points at which fluxes and forces are evaluated are represented by the triangles.

To describe the computational mesh, the mesh element Δ_n (where $n=1, 2$ and indicates the coordinate involved), is defined as the distance between two points x_{n_i} and $x_{n_{i+1}}$ where $\bar{x}_n = \{x_1, x_2\}$ is represented in orthogonal curvilinear coordinates. This can be described as:

The Finite Difference Computational Mesh

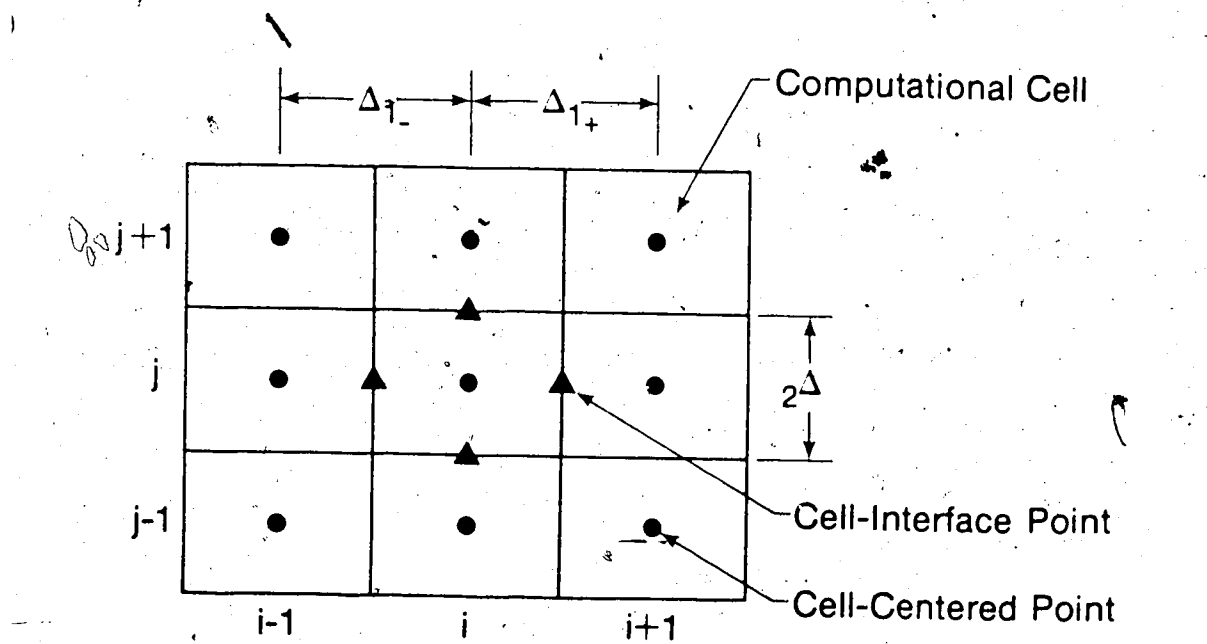


Fig. 4.1 The finite difference computational mesh.

$$\begin{aligned}
 \Delta_{1+} &= x_{1_{i+1}} - x_{1_i} \\
 \Delta_{1-} &= x_{1_i} - x_{1_{i-1}} \\
 \Delta_{2+} &= x_{2_{j+1}} - x_{2_j} \\
 \Delta_{2-} &= x_{2_j} - x_{2_{j-1}}
 \end{aligned} \tag{4.25}$$

The nonuniform mesh can be specified by the variable Δ 's presented in Eqns. 4.25.

The distances between cell interfaces are represented by Δ and are given by:

$$\Delta = \frac{1}{2}(\Delta_{1+} + \Delta_{1-}) \tag{4.26}$$

$$\Delta = \frac{1}{2}(\Delta_{2+} + \Delta_{2-})$$

The value of a variable at the cell interface is equivalent to the average of the variable at the two adjacent cells and is defined by:

$$\begin{aligned}
 \bar{M}_{1+} &= \frac{1}{2}(M_{1_{i+1}} + M_{1_i}) \\
 \bar{M}_{1-} &= \frac{1}{2}(M_{1_{i-1}} + M_{1_i}) \\
 \bar{M}_{2+} &= \frac{1}{2}(M_{2_{j+1}} + M_{2_j}) \\
 \bar{M}_{2-} &= \frac{1}{2}(M_{2_{j-1}} + M_{2_j})
 \end{aligned} \tag{4.27}$$

The δ operators give the flux or force differences across the interface, these represent the forward and backward differencing scheme, and are defined along the x , direction as

$$\delta_{1+}(\mathbf{F}) = \frac{1}{\Delta_{1+}}(F_{1+1} - F_1) \quad (4.28a)$$

$$\delta_{1-}(\mathbf{F}) = \frac{1}{\Delta_{1-}}(F_1 - F_{1-1}) \quad (4.28b)$$

Similarly, the δ operator for the x_2 -direction produces

$$\delta_{2+}(\mathbf{F}) = \frac{1}{\Delta_{2+}}(F_{2+1} - F_2) \quad (4.29)$$

$$\delta_{2-}(\mathbf{F}) = \frac{1}{\Delta_{2-}}(F_2 - F_{2-1})$$

~~4.6 SPATIAL FINITE DIFFERENCING~~

In the Gas Dynamic Equations A.16, there are two basic types of terms. The first type are terms that arise from the divergence of fluxes in the conservative equations as a result of advection and viscous processes. In the expanded GD equations, all terms of the form $\frac{\partial}{\partial x_i}(\alpha F)$, where F is any general factor including differential terms and α is usually a transport coefficient, are called flux terms. Sometimes F may take the form $\frac{\partial \psi}{\partial x_2}$, therefore both plane second derivatives and mixed second derivatives are subsets of the flux terms. The second type of term that exists in the GD equations A.16 has the form $\beta \frac{\partial F}{\partial x_i}$, where β is some function of the state vector \vec{u} . These terms arise from the pressure gradient forces and are called force terms. These force terms are usually found in the momentum and energy equations. The titles flux and force are used to categorize the type of finite differencing that will be applied.

throughout the GD equations and not to label their physical significance.

When we apply the spatial finite difference technique to the set of differential equations, we form a system of algebraic equations which describe changes to the cell-centered quantities. These variations are due to the transport of fluxes into and out of each cell which result from forces being applied to these cells. In this case, flux and force terms must be calculated at the cell interfaces.

In the following two sub-sections, finite difference approximations to the differential equations given by A.16 will be developed, in the same way as was done by Finan [124].

4.6.1 FLUX TERM DIFFERENCING

The flux terms measure the flow into or out of the computational cell. Therefore these terms must be evaluated at the cell boundaries. Therefore, the finite difference form is given by:

$$\frac{\partial}{\partial x_i} (\alpha F) \rightarrow \frac{\alpha F_+ - \alpha F_-}{\Delta}, \quad (4.30)$$

where α and F are the average of two adjacent cells as described by Eqns. 4.27 in section 4.5. In the case when F represents a derivative term (e.g. $F = \frac{\partial G}{\partial x_i}$), the finite difference equation takes the form:

$$\frac{\partial}{\partial x_1} (\alpha \frac{\partial G}{\partial x_1}) \rightarrow \frac{\alpha \delta_+ (G) - \alpha \delta_- (G)}{\Delta}, \quad (4.31)$$

where the δ operator is the difference across the cell interface and is defined by Eqns. 4.28 and Eqns. 4.29. In the case of a uniform mesh and a constant α , the definitions given in Eqns. 4.30 and Eqns. 4.31 reduce to the normal first and second derivative finite difference approximations as:

$$\frac{\partial}{\partial x_1} (\alpha F) \rightarrow \alpha \frac{F_{i+1} - F_{i-1}}{2\Delta x} \quad (4.32)$$

and

$$\frac{\partial}{\partial x_1} (\alpha \frac{\partial G}{\partial x_1}) \rightarrow \alpha \frac{G_{i+1} - 2G_i + G_{i-1}}{(\Delta x)^2} \quad (4.33)$$

However, in our analysis a nonuniform mesh will be used, and therefore Eqns. 4.30 and Eqns. 4.31 are required.

For mixed derivatives, where

$$F' = \frac{\partial G}{\partial x_2} \quad (4.34)$$

we first take the derivative in the x_2 direction at the points B_+ , B_- in Fig. 4.2 and average them to arrive at a value F_+ at the cell interface. Then we repeat the same process by taking the derivative in the x_2 direction at the points A_+ , A_- and average them to obtain the value F_- at the cell interface. In this case the differential with respect

The Mesh Points Used in Mixed Derivative Calculations

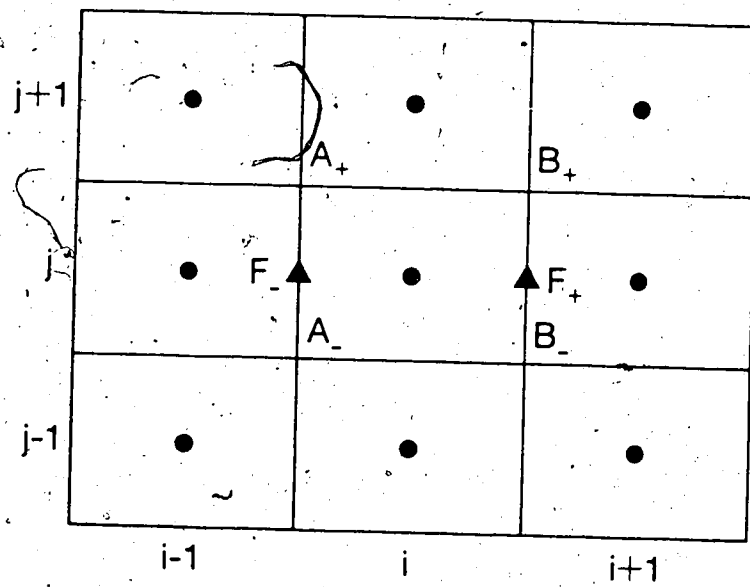


Fig. 4.2 Mesh points used in mixed derivative calculations.

to x_1 gives:

$$\frac{\partial}{\partial x_1} (\alpha \frac{\partial G}{\partial x_2}) \rightarrow \frac{\alpha_+ F_+ - \alpha_- F_-}{\Delta} = \left[\alpha_+ \left(\frac{\partial G}{\partial x_2} \right)_+ - \alpha_- \left(\frac{\partial G}{\partial x_2} \right)_- \right] / \Delta \quad (4.35)$$

where

$$\begin{aligned} \left(\frac{\partial G}{\partial x_2} \right)_+ &= \frac{1}{2} \left\{ \left[\frac{1}{2} (G_{i+1,j+1} + G_{i,j+1}) - \frac{1}{2} (G_{i+1,j} + G_{i,j}) \right] / \Delta_+ \right. \\ &\quad \left. + \left[\frac{1}{2} (G_{i+1,j} + G_{i,j}) - \frac{1}{2} (G_{i+1,j-1} + G_{i,j-1}) \right] / \Delta_- \right\} \end{aligned} \quad (4.36a)$$

and

$$\begin{aligned} \left(\frac{\partial G}{\partial x_2} \right)_- &= \frac{1}{2} \left\{ \left[\frac{1}{2} (G_{i,j+1} + G_{i-1,j+1}) - \frac{1}{2} (G_{i,j} + G_{i-1,j}) \right] / \Delta_+ \right. \\ &\quad \left. + \left[\frac{1}{2} (G_{i,j} + G_{i-1,j}) - \frac{1}{2} (G_{i,j-1} + G_{i-1,j-1}) \right] / \Delta_- \right\} \end{aligned} \quad (4.36b)$$

It must be noticed that the terms are evaluated at the center of the interfaces in all cases.

4.6.2 FORCE TERM DIFFERENCING

The force terms measure the total effect on the edges of the computational mesh that has been done by the applied forces. Therefore, these terms are defined as the average of the forces applied on each cell face as:

$$\beta \frac{\partial F}{\partial x_1} \rightarrow \frac{1}{2} \left[\beta_+ \delta_{1+}(F) + \beta_- \delta_{1-}(F) \right] \quad (4.37)$$

Where the operator $\delta_{1\pm}$ has been given in section 3.5.

Finally, products of derivatives which are usually found in the energy equation, can be put in the form:

$$\beta \frac{\partial F}{\partial x_1} + \frac{\partial G}{\partial x_2} \frac{\partial F}{\partial x_1} = \frac{1}{2} \left\{ \left(\frac{\partial G}{\partial x_2} \right)_{1+1/2} \delta_{1+}^+(F) + \left(\frac{\partial G}{\partial x_2} \right)_{1-1/2} \delta_{1-}^-(F) \right\} \quad (4.38)$$

Here, the term $\left(\frac{\partial G}{\partial x_2} \right)_{1+1/2}$ is determined in a way similar to $\left(\frac{\partial G}{\partial x_2} \right)_{1-1/2}$ in the flux terms as given by Eqns. 4.36.

4.7 TEMPORAL FINITE DIFFERENCING

As was mentioned earlier, the computer code IGCP uses the alternating direction implicit (ADI) technique first described by Peaceman and Rachford [129], to advance the solution in time. This necessitates that the set of Equations 4.15 be represented in the vector form given by Eqn. 4.16.

The alternating direction implicit (ADI) finite difference method can now be applied to the system of equations presented in Eqns. 4.16. In this technique, the derivative terms in the x-direction are replaced by implicit difference terms over the first half time step $\Delta t/2$, while the derivative terms in the y-direction are treated explicitly. The process then reversed over the second half time step, where the derivative terms in the y-direction are replaced by the implicit finite differences and the derivative terms in the x-direction are treated explicitly. This time-centering ADI technique is described by the

following two-step process:

$$\frac{(\vec{M}(\vec{u}^*) - \vec{M}(\vec{u}^n))}{\Delta t/2} + \vec{F}(\vec{u}^*, \vec{u}^n) + \vec{G}(\vec{u}^n) = 0 \quad (4.39a)$$

and

$$\frac{(\vec{M}(\vec{u}^{n+1}) - \vec{M}(\vec{u}^*))}{\Delta t/2} + \vec{F}(\vec{u}^*) + \vec{G}(\vec{u}^{n+1}, \vec{u}^*) = 0 \quad (4.39b)$$

where

\vec{u}^n is the state vector at the old time step,

\vec{u}^* is the intermediate value of the state vector at the end of the first half time step, and

\vec{u}^{n+1} is the state vector at the end of the second half time step (that is, the solution at time t^{n+1}).

During the first half time step, Eqn. 4.39a is used to solve for the intermediate values \vec{u}^* . Then \vec{u}^* are used in Eqn. 4.39b during the second half time step to determine the solution \vec{u}^{n+1} at the end of the time step Δt . Although each of Eqns. 4.39 is first order accurate in Δt , the combination of the two equations is second order accurate [124]. Equations 4.39, which represent a predictive-corrective method, describe the time advancement scheme used in the Implicit Gasdynamic Computer Program (IGCP).

It may be noted that the forms of the functions $\vec{F}(\vec{u})$ and $\vec{G}(\vec{u})$ in Eqn. 4.16 are well defined except for mixed and product derivative terms. To avoid the complication in dealing with these terms, we choose to treat the mixed and

product terms fully explicitly, as was done by Finan [124] and by Antoniuk [130]. Although this lowers the accuracy to order Δt for these terms and introduces a Courant limit on the time step size, the simplicity of using this method balances the occurrence of any slight inaccuracies. A variation on this explicit method for the product terms that gives some time centering is [124]:

$$\left(\frac{\partial F}{\partial x_1} \frac{\partial G}{\partial x_2} \right)^n \rightarrow \frac{1}{2} \left(\frac{\partial F^n}{\partial x_1} \frac{\partial G^{n+1}}{\partial x_2} + \frac{\partial F^{n+1}}{\partial x_1} \frac{\partial G^n}{\partial x_2} \right) \quad (4.43)$$

In the next chapter, the linearization and solution of the difference equations and the different boundary conditions for the problem under investigation, will be presented.

CHAPTER 5

LINEARIZATION AND SOLUTION OF THE FINITE DIFFERENCE EQUATIONS

5.1 INTRODUCTION

In the previous chapter we presented the gasdynamic (GD) differential equations, and described the finite difference schemes which can be used to transfer these differential equations into difference equations. When we apply the spatial and temporal finite difference techniques to the GD equations a set of nonlinear difference equations is obtained. In this chapter, the linearization and solution of the set of nonlinear difference equations will be described.

5.2 LINEARIZATION OF THE FINITE DIFFERENCE EQUATIONS

A set of nonlinear algebraic equations of the following form is obtained when spatial and temporal finite differences approximations are used in Eqns. A.16;

$$\vec{M}(\vec{u}^*) - \vec{M}(\vec{u}^n) + \frac{\Delta t}{2} \vec{F}(\vec{u}^*, \vec{u}^n) + \frac{\Delta t}{2} \vec{G}(\vec{u}^n) = 0 \quad (5.1)$$

where

$$\vec{u} = \begin{bmatrix} v \\ u \\ \rho \\ T \end{bmatrix} \quad (5.2)$$

and

$$\vec{M}(\vec{u}) = \begin{bmatrix} \rho v \\ \rho u \\ \rho \\ T \end{bmatrix} \quad (5.3)$$

In Eqn. 5.1, the nonlinear terms ρv and ρu are present when terms such as v , u , ρ and T are to be determined at the following time step. Therefore the system of equations 5.1 cannot be solved in a direct and straightforward way.

However, this difficulty can be overcome by using an iterative technique to solve these nonlinear equations. The system of equations must then be linearized. Since our differencing is of a second order in time, we would like to linearize the equations in a manner as to retain the same accuracy in Δt in the remaining terms. The nonlinear system of equations given by Eqn. 5.1 can be written in a form that is comprised of explicit and implicit terms as follows:

$$\vec{T}(\vec{u}^n, \vec{u}^*) = \vec{T}_e(\vec{u}^n) + \vec{T}_i(\vec{u}^n, \vec{u}^*) = 0, \quad (5.4)$$

where $\vec{T}_e(\vec{u}^n)$ is the explicit term which depends only on \vec{u}^n , and $\vec{T}_i(\vec{u}^n, \vec{u}^*)$ is the implicit term which in general depends on both \vec{u}^* and \vec{u}^n .

A Taylor series expansion in time can be used to linearize the set of nonlinear equations. This requires that the function $\vec{T}(\vec{u}^n, \vec{u}^*)$, in Eqn. 5.4 be continuous and differentiable, so that the function $\vec{T}(\vec{u}^{n+1}, \vec{u}^*)$ can be

expressed in terms of the function and its derivatives at an earlier stage (\vec{u}^*) as:

$$\ell+1\vec{T} = \ell\vec{T} + \hat{J}^\ell \cdot \left[\frac{\partial \vec{u}^*}{\partial t} \right]^\ell \Delta t + O(\Delta t)^2$$

or

$$\ell+1\vec{T} = \ell\vec{T} + \left[\frac{\partial \vec{T}}{\partial \vec{u}^*} \right]^\ell \cdot \left[\frac{\partial \vec{u}^*}{\partial t} \right]^\ell \Delta t + O(\Delta t)^2 \quad (5.5)$$

where $\hat{J} = \frac{\partial \vec{T}}{\partial \vec{u}^*}$ is the standard Jacobian which involves the \vec{u}^* dependence only, and its elements are given by:

$$\hat{J} = \frac{\partial \vec{T}}{\partial \vec{u}^*} = \frac{\partial (T_1, T_2, T_3, T_4)}{\partial (v^*, u^*, \rho^*, T^*)} \quad (5.6)$$

In this equation, only the implicit terms of $\vec{T}(\vec{u}^*, \vec{u}^*)$ are involved in the differentiation.

In Eqn. 5.5, $\ell+1\vec{T} = \vec{T}(\ell+1\vec{u})$ where ℓ is the iteration index.

This expansion procedure can be carried one step further so that this can be expressed as the first step in a generalized Newton-Raphson iteration. In Eqn. 5.4, the set of nonlinear algebraic equations $\vec{T}(\vec{u}^*, \vec{u}^*)$ is equal zero, consequently the desired solution for $\ell+1\vec{T}$ in Eqn. 5.5 is zero. Therefore, by expanding the term $\left[\frac{\partial \vec{u}^*}{\partial t} \right]^\ell$, Eqn. 5.5 can be written as:

$$0 = \ell\vec{T} + \left[\frac{\partial \vec{T}}{\partial \vec{u}^*} \right]^\ell \cdot \left[\left(\frac{\ell+1\vec{u} - \ell\vec{u}}{\Delta t} \right) \right] \Delta t + O(\Delta t)^2,$$

or

$$0 = \ell\vec{T} + \ell\hat{J} \cdot (\ell+1\vec{u} - \ell\vec{u}) + O(\Delta t)^2, \quad (5.7)$$

which can be rearranged to represent a generalized Newton-Raphson iteration method which provides second order

convergence as:-

$$\hat{\ell}_J \cdot \hat{\ell}^{+1} \vec{u} = \hat{\ell}_J \cdot \hat{\ell} \vec{u} - \hat{\ell}_T. \quad (5.8)$$

Equation 5.8 represents the actual expression to be solved. In this equation, the first iteration \vec{u} takes on the value of \vec{u} at the old level t^n .

As was pointed out earlier, the second order derivatives are involved at the point i so that the difference equations will involve values of the state vector at the grid points $i-1, i$, and $i+1$. Hence, the solution of Eqn. 5.1 at the grid point i requires evaluation of the state vector at the three points. Therefore, in the ADI technique, when the finite difference equations are treated implicitly in the i th direction, and the generalized Newton-Raphson iterative scheme as indicated in Eqn. 5.8 is applied, the resulting equation obtained is of the form:

$$\begin{aligned} & \hat{\ell}_{J_{i+1,j}} \cdot \hat{\ell}^{+1} \vec{u}_{i+1,j} + \hat{\ell}_{J_{i,j}} \cdot \hat{\ell}^{+1} \vec{u}_{i,j} + \hat{\ell}_{J_{i-1,j}} \cdot \hat{\ell}^{+1} \vec{u}_{i-1,j} = \\ & \hat{\ell}_{J_{i+1,j}} \cdot \hat{\ell} \vec{u}_{i+1,j} + \hat{\ell}_{J_{i,j}} \cdot \hat{\ell} \vec{u}_{i,j} + \hat{\ell}_{J_{i-1,j}} \cdot \hat{\ell} \vec{u}_{i-1,j} - \hat{\ell}_T, \end{aligned} \quad (5.9)$$

where the function $\hat{\ell}_T$ contains all the explicit terms including the explicit product and mixed derivative terms.

Equation 5.9 can be expressed in the normal form obtained in an ADI solution as:

$$-\hat{A}_{i,j} \cdot \hat{\ell}^{+1} \vec{u}_{i+1,j} + \hat{B}_{i,j} \cdot \hat{\ell}^{+1} \vec{u}_{i,j} - \hat{C}_{i,j} \cdot \hat{\ell}^{+1} \vec{u}_{i-1,j} = \hat{D}_{i,j} \quad (5.10)$$

where \hat{A} , \hat{B} and \hat{C} are the Jacobians evaluated on the lattice.

points $(i+1, j)$, (i, j) and $(i-1, j)$ respectively. The vector \vec{D} contains all the explicit terms and is given by:

$$\vec{D}_{i,j} = -\hat{A}_{i,j} \cdot \vec{u}_{i+1,j} + \hat{B}_{i,j} \cdot \vec{u}_{i,j} - \hat{C}_{i,j} \cdot \vec{u}_{i-1,j} - \vec{f}_T. \quad (5.11)$$

Equations 5.10 and 5.11 are uncoupled with respect to j , therefore a two dimensional problem can be regarded as two problems in which only one dimension is advanced implicitly per half time step. In Eqn. 5.10 the matrix takes on a block tridiagonal form [124], where each block is an $m \times m$ submatrix, where m is the number of components in the state vector \vec{u} . In our case, $m=4$ and \vec{u} is given by Eqn. 5.2.

During the first half time step $\Delta t/2$ with the finite difference equations treated implicitly in the i th direction, the resulting diagonal matrix takes the form:

$$\begin{bmatrix} \hat{B}_1^n & -\hat{C}_1^n & & \\ -\hat{A}_2^n & \hat{B}_2^n & -\hat{C}_2^n & 0 \\ -\hat{A}_3^n & \hat{B}_3^n & -\hat{C}_3^n & \\ \vdots & \vdots & \ddots & \\ -\hat{A}_i^n & \hat{B}_i^n & -\hat{C}_i^n & \\ \vdots & \vdots & \ddots & \\ 0 & -\hat{A}_{N-1}^n & \hat{B}_{N-1}^n & -\hat{C}_{N-1}^n \\ -\hat{A}_N^n & \hat{B}_N^n & & \end{bmatrix} \begin{bmatrix} \vec{u}_1^* \\ \vec{u}_2^* \\ \vec{u}_3^* \\ \vdots \\ \vec{u}_i^* \\ \vdots \\ \vec{u}_{N-1}^* \\ \vec{u}_N^* \end{bmatrix} = \begin{bmatrix} \vec{D}_1^n \\ \vec{D}_2^n \\ \vec{D}_3^n \\ \vdots \\ \vec{D}_i^n \\ \vdots \\ \vec{D}_{N-1}^n \\ \vec{D}_N^n \end{bmatrix} \quad (5.12)$$

where each block is represented by a Jacobian matrix. The system of equations given by (5.12) is obtained along all rows of the spatial grid, that is $j = 1$ to $j = M$. Similarly, during the second half time step $\Delta t/2$, with the finite difference equations treated implicitly in the j th direction, Eqn. 5.9 takes the form:

$$\begin{aligned} \hat{J}_{1,j+1}^{t+1} \vec{u}_{1,j+1} + \hat{J}_{1,j}^{t+1} \vec{u}_{1,j} + \hat{J}_{1,j-1}^{t+1} \vec{u}_{1,j-1} &= \\ \hat{J}_{1,j+1}^{t+1} \vec{u}_{1,j+1} + \hat{J}_{1,j}^{t+1} \vec{u}_{1,j} + \hat{J}_{1,j-1}^{t+1} \vec{u}_{1,j-1} - \vec{u}_T &. \end{aligned} \quad (5.13)$$

In this case, the resulting diagonal matrix takes the form:

$$\left[\begin{array}{cccccc} \hat{B}_1^* & -\hat{C}_1^* & & & & \\ -\hat{A}_2^* & \hat{B}_2^* & -\hat{C}_2^* & & & \\ -\hat{A}_3^* & \hat{B}_3^* & -\hat{C}_3^* & & & \\ \vdots & \vdots & \vdots & \ddots & & \\ -\hat{A}_j^* & \hat{B}_j^* & -\hat{C}_j^* & & & \\ \vdots & \vdots & \vdots & \ddots & & \\ 0 & -\hat{A}_{M-1}^* & \hat{B}_{M-1}^* & -\hat{C}_{M-1}^* & & \\ -\hat{A}_M^* & \hat{B}_M^* & & & & \end{array} \right] \left[\begin{array}{c} \vec{u}_1^{n+1} \\ \vec{u}_2^{n+1} \\ \vec{u}_3^{n+1} \\ \vdots \\ \vec{u}_j^{n+1} \\ \vdots \\ \vec{u}_{M-1}^{n+1} \\ \vec{u}_M^{n+1} \end{array} \right] = \left[\begin{array}{c} \vec{D}_1^* \\ \vec{D}_2^* \\ \vec{D}_3^* \\ \vdots \\ \vec{D}_j^* \\ \vdots \\ \vec{D}_{M-1}^* \\ \vec{D}_M^* \end{array} \right] \quad (5.14)$$

where the above system holds for all columns of the spatial grid, i.e. $i = 1$ to $i = N$.

In the next sections, the solution of the difference equations as well as the appropriate boundary conditions for the problem under investigation, will be presented.

5.3. SOLUTION OF THE FINITE DIFFERENCE EQUATIONS

As a result of the linearization process, described in the previous section, the two-dimensional nonlinear partial differential equations are reduced to a set of simultaneous linear algebraic equations. In this section we will describe the solution of the finite difference equations for the basic case of two-electrode scheme. This solution procedure will then be modified for the three-electrode scheme in which only half the structure will be considered. Now, following the alternating direction implicit (ADI) technique [124, 128], the resulting set of linear equations after the first half time step can be represented by:

$$- \hat{A}_{i,j}^n \cdot \hat{\vec{u}}_{i,j+1}^n + \hat{B}_{i,j}^n \cdot \hat{\vec{u}}_{i,j}^n - \hat{C}_{i,j}^n \cdot \hat{\vec{u}}_{i-1,j}^n = \hat{\vec{D}}_{i,j}^n. \quad (5.15a)$$

With the equations treated implicitly in the other direction during the second half time step, the resulting set of linear equations takes the form:

$$- \hat{A}_{i,j}^* \cdot \hat{\vec{u}}_{i,j+1}^{n+1} + \hat{B}_{i,j}^* \cdot \hat{\vec{u}}_{i,j}^{n+1} - \hat{C}_{i,j}^* \cdot \hat{\vec{u}}_{i-1,j}^{n+1} = \hat{\vec{D}}_{i,j}^*, \quad (5.15b)$$

where \hat{A} , \hat{B} and \hat{C} are the Jacobians. For a set of m partial differential equations, these Jacobians represent $m \times m$ matrices. On the other hand, $\hat{\vec{u}}$ and $\hat{\vec{D}}$ are vectors of m components each. Equations 5.1 are valid only over the

interior grid points defined by $i=2,3,\dots,N-1$ and $j=2,3,\dots,M-1$. The boundary conditions provide the necessary equations at $i=1$ and $i=N$ for all values of j , and for $j=1$ and $j=M$ for all values of i .

The boundary conditions on the first half time step may be written in the following general form [130,132]:

$$\hat{G}_{1,j}^n \cdot \vec{u}_{1,j}^* = \hat{H}_{1,j}^n \cdot \vec{u}_{2,j}^* + \vec{I}_{1,j}^n, \quad (5.16a)$$

and

$$\hat{G}_{N,j}^n \cdot \vec{u}_{N,j}^* = \hat{H}_{N,j}^n \cdot \vec{u}_{N-1,j}^* + \vec{I}_{N,j}^n, \quad (5.16b)$$

for all values of j which satisfies $1 < j < M$.

Also,

$$\hat{G}_{1,i}^n \cdot \vec{u}_{1,i}^* = \hat{H}_{1,i}^n \cdot \vec{u}_{1,2}^* + \vec{I}_{1,i}^n, \quad (5.17a)$$

and

$$\hat{G}_{1,M}^n \cdot \vec{u}_{1,M}^* = \hat{H}_{1,M}^n \cdot \vec{u}_{1,M-1}^* + \vec{I}_{1,M}^n, \quad (5.17b)$$

for all values of i which satisfies $1 < i < N$.

On the second half time step, the boundary conditions are represented by:

$$\hat{G}_{1,j}^* \cdot \vec{u}_{1,j}^{n+1} = \hat{H}_{1,j}^* \cdot \vec{u}_{2,j}^{n+1} + \vec{I}_{1,j}^*, \quad (5.18a)$$

and

$$\hat{G}_{N,j}^* \cdot \vec{u}_{N,j}^{n+1} = \hat{H}_{N,j}^* \cdot \vec{u}_{N-1,j}^{n+1} + \vec{I}_{N,j}^*, \quad (5.18b)$$

for all values of j which satisfies $1 < j < M$.

Also,

$$\hat{G}_{1,1}^* \cdot \vec{u}_{1,1}^{n+1} = \hat{H}_{1,1}^* \cdot \vec{u}_{1,2}^{n+1} + \vec{I}_{1,1}^*, \quad (5.19a)$$

and

$$\hat{G}_{1,M}^* \cdot \vec{u}_{1,M}^{n+1} = \hat{H}_{1,M}^* \cdot \vec{u}_{1,M-1}^{n+1} + \vec{I}_{1,M}^*, \quad (5.19b)$$

for all values of i which satisfies $1 < i < N$.

To solve the system of equations, we adopt the method described by Richtmyer and Morton [132], after generalizing it to vector equations with matrix coefficients [130] instead of scalar equations with scalar coefficients. Examining equations 5.15a and 5.16 we note that these equations are uncoupled with respect to the index j . Therefore, the vector \vec{u}^* along lines of constant j can be obtained independent of \vec{u}^* along other lines of constant j . Therefore, we can write a recursion relationship between the \vec{u}^* values at adjacent grid points on the end of the first half time step as:

$$\vec{u}_{1,j}^* = \hat{E}_{1,j}^n \cdot \vec{u}_{1,j+1}^* + \vec{F}_{1,j}^n, \quad (5.20)$$

for $i = 1, 2, 3, \dots, N-1$.

In the same manner, Eqns. 5.15b and 5.19 are uncoupled in i , and therefore the vector \vec{u}^{n+1} along lines of constant i can be obtained independent of \vec{u}^{n+1} along other lines of constant i . Hence, at the end of the second half time step we can write:

$$\vec{u}_{1,j}^{n+1} = \hat{E}_{1,j}^* \cdot \vec{u}_{1,j+1}^{n+1} + \vec{F}_{1,j}^n, \quad (5.21)$$

for $j = 1, 2, 3, \dots, M-1$.

The following steps will illustrate the calculation of \hat{u}^* for all values of i and j on the simulation mesh during the first half time step. By considering Eqn. 5.20, we first determine the values of the matrix $\hat{E}_{i,j}^n$ and vector $\hat{F}_{i,j}^n$ at $i=1$ by solving Eqn. 5.16a for $\hat{u}_{i,j}^*$ as:

$$\hat{u}_{1,j}^* = (\hat{G}_{1,j}^n)^{-1} \cdot \hat{H}_{1,j}^n \cdot \hat{u}_{2,j}^* + (\hat{G}_{1,j}^n)^{-1} \cdot \hat{I}_{1,j}^n. \quad (5.22)$$

By comparing Eqn. 5.22 with Eqn. 5.20 at $i=1$, we get:

$$\hat{E}_{1,j}^n = (\hat{G}_{1,j}^n)^{-1} \cdot \hat{H}_{1,j}^n \quad (5.23a)$$

and

$$\hat{F}_{1,j}^n = (\hat{G}_{1,j}^n)^{-1} \cdot \hat{I}_{1,j}^n \quad (5.23b)$$

The coefficients $\hat{E}_{i,j}^n$ and $\hat{F}_{i,j}^n$ for $1 < i < N$ are determined by substituting $\hat{u}_{i,j}^*$ from Eqn. 5.20 into Eqn. 5.15a as follows:

At $i=1$ Eqn. 5.20 gives:

$$\hat{u}_{1,j}^* = \hat{E}_{1,j}^n \cdot \hat{u}_{2,j}^* + \hat{F}_{1,j}^n. \quad (5.24)$$

Substituting Eqn. 5.24 into Eqn. 5.15a yields:

$$-\hat{A}_{1,j}^n \cdot \hat{u}_{1,j}^* + \hat{B}_{1,j}^n \cdot \hat{u}_{2,j}^* - \hat{C}_{1,j}^n \cdot \hat{E}_{1,j}^n \cdot \hat{u}_{2,j}^* - \hat{C}_{1,j}^n \cdot \hat{F}_{1,j}^n = \hat{D}_{1,j}^n$$

or

$$-\hat{A}_{1,j}^n \cdot \hat{u}_{1,j}^* + (\hat{B}_{1,j}^n - \hat{C}_{1,j}^n \cdot \hat{E}_{1,j}^n) \cdot \hat{u}_{2,j}^* = \hat{D}_{1,j}^n + \hat{C}_{1,j}^n \cdot \hat{F}_{1,j}^n, \quad (5.25)$$

and by solving Eqn. 5.25 for $\hat{u}_{1,j}^*$, we get:

$$\begin{aligned} \hat{\vec{u}}_{i,j}^* &= (\hat{B}_{i,j}^n - \hat{C}_{i,j}^n \cdot \hat{E}_{i-1,j}^n)^{-1} \cdot \hat{A}_{i,j}^n \cdot \hat{\vec{u}}_{i,j}^* \\ &\quad + (\hat{B}_{i,j}^n - \hat{C}_{i,j}^n \cdot \hat{E}_{i-1,j}^n)^{-1} \cdot (\hat{D}_{i,j}^n + \hat{C}_{i,j}^n \cdot \hat{F}_{i-1,j}^n) . \end{aligned} \quad (5.26)$$

By comparing Eqn. 5.26 with Eqn. 5.20, we obtain expressions for the recurrence relation terms \hat{E}^n and \hat{F}^n as:

$$\hat{E}_{i,j}^n = (\hat{B}_{i,j}^n - \hat{C}_{i,j}^n \cdot \hat{E}_{i-1,j}^n)^{-1} \cdot \hat{A}_{i,j}^n , \quad (5.27a)$$

and

$$\hat{F}_{i,j}^n = (\hat{B}_{i,j}^n - \hat{C}_{i,j}^n \cdot \hat{E}_{i-1,j}^n)^{-1} \cdot (\hat{D}_{i,j}^n + \hat{C}_{i,j}^n \cdot \hat{F}_{i-1,j}^n) , \quad (5.27b)$$

here, Eqns. 5.27 are valid for $i = 2, 3, 4, \dots, N-1$.

In order to determine $\hat{\vec{u}}_{N,j}^*$, we first obtain the recursion relation of Eqn. 5.20 at $i = N-1$ as:

$$\hat{\vec{u}}_{N-1,j}^* = \hat{E}_{N-1,j}^n \cdot \hat{\vec{u}}_{N,j}^* + \hat{F}_{N-1,j}^n . \quad (5.28)$$

Equation 5.28 is then used in Eqn. 5.16b to get:

$$\hat{G}_{N,j}^n \cdot \hat{\vec{u}}_{N,j}^* = \hat{H}_{N,j}^n \cdot (\hat{E}_{N-1,j}^n \cdot \hat{\vec{u}}_{N,j}^* + \hat{F}_{N-1,j}^n) + \hat{I}_{N,j}^n ,$$

or

$$\hat{G}_{N,j}^n \cdot \hat{\vec{u}}_{N,j}^* - \hat{H}_{N,j}^n \cdot \hat{E}_{N-1,j}^n \cdot \hat{\vec{u}}_{N,j}^* = \hat{H}_{N,j}^n \cdot \hat{F}_{N-1,j}^n + \hat{I}_{N,j}^n ,$$

which gives:

$$\hat{\vec{u}}_{N,j}^* = (\hat{G}_{N,j}^n - \hat{H}_{N,j}^n \cdot \hat{E}_{N-1,j}^n)^{-1} \cdot (\hat{H}_{N,j}^n \cdot \hat{F}_{N-1,j}^n + \hat{I}_{N,j}^n) . \quad (5.29)$$

In summary, the above method consists of calculating the recurrence values of E and F by making a forward sweep through the mesh from $i = 1$ to $N-1$ using Eqns. 5.23 and 5.27, then $\hat{\vec{u}}_{N,j}^*$ can be computed using Eqn. 5.29. The values

of \vec{u}^* for $i = N-1, N-2, \dots, 2, 1$ can now be determined by backsubstitution using Eqn. 5.20.

So far, this method makes possible the calculation of \vec{u}^* on the first half time step for all values of i with j greater than 1 and less than M . Values of \vec{u}^* for $i = 2, 3, \dots, N-1$ at j equal 1 and M can be calculated by rearranging Eqns. 5.17 as follows:

$$\vec{u}_{1,1}^* = (\hat{G}_{1,1}^n)^{-1} \cdot (\hat{H}_{1,1}^n \cdot \vec{u}_{1,2}^* + \vec{I}_{1,1}^n), \quad (5.30a)$$

and

$$\vec{u}_{1,M}^* = (\hat{G}_{1,M}^n)^{-1} \cdot (\hat{H}_{1,M}^n \cdot \vec{u}_{1,M-1}^* + \vec{I}_{1,M}^n), \quad (5.30b)$$

Here Eqns. 5.30 use values previously calculated by Eqn. 5.20.

Finally, the values of \vec{u}^* at the four corner points $(1,1)$, $(N,1)$, $(1,M)$ and (N,M) can be calculated by passing a polynomial through the adjacent mesh points, at which the values of \vec{u}^* have been obtained before. This procedure was reported by Lindemuth [133], where a second-order-accurate polynomial for the corner point $(1,1)$ gives:

$$\vec{u}_{1,1}^* = \vec{u}_{1,2}^* + \vec{u}_{2,1}^* - \vec{u}_{2,2}^*. \quad (5.31)$$

The values of \vec{u}^* at the other three corner points can be obtained in the same way. This completes the calculations of \vec{u}^* for all values of i and j at the end of the first half time step.

During the second half time step, Eqn. 5.15b, is the equation to be solved. The solution of this difference equation is performed by working along rows of constant i by using Eqn. 5.21. The procedure is similar to that used on the first half time step, except the equations are now treated implicitly in the j -direction and explicitly in the i -direction. The values of \bar{u}^{n+1} can then be calculated for all values of i and j at the end of the second half time step, in a manner similar to that used for the first half time step. The final solution is represented by \bar{u}^{n+1} .

It is clear from the above discussion that it is possible to calculate the values of \bar{u} , for all mesh points in an $M \times N$ mesh at times t' and t'' if the values are known at t^n . It is also clear that because of the advantage of the block tridiagonal nature of the alternating direction implicit (ADI) finite difference technique, the number of matrices to be inverted is reduced from $m \times M \times N$ to $Mm \times m$ matrices along one dimension plus $Nm \times m$ matrices along the other dimension. Therefore this method is quite efficient from a computer operating-time point of view.

5.4 NUMERICAL BOUNDARY CONDITIONS

5.4.1 INTRODUCTION

In this section, the boundary conditions are described in the form which can be implemented in our implicit

computer code (IGCP). Of great concern to us is the accuracy of these boundary conditions and its compatibility with the block tridiagonal form of the alternating direction implicit (ADI), solution procedure. A proper solution for the difference equations over the entire simulation mesh can only be obtained if these two essential requirements be satisfied.

As was mentioned in section 5.3, the block tridiagonal form of the standard ADI equation can accommodate a boundary condition of the form:

$$G \cdot \vec{u}_{BP} = H \cdot \vec{u}_{INT} + I, \quad (5.32)$$

where \vec{u}_{BP} is the boundary point and \vec{u}_{INT} is the next interior point. The Dirichlet (specified function value), Neumann (specified normal gradient) and mixed boundary conditions can be represented by the equation:

$$\alpha \cdot \frac{\partial \vec{u}}{\partial n} + \beta \cdot \vec{u} = \gamma, \quad (5.33)$$

where $\frac{\partial}{\partial n}$ is the derivative normal to the boundary, and \vec{n} is the unit normal vector outward from the boundary wall.

To facilitate using the boundary conditions in our computer code (IGCP), we first apply the finite difference technique to the equations in the form of Eqn. 5.33 and then arrange the results in the form of Eqn. 5.32 to be used in the block tridiagonal form. The ghost point boundary conditions [124], in which the boundary walls lie halfway

between mesh rows, are used. In the case of two-electrode structure, the walls (Cathode and Anode) lie along the rows $j = 1 + \frac{1}{2}$ and $j = M - \frac{1}{2}$ respectively, as shown in Fig. 5.1. In the case of three-electrode scheme, the walls are determined by the rectangular step at the centerline, and the top plate at $j = M - \frac{1}{2}$ as shown in Fig. 5.2. This procedure provides second order accurate finite difference approximation to the derivatives along the boundary.

In the following section, the boundary conditions for the three-electrode scheme will be described. A similar analysis for the two-electrode structure, which was used for code verification and preliminary testing, will be described in Appendix B.

5.4.2 BOUNDARY CONDITIONS OF THE OPEN CHANNEL FLOW LASER GAS DISCHARGE

Figure 5.3 shows the electrode configuration which represents the actual experimental set up. The discharge length which extends over the z-direction provides a symmetry along this axis. The gas flow is in the x-direction as shown. To simplify the problem, we take advantage of the symmetry about the A-A axis and perform our simulation analysis over only one half of this structure. We also approximate the cylindrical shape to a rectangular single step structure as shown in Figure 5.4. Kawaguti [134] used a similar approximation and performed his analysis on a finite rectangular region, rather than on a half cylinder.

**Simulation Mesh Configuration for
the Two-electrode System**

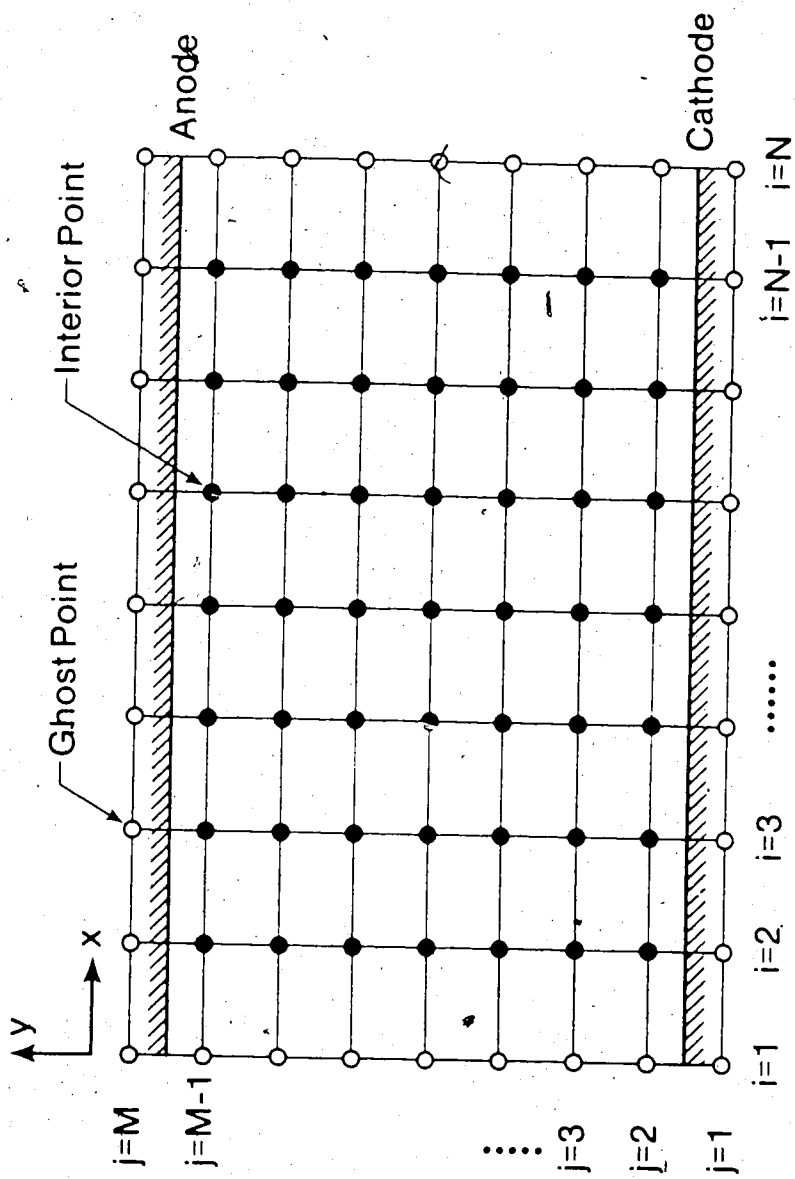


Fig. 5.1 Simulation mesh configuration for the two-electrode system.

Simulation Mesh Configuration for
the Three-electrode System

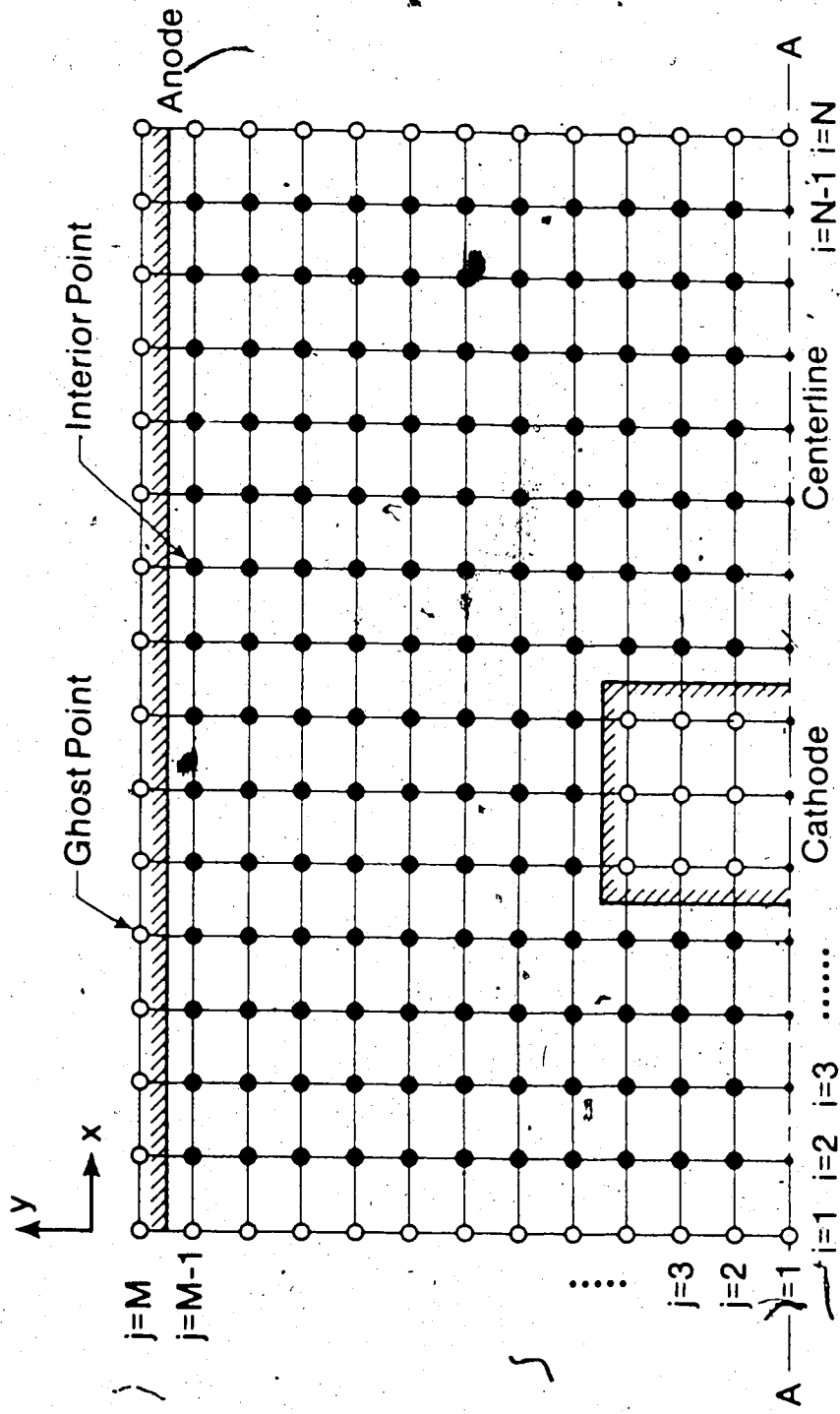


Fig. 5.2 Simulation mesh configuration for half the structure of the three-electrode system.

Basic Geometry of the Three-electrode System

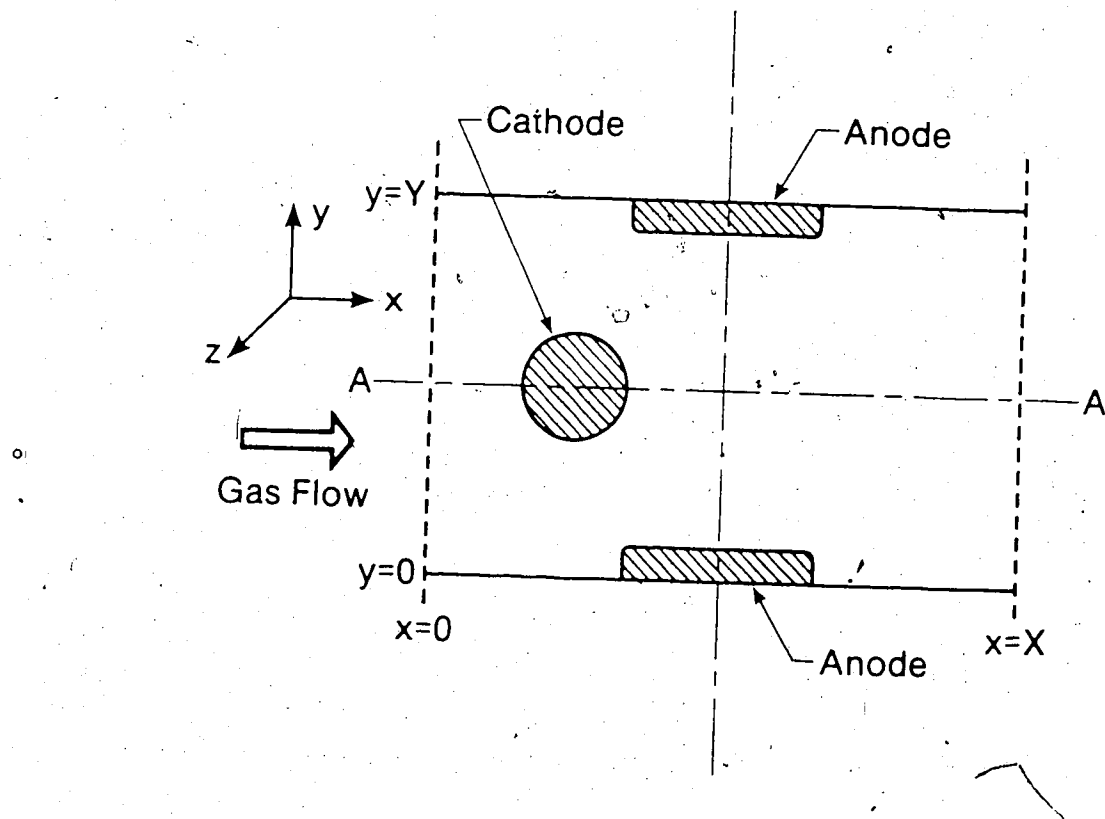


Fig. 5.3 Basic geometry of the three-electrode system.

Boundaries of the Single Step Configuration

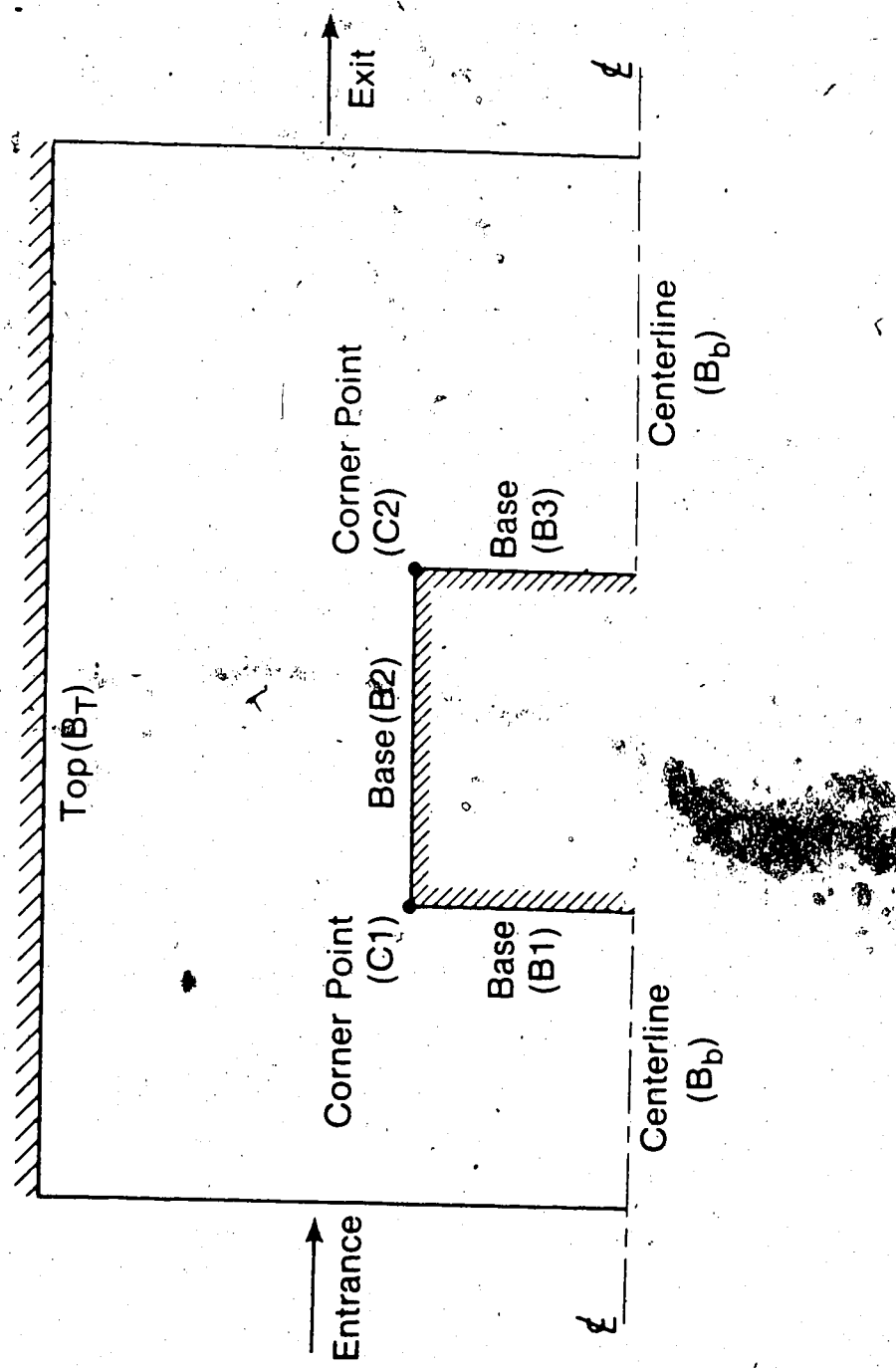


Fig. 5.4 Boundaries of the single step configuration.

1. BOUNDARY CONDITIONS AT THE TOP ELECTRODE (B_T)

The appropriate boundary conditions that are applied at the upper solid electrode (B_T) for the velocity components v and u are as follows:

$$v(x, y=Y) = 0 \quad (\text{no-slip condition}), \quad (5.34)$$

$$u(x, y=Y) = 0 \quad (\text{zero normal flow}). \quad (5.35)$$

At the electrode surface, we assume that the neutral mass density (ρ) is constant, this assumption provides the Neumann boundary condition:

$$\left(\frac{\partial \rho}{\partial y}\right)_{x,y=Y} = 0 \quad (5.36)$$

Finally, at the top boundary, and assuming adiabatic wall,

we have:

$$T = T_w \quad (5.37)$$

Now, application of the finite difference scheme and comparison with Eqn. 5.32 gives the submatrix elements:

$$\hat{G}_T = \begin{bmatrix} 1 & 0 & 0 & 0 \\ 0 & 1 & 0 & 0 \\ 0 & 0 & 1 & 0 \\ 0 & 0 & 0 & 1 \end{bmatrix} \quad (5.38a)$$

$$H_T = \begin{bmatrix} -1 & 0 & 0 & 0 \\ 0 & -10 & 0 & 0 \\ 0 & 0 & 1 & 0 \\ 0 & 0 & 0 & -1 \end{bmatrix} \quad (5.38b)$$

and

$$I_T = \begin{bmatrix} 0 \\ 0 \\ 0 \\ 2T_v \end{bmatrix} \quad (5.38c)$$

the subscript T refers to the top boundary.

2. BOUNDARY CONDITIONS AT THE ENTRANCE

Referring to Fig. 5.4, the boundary conditions at the entrance to the test region are considered. The laser gas mixture is assumed to enter the test region with a velocity v in the x-direction such that:

$$v(x=0, y) = v_i \quad (5.39a)$$

where v_i is the initial velocity.

It is also assumed that the flow at the entrance is laminar, so that the velocity u is subject to a Dirichlet boundary condition as:

$$u(x=0, y) = 0 \quad (5.39b)$$

The pressure drop across the discharge region used in this simulation was chosen to match the experimentally measured value (measurements described in Chapter 7).

At the entrance, an initial pressure P_i is specified, so

that the gas density ρ is given by:

$$\rho(x=0, y) = \rho(T_{en}, P_i), \quad (5.39c)$$

where T_{en} is the temperature at the entrance. During the computational run, the density ρ is continually adjusted so as to get:

$$P(x=0, y) = 1.1P(x=X, y),$$

where P is the pressure. In this case, a pressure difference of 10% is maintained across the test region.

Finally, at the entrance we have:

$$T(x=0, y) = T_{en}. \quad (5.39d)$$

Applying the finite difference scheme to Eqns. 5.39 and comparing with Eqn. 5.32, we obtain the submatrix elements as:

$$G_L = \begin{bmatrix} 1 & 0 & 0 & 0 \\ 0 & 1 & 0 & 0 \\ 0 & 0 & 1 & 0 \\ 0 & 0 & 0 & 1 \end{bmatrix} \quad (5.40a)$$

$$H_L = \begin{bmatrix} -1 & 0 & 0 & 0 \\ 0 & -1 & 0 & 0 \\ 0 & 0 & -1 & 0 \\ 0 & 0 & 0 & -1 \end{bmatrix} \quad (5.40b)$$

$$\vec{I}_L = \begin{bmatrix} 2v_1 \\ 0 \\ 2\rho_1(T_{en}, P_1) \\ 2T_{en} \end{bmatrix} \quad (5.40c)$$

where the subscript L refers to the entrance and:

$$\rho_1(T_{en}, P_1) = \left(\frac{m}{K}\right)\left(\frac{P_1}{T_{en}}\right)^{\frac{1}{\gamma-1}} \quad (5.41)$$

3. BOUNDARY CONDITIONS AT THE EXIT

The boundary conditions at the exit, downstream of the test section are now considered. At the exit end, no variation in v with x is assumed; i.e. no acceleration or deceleration. Therefore a Neumann boundary condition prevails at the exit as:

$$\frac{\partial}{\partial x} v(x=X, y) = 0 \quad (5.42a)$$

Moreover, the flow is assumed to be laminar, giving a Dirichlet boundary condition:

$$u(x=X, y) = 0 \quad (5.42b)$$

The assumption that the pressure does not vary with x at the exit leads to a Neumann boundary condition imposed on the gas density. That is,

$$\frac{\partial}{\partial x} \rho(x=X, y) = 0 \quad (5.42c)$$

Finally, a Neumann boundary condition is imposed on the temperature T so that:

$$\frac{\partial}{\partial x} T(x=x, y) = 0 . \quad (5.42d)$$

Application of the finite difference scheme to Eqns. 5.42 and comparison with Eqn. 5.32 gives the submatrix elements as:

$$G_R = \begin{bmatrix} 1 & 0 & 0 & 0 \\ 0 & 1 & 0 & 0 \\ 0 & 0 & 1 & 0 \\ 0 & 0 & 0 & 1 \end{bmatrix}, \quad (5.43a)$$

$$H_R = \begin{bmatrix} 1 & 0 & 0 & 0 \\ 0 & -1 & 0 & 0 \\ 0 & 0 & 1 & 0 \\ 0 & 0 & 0 & 1 \end{bmatrix}, \quad (5.43b)$$

and

$$I_R = \begin{bmatrix} 0 \\ 0 \\ 0 \\ 0 \end{bmatrix}, \quad (5.43c)$$

where the subscript R refers to the exit.

4. BOUNDARY CONDITIONS AT THE BASE (B2)

For compressible viscous flow, the boundary conditions along the walls are accommodated by either a mesh system in which the node (cell center) points are located on the surface, or one in which the walls lie between node (cell center) points. In the case of no slip walls for viscous flow, the density is evaluated using the second mesh system. The other variables (v , u , T) are treated in the first mesh

system.

In our simulation, v_w and u_w (where the subscript w identifies quantities along a surface wall) are subject to Dirichlet boundary condition as:

$$v_w = 0, \quad (5.44a)$$

and

$$u_w = 0. \quad (5.44b)$$

At the surface of the cathode we have:

$$T_w = T_k, \quad (5.44c)$$

where T_k is the cathode temperature.

The density ρ is evaluated using the staggered mesh system [135] shown in Fig. 5.5. This method is used because it provides a second order accuracy for the solution when advanced during a half time step from t^n to $t^n + \Delta t/2$. In this case, old values of density ρ^s are defined near the wall from ρ -values in the mesh system whose centers are denoted by the crosses in Fig. 5.5. This gives:

$$\rho_{i-1,j}^s = 1/4 (\rho_{i,w} + \rho_{i,w+1} + \rho_{i-1,w} + \rho_{i-1,w+1}) \quad (5.45a)$$

$$\rho_{i,j}^s = 1/4 (\rho_{i+1,w} + \rho_{i+1,w+1} + \rho_{i,w} + \rho_{i,w+1}) \quad (5.45b)$$

$$\rho_{i+1,j}^s = 1/4 (\rho_{i+2,w} + \rho_{i+2,w+1} + \rho_{i+1,w} + \rho_{i+1,w+1}) \quad (5.45c)$$

and

$$\rho_{i,j+1}^s = 1/4 (\rho_{i+1,w+1} + \rho_{i+1,w+2} + \rho_{i,w+1} + \rho_{i,w+2}) \quad (5.45d)$$

Then new values of density in the original coordinate along

Staggered (Hybrid) Mesh System

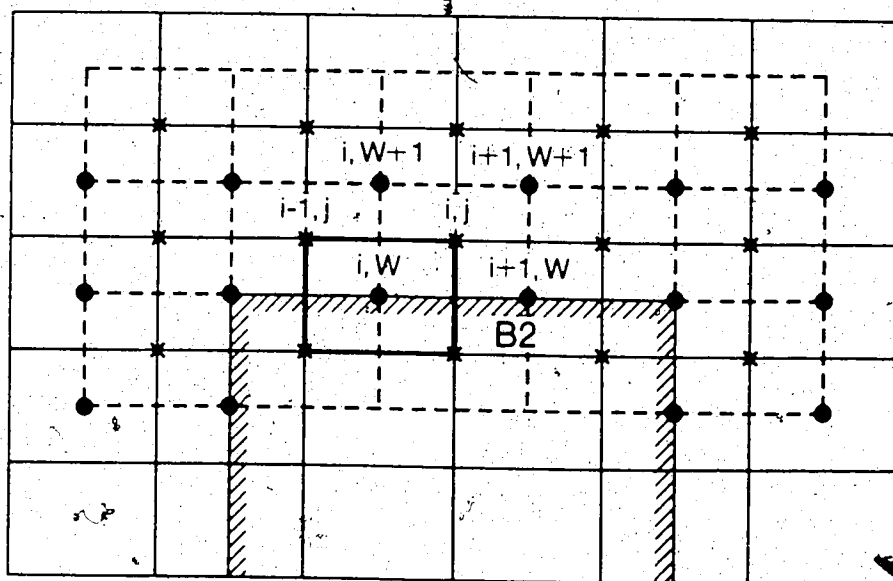


Fig. 5.5 Staggered (hybrid) mesh system.

which boundary is treated is obtained at one half time step by the staggered-mesh equation [135], where:

$$\rho = \rho_{\text{old}} + \frac{\text{net flux}}{\text{volume}} \quad (5.46a)$$

As an example, the mass density in the cell i, w (shown in bold in Fig. 5.5) at the time $t^n + \Delta t/2$ is:

$$\rho = \rho_{\text{old}} + \frac{\text{net flux into cell}}{\text{cell volume}} \quad (5.46b)$$

It must be noted that at the surface, a volume which is half that of a cell is considered since at the boundary only one half cell is permeable. This gives the density ρ^b (where b refers to a point on the boundary) as:

$$\begin{aligned} \rho_{i,w}^b = \rho_{i,j}^s & - \left[1/2(v_{i+1,w} + v_{i+1,w+1}) \rho_{i,j}^s \right. \\ & - 1/2(v_{i,w} + v_{i,w+1}) \rho_{i-1,j}^s \Big] \Delta t / \Delta x \\ & - \left[1/2(u_{i+1,w+1} + u_{i,w+1}) \rho_{i,j}^s \right. \\ & \left. - 1/2(u_{i+1,w} + u_{i,w}) \rho_{i-1,j}^s \right] \Delta t / \Delta y. \end{aligned} \quad (5.46c)$$

After new temperatures have been calculated from the energy equation, the new pressure and density values in the \bullet -mesh are then calculated from [135]:

$$P_{i,w} = - P_{i,w+1} + R (\rho_{i-1,j}^s + \rho_{i,j}^s) (T_{i,w+1} + T_{i,w}) / 2 \quad (5.47)$$

and

$$\rho_{i,w} = P_{i,w} / R T_{i,w} \quad (5.48)$$

where $R_g = C_p - C_v$, and T is the temperature.

Although this method is a cumbersome one, it is second order

* accurate and dependable [135].

Now, we can write the boundary conditions at the base (B2) as

$$v_w = 0, \quad (5.49a)$$

$$u_w = 0, \quad (5.49b)$$

$$\rho_w = \rho_{1,w}, \quad (5.49c)$$

and

$$T_w = T_k, \quad (5.49d)$$

where ρ_w is given by Eqn 5.48.

By applying the finite difference technique described in section 4.6 to Eqns. 5.49, a set of difference equations is obtained, which represent the boundary conditions. By comparing these difference equations with Eqn. 5.32, we obtain the submatrix elements, which can be used in the block tridiagonal scheme as

$$G_{B2} = \begin{bmatrix} 1 & 0 & 0 & 0 \\ 0 & 1 & 0 & 0 \\ 0 & 0 & 1 & 0 \\ 0 & 0 & 0 & 1 \end{bmatrix} \quad (5.50a)$$

$$H_{B2} = \begin{bmatrix} -1 & 0 & 0 & 0 \\ 0 & -1 & 0 & 0 \\ 0 & 0 & -1 & 0 \\ 0 & 0 & 0 & -1 \end{bmatrix} \quad (5.50b)$$

$$\vec{I}_{B2} = \begin{bmatrix} 0 \\ 0 \\ 2\rho \\ 2T \end{bmatrix} \quad (5.50c)$$

where the subscript B2 refers to the boundary base B2.

5. BOUNDARY CONDITIONS AT THE SHARP CORNERS

The corners which are concave to the fluid present almost no difficulties, but those where the wall projects into the fluid, as in our case, demand special treatment. One of the methods which deal with the corner points was described by Thom and Apelt [136]. In this method a function is calculated at points in a diamond structured cell around the corner point. By successive and repeated calculations at these points, and going towards the corner point until finally cited on it, the value of the function at the corner point can be obtained. This method is not recommended since it is not accurate.

In our case, we adopt the method described by Roache [137], where the boundary conditions at the sharp corners C1 and C2 require that some variables be double-valued. The corner points C1 and C2 are shown in Fig. 5.6. The boundary conditions on v, u and T are obtained in a mesh system in which the node points are located on the surface (•-mesh in Fig. 5.6). In the case of the density ρ , a mesh system in which the walls lie between node points (o-mesh in Fig. 5.6)

Sharp Corner Cell Treatment

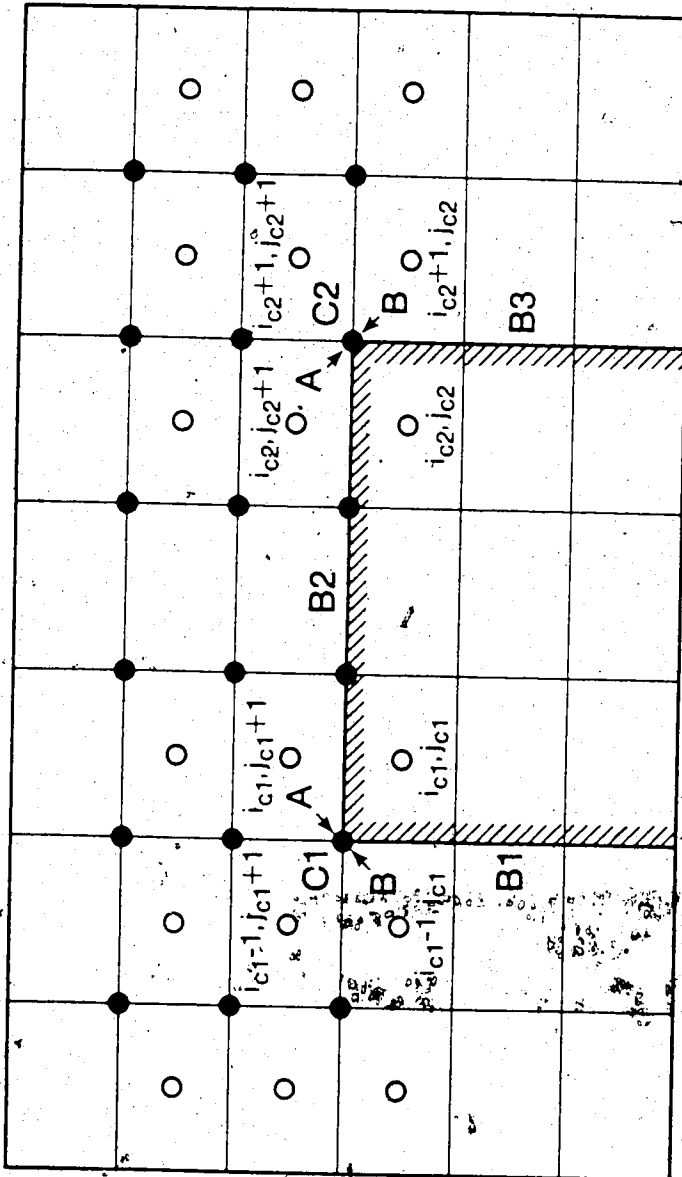


Fig. 5.6 Sharp corner cell treatment.

is considered.

In our simulation, the velocity components v , and u , at the corner point C1 are subject to Dirichlet boundary condition such that:

$$v_1 = 0, \quad \{ \quad (5.51)$$

and

$$u_1 = 0. \quad (5.52)$$

Since the corner point is located on the electrode surface, the temperature is given by:

$$T_{C1} = T_K, \quad (5.53)$$

where T_K is the cathode temperature.

The density ρ is now calculated in the second mesh system (o-mesh in Fig. 5.6) where a fictitious point (i_{c1}, j_{c1}) is used [137]. Here, we define:

$$\rho_{1A} = \rho(i_{c1}, j_{c1} + 1), \quad (5.54)$$

and

$$\rho_{1B} = \rho(i_{c1} - 1, j_{c1}), \quad (5.55)$$

and when new values are calculated at $(i_{c1}, j_{c1} + 1)$, we momentarily set:

$$\rho_{i_{c1}, j_{c1}} = \rho_{1A}. \quad (5.56)$$

Similarly, for new values at $(i_{c1} + 1, j_{c1})$, we momentarily set

$$\rho_{i_{c1}, j_{c1}} = \rho_{1B}. \quad (5.57)$$

Therefore, at the sharp corner C₁, we can write the boundary conditions as:

$$v = 0, \quad (5.58a)$$

$$u = 0, \quad (5.58b)$$

$$\rho_{C1A} = \rho(i_{c1}, j_{c1} + 1), \quad (5.58c)$$

$$\rho_{C1B} = \rho(i_{c1} - 1, j_{c1}), \quad (5.58d)$$

and,

$$T_{c1} = T_K. \quad (5.58e)$$

Applying the finite difference technique to the above equations and comparing with Eqn. 5.32, we obtain the submatrix elements as:

$$G_{c1} = \begin{bmatrix} 1 & 0 & 0 & 0 \\ 0 & 1 & 0 & 0 \\ 0 & 0 & 1 & 0 \\ 0 & 0 & 0 & 1 \end{bmatrix} \quad (5.59a)$$

$$H_{c1} = \begin{bmatrix} -1 & 0 & 0 & 0 \\ 0 & -1 & 0 & 0 \\ 0 & 0 & -1 & 0 \\ 0 & 0 & 0 & -1 \end{bmatrix} \quad (5.59b)$$

$$I_{c1A} = \begin{bmatrix} 0 \\ 0 \\ 2\rho_{c1A}(i_{c1}, j_{c1} + 1) \\ 2T_K \end{bmatrix} \quad (5.59c)$$

and

$$\vec{f}_{C1B} = \begin{bmatrix} 0 \\ 0 \\ 2\rho_{1B}(i_{c1}-1, j_{c1}) \\ 2T_K \end{bmatrix}, \quad (5.59d)$$

where the subscript C1 refers to the corner point C1, and the subscripts C1A and C1B refer to the upper and lower sides at the corner point C1.

Similarly, at the sharp corner point C2, we write the following boundary conditions:

$$v_2 = 0, \quad (5.60a)$$

$$u_2 = 0, \quad (5.60b)$$

$$\rho_{c2A} = \rho(i_{c2}, j_{c2}+1), \quad (5.60c)$$

$$\rho_{c2B} = \rho(i_{c2}+1, j_{c2}), \quad (5.60d)$$

and

$$T_{c2} = T_K. \quad (5.60e)$$

Now, applying the finite difference technique to Eqns. 5.60 and then comparing with Eqn. 5.32, we obtain the following submatrix elements:

$$\hat{G}_{c2} = \begin{bmatrix} 1 & 0 & 0 & 0 \\ 0 & 1 & 0 & 0 \\ 0 & 0 & 1 & 0 \\ 0 & 0 & 0 & 1 \end{bmatrix} \quad (5.61a)$$

$$H_{C2} = \begin{bmatrix} -1 & 0 & 0 & 0 \\ 0 & -1 & 0 & 0 \\ 0 & 0 & -1 & 0 \\ 0 & 0 & 0 & -1 \end{bmatrix} \quad (5.61b)$$

$$\vec{I}_{C2A} = \begin{bmatrix} 0 \\ 0 \\ 2\rho_{2A}(i_{C2}, j_{C2} + 1) \\ 2T_K \end{bmatrix} \quad (5.61c)$$

and

$$\vec{I}_{C2B} = \begin{bmatrix} 0 \\ 0 \\ 2\rho_{2B}(i_{C2} + 1, j_{C2}) \\ 2T_K \end{bmatrix} \quad (5.61d)$$

where the subscripts C2, C2A and C2B define the corner point C2.

6. BOUNDARY CONDITIONS AT THE BASES B1 AND B3

At the bases B1 and B3, and for no-slip condition, the following boundary conditions are satisfied:

$$\frac{\partial v}{\partial x} = 0, \quad (5.62a)$$

$$u = 0, \quad (5.62b)$$

$$\frac{\partial \rho}{\partial x} = 0, \quad (5.62c)$$

and

$$T = T_K, \quad (5.62d)$$

By applying the finite difference technique to this set of

equations, and comparison of the results with Eqn. 5.32 gives the following sub-matrix elements:

$$\hat{G}_{B1} = \hat{G}_{B3} = \begin{bmatrix} 1 & 0 & 0 & 0 \\ 0 & 1 & 0 & 0 \\ 0 & 0 & 1 & 0 \\ 0 & 0 & 0 & 1 \end{bmatrix} \quad (5.63a)$$

$$\hat{H}_{B1} = \hat{H}_{B3} = \begin{bmatrix} -1 & 0 & 0 & 0 \\ 0 & -1 & 0 & 0 \\ 0 & 0 & 1 & 0 \\ 0 & 0 & 0 & -1 \end{bmatrix} \quad (5.63b)$$

and

$$\hat{I}_{B1} = \hat{I}_{B3} = \begin{bmatrix} 0 \\ 0 \\ 0 \\ 2T_x \end{bmatrix} \quad (5.63c)$$

where the subscripts B1 and B3 refer to the bases B1 and B3.

7. BOUNDARY CONDITIONS AT THE CENTERLINE (B_b)

The following boundary conditions are imposed at the symmetry surfaces (Centerline B_b):

$$\frac{\partial v}{\partial x} = 0, \quad (5.64a)$$

$$\frac{\partial u}{\partial x} = 0, \quad (5.64b)$$

$$\frac{\partial \rho}{\partial x} = 0, \quad (5.64c)$$

and

$$\frac{\partial T}{\partial x} = 0, \quad (5.64d)$$

using finite differencing and comparison with Eqn. 5.32

yields the submatrix elements:

$$G_{B_b} = \begin{bmatrix} 1 & 0 & 0 & 0 \\ 0 & 1 & 0 & 0 \\ 0 & 0 & 1 & 0 \\ 0 & 0 & 0 & 1 \end{bmatrix} \quad (5.65a)$$

$$G_{B_b} = \begin{bmatrix} 1 & 0 & 0 & 0 \\ 0 & -1 & 0 & 0 \\ 0 & 0 & 1 & 0 \\ 0 & 0 & 0 & 1 \end{bmatrix} \quad (5.65b)$$

and

$$I_{B_b} = \begin{bmatrix} 0 \\ 0 \\ 0 \\ 0 \end{bmatrix} \quad (5.65c)$$

where the subscript B_b refers to the centerline.

5.5 CODE VERIFICATION

To check the validity of the IGCP computer code, several tests were performed. During the initial test of the code, the equation of conservation of energy was not included. Only the continuity equation and the equation of conservation of momentum were involved in the computations.

The two-dimensional compressible flow of a laser gas mixture ($\text{CO}_2 : \text{N}_2 : \text{He}$) in open channel flow is considered in these tests.

In the first test, the simple geometry of a two-electrode system as shown in Fig. 5.1 was considered. The boundary conditions were obtained in a way similar to that described in section 5.4. The simulation mesh used is shown in Fig. 5.1. The results of this test, including velocity profiles and mass flow distributions, as well as a full discussion will be presented in Chapter 6. The results showed the validity of our computer code for simulating open channel flow in this simple structure.

The results of the first test suggested that the computer code could be used to simulate open channel flow in a more complicated geometry. In this case, the three electrode geometry shown in Fig. 5.3 was considered. Since we are solving the equations of conservation of mass and momentum only in this case, the variables involved in the computations are two velocity components in the x- and y-directions and the neutral mass density. The temperature is kept constant at 300 °k for these analysis. Also, the thermodynamic equation of state $P = \rho RT$ was used to close the system of equations. To simplify the problem, we took advantage of the symmetry about the x-axis and performed our analysis on only one half of the structure.

The electrode shape was approximated to either a single step structure (referred to as the second test), or a double step structure (referred to as the third test). In the case of single step configuration, the procedure used to obtain

Basic Geometry of the Two-electrode System

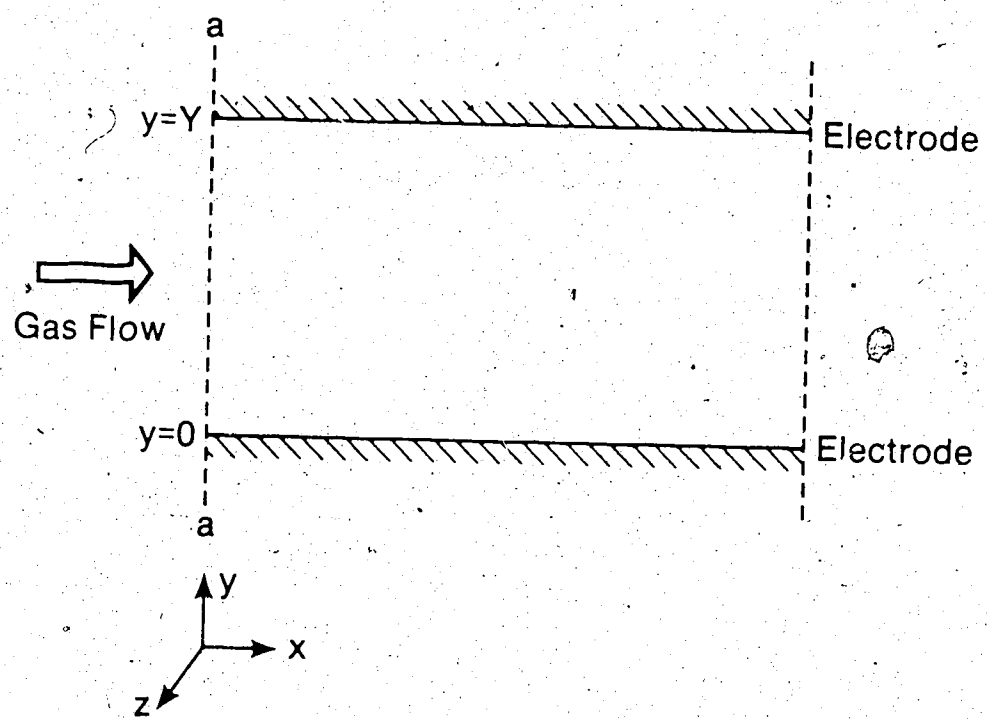


Fig. 5.7 Basic geometry of the two-electrode system.

the boundary conditions is similar to that in section 5.4.2.

The results of the second test, including velocity vector distributions, mass flow, and velocity profiles will be presented in Chapter 6. The results of this test were encouraging, and indicated potential success in simulating the three-electrode open channel flow problem in which heat transport was still to be added.

In the third test, we wanted to check the accuracy of approximating the electrode structure by a single step rectangular shape, rather than a half cylinder [134]. For this purpose, the electrode shape was approximated to the double-step structure as shown in Fig. 5.8, where two more corner points (C3 and C4) and two more bases (B4 and B5) were added. The boundary conditions were obtained in the same way as explained in section 5.4.2.

The results, which will be presented in Chapter 6, are very similar to those of the single step structure. These results suggest that our approximation is valid and no more tests using more steps are required. At this point, we were in a position to modify our computer code to include the energy equation and thereby simulate an open channel flow laser gas discharge. A brief description of the boundary conditions derived for the above test will be presented in Appendix B.

Boundaries of the Double Step Configuration

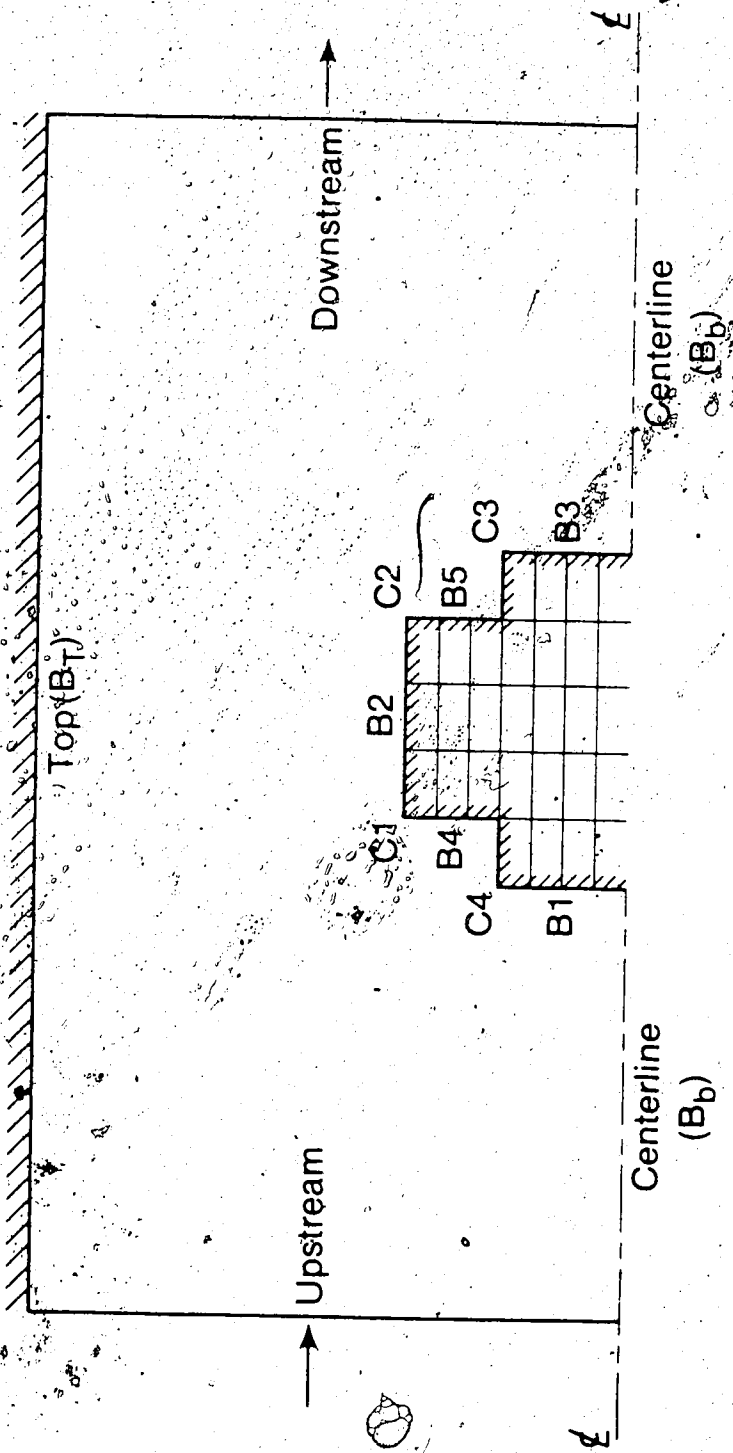


Fig. 5.8 Boundaries of the double step configuration.

5.6 ITERATION CONTROLS

As stated before, in the IGCP computer code we advance the mesh one row at a time. This allows many iterations toward a solution to be made on rows involving large changes until convergence is attained. Rows that have little change will require just a few iterations. This can be done because we are using the ADI technique, which decouples the rows of the mesh. In this case the variation of the number of iterations per row depends only upon the change in the state variable along that row. Convergence can be achieved by testing for the maximum variation of the state vector between iterations versus the average value of the iterations for each row. The convergence criterion ϵ is defined as:

$$\epsilon = \max \left| 2(\vec{u}_{i,j}^{l+1} - \vec{u}_{i,j}^l) / (\vec{u}_{i,j}^{l+1} + \vec{u}_{i,j}^l) \right| \quad (5.66)$$

This criterion is subject to a floor value, such that if $\vec{u}_{i,j}$ is less than the floor value, then the floor value is used for $\vec{u}_{i,j}^{l+1}$ in the denominator of Eqn. 5.66. The maximum value of ϵ along a row is compared with an allowed convergence criterion ϵ_{\max} . If ϵ is less than the criterion ϵ_{\max} , the row is declared converged. If $\epsilon \geq \epsilon_{\max}$, the iteration procedure is continued. A typical value for the convergence criterion is $\epsilon_{\max} < 10^{-5}$.

5.7 DYNAMIC TIME STEP CONTROLS

For an efficient and economical use of computer time, a dynamic time stepping algorithm was implemented. This algorithm permitted the program to operate over a range of allowable time steps, by providing an initial time step and a maximum and minimum time step increment. The maximum change of the state variable on the mesh was monitored between time steps. This is subject to a floor condition, below which no check was performed on the state variable.

The floor value is revised each time to 5 % of the maximum mesh velocity, so that the time step will not be limited by small variations on the mesh. The maximum variation over the mesh is expressed as:

$$V_{\max} = \max | (\vec{u}_{i,j}^{n+1} - \vec{u}_{i,j}^n) / \vec{u}_{i,j}^n |. \quad (5.67)$$

The maximum variation V_{\max} is compared to an allowed change C. If V_{\max} is less than 0.8 C we increase the time step. If $V_{\max} > 1.5 C$, a recycle is needed. On the other hand, if $0.8 C \leq V_{\max} \leq 1.5 C$, we decrease the time step according to the relation:

$$\Delta t = 0.8 \Delta t (C/V_{\max}) \quad (5.68)$$

- These time step controls are useful in the way we can check the variation of velocity, momentum or even energy between iterations. Also, the use of these time step controls preserves the code's efficiency, with respect to computation running costs.

CHAPTER 6

NUMERICAL AND EXPERIMENTAL RESULTS OF THE OPEN CHANNEL FLOW (ISOTHERMAL CASE)

6.1 INTRODUCTION

In this chapter, the verification of the code (results of the three tests described in section 5.5) for the two-electrode and three-electrode systems will be presented and discussed. This includes the results of both single and double step structures. Numerical results obtained using the equations of conservation of mass and momentum will be presented in section 6.2. The preliminary experimental results for the open channel flow, where the discharge is not on, will also be presented and discussed in section 6.3.

6.2 NUMERICAL RESULTS OF THE OPEN CHANNEL FLOW

6.2.1 NUMERICAL RESULTS OF THE TWO-ELECTRODE SYSTEM

(FIRST TEST)

In this section, the numerical results of the first test for the two-electrode system will be presented and discussed. The basic electrode geometry has been presented in Fig. 5.7. The two electrodes extend in the x-z plane. The channel height (y) is assumed to be 10 cm. The simulation

mesh configuration has been presented in Fig. 5.1 and consists of 30×30 cell field. The mesh extends over an area of $20 \text{ cm} \times 10 \text{ cm}$ in the X-Y plane with $\Delta X/\Delta Y=2$, and includes the area between the electrodes with the ghost points located inside the electrodes.

Figure 6.1 presents the profiles of the gas flow velocity obtained using the first version of the computer code IGCP (Implicit Gasdynamic Computer Program). In Fig. 6.1, curve 1 represents the initial profile after one time-step, while curve 2 represents the desired profile after 500 time steps (iterations) where the flow is fully developed. A steady state condition is assumed to be reached, after no further changes in the profile occur.

During the development of a steady state flow profile in the channel, viscous forces will slow fluid layers in the neighborhood of the solid boundary. Since the velocity of the fluid in the growing boundary layer is being decelerated, and if the mass flow rate is to remain constant, the velocity of the central layers of the flow must increase. This continues until a fully developed state is reached, in which the velocity profile remains unchanged.

To estimate the number of iterations required for the flow to reach the fully developed status, we first determine the Reynolds number Re in this case. For the case of flow in an open channel, the Reynolds number is given by [138] $Re = 2\rho vr/\mu$. In our case, Re is calculated to be 2022. The

Initial and Final Velocity Profiles

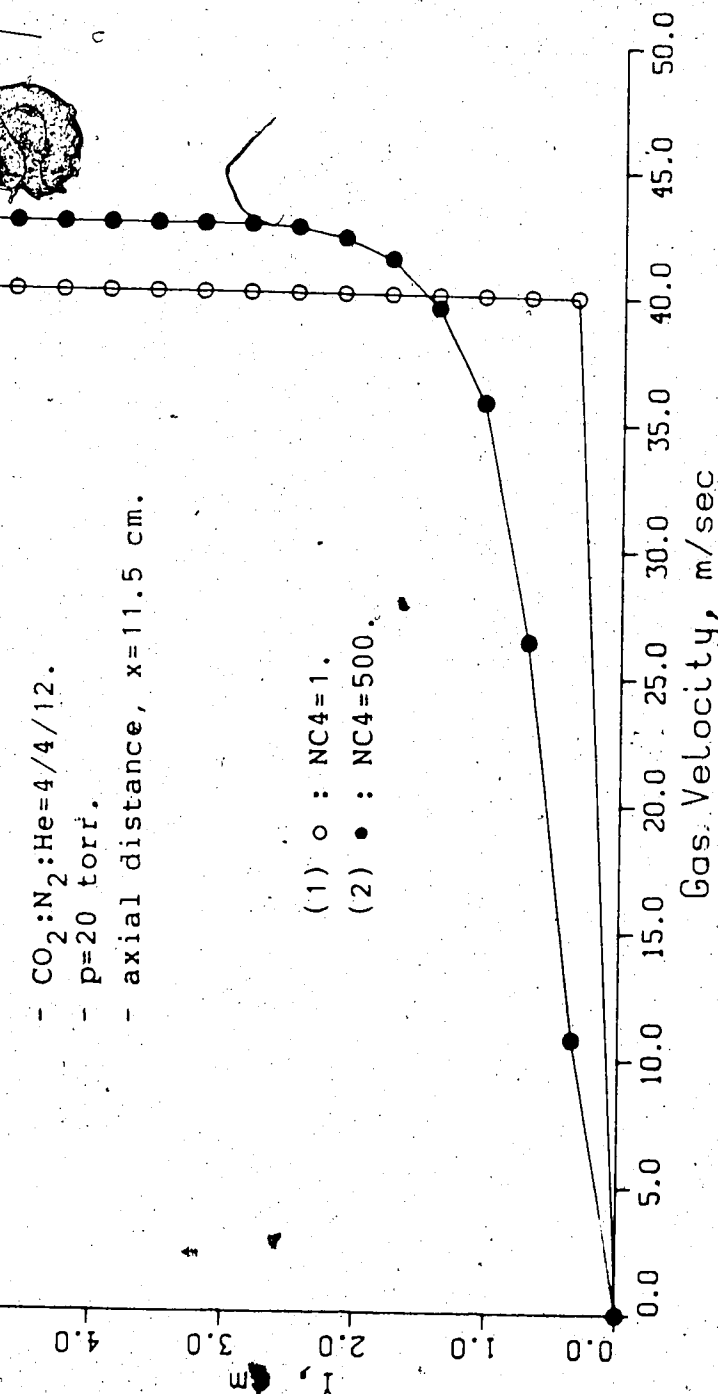


Fig. 6.1 Initial and final velocity profiles, number of iterations are NC4=1 and NC4=500.

distance L for fully developed flow to take place can be estimated from the relation [139], $L = 0.058 D Re$. The x -dimension of the computational grid has a length of $x=20$ cm, therefore the number of iterations ($NC4$) required to reach the fully developed status is $NC4=L/x$. In our case this is calculated as 59 iterations. However, by running the program for 500 iterations we ensure that a steady state condition is reached.

From the above discussion, we can see that both the velocity profile and the mass flow distribution must be considered at steady state conditions, in order to determine whether the code is working properly. Figure 6.2 illustrates the distribution of the mass flow across the test section, obtained for the same conditions of Fig. 6.1. The program was run for 500 iterations. The code results were time averaged over the last 100 iterations and spatially averaged across the height of the channel (y) at each point (30 points) on the x -axis. As it can be seen from Fig. 6.2, the mass flow is constant over the test section, i.e. it indicates that the conservation of mass is well maintained.

The preceding results indicate that the open channel flow scheme is well handled by the computer program in a numerically stable manner. The size of the time step was increased to twice the CFL limit without any loss of stability. This means that the IGCP program can accommodate large time step size in excess of the CFL limit. The

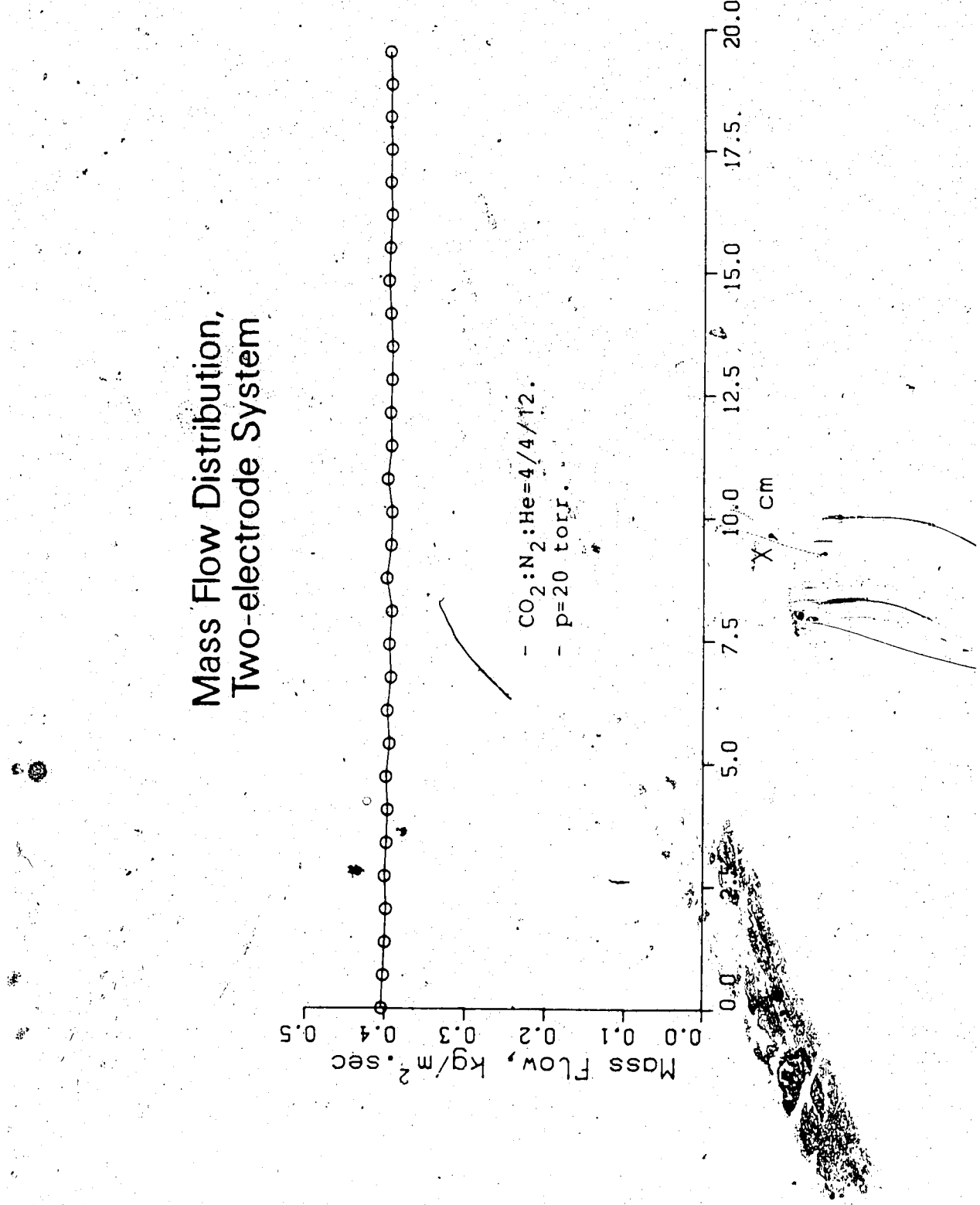


Fig. 6.2 Mass flow distribution along the x-axis.

computer code was then modified to simulate gas flow in a three-electrode system. These results are presented in the next section.

6.2.2 NUMERICAL RESULTS OF THE THREE-ELECTRODE SYSTEM

In this section the numerical results of the second and third tests described in section 5.5 for the three electrode system will be presented and discussed. It must be noted that these tests were made when only the mass and momentum conservation equations are being solved. The basic electrode geometry has been presented in Fig. 5.3. The flat anode sections are located at the top and bottom of the channel, while the cylindrical cathode is located at the center of the channel, just upstream of the anode sections. As was mentioned earlier, the cylindrical shape of the cathode was approximated by a single or double step rectangular structure. The simulations were performed on the upper half of the structure of Fig. 5.3 between the centerline (A-A) and the top anode section. The flowing fluid in the system is assumed to be a laser gas mixture of $\text{CO}_2/\text{N}_2/\text{He}$, in the proportion of 4:4:12 torr at a pressure of 20 torr and at room temperature (300°k). The results of the single and double step configurations are presented in sections A and B below.

A. RESULTS OF THE SINGLE-STEP APPROXIMATION (SECOND TEST)

In this case, the simulation mesh extends over a region of 20 cm x 5 cm which is located between the centerline (A-A) and the top anode section of Fig. 5.3. In the basic mesh configuration of Fig. 5.4, a rectangular step of 2.5 cm width (base B2) and 1.25 cm height (base B1 or base B3) is located such that the base B1 is 4.5 cm downstream of the entrance.

Figure 6.3 shows the velocity distribution obtained by using the IGCP computer code. The circulated gas flow in the discharge region is deflected over the cathode (obstacle), and then compressed between the two electrodes where the gas velocity is increased considerably so as to conserve the mass flow. The phenomenon of flow separation is observed, and it occurs below the sharp corner c2 (Fig. 5.4) just downstream of the cathode.

Figure 6.4 shows the time averaged mass flow across the discharge cross section, which is obtained numerically by the IGCP computer code for the same conditions of Fig. 6.3. The program was run for 500 time steps with a maximum time step being equal 96% of the CFL limit. The code results were time averaged over the last 100 time steps and spatially averaged across the height of the channel (y) at each mesh point on the x -axis. As can be seen, the mass flow is

Velocity Distribution For Single-step Structure

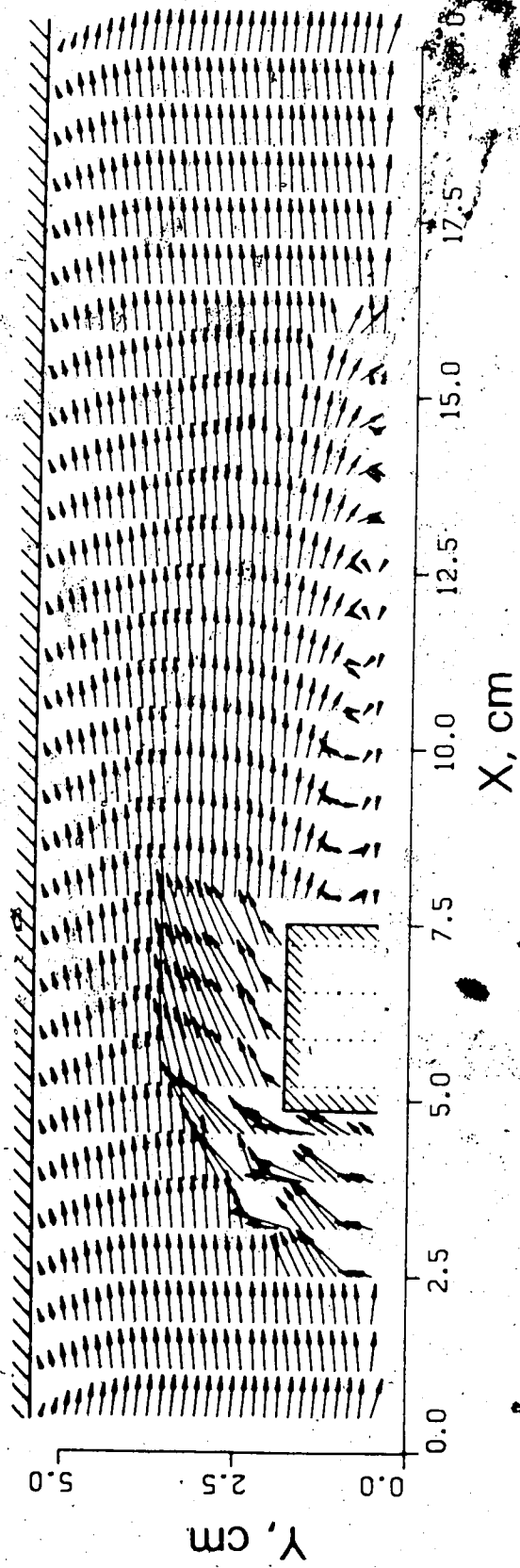


Fig. 6.3 Velocity vector distribution in the single step structure scheme.

Mass-Flow Distribution, Single-step Structure

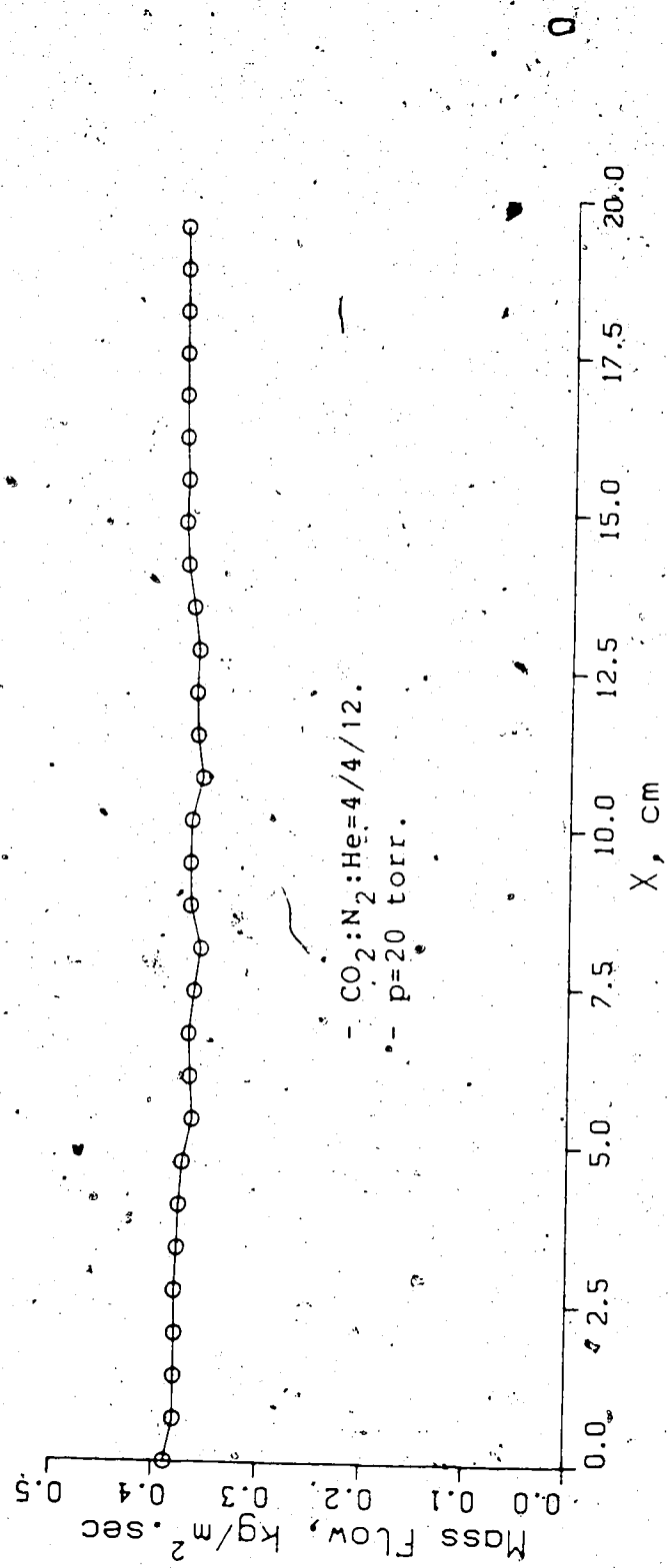


Fig. 6.4 Mass flow distribution along the x-direction in the single step case

uniform over the discharge section. Consequently, the mass flow is conserved.

The velocity profiles obtained using the IGCP computer code are plotted in Fig. 6.5. The profiles are displayed at three different locations downstream of the cathode surface (which is located at $X=7.5$ cm on the scale in Fig. 6.3). The first curve represents the velocity profile at $x=2.5$ cm downstream from the cathode surface. The negative points on the profile indicate a velocity reflection in this region, which agree with the velocity distribution shown in Fig. 6.3. As the flow advances further downstream, it starts to flatten as indicated by curves 2 and 3 in Fig. 6.5. This result is in good agreement with the experimental findings to be presented later in this chapter.

B. RESULTS OF THE DOUBLE-STEP APPROXIMATION

(THIRD TEST)

The cathode electrode in this case is approximated by a double step structure, in which the first is 4 cm x 0.8 cm block with a 2.5 cm x 0.45 cm block located on the top of this. This double step is located in a 30x30 cell field similar to that of the single step case and at the same location in the cell field. The inflow and top boundary have the same relative position to the double step as that in the single step case. The laser-gas mixture and the gas pressure are also same as those used in the single step case.

**Velocity Profiles : Axial Distance X
Single-Step Structure**

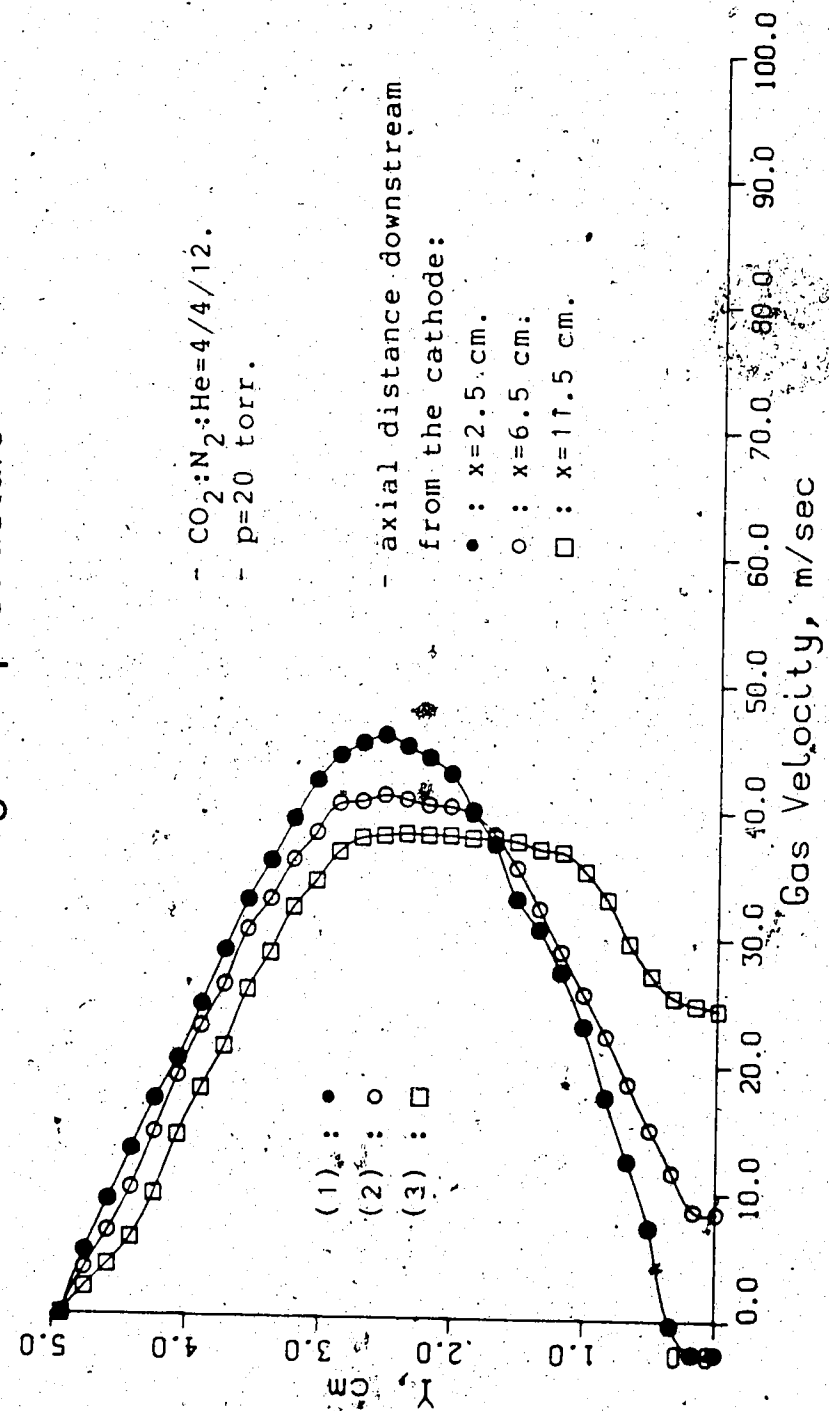


Fig. 6.5 Velocity profiles at different points on the x-axis, for the single step structure.

Figure 6.6 shows the distribution of the velocity vectors predicted by the IGCP computer code. The laser gas flow profile obtained with the double step approximation for the electrode shows a similar behavior to that obtained for the single step approximation. Some minor changes in the amplitude and orientation of the velocity vectors do occur upstream of the cathode. Also, the flow structure shows the same phenomenon of flow separation observed in the previous case with a single-step structure.

Figure 6.7 shows the averaged mass flow obtained for the same parameters as used in obtaining Fig. 6.6. The mass flow distribution is uniform and verifies the conservation of mass by the simulation code along the flow path in the simulations. Therefore, the flow pressure and circulation are well maintained. The velocity profile was also monitored at three locations downstream of the cathode. The results are shown in Fig. 6.8 and are similar to those obtained for the single step approximation.

The above results suggest that the approximation of the cathode shape to a single step or even double step structure is sufficient. It suggests also that the phenomenon of flow separation observed in both single and double step structures does not depend on the variation in the boundary conditions. This latter result agrees with, and supports the results of fluid flow over an obstacle which was obtained before using different numerical methods [140-142].

Velocity Distribution For Double-step Structure

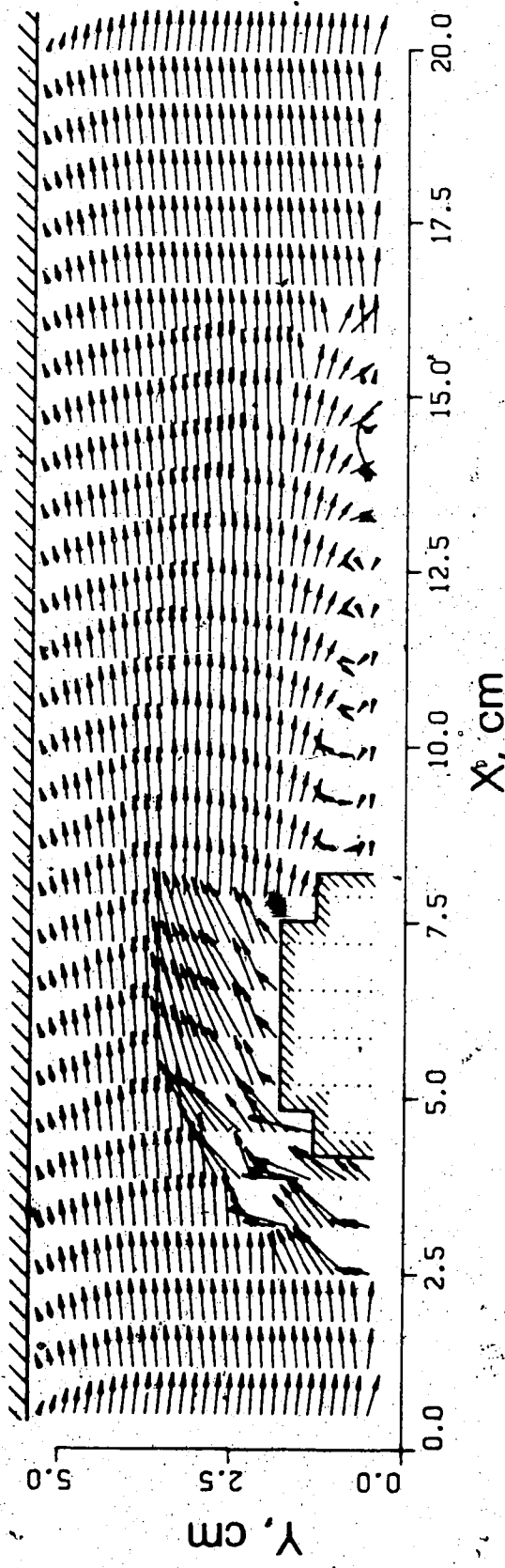


Fig. 6.6 Velocity vector distribution in the double step structure scheme.

Mass Flow Distribution Double-step Structure

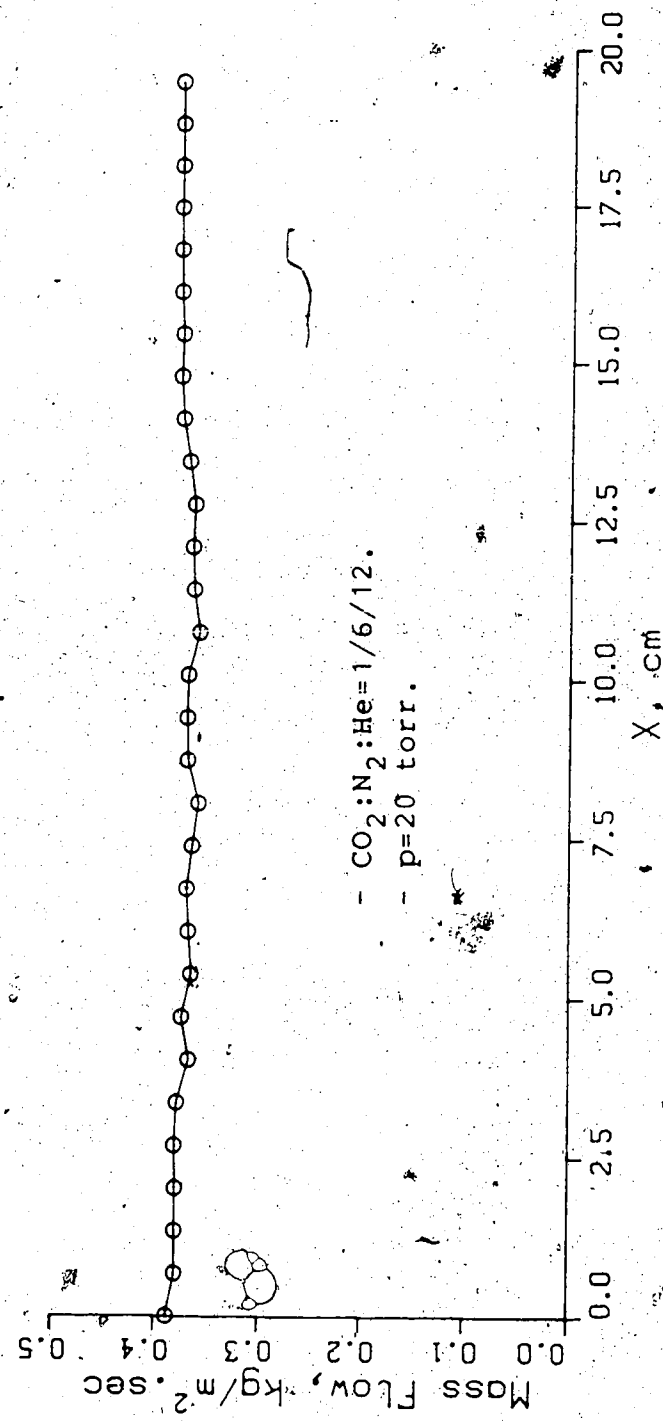


Fig. 6.7 Mass flow distribution along the x -direction in the double step case.

**Velocity Profiles : Axial Distance X
Double-step Structure**

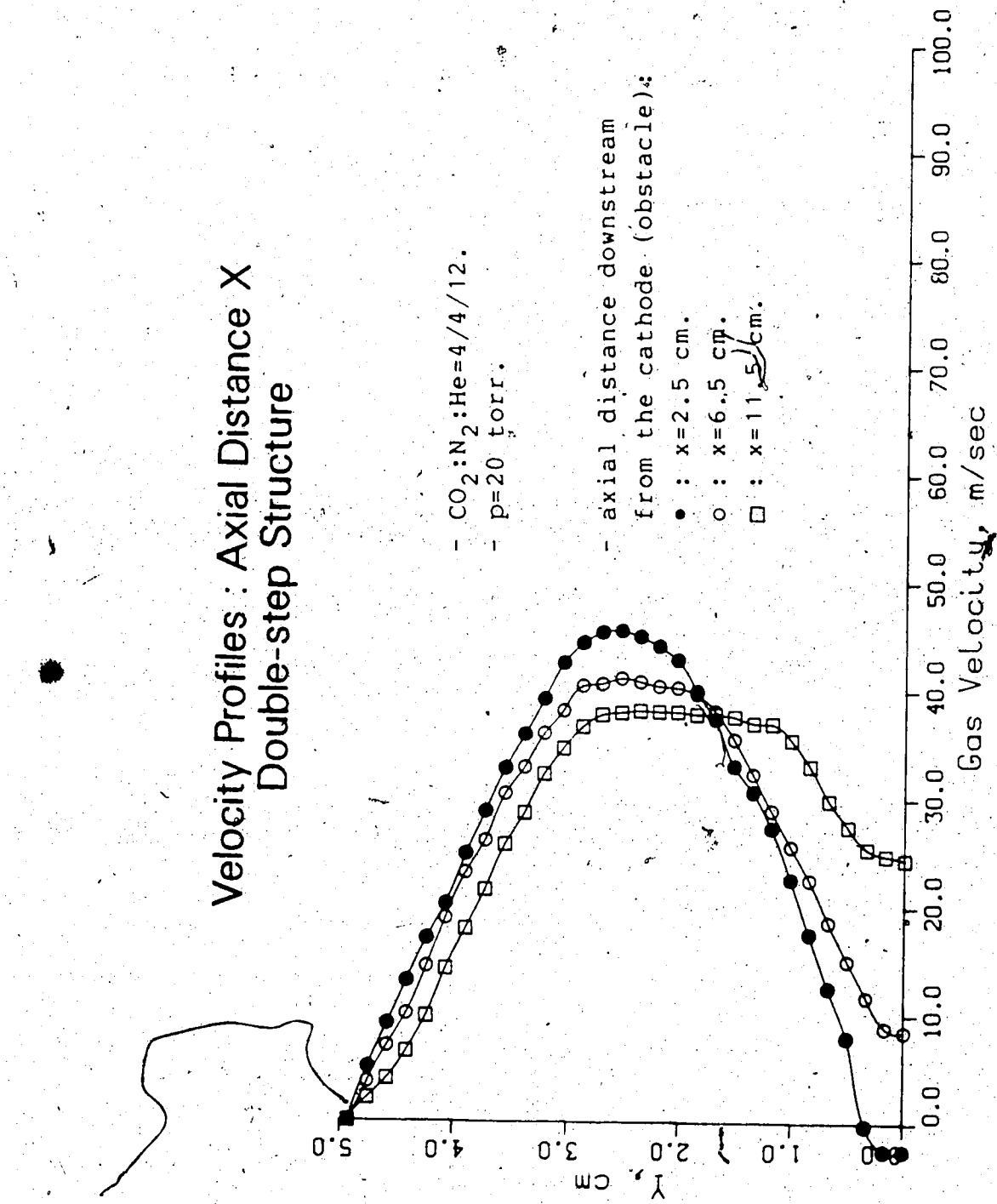


Fig. 6.8 Velocity profiles at different points on the x-axis, for the double step structure.

It may be noted that the numerical results for the single and double step approximations for the cathode were obtained by running the computer program with a time size equal to 20% of the CFL limit for 500 time steps (iterations); at which time steady state conditions were obtained. These runs were repeated with a time size equal to 96% of the CFL limit, and the same results obtained. The stability of the iterative ADI computer code used in our program was also tested by increasing the size of the time step to twice the CFL limit. The results showed that even with this very large time step, the program is very stable. Consequently, we can obtain the same results in a fewer number of time steps and effectively reduce the computational time and running costs.

6.3 EXPERIMENTAL RESULTS OF THE OPEN CHANNEL FLOW

6.3.1 EXPERIMENTAL RESULTS OF THE TWO-ELECTRODE SYSTEM

The gas flow velocity of a laser gas mixture at room temperature was measured across a 10 cm high channel. The two-electrode channel is shown in Fig. 5.7. The measurements were done using a Pitot tube connected to a capacitance manometer. A gas mixture of $\text{CO}_2/\text{N}_2/\text{He}$ (4:4:12 torr) was used at a pressure of 20 torr. The measurements were made 1.5 cm downstream of a reference point, which is located at the cross section (a-a) in Fig. 5.7. The gas velocity

distributions across the channel are shown in Fig. 6.9. The measured velocity profiles are in good agreement with the computer simulation results, as can be seen from Fig. 6.10. These fully developed flow profiles are found to be independent of the gas pressure and the location from the reference point (a-a) in the scanned test region.

6.3.2 EXPERIMENTAL RESULTS OF THE THREE-ELECTRODE SYSTEM

The experimental measurements for the three-electrode system were carried out in a similar way to that used in the two-electrode case. The gas flow velocity was measured across the channel using a Pitot tube connected to a capacitance manometer. The laser gas mixture used was CO₂/N₂/He in the proportion 4:4:42 at a total pressure of 20 torr. With reference to Fig. 5.3, the measurements were made at 11.5 cm and 31.5 cm from the downstream surface of the cathode (obstacle) at room temperature (300 °k).

Figure 6.11 presents the measured velocity profile near and far from the cathode. Curve (1) in Fig. 6.11 shows the effect of the cathode (obstacle) on the velocity profile. A stagnation point formed downstream close to the cathode is believed to be responsible for this effect. At the far point downstream of the cathode, the velocity profile flattens since the effect of the obstacle is reduced. These results are in good agreement with the numerical results obtained from the IGCP computer program as can be seen in Fig. 6.12.

Measured Velocity Profiles : Axial Distance X Two-electrode System

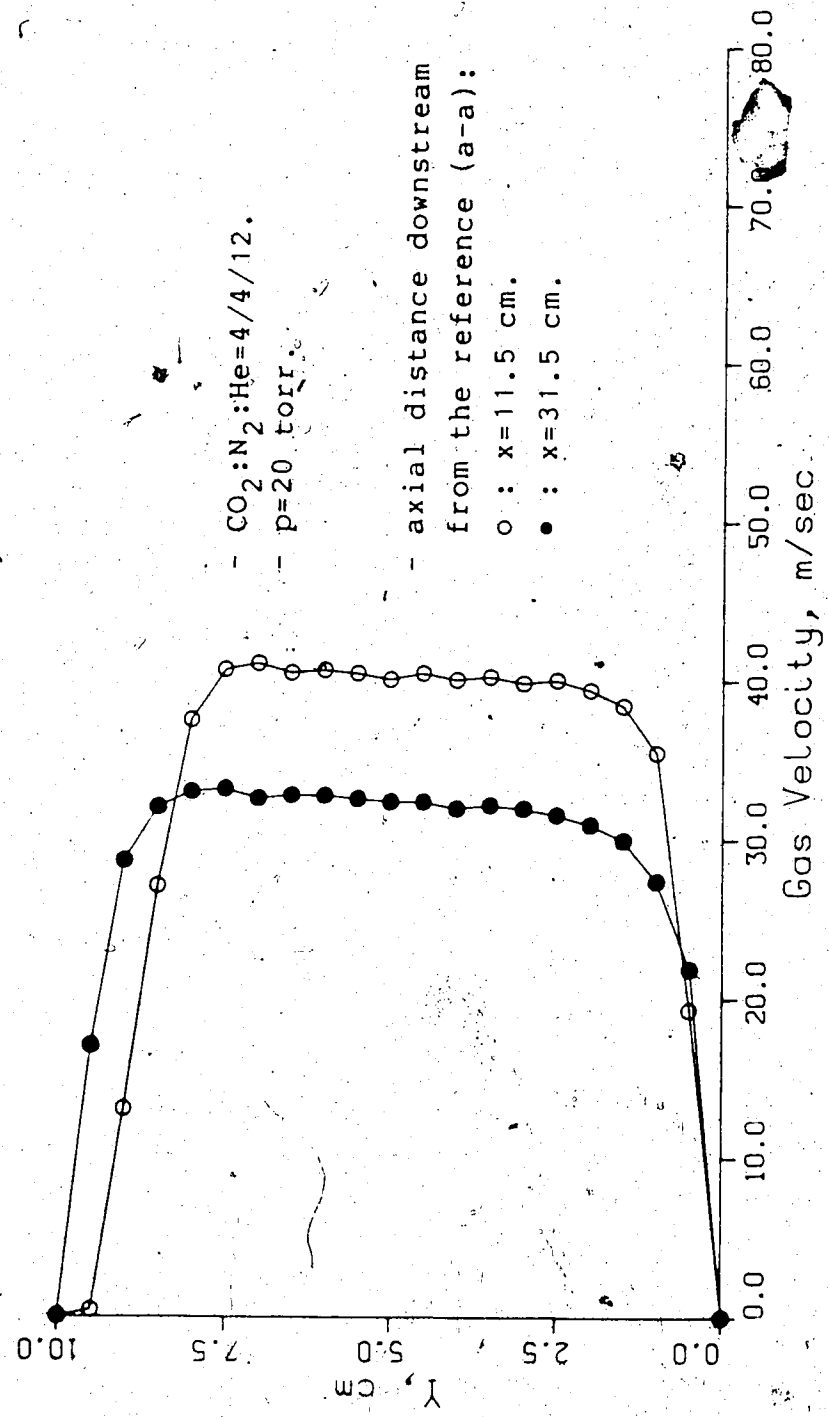


Fig. 6.9 Measured velocity distribution across the channel
for the two-electrode system.

**Computed And Measured Velocity Profiles
Two-electrode System**

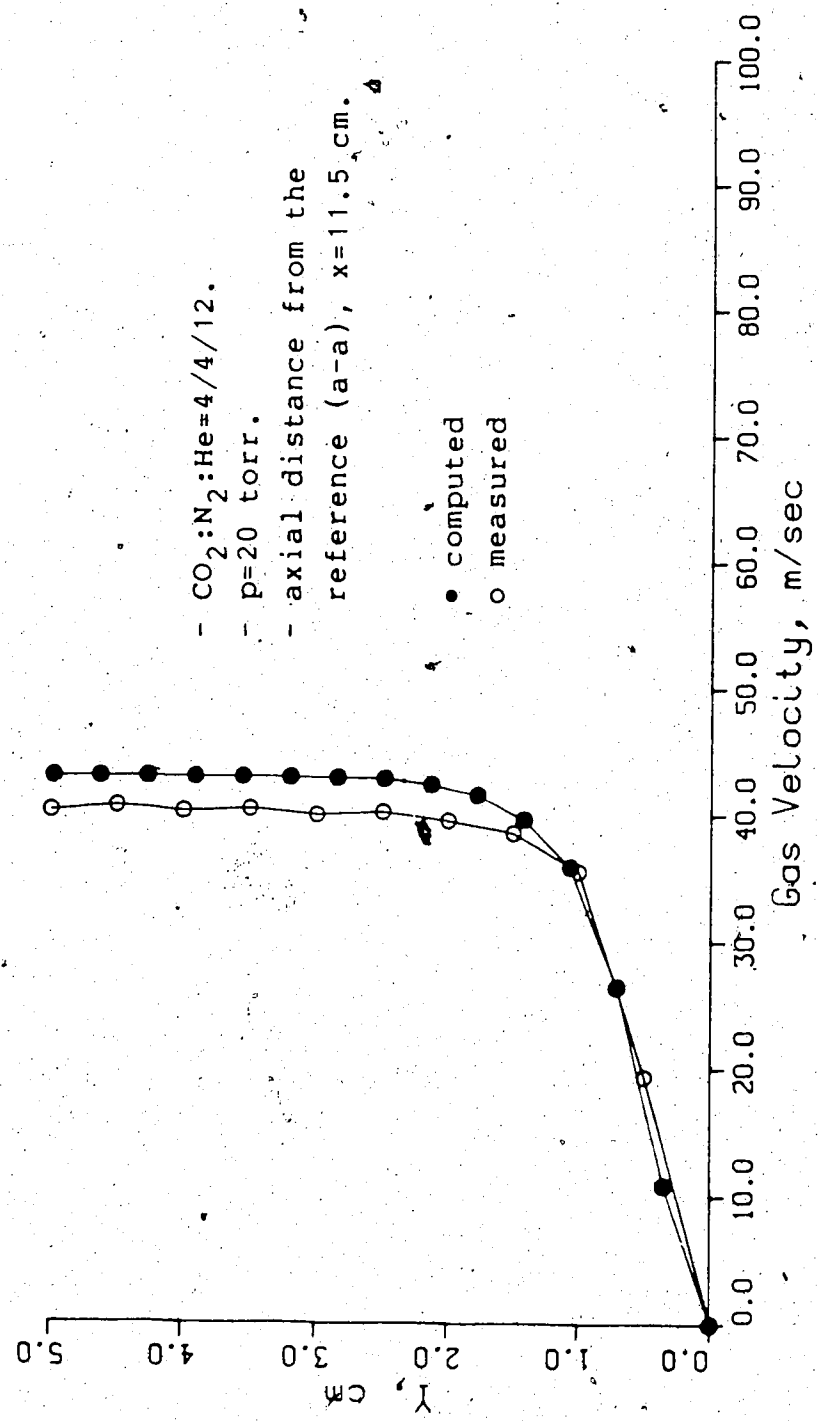


Fig. 6.10 Comparison of computed and measured velocity profiles for the two-electrode system.

Measured Velocity Profiles : Axial Distance X Three-electrode System

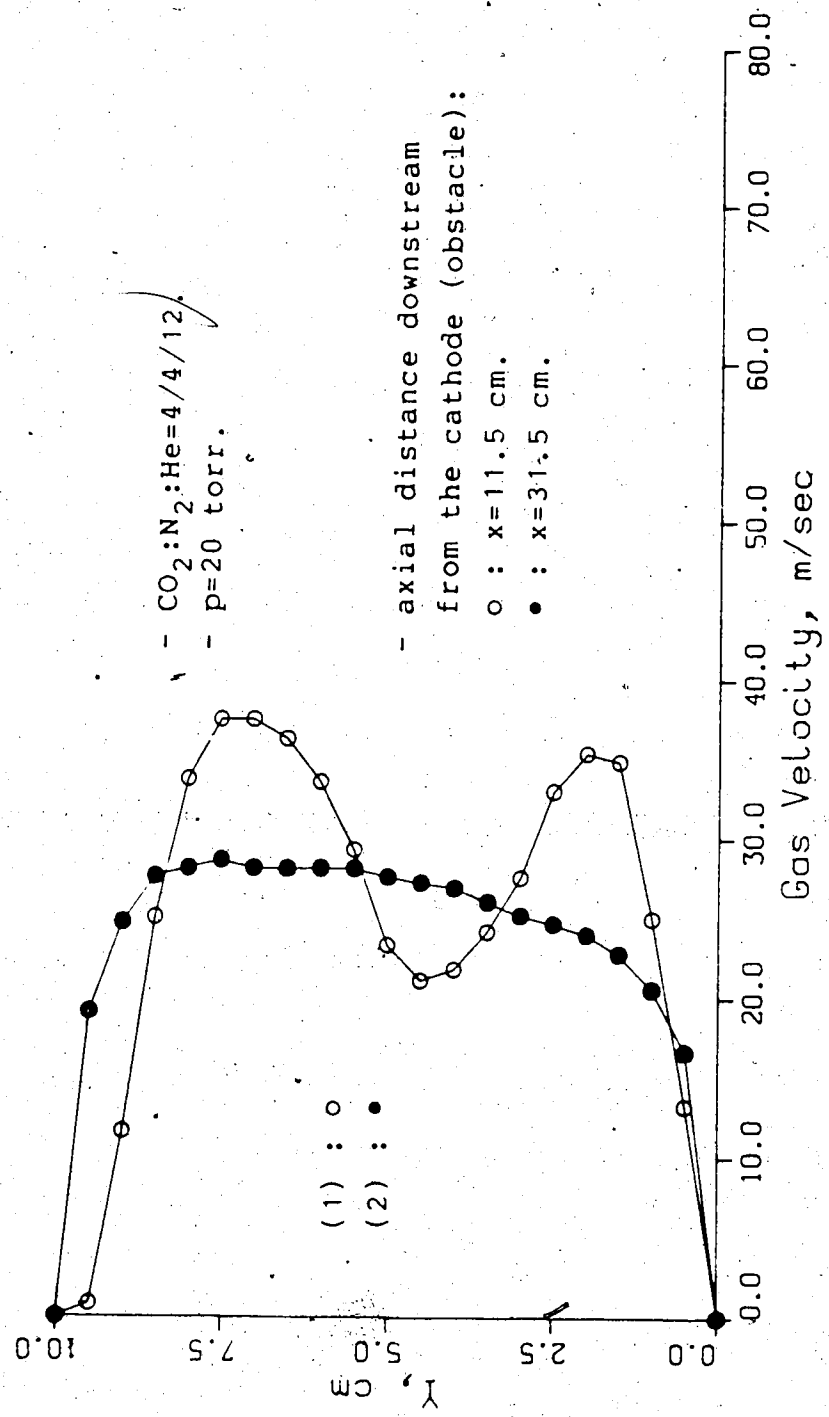


Fig. 6.11 Measured gas velocity distribution across the channel for the three-electrode system.

**Computed And Measured Velocity Profiles
Three-electrode System**

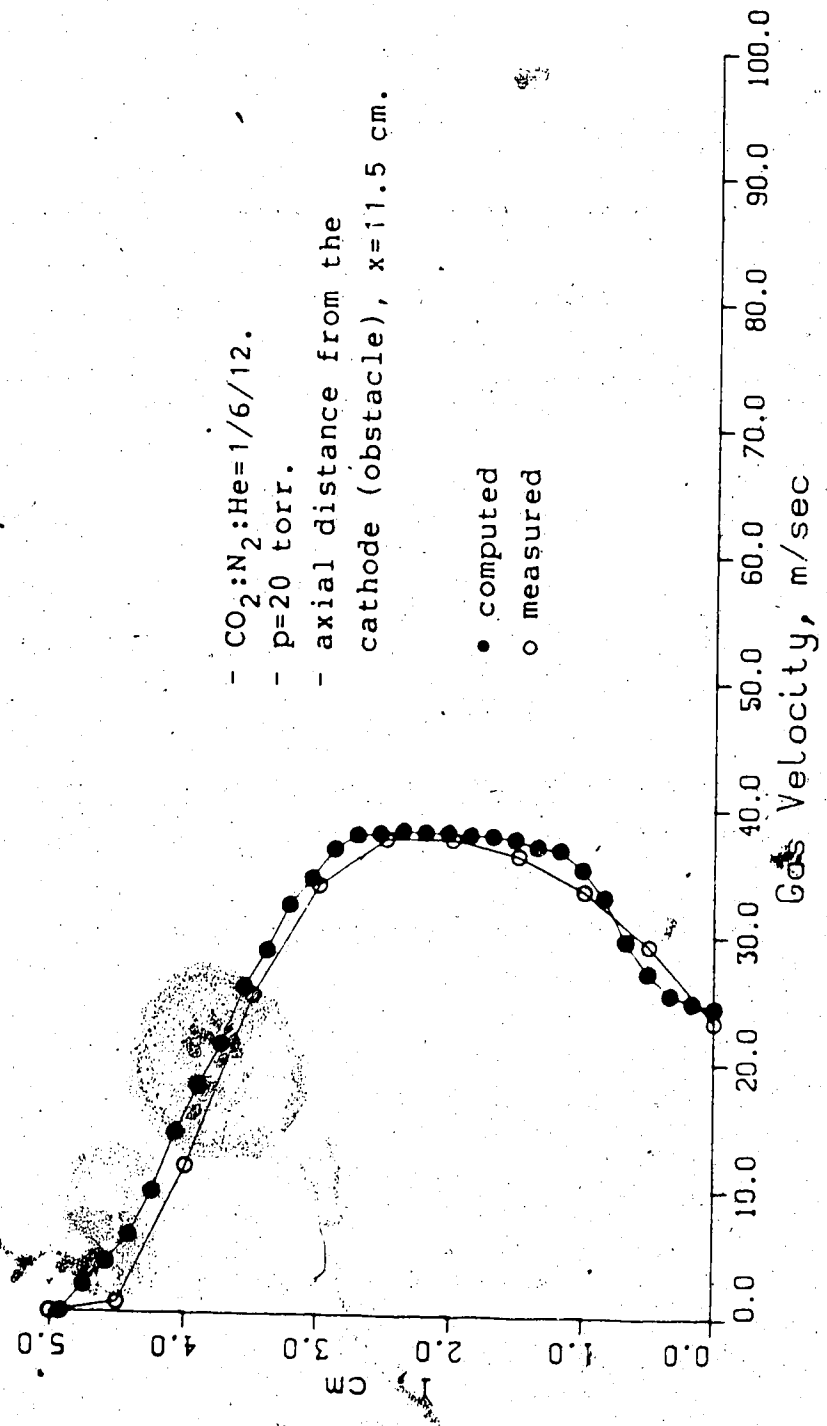


Fig. 6.12 Comparison of computed and measured velocity profiles for the three-electrode system.

They are also in good agreement with the experimental results obtained by Kovasznay [143] who measured the flow velocity around a circular cylinder.

As a conclusion, the experimental results for both two and three-electrode systems are in good agreement with the computer simulation results obtained from the computer code IGCP. The numerical results presented in this chapter are intended to verify the ability of the IGCP computer code to correctly treat open channel flow.

CHAPTER 7

NUMERICAL AND EXPERIMENTAL RESULTS OF THE OPEN CHANNEL FLOW LASER GAS DISCHARGE

7.1 INTRODUCTION

In chapters 4 and 5, the computer code IGCP was developed to simulate steady state in an open channel flow laser gas discharge. The boundary conditions were treated in detail for the different electrode structures under consideration. In chapter 6, results of several tests on the code were presented. In those tests only the equations of conservation of mass and momentum were considered. The numerical results of the tests verified the ability of the IGCP computer code to correctly treat open channel flow. In this chapter, the numerical and experimental results for the three-electrode system are presented and discussed. Numerical solutions using the complete computer code including conservation of mass, momentum and energy equations are presented in section 7.2.

7.2 NUMERICAL RESULTS OF THE OPEN CHANNEL FLOW LASER GAS DISCHARGE

The basic electrode geometry has been presented in Fig. 5.3. The flat anode sections are located at the top and

bottom of the channel, while the cylindrical cathode is located at the center of the channel, just upstream of the anode sections. As was mentioned earlier, the cylindrical shape of the cathode was approximated by a rectangular single step structure. The simulations will describe the flow pattern in the upper half of the structure of Fig. 5.3, between the centerline (A-A) and the top anode section. Only the upper half of the structure will be investigated because of the symmetry about the (A-A) centerline.

The mesh configuration used in this case consists of a 4x8 cell single step (for modeling the cathode) in a 30x30 cell field with $\Delta X/\Delta Y=4$. The simulation mesh extends over the upper half region which is 20 cm x 5 cm. Referring to the configuration of Fig. 5.4, a rectangular step of 2.5 cm width (base B2) and 1.25 cm height (base B1) is located such that the base B1 is 4.5 cm downstream from the entrance. The flowing fluid in the system is a laser gas mixture of $\text{CO}_2/\text{N}_2/\text{He}$ in the proportion of 1:6:12 at a total pressure of 20 torr. The calculated mass density of the mixture is 0.01 kg/m³. The shear viscosity of the laser gas mixture [144-146], is calculated to be 5.39×10^{-6} kg/m.sec.

7.2.1 VELOCITY VECTOR DISTRIBUTION

Analysis of the steady state open channel flow was performed for a laser gas mixture of $\text{CO}_2/\text{N}_2/\text{He} = 1:6:12$ at a pressure of 20 torr. The input power was 1.56 kW and the

corresponding cathode temperature was estimated at 420°K . The input power was introduced into the code through the external heat source term Q (per unit mass) which represents Ohmic heating. This heat source term was introduced in the discharge region only, i.e. in the area between the anode and the cathode.

Figure 7.1 shows the velocity pattern obtained numerically by the IGCP code. The plot is translated 5 mm from both the x - and y - axes to improve clarity. The arrows indicate the direction and magnitude of the gas flow velocity after 500 time steps. The longest arrow corresponds to a velocity of 82.5 m/sec. The time step used during this run was 96% of the Courant limit. The corresponding time in the simulation (after 500 steps) is ≈ 5 ms and is sufficient for steady state flow conditions to be established. This is sufficient for the fluid to cross the channel sixteen times. The circulated gas flow in the discharge region is seen to deflect over the cathode (obstacle) as shown in Fig. 7.1, and then compress between the two electrodes where the amplitude of the gas velocity increased considerably, so as to conserve the mass flow.

The gas flow which is constricted between the two electrodes is now expanded and convected through the channel. However, behind the cathode (obstacle) the flow is unable to follow the turn around the rear of such an obstacle, which is a region of decreasing velocity for real

Velocity Distribution, Input Power=1.56 kW

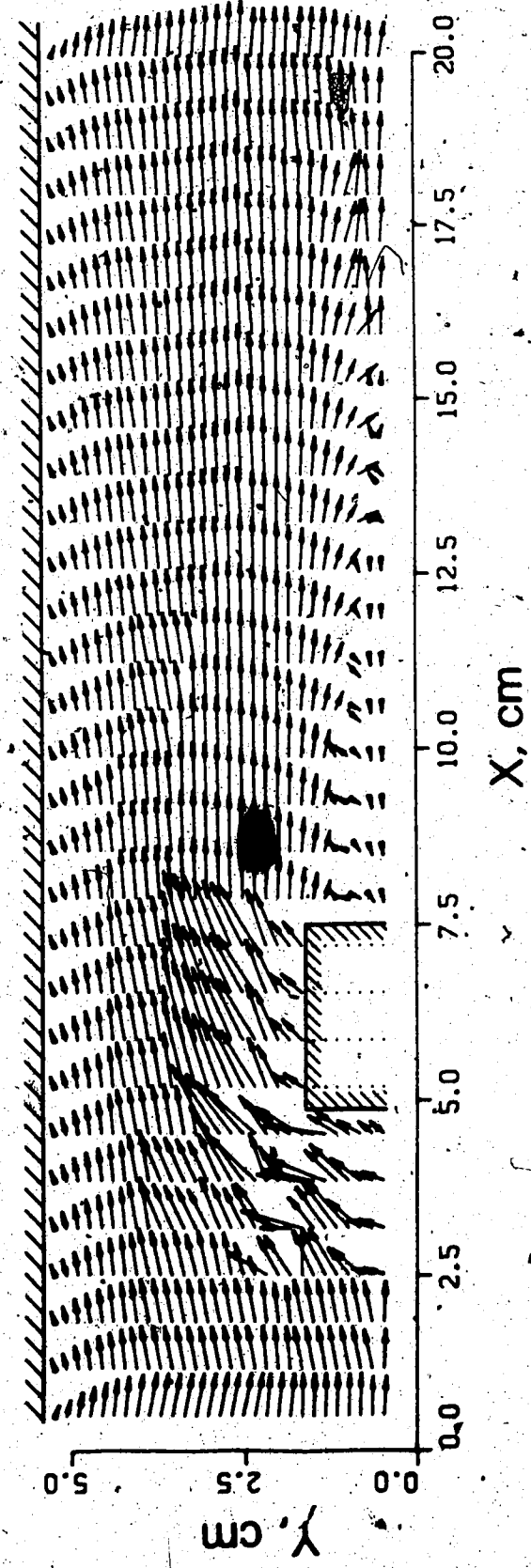


Fig. 7.1 Velocity vector distribution for 1.56 kW input power and a cathode temperature of 420 °k.

fluids of finite viscosity. The flow then separates [147] or breaks away from the rear, and a broad wake forms behind the cathode as can be seen in Fig. 7.1. This phenomenon of flow separation, which occurs below the sharp corner C2 just downstream of the cathode, agree with the results of fluid flow over an obstacle which have been obtained by previous authors [109, 134, 148-151].

For example, Takemitsu [109] observed a similar result in steady flow past a backward-facing step using a finite difference method with invariant implicit iterations to solve the incompressible Navier-Stokes equations. In another example, Thoman and Szewczyk [148] reported a similar result when treating time-dependent viscous flow over a circular cylinder, using an explicit finite difference method. A wide range of Reynolds numbers were considered. Also, the same phenomenon was observed by Roache and Müller [149] when they studied compressible and incompressible viscous flow over a backstep geometry. Moreover, the separation phenomenon for viscous flow past a circular cylinder was observed for even very small viscosity and very large Reynolds number [152, 153].

A series of computational runs with the IGCP code were performed for different values of input power and cathode temperature. Figure 7.2 illustrates the velocity distribution for an input power of 3.16 kW and an estimated cathode temperature of 500 °K. The velocity distribution is

Velocity Distribution, Input Power=3.16 kW

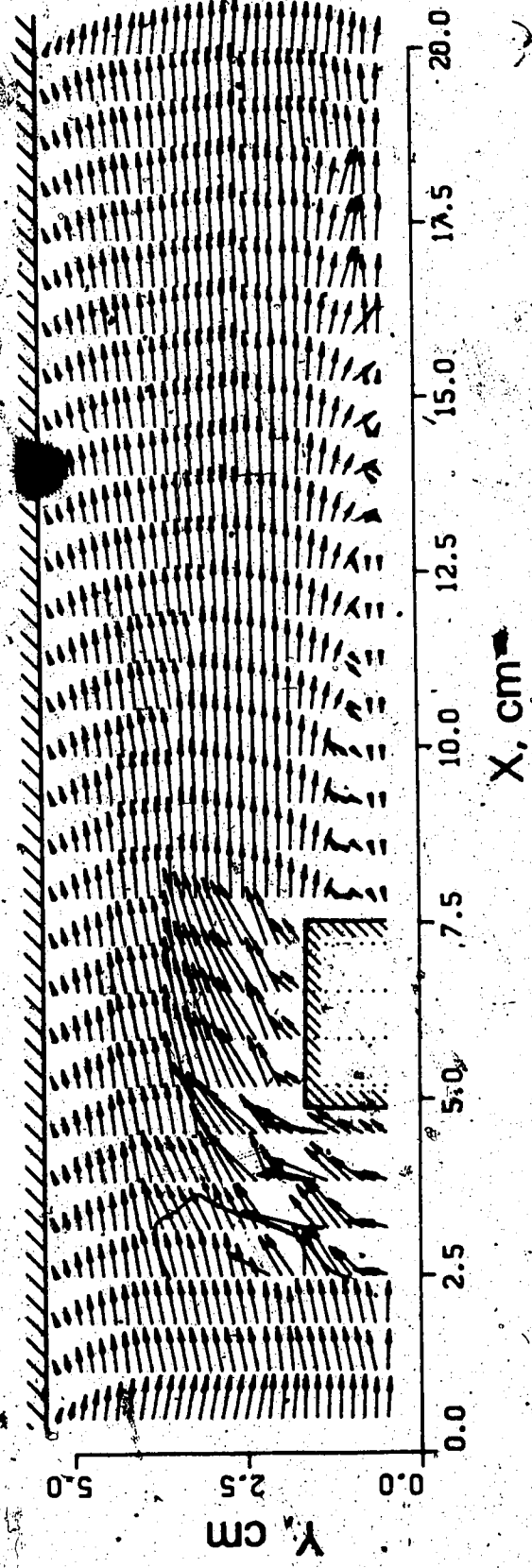


Fig. 7.2. Velocity vector distribution for 3.16 kW input power and a cathode temperature of 500°k .

similar to that of Fig. 7.1, but with the gas velocity increased due to the increase in the input power to the system. Further increase in the input power and cathode temperature results in a corresponding increase in the gas velocity. This effect is observed again in Fig. 7.3. In this case the velocity distribution was obtained for 5.01 kW's of input power and a cathode temperature of 600 °k.

The numerical results presented above were first obtained by running the computer program for 500 time steps using a time-step size of 20% of the CFL limit. The computational runs were then repeated using a time step size of 96% of the CFL limit and the same results were obtained. The stability of the iterative ADI computer code used in our computer program was also tested by increasing the size of the time step to twice the CFL limit. The results showed that even with this very large time step, the program is still very stable. Consequently, we can obtain the same results in a fewer number of time steps, and effectively reduce the computation time and the running cost.

7.2.2 VELOCITY PROFILES (COMPUTATIONAL)

The velocity profiles (v_x) obtained by using the IGCP computer code will be presented in this section. The v_x profiles are displayed at three different locations downstream of the cathode. Curve (1) in Fig. 7.4 shows the velocity profile at 2.5 cm downstream of the cathode

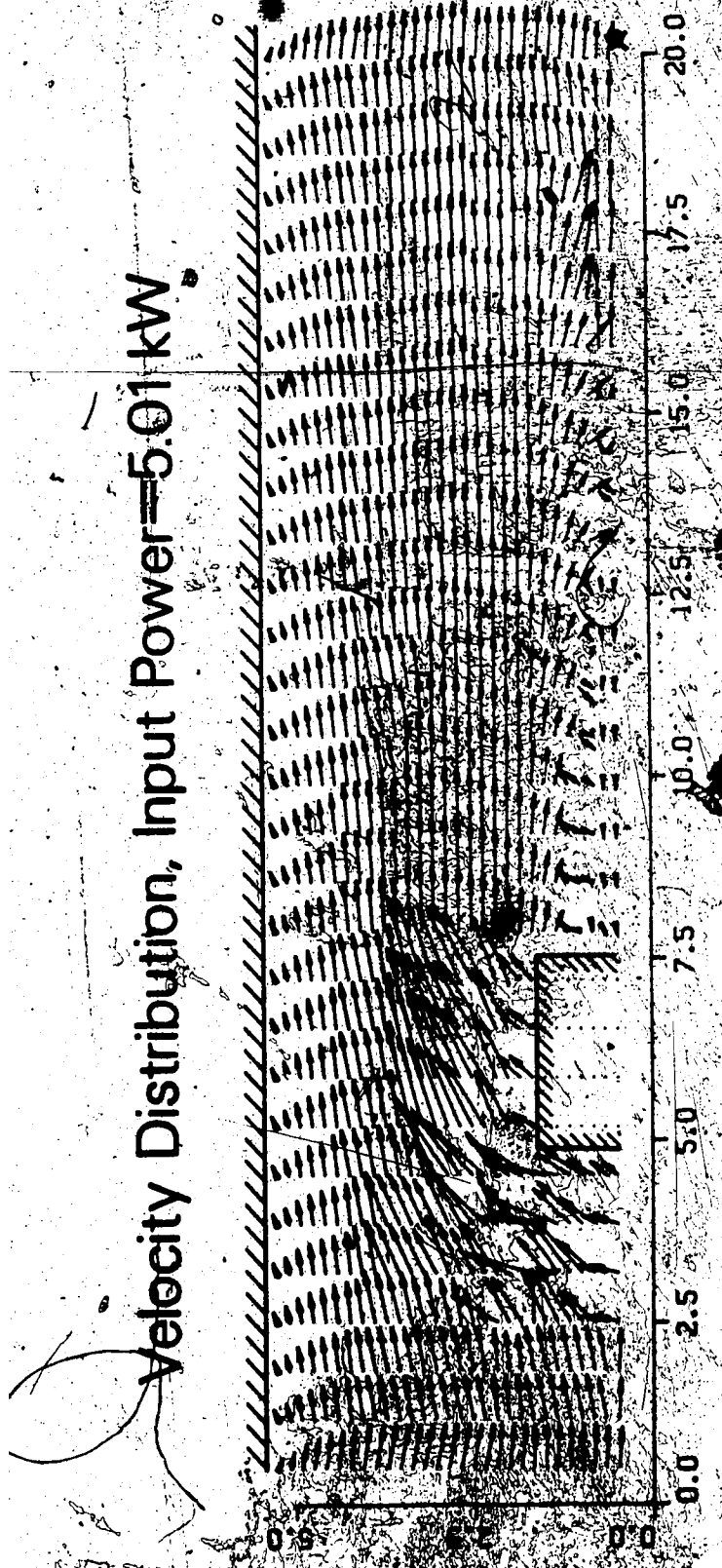


Fig. 7.3 Velocity vector distribution for 5.01 kw input power and a cathode temperature of 600°K .

**Velocity Profiles : Axial Distance X
Input Power=1.56 kW**

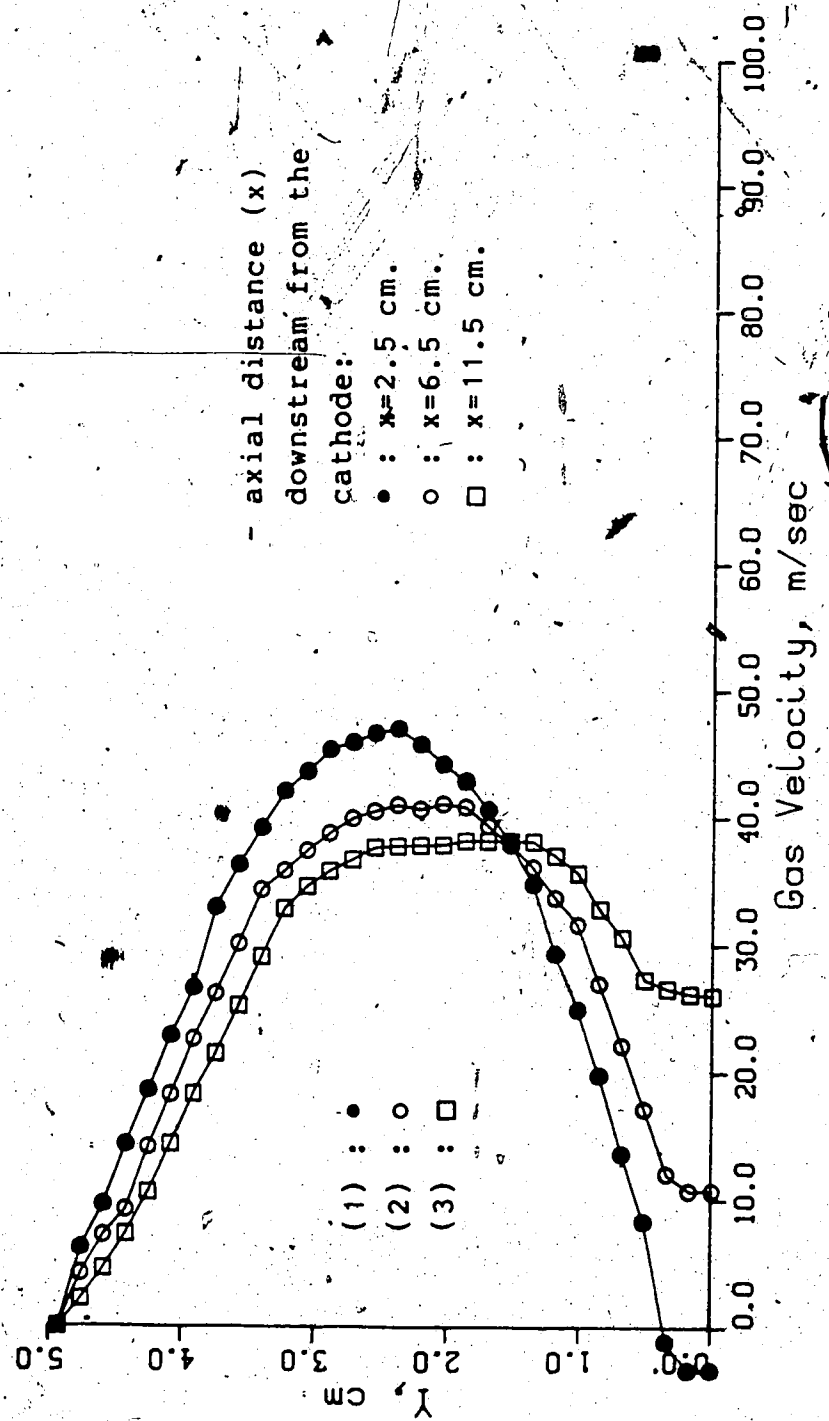


Fig. 7.4 Velocity profiles at different axial distances
downstream, $P_{inp} = 1.56$ kW.

surface. The x-axis represents the magnitude of the velocity v_x , while the y-axis represents the distance from the centerline of the discharge device. The negative velocity points on the profile indicate a velocity reflection in this region which agree well with the velocity distribution presented in the previous section. This result is also in agreement with the results reported by Kawaguti [134], who solved the Navier-Stokes equations for flow around a circular cylinder. The velocity distribution in the wake and along the x-axis was obtained.

For the same conditions used above, the velocity profile was obtained at 6.5 cm downstream of the cathode and away from the wake region. The magnitude of the gas velocity v_x is in the positive direction and the profile tends to flatten as shown by curve (2) in Fig. 7.4. As the flow goes further downstream, the velocity profile flattens as shown by curve (3) in Fig. 7.4 (drawn at 11.5 cm downstream of the cathode). The relative variation in the shape of the velocity profiles with the axial distance is illustrated in Fig. 7.4. Other computational runs were performed at higher input powers and cathode temperatures. Figure 7.5 shows a plot similar to that in Fig. 7.4 but with an input power of 3.16 kW and a cathode temperature of 500 °k. It is apparent that the gas velocity increases by increasing the input power. Again, higher gas velocities were achieved with higher input powers as illustrated in Fig. 7.6, where an input power of 5.01 kW and a cathode temperature of 600 °k

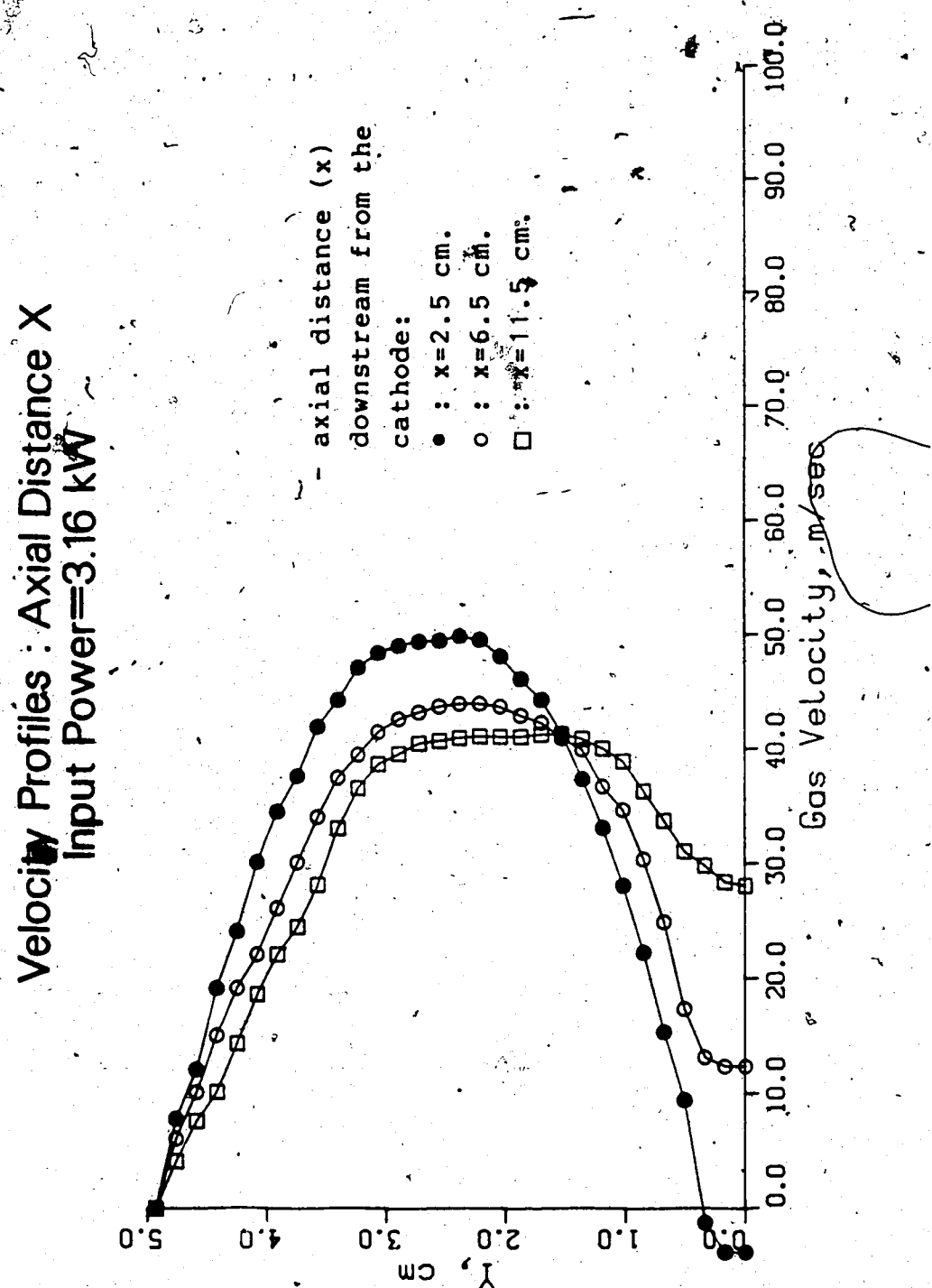


Fig. 7.5 Velocity profiles at different axial distances downstream, Input Power = 3.16 kW.

Velocity Profiles : Axial Distance X
Input Power = 5.01 kW

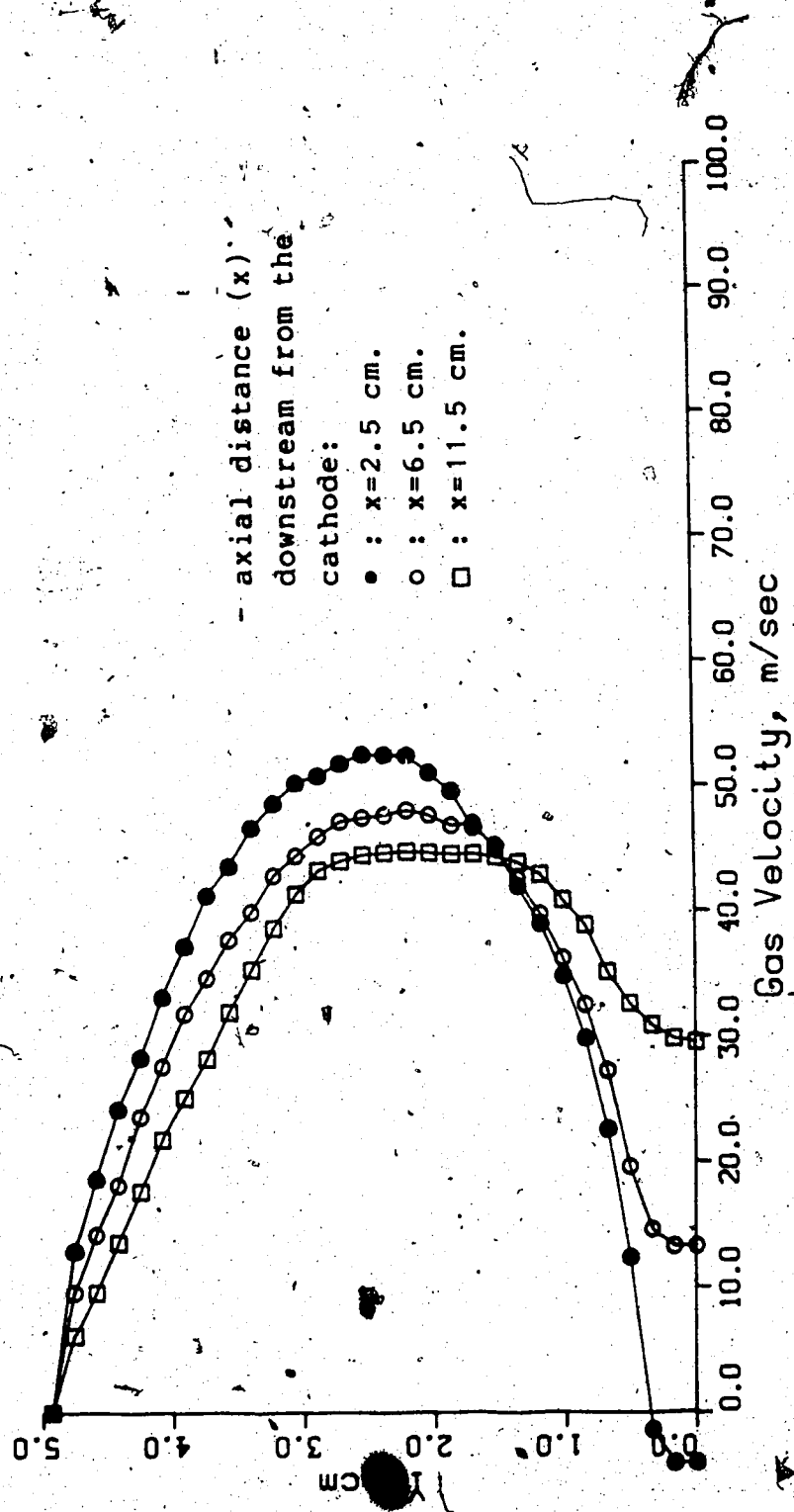


Fig. 7.6 Velocity profiles at different axial distances downstream, $P_{inp} = 5.01$ kW.

were used. This result is in agreement with our experimental measurements which will be presented later in this chapter.

Figure 7.7 illustrates the velocity profiles 11.5 cm downstream of the cathode as a function of the input power.

As was indicated before, the increase in the input power results in an increase in the gas velocity. From this result, an average increase in the gas velocity of about 20% of the initial velocity was achieved over the range of input powers used. This is in good agreement with experimental results, where an average increase in the gas velocity of about 17% was measured for the same range of power loading.

7.2.3. TEMPERATURE DISTRIBUTION

In a gas discharge system, designed for a high power laser operation, it is desirable to have the temperature of the laser medium below a maximum allowable value of about 600 °k [88]. Including the energy equation in our computer code is of great importance, since it allows us to predict the gas temperature within the discharge region. Figure 7.8 shows the predicted gas temperature distributions at 2.5 cm, 6.5 cm and 11.5 cm downstream of the cathode surface. This simulation was made for a laser gas mixture of CO₂/N₂/He in the proportion 1:6:12, at a pressure of 20 torr. The input power used was 1.56 kW at a corresponding estimated cathode temperature of 420 °k.

Velocity Profiles : Input Power

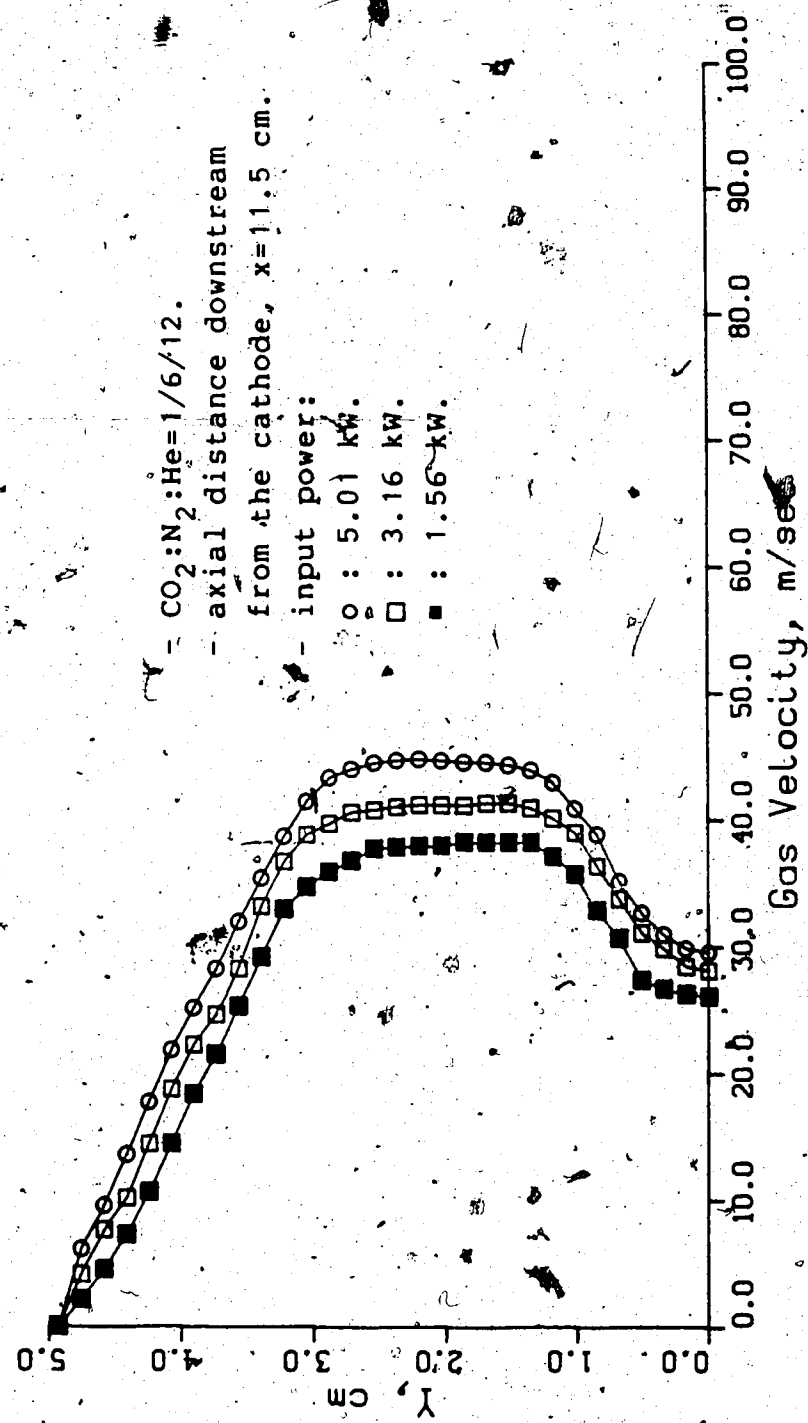


Fig. 7.7 Velocity profiles for different levels of input power at x = 11.5 cm downstream.

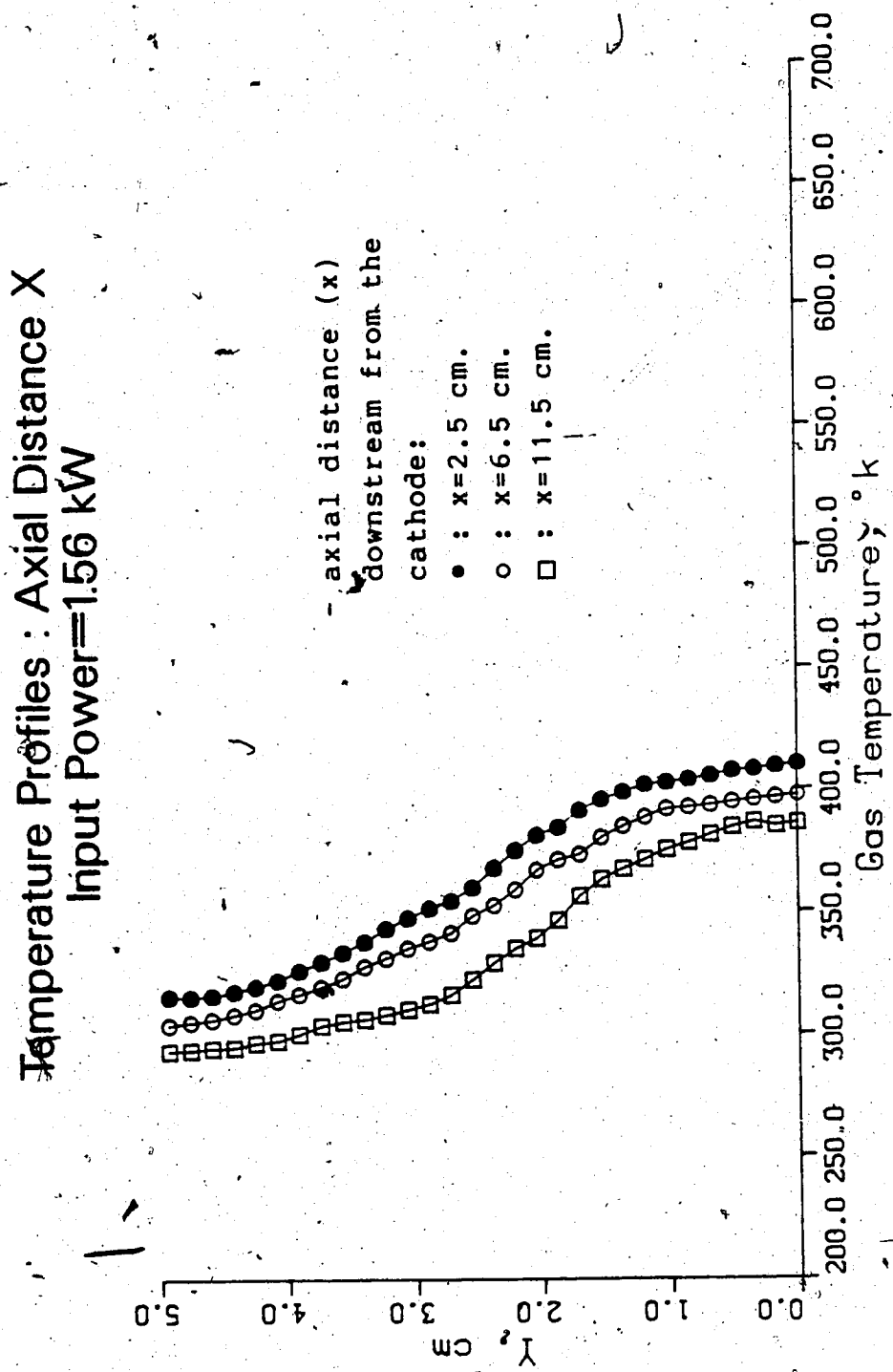


Fig. 7.8 Gas temperature profiles at different axial distances, $P_{\text{inp}} = 1.56 \text{ kW.}$

As can be seen from Fig. 7.8, the gas temperature reaches its maximum at the centerline which passes through the center of the cathode. In this region a stagnation point is formed by the presence of the cathode in the middle of the discharge section. This region, where the gas velocity is minimum, contains hot gas which is then cooled by convective flow downstream. The gas temperature also decreases in a direction towards the anode. In the mid region between cathode and anode, the gas velocity reaches its maximum and consequently more convective cooling occurs; thereby resulting in a lower temperature.

By increasing the input power and consequently the cathode temperature, the gas is further heated and its temperature is increased. Figure 7.9 shows the temperature distribution across the discharge region for 3.16 kW input power and a cathode temperature of 500 °k. Further increase in the input power and cathode temperature results in a still higher gas temperature, as can be seen in Fig. 7.10; where 5.01 kW of input power was used at an estimated cathode temperature of 600 °k.

Figure 7.11 shows the gas temperature distribution predicted at 11.5 cm downstream of the cathode for three input power values and cathode temperatures. It is apparent that the gas temperature increases considerably in the region downstream of the cathode and close to the center of the channel. Away from the cathode region and across the

Temperature Profiles : Axial Distance X
Input Power = 3.16 kW

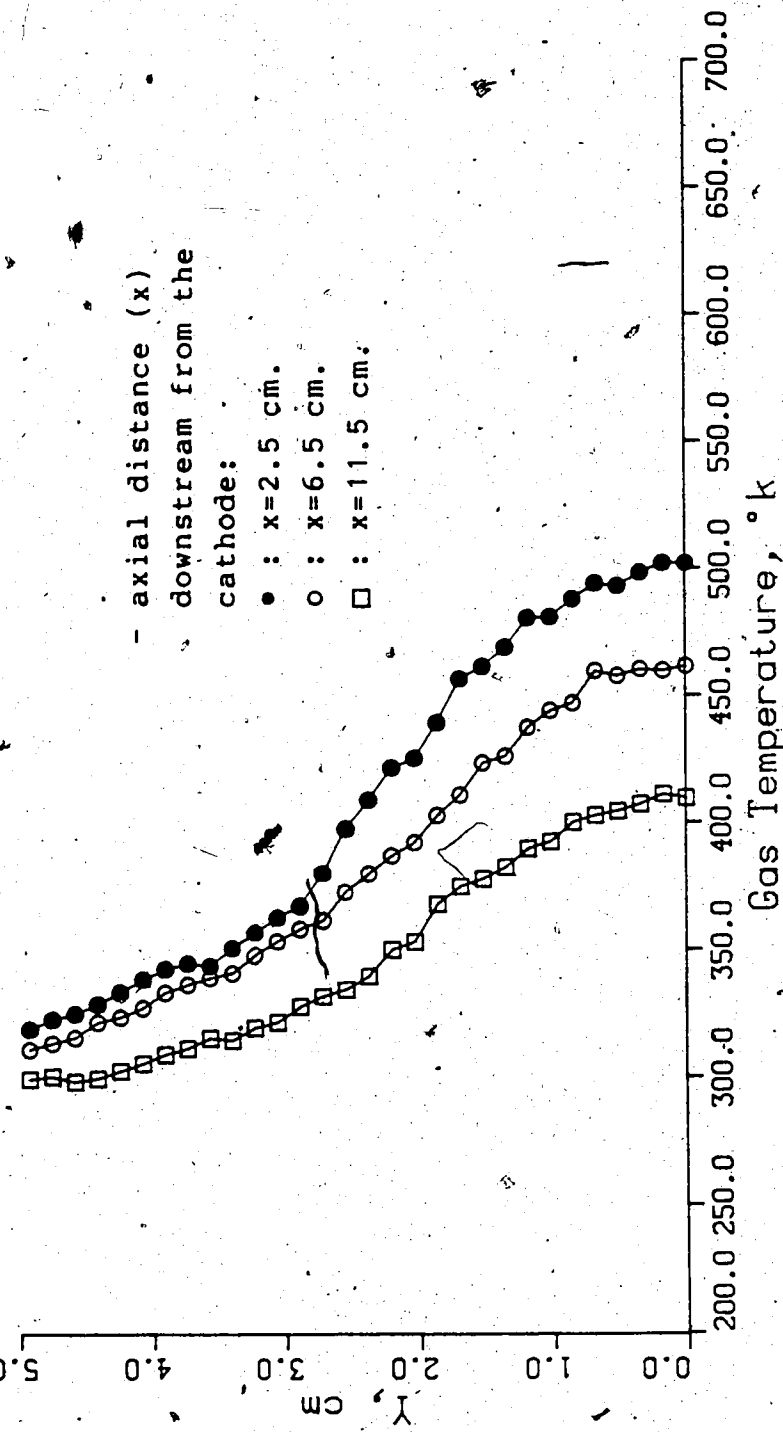


Fig. 7.9 Gas temperature profiles at different axial
distances, $P_{\text{inp}} = 3.16 \text{ kW}$.

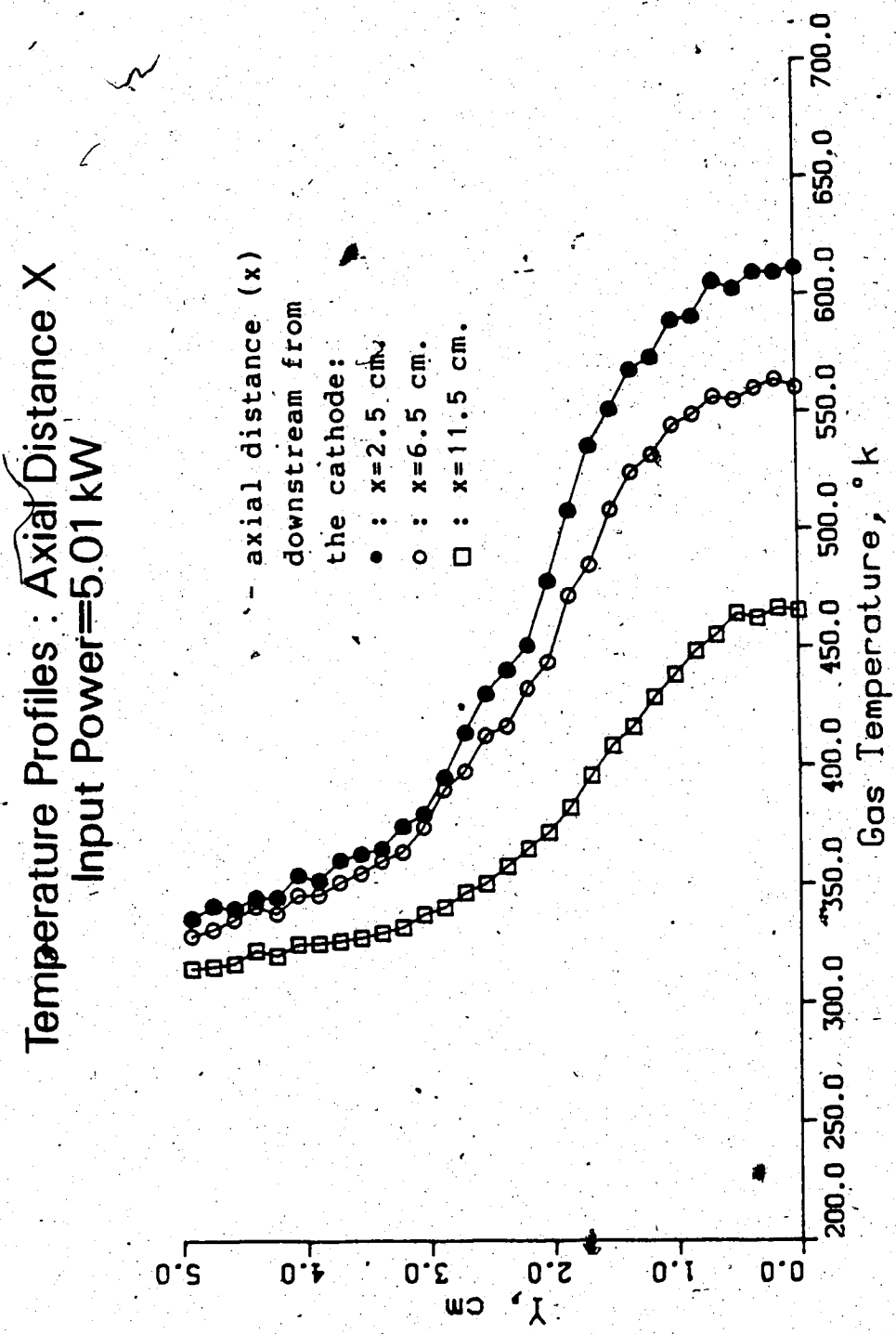


Fig. 7.10 Gas temperature profiles at different axial distances, $P_{inp} = 5.01 \text{ kW}$.

Temperature Profiles : Input Power

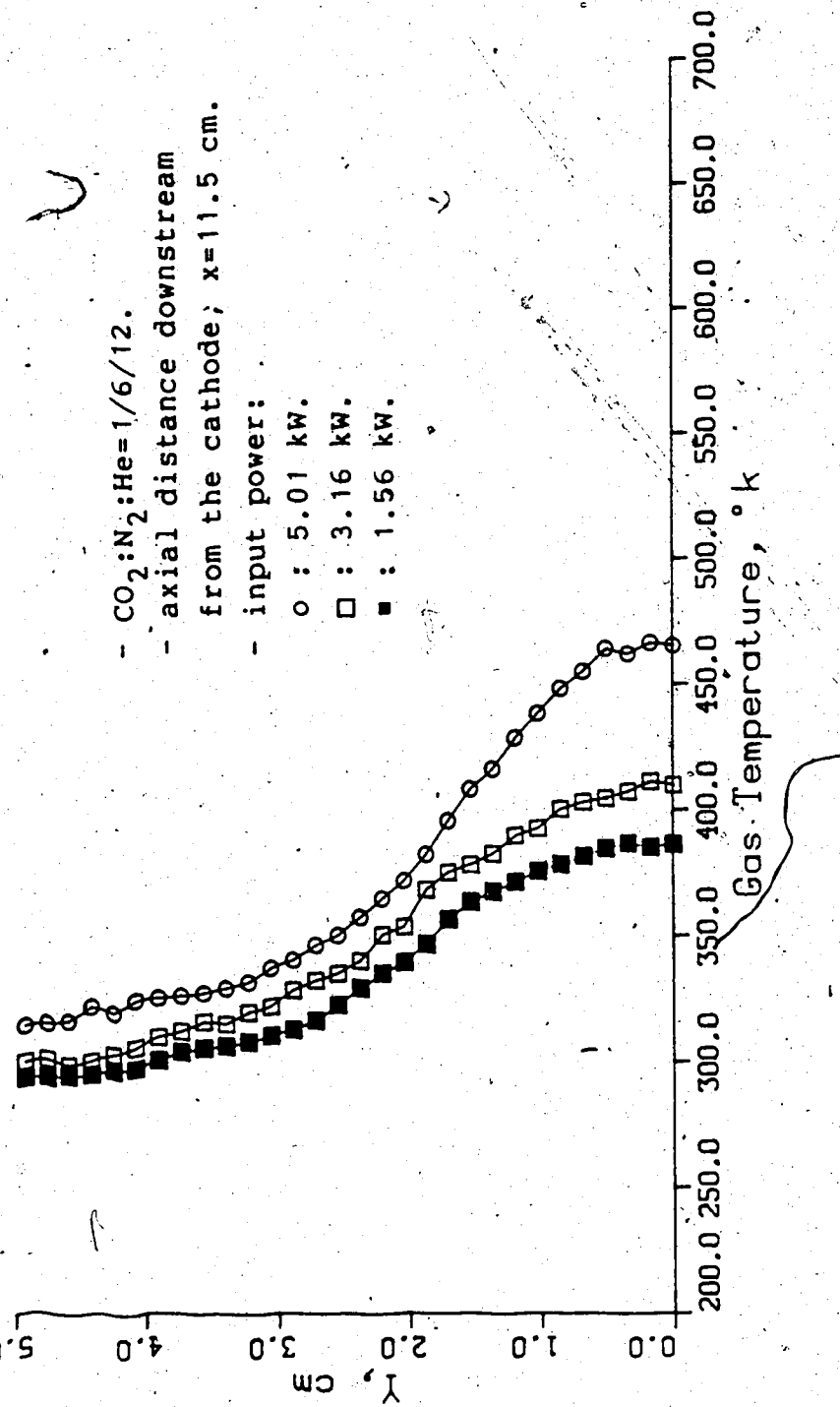


Fig. 7.11 Temperature profiles for different input powers at $x = 11.5 \text{ cm}$ downstream from the cathode.

discharge channel to the boundary surface, the temperature is seen to increase and stabilize at lower values, due to the effect of convection in the mid region.

In all of the above cases, the gas temperature is seen to increase in the low velocity regions and decrease in regions where the gas velocity is high. This result is in good agreement with our experimental measurements which will be presented later in this chapter.

7.2.4 PRESSURE DISTRIBUTION

In this section, the gas pressure distribution obtained from the numerical results is presented. The computational runs were taken for the same laser gas mixture and the same previous conditions. The total gas pressure (p) as a function of the gas temperature (T) was calculated from the relation:

$$p = \rho K_B T / m_{\text{mix}} \quad (7.1)$$

where, K_B is Boltzmann constant, ρ is the neutral gas density, and m_{mix} is the average molecular mass of the gas mixture and is given by [146]:

$$m_{\text{mix}} = \sum_i f_i M_i / N_A \quad (7.2)$$

where, f_i is the fractional percentage of the i th gas, M_i is the molecular weight, and N_A is Avogadro's number.

For typical laser gas discharge parameters with a mixture ratio of $\text{CO}_2/\text{N}_2/\text{He} = 1:6:12$, the average molecular mass m_{mix} is equivalent to 2.2718×10^{-26} kg. The gas pressure distribution across the channel was monitored at different locations upstream and downstream of the cathode. The input power was 1.56 kW, at an estimated cathode temperature of 420 °K. Figure 7.12 shows the gas pressure distribution along the y-direction at $x=1.5$ and 5.5 cm from the entrance. Curve 1 (at $x=1.5$ cm) indicates that the pressure is almost uniform across the channel and its amplitude is close to that of the flow at the entrance.

As the flow advances into the discharge region, the gas pressure was monitored in the cathode-anode region across the channel as shown by curve 2 (at $x=5.5$ cm from the entrance). Some pressure drop has occurred and the distribution has some irregularity across the channel. In Fig. 7.12, the pressure at the bottom of curve 2, i.e. at a point on the surface of the cathode is equal to zero. This point is on a polar line which has an approximately 50° angle from the centerline in the clockwise direction. This result is in good agreement with that obtained by Allen and Southwell [150] who used relaxation techniques to determine the motion, in two dimensions, of a viscous fluid past a fixed cylinder.

The gas pressure was predicted also at three different locations downstream of the cathode. Figure 7.13 shows the

Pressure Profiles at $X=1.5$ and 5.5 cm
from the Entrance

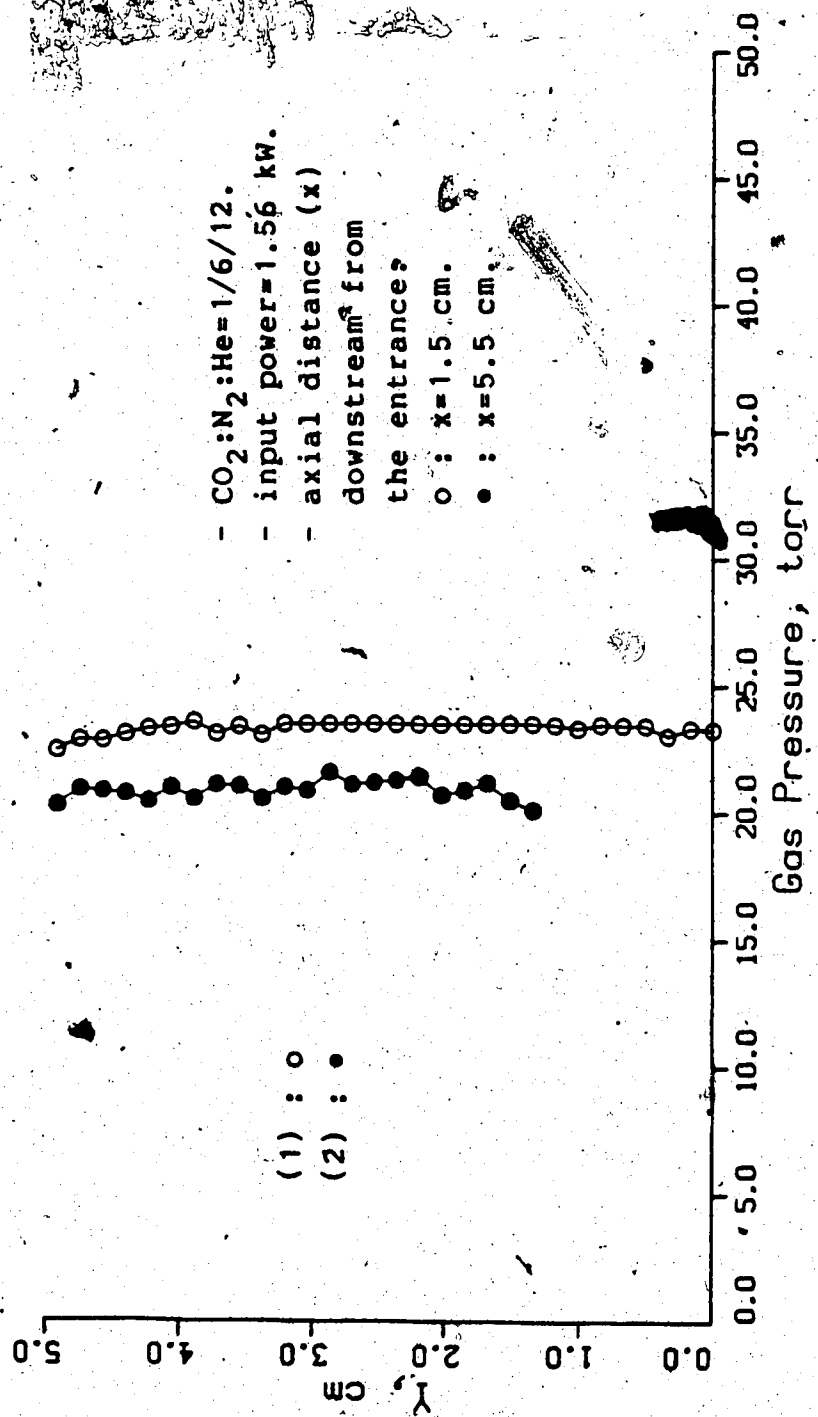


Fig. 7.12 Pressure profiles at $x=1.5$ and 5.5 cm from the entrance, $P_{\text{inp}} = 1.56 \text{ kW}$.

Pressure Profiles : Axial Distance X

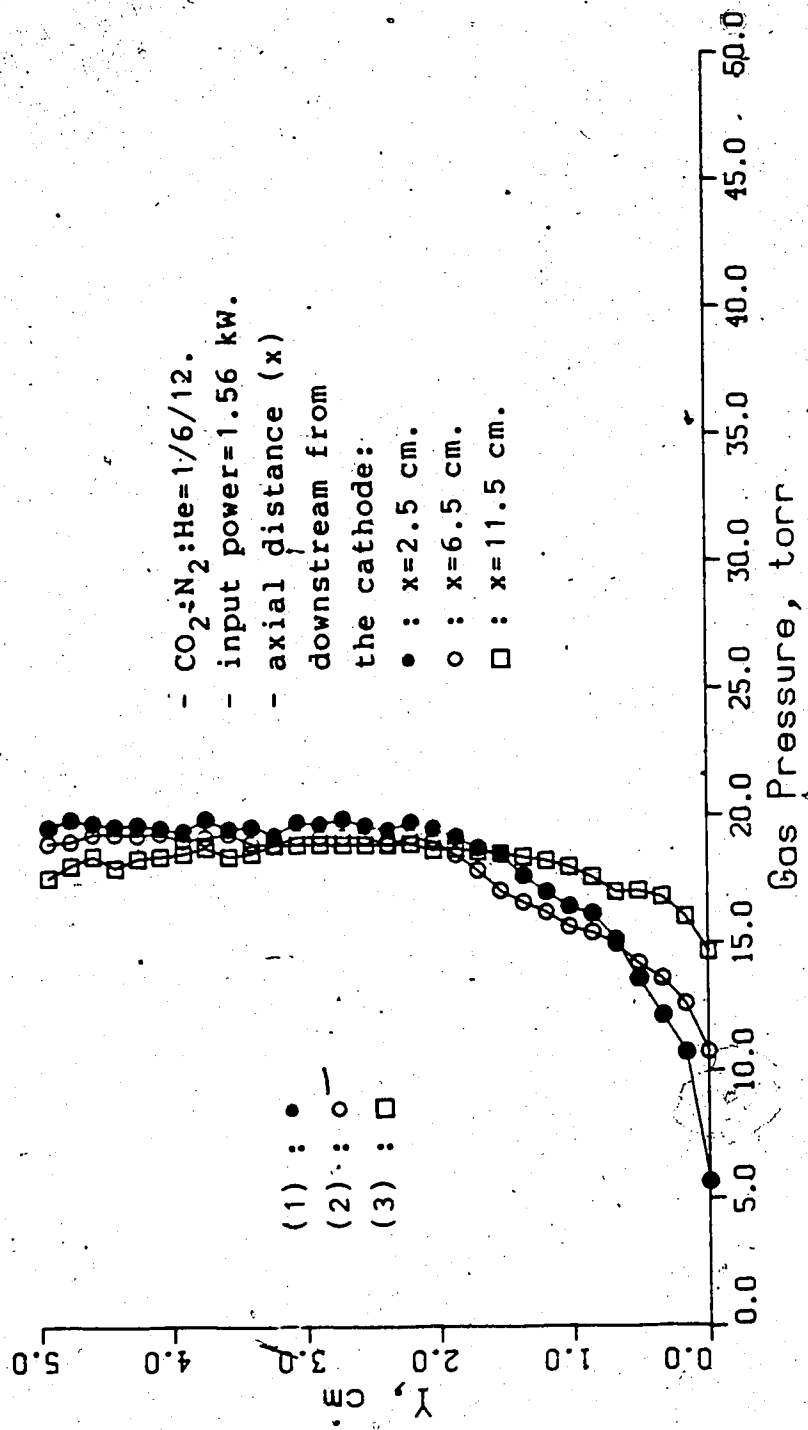


Fig. 7.13 Pressure profiles at different axial distances,
 $P_{\text{inp}} = 1.56 \text{ kW}$.

pressure distribution along the y -direction at $x=2.5$, 6.5 and 11.5 cm from the cathode surface. As can be seen in curve (1), the pressure drops significantly in the region just downstream of the cathode (where a stagnation-point exists). As y increases, the pressure increases until almost to the middle of the channel, where the pressure is seen to be distributed uniformly across y . The same behavior was obtained when the pressure was monitored at $x=6.5$ cm downstream of the cathode as shown in curve (2). But in this case, the pressure in the region close to the centerline is higher than that in curve (1). At $x=11.5$ cm far downstream, the gas pressure distribution is almost uniform across the channel height as shown in curve (3).

These results show that the presence of the cathode in the middle of the channel (as an obstacle) affects the distribution of the gas pressure in the region downstream of the cathode. The gas pressure distribution recovers to its uniform status further downstream where the effect of the stagnation region diminishes. Also, the impact of the flow decreases slightly as it advances downstream, as can be seen from Fig. 7.13, where the pressure decreases in the x -direction.

Another computational run was obtained for higher input power. It was found that increasing the input power and the cathode temperature, resulted in an increased pressure. Figure 7.14 shows the pressure distribution across the

Pressure Profiles : Input Power
at $X=2.5$ cm

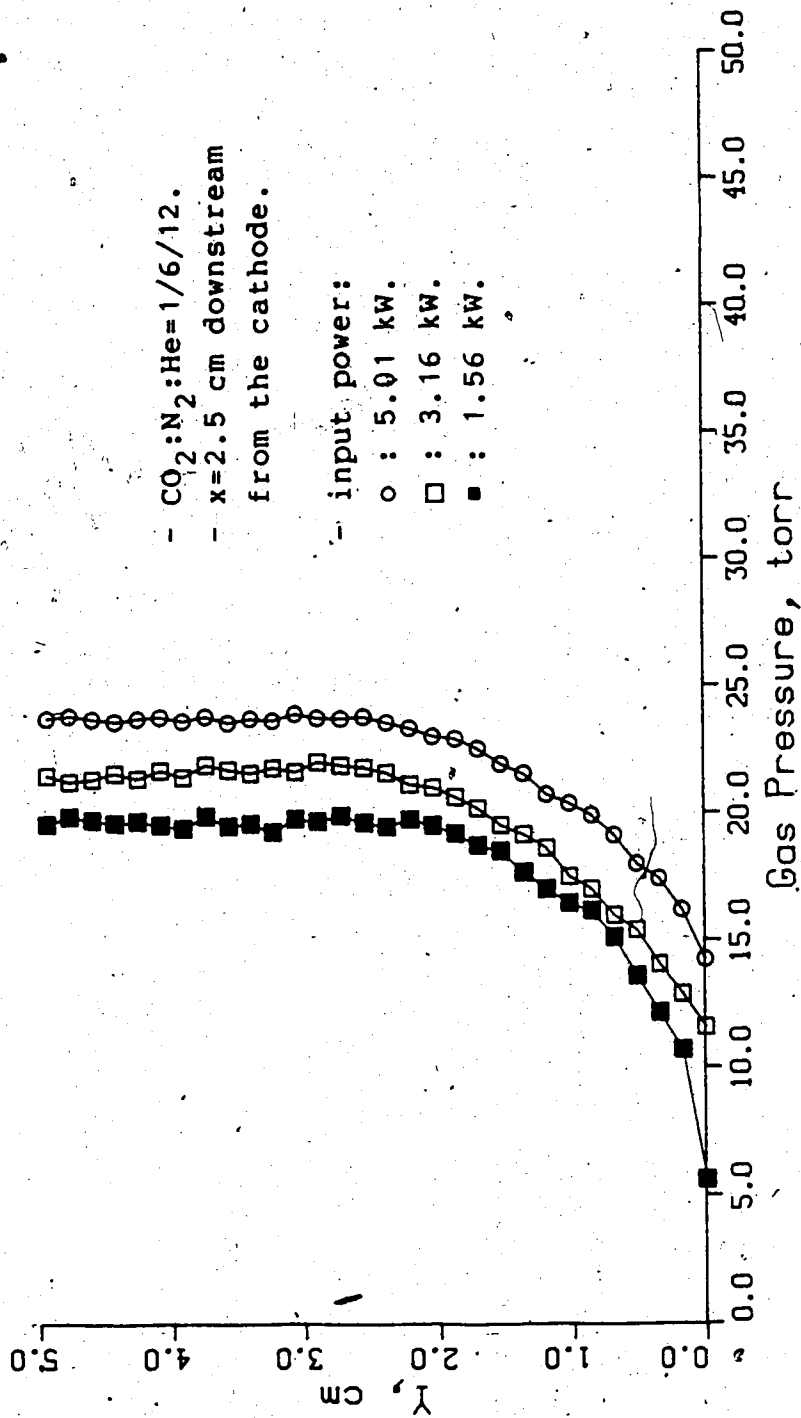


Fig. 7.14 Pressure profiles for different input power values
at $x=2.5$ cm downstream from the cathode.

channel at $x=2.5$ cm downstream of the cathode surface, for three input power settings. The pressure distribution was monitored also at $x=6.5$ cm and $x=11.5$ cm downstream. The results are illustrated in Figs. 7.15 and 7.16. These results show a positive response in pressure, due to an increase in the input power.

Finally, the pressure distribution across the discharge region (in the x -direction) was obtained at a distance $y=24.5$ mm from the center of the cathode. The pressure is almost steady and decreases slightly in the downstream direction, as can be seen in Fig. 7.17. A similar results was obtained at $y=33.0$ mm from the center of the cathode and is shown in Fig. 7.18. This flow is maintained through an imposed 10% pressure differential across the test section. The uniformity of the pressure across the discharge channel is in good agreement with the results obtained by Finlay [154], in a simulation of open channel flow, using a Lagrangian fluid particle technique.

7.2.5 MASS FLOW DISTRIBUTION AND SIMULATION MATCH TO EXPERIMENTS

During the course of a simulation, it was necessary to check the uniformity of the mass flow distribution across the test section. The program was run for 500 time steps and with time step size equal to 96% of the CFL limit. The code results were time averaged over the last 100 time steps and

Pressure Profiles : Input Power
at $X=6.5$ cm

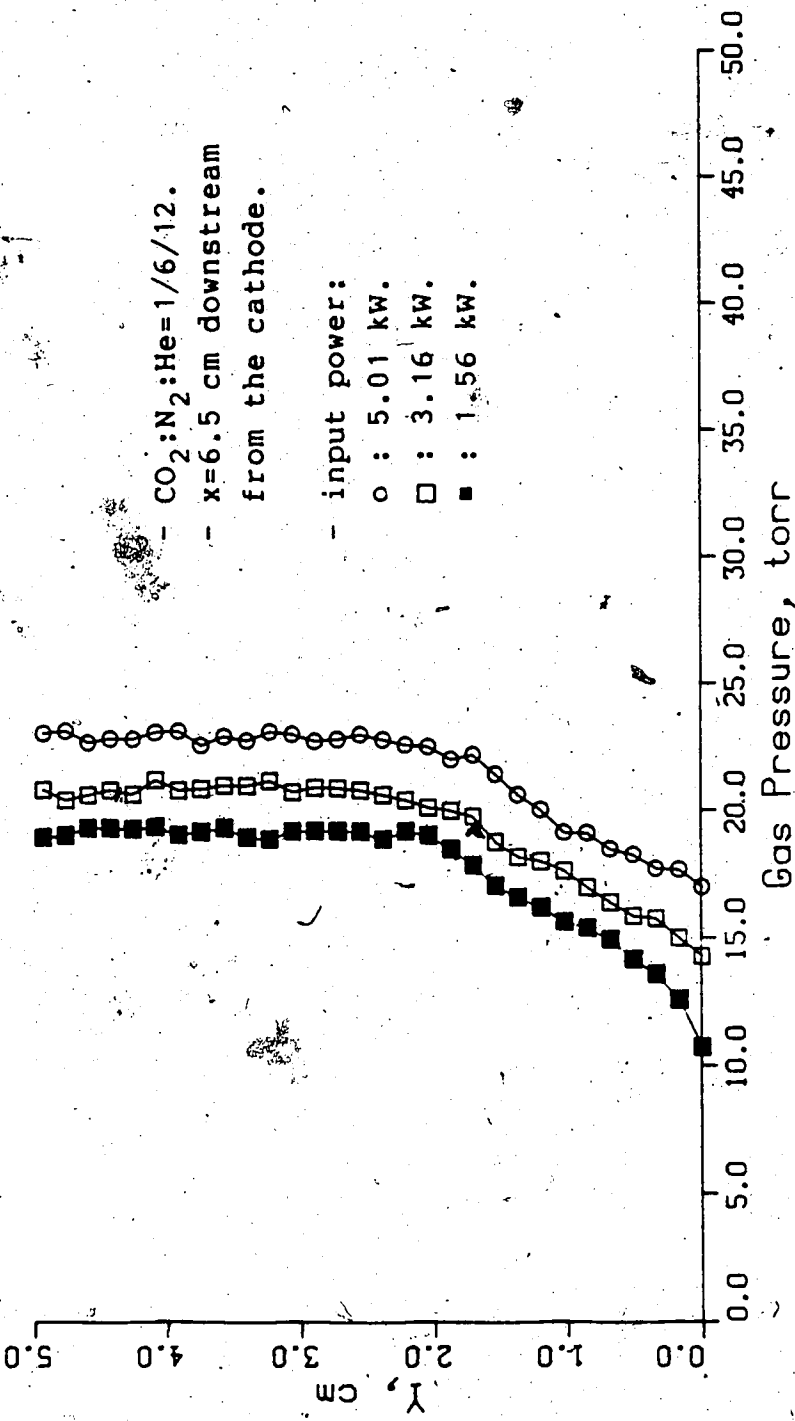


Fig. 7.15 Pressure profiles for different input power values
at $x=6.5$ cm downstream from the cathode.

**Pressure Profiles : Input Power
at X=11.5 cm**

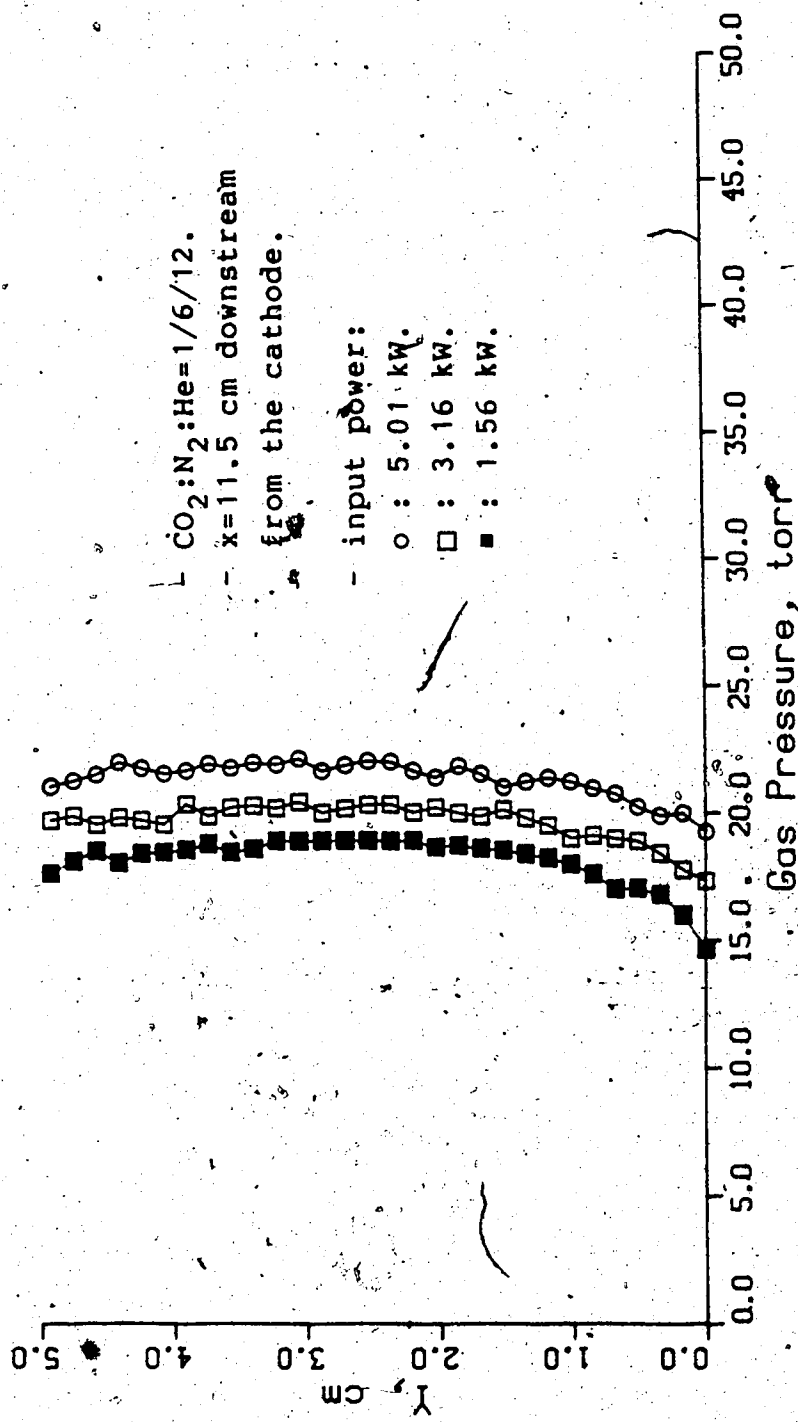


Fig. 7.16 Pressure profiles for different input power values
at $x=11.5 \text{ cm}$ downstream from the cathode.

Pressure Profile along the Flow Direction
at $y=24.5$ mm

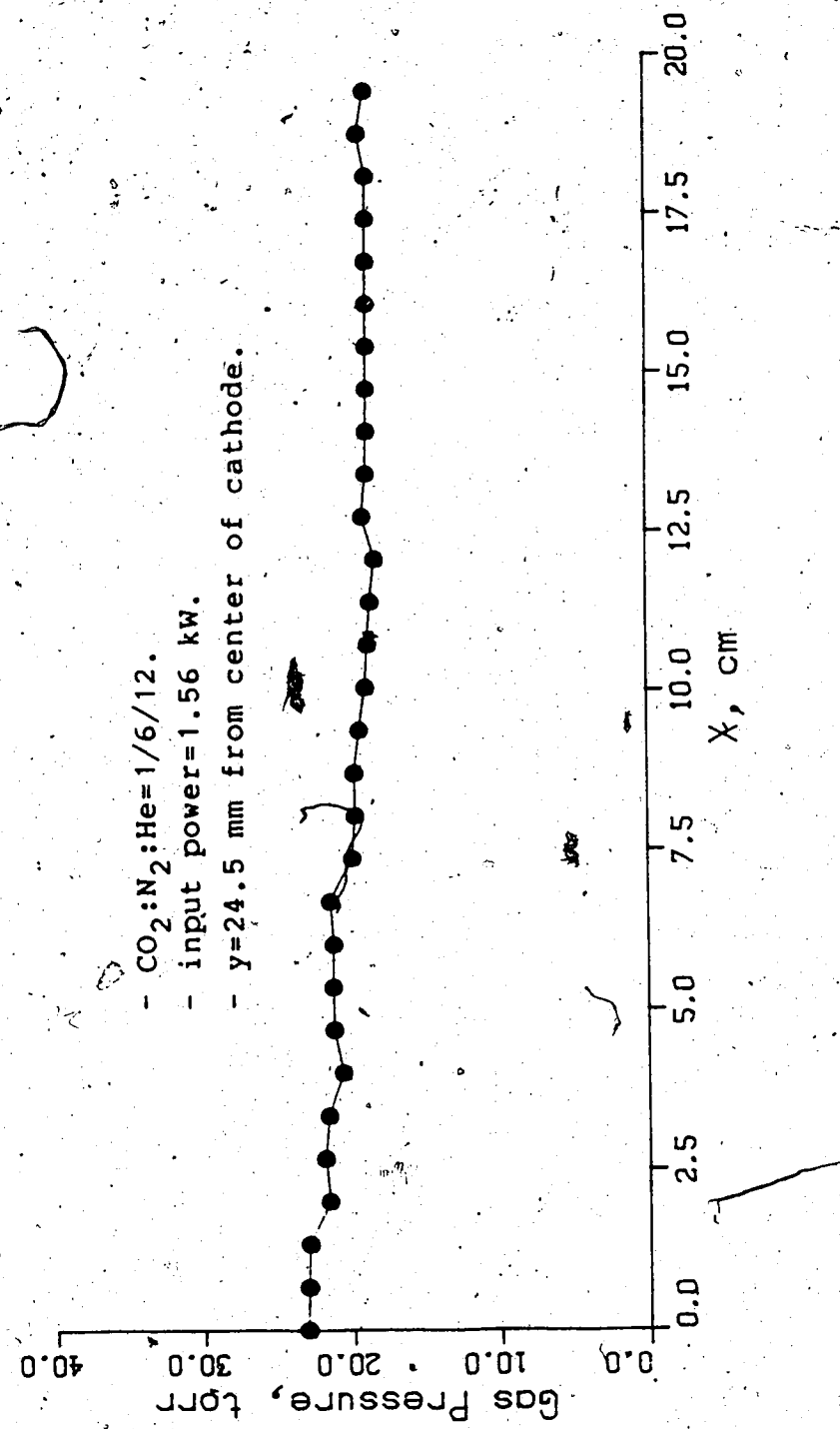


Fig. 7.17 Pressure profile along the flow direction (x), at $y=24.5$ mm from the center of the cathode.

**Pressure Profile along the Flow Direction
at $y=33.0$ mm**

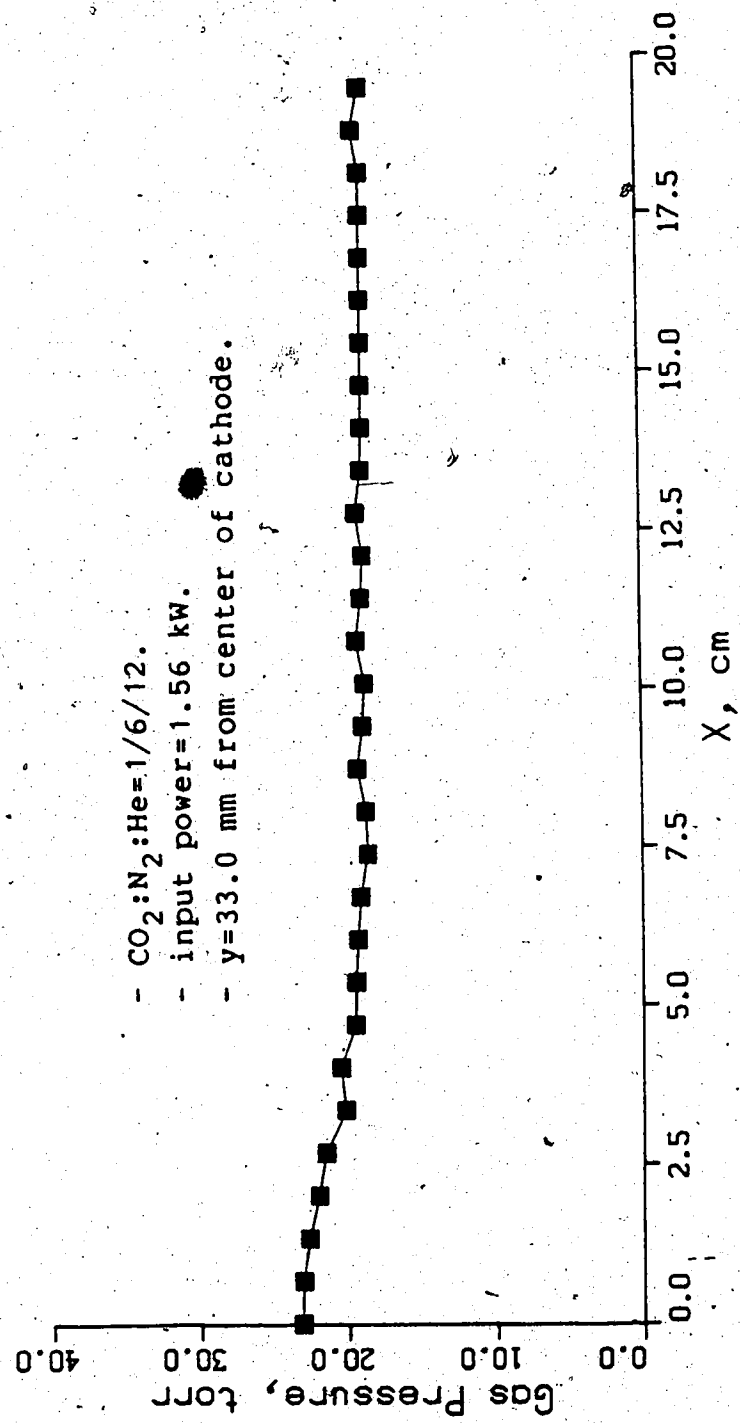


Fig. 7.18 Pressure profile along the flow direction (x), at $y=33.0$ mm from the center of the cathode.

spatially averaged across the height of the channel (y) at each point (30 points) on the x -axis. The result is shown in Fig. 7.19 for an input power of 1.56 kW and an estimated cathode temperature of 420 °k. As it can be seen from this figure, the mass flow is maintained constant all over the discharge section. This implies a good conservation of mass by the simulation code.

In order to match the simulation results to experimental findings, some parameters must be specified. From the experimental parameters and data, specific input power values and the corresponding cathode temperature were determined. These values were implemented in the computer program for simulation purposes. Also the mass flow rate and the pressure drop across the test section were estimated from the experimental results. This is shown in Fig. 7.20, where the mass flow rate is plotted against the percentage pressure difference across the test region. From this figure a pressure difference of 10% was chosen as the match parameter, at which the estimated experimental mass flow is comparable to the computed value.

It is believed that matching the input power, cathode temperature, mass flow rate and the pressure drop, as well as gas composition, actual dimensions of the discharge region and gas viscosity fulfil the requirements to match the simulation results to the experimental ones.

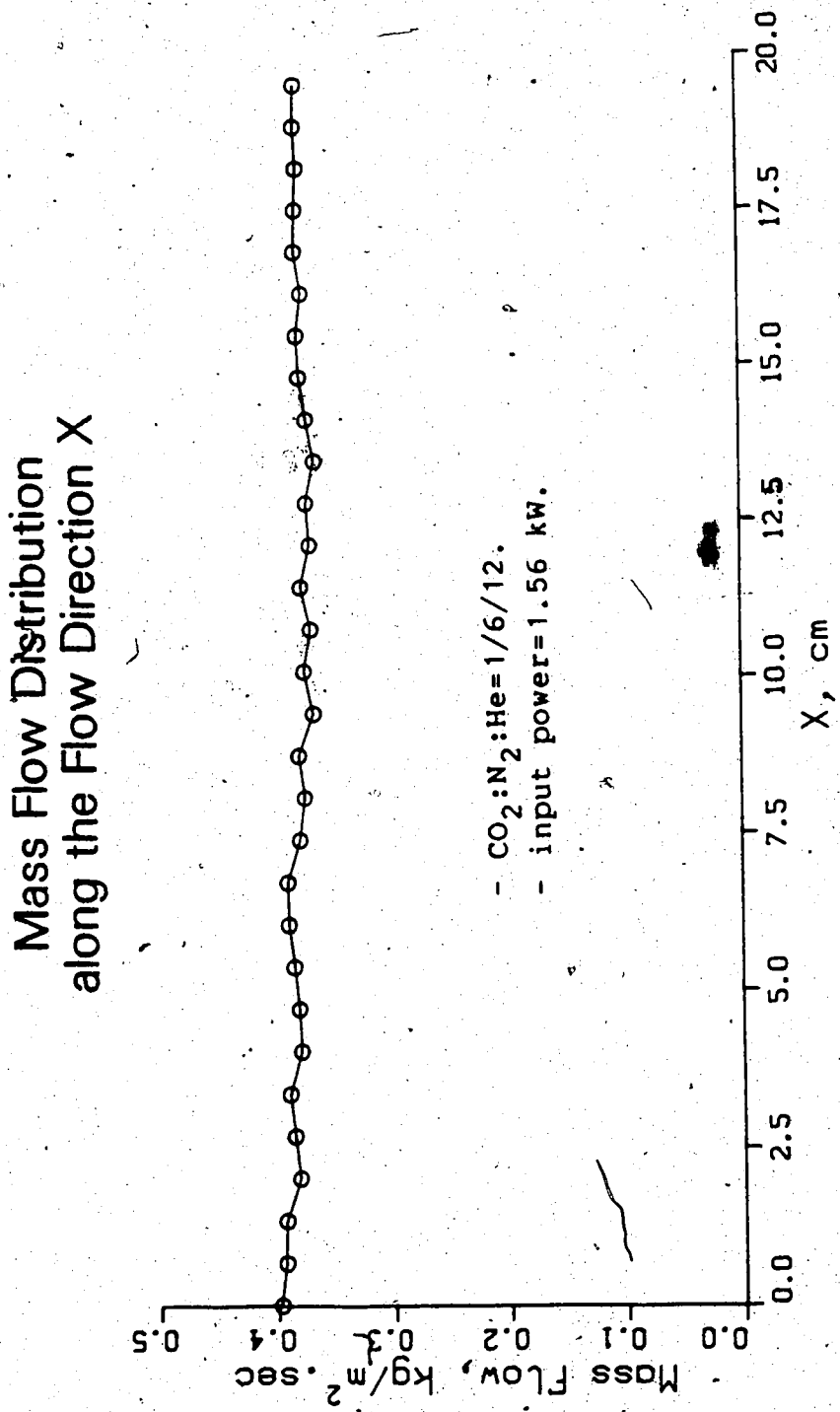


Fig. 7.19 Mass flow distribution along the flow direction
for input power of 1.56 kW.

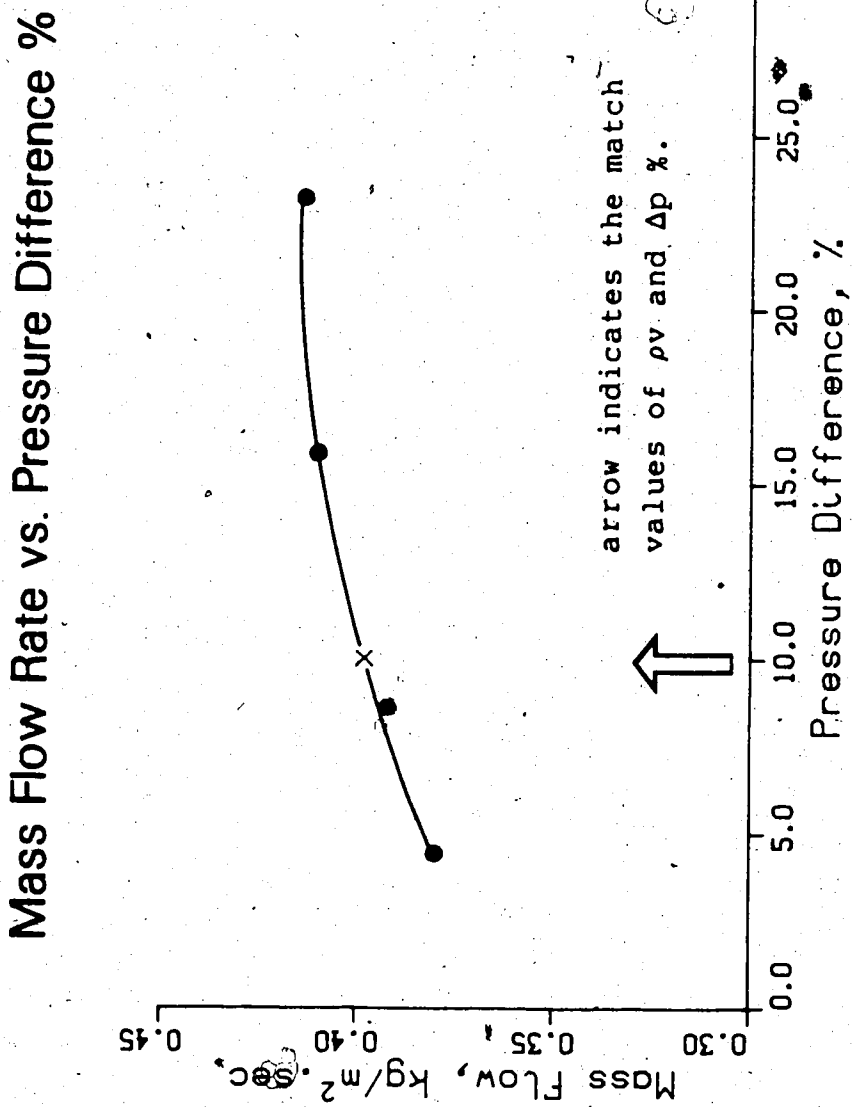


Fig. 7.20 Mass flow rate as a function of the pressure difference percentage.

In section 7.3, the experimental results of the open channel flow laser gas discharge will be presented and discussed. A comparison between the experimental and theoretical results will be reported in section 7.4.

7.3 EXPERIMENTAL RESULTS OF THE OPEN CHANNEL FLOW LASER GAS DISCHARGE

7.3.1 SYSTEM OPERATION

In chapter 3, the experimental system design was presented. Once the TE CW CO₂ laser gas discharge system had been assembled and tested, measurements were made to investigate the gas velocity profiles and the temperature distribution in this system. During the operation, the system was first pumped down to a pressure of 100 μ (or 0.1 torr) and then backfilled with a laser gas mixture to the appropriate working pressure. Most of the experimental runs were taken for a laser gas mixture of CO₂/N₂/He, in the proportion of 1:6:12, at a total pressure of 20 torr.

Figure 7.21 shows two photographs of the glow discharge in this system, at two input power settings. At low input power ($P_{inp} = 1.56$ kW), the glow discharge is quite uniform. At higher input power, ($P_{inp} = 5.01$ kW), the glow discharge is still uniformly distributed throughout the interelectrode region. However, in this case the uniform discharge is more intense in the region between the anode and the cathode. The

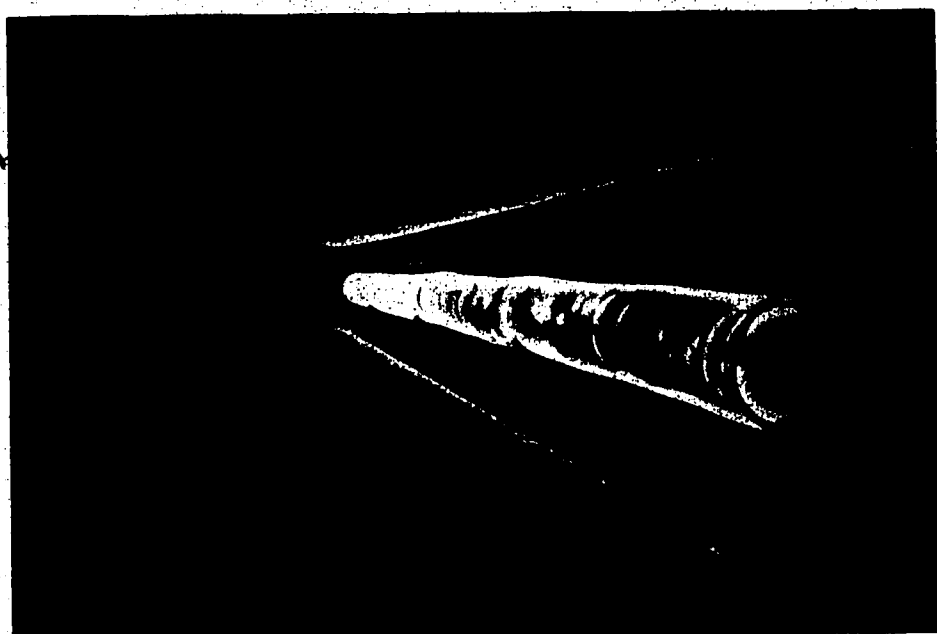
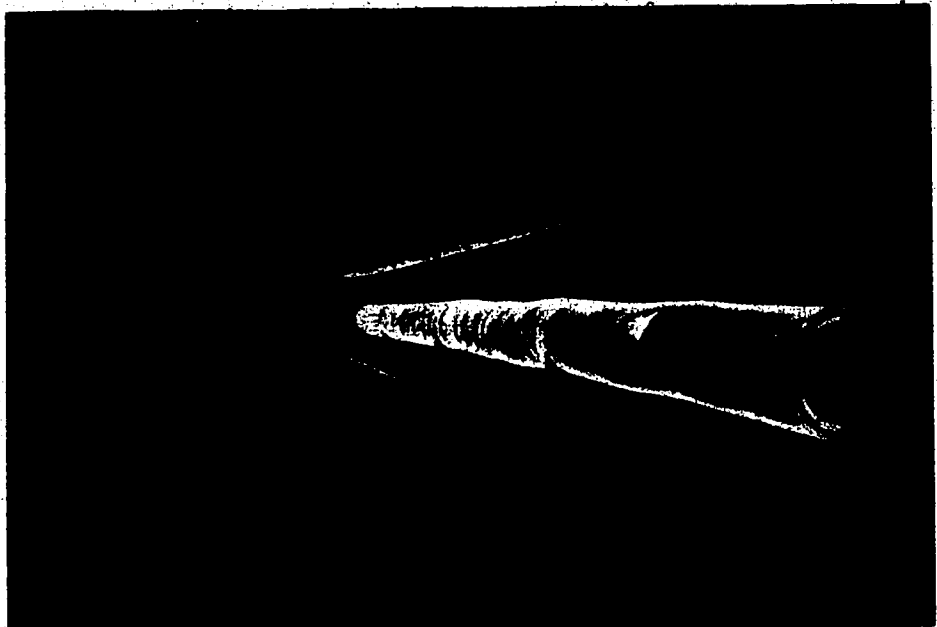


Fig. 7.21 Transverse-electric CW CO₂ glow discharge.

intensity of the uniform discharge was found to increase with increasing input power to the system. The discharge is totally self-sustained, and no external source is used throughout this study.

Figure 7.22 shows the terminal V-I characteristic. As can be seen in this figure, the terminal voltage is almost independent of the terminal current over this specified range. In this case, the discharge behaves as a normal glow [155, 156].

7.3.2 VELOCITY PROFILE MEASUREMENTS

Experiments were carried out to obtain the velocity profiles in the discharge region and downstream of the cathode. The gas flow velocity was measured using a pitot tube attached to a capacitance manometer as was explained in section 3.5. In this section, results of the dependence of gas velocity profile on the gas pressure, laser gas mixture ratio, and the input power to the system are presented. The results of the velocity profile measurements along the laser axis (z-axis) and along the discharge width downstream of the cathode (in the x-direction) are also presented.

A. PRESSURE DEPENDENCE

Figure 7.23 shows the velocity profiles across the channel (in the y-direction) for various gas pressures. The measurements were taken at $x=11.5$ cm downstream of the

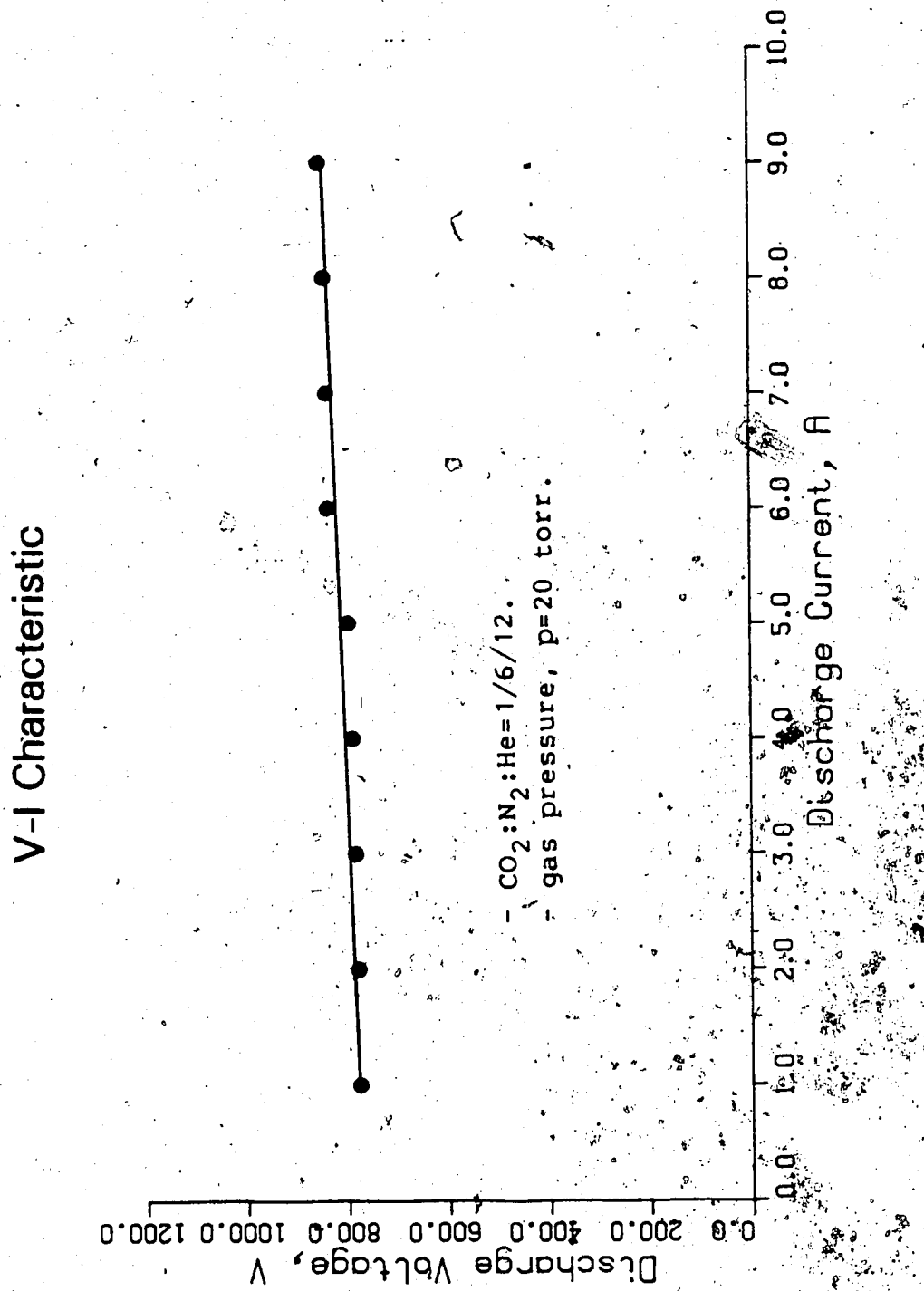


Fig. 7.22 V-I characteristic, laser gas mixture is CO₂/N₂/He
in the proportion 1:6:12 and p=20 torr.

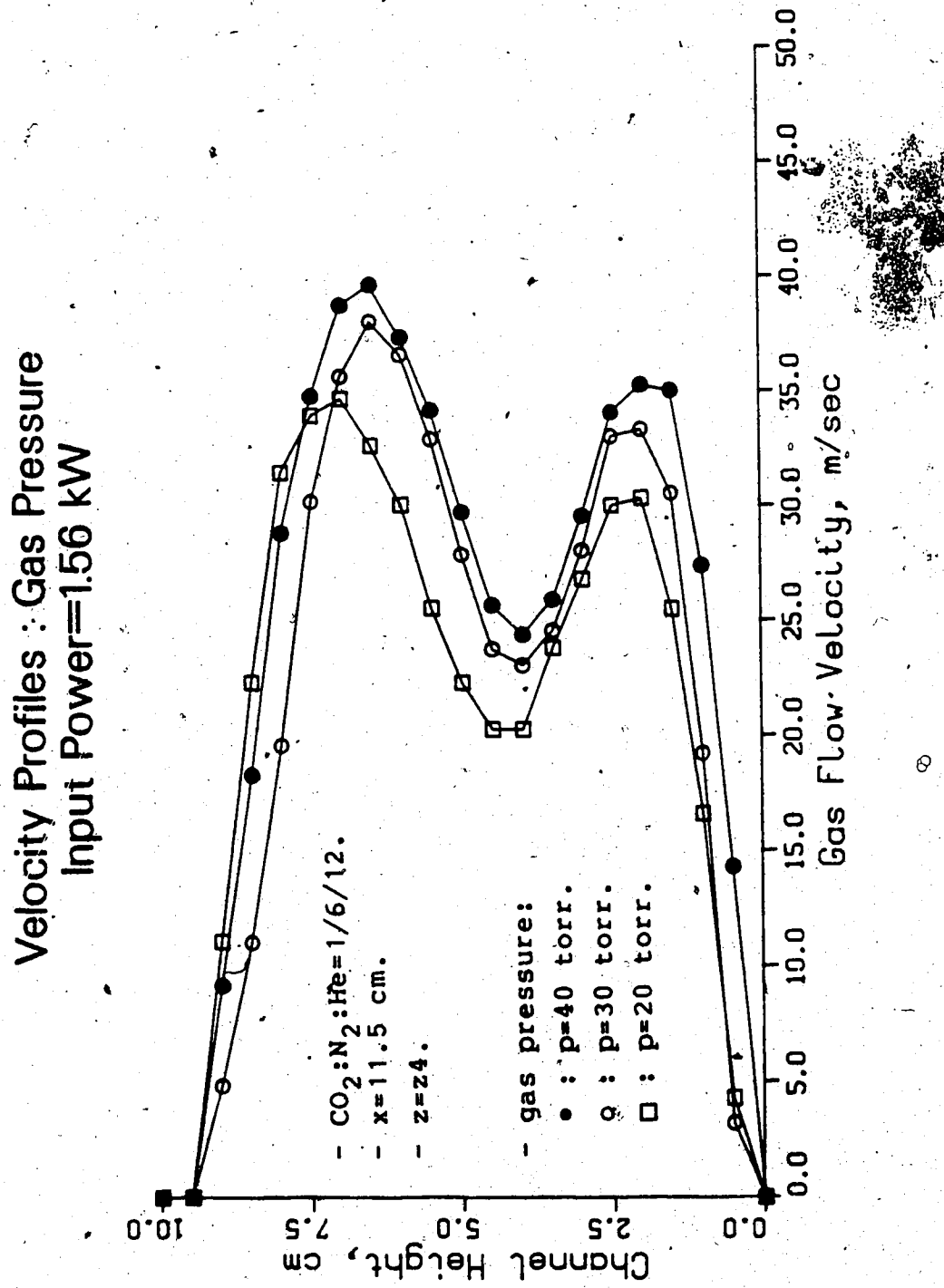


Fig. 7.23 Velocity profiles at different gas pressures,

$P_{\text{inp}} = 1.56 \text{ kW.}$

cathode, at $z=z_4$. A laser gas mixture of $\text{CO}_2/\text{N}_2/\text{He}$ in the proportion of 1:6:12 was used. The input power to the system was 1.56 kW and the cathode temperature was estimated to be 420 °k. As can be seen from this figure, the gas velocity increases with increased gas pressure.. Also, an increase in the gas velocity was observed by increasing the input power ($P_{\text{inp}} = 3.16$ kW) at all pressure settings as shown in Fig. 7.24. Further increase in the input power ($P_{\text{inp}} = 5.01$ kW) results in an increased gas velocity at all pressures, as can be seen in Fig. 7.25.

B. LASER GAS MIXTURE DEPENDENCE

The velocity profile across the channel height was also obtained for different laser gas mixture ratios, at a total gas pressure of 20 torr. The results are shown in Fig. 7.26 for $P_{\text{inp}} = 5.01$ kW, $x=14.5$ cm and $z=z_4$. It was found that the mixture with a high nitrogen component (1:6:12) "has the best performance amongst the gas mixtures used. A 25% increase in the gas velocity was observed using this particular gas mixture. It was also found that increasing the He ratio in the gas mixture resulted in an increase in the gas velocity. The laser gas mixture ratio 1:6:12 was used throughout the remaining measurements.

C. VELOCITY PROFILES ALONG THE DISCHARGE LENGTH

As was mentioned earlier, the gas discharge in our device has a length of 135 cm along the z-direction.

**Velocity Profiles : Gas Pressure
Input Power=3.16 kW**

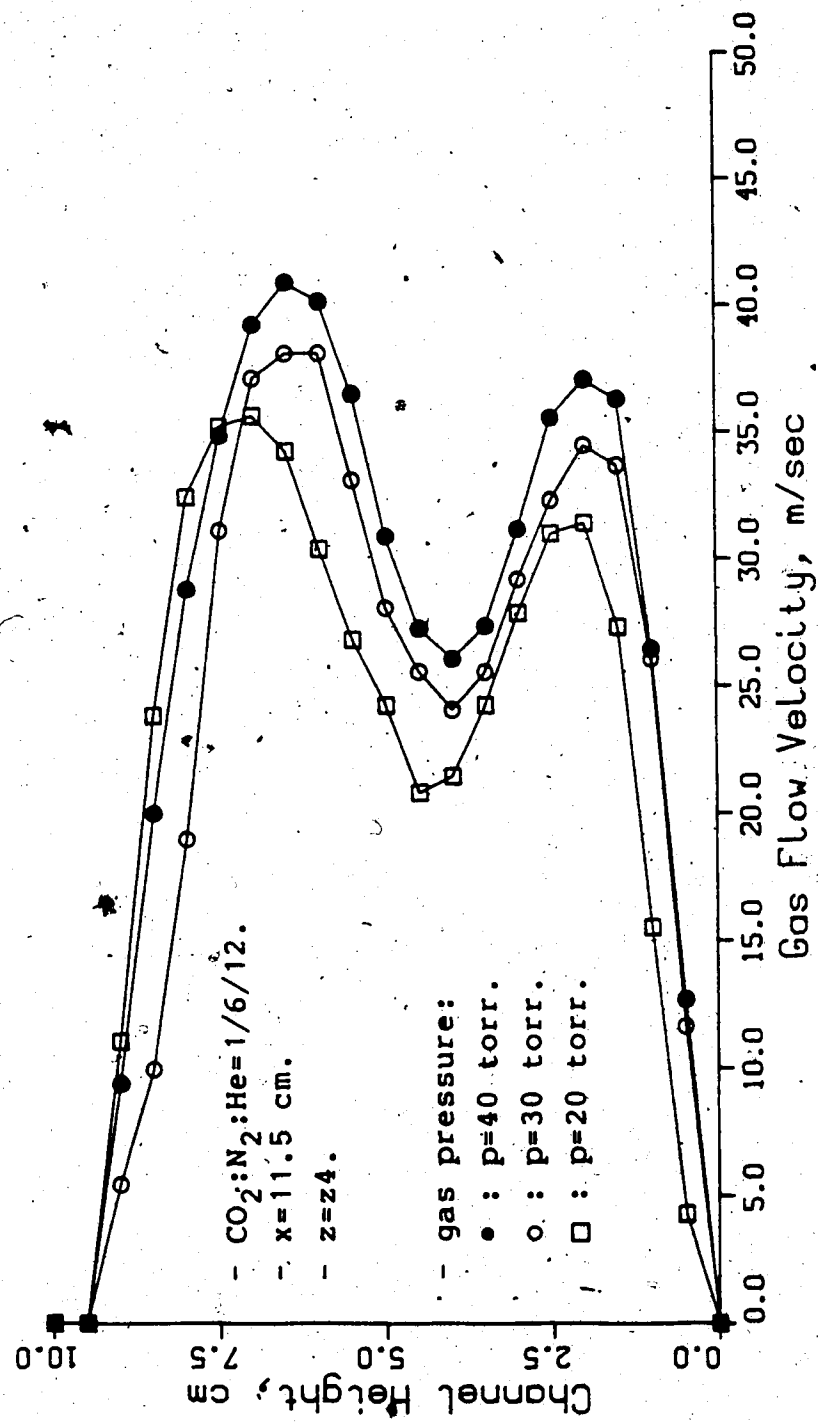


Fig. 7.24 Velocity profiles at different gas pressures,

$P_{\text{inp}} = 3.16 \text{ kW}$.

**Velocity Profiles : Gas Pressure
Input Power=5.01 kW**

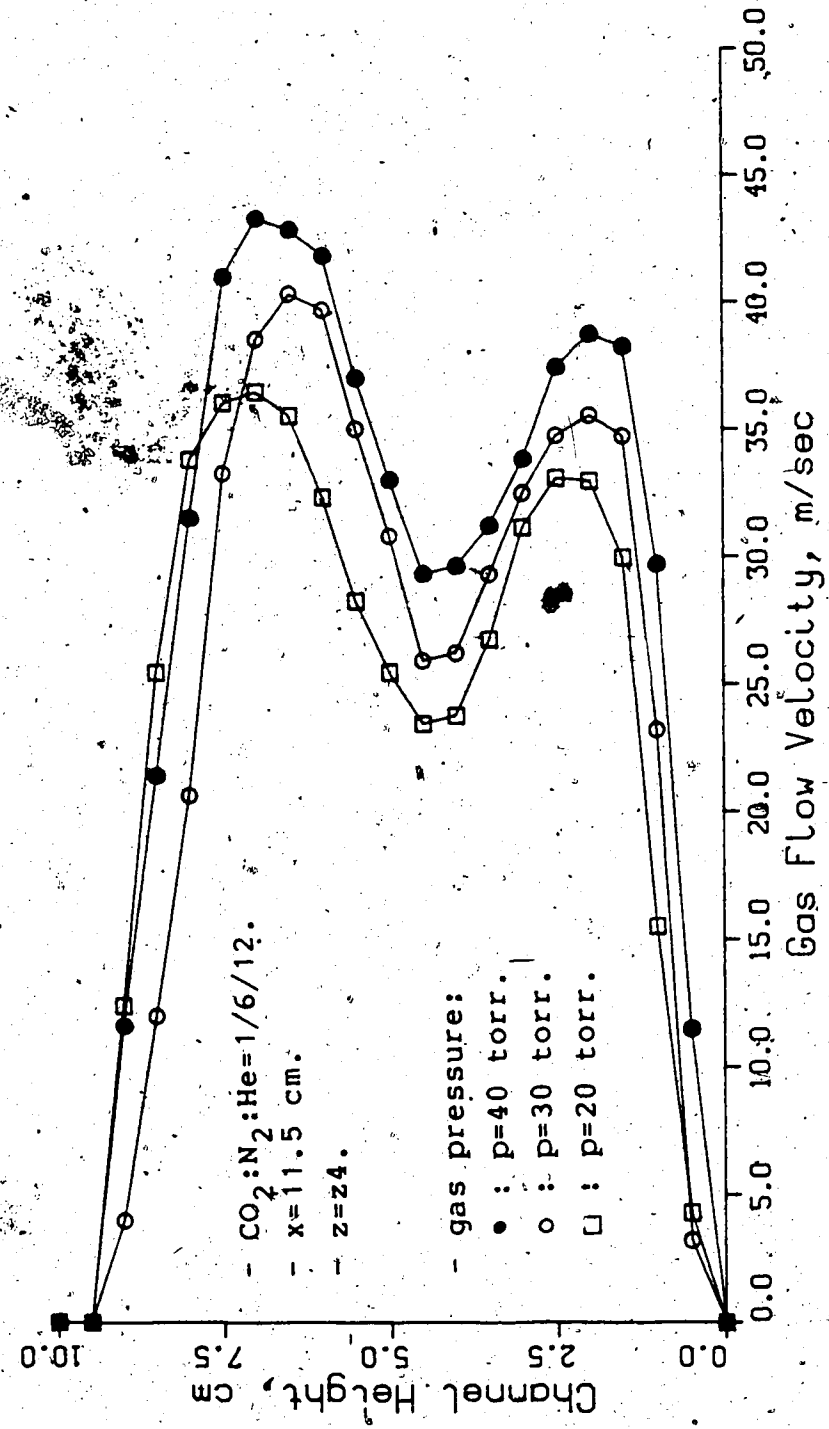


Fig. 7.25 Velocity profiles at different gas pressures,
 $P_{\text{inp}} = 5.01 \text{ kW}$,

Velocity Profiles : Laser Gas Mixture

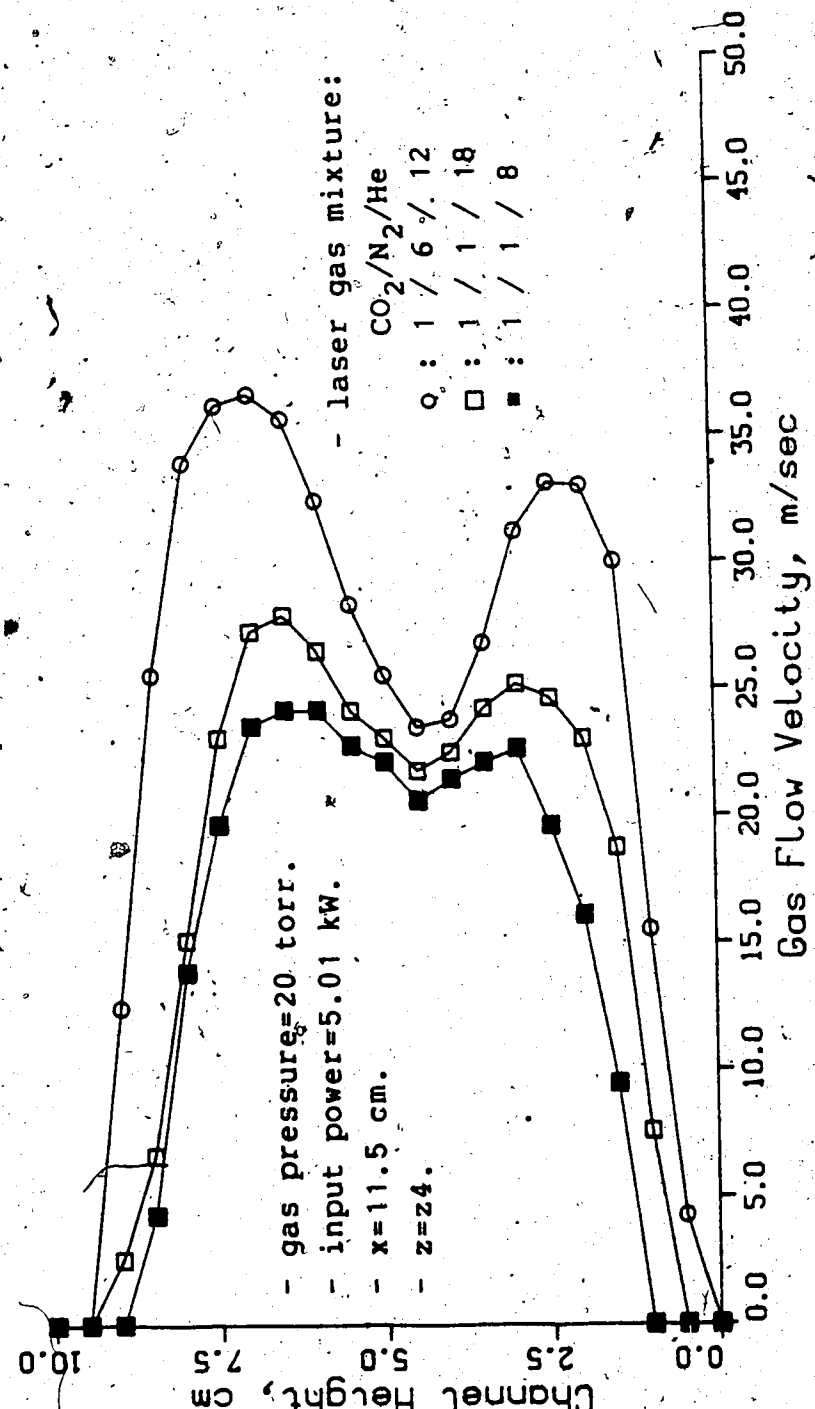


Fig. 7.26 Velocity profiles at different laser gas mixtures.

Therefore it was necessary to monitor the velocity profile at different points along the discharge length. These measurements were required to ensure that the velocity distribution along the discharge length is uniform. The velocity profile was obtained at points z_1 , z_2 , z_3 and z_4 on the z -axis (Fig. 3.6) for a laser gas mixture of $\text{CO}_2/\text{N}_2/\text{He}$ in the proportion 1:6:12. The gas pressure was 20 torr and the input power was 5.01 kW. The measurements were made at $x=11.5$ cm, and across the channel along the y -direction. The results are shown in Fig. 7.27. The velocity profiles measured at each point along the discharge length are similar in shape.

The maximum velocity of each profile was plotted against the z -displacement. Figure 7.28 shows this result for two input power settings. As can be seen from this figure, the velocity distribution is uniform along the discharge length with the exception of the edges. The velocity drops to about 85% of its maximum value, at the edges (at z_1 and z_4). At distances less than z_1 and larger than z_4 , a larger drop in the velocity is expected, particularly in the regions close to the walls because of boundary layer effects [104,105].

The effect of input power on the velocity profile along the discharge length was investigated. The velocity distribution was obtained at the points z_1 , z_2 , z_3 and z_4 for two input power settings, and was compared to that

Velocity Profiles : Discharge Length Z

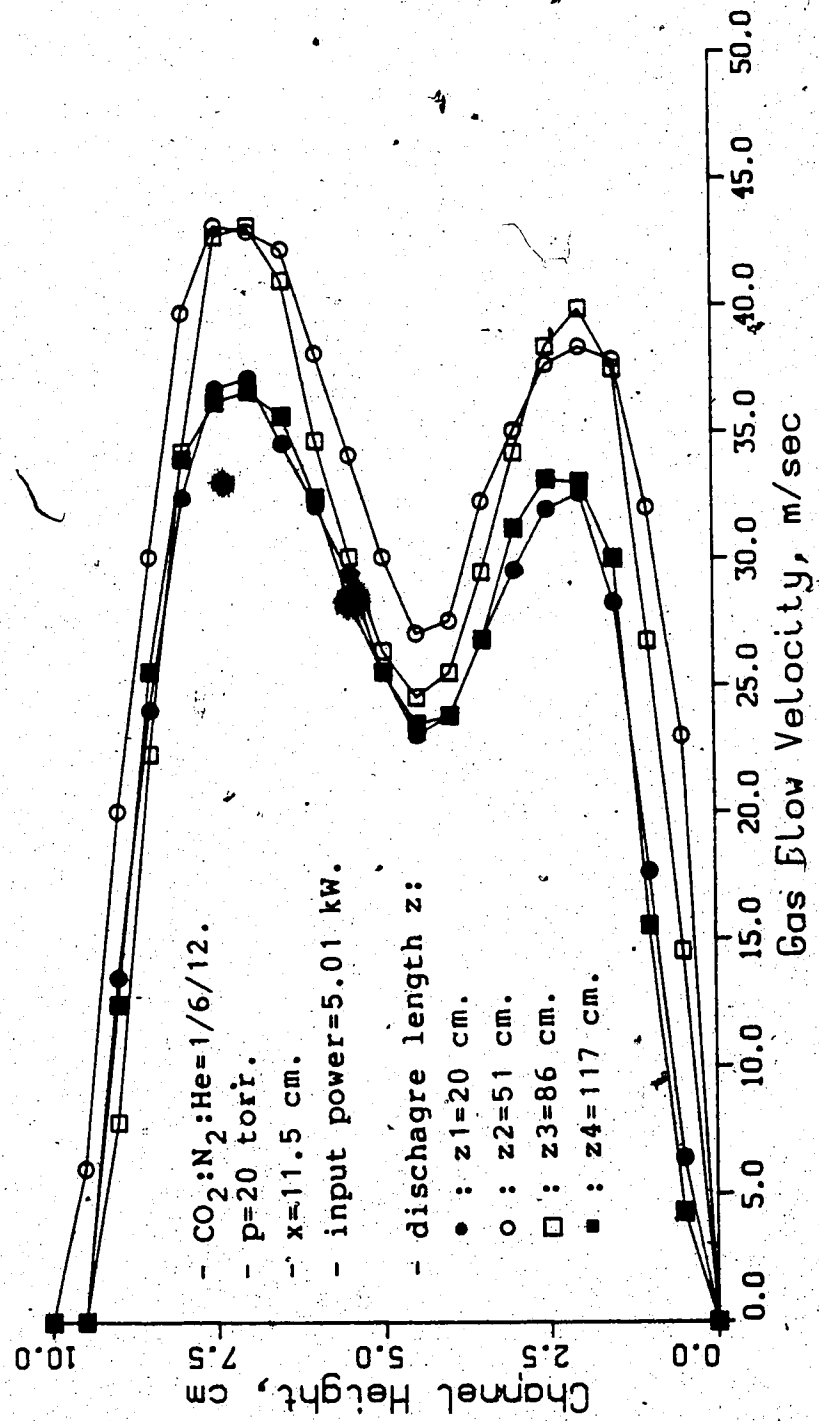


Fig. 7.27 Velocity profiles at $z=z_1, z_2, z_3$ and z_4 .

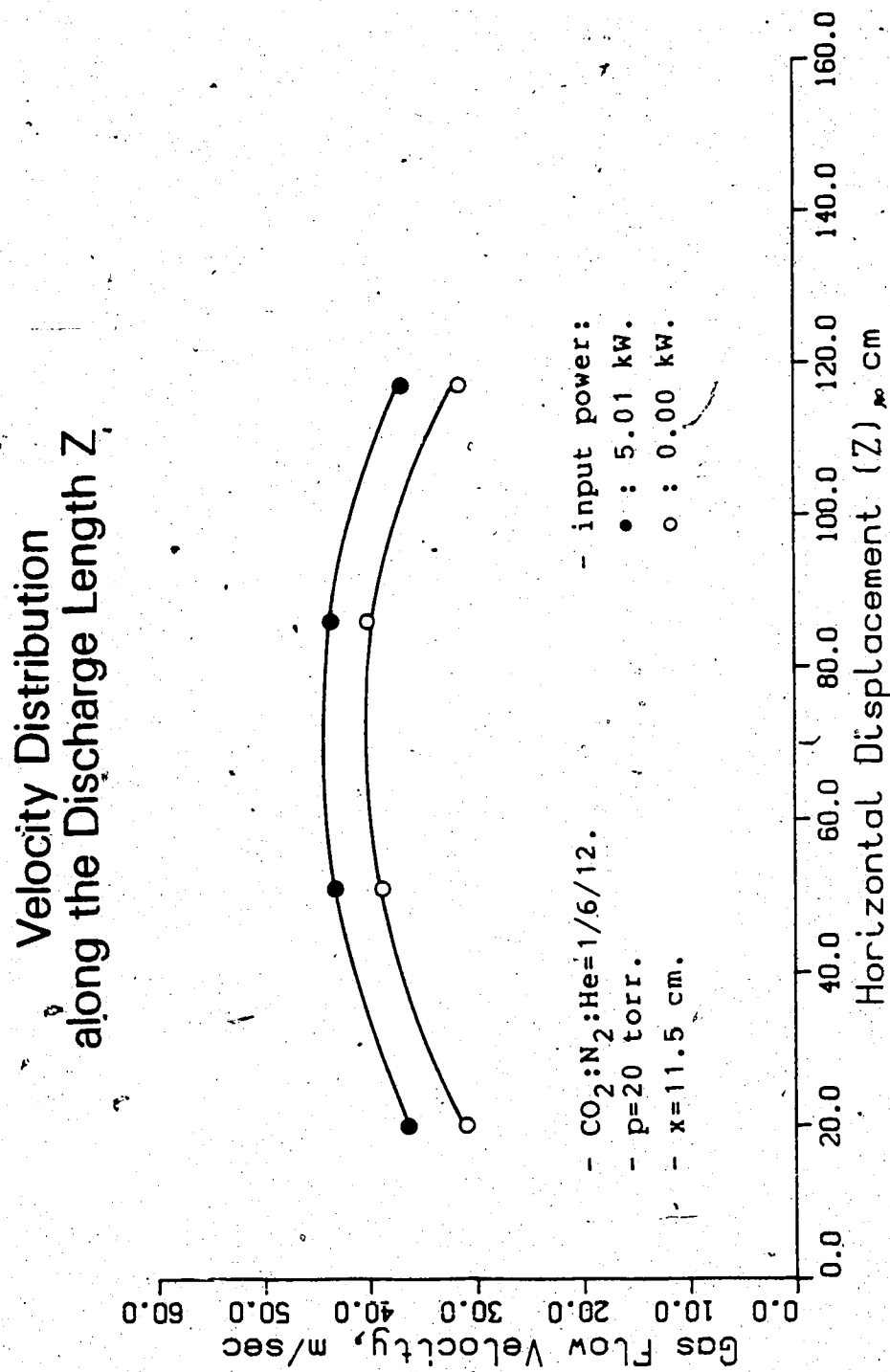


Fig. 7.28 Velocity distribution along the discharge length (z) at $p=20 \text{ torr}$.

obtained with no discharge. Figures 7.29-7.32 illustrate the velocity profiles for input powers of 0.0 kW, 1.56 kW and 5.01 kW. The measurements were obtained at $x=11.5$ cm downstream of the cathode. An increase of up to 17% in the gas velocity was achieved by increasing the input power to 5.01 kW, as compared to the isothermal case.

D. VELOCITY PROFILE DEPENDENCE ON INPUT POWER AND AXIAL FLOW DISTANCE

The velocity profiles were measured at different points downstream of the electrodes. Figure 7.33 shows the velocity profiles at $x=11.5$, 21.5 and 31.5 cm downstream of the cathode at $z=z_4$. The input power to the system was 1.56 kW. A laser gas mixture of $\text{CO}_2/\text{N}_2/\text{He}$ in the proportion 1:6:12 was used with a total pressure of 20 torr. As was mentioned earlier, the placement of the cathode in the middle of the channel creates a stagnation point along the downstream direction. The gas velocity is reduced to its minimum value in the stagnation region. A maximum velocity occurs in the mid regions between the centerline (A-A) (Fig. 5.3) and the anode.

The effect of the stagnation point on the gas velocity decreases as the flow advances downstream as can be seen in Fig. 7.33. In this case, the velocity profile tends to flatten as the flow proceeds downstream, where the stagnation point effect is minimal at $x=31.5$ cm. This result

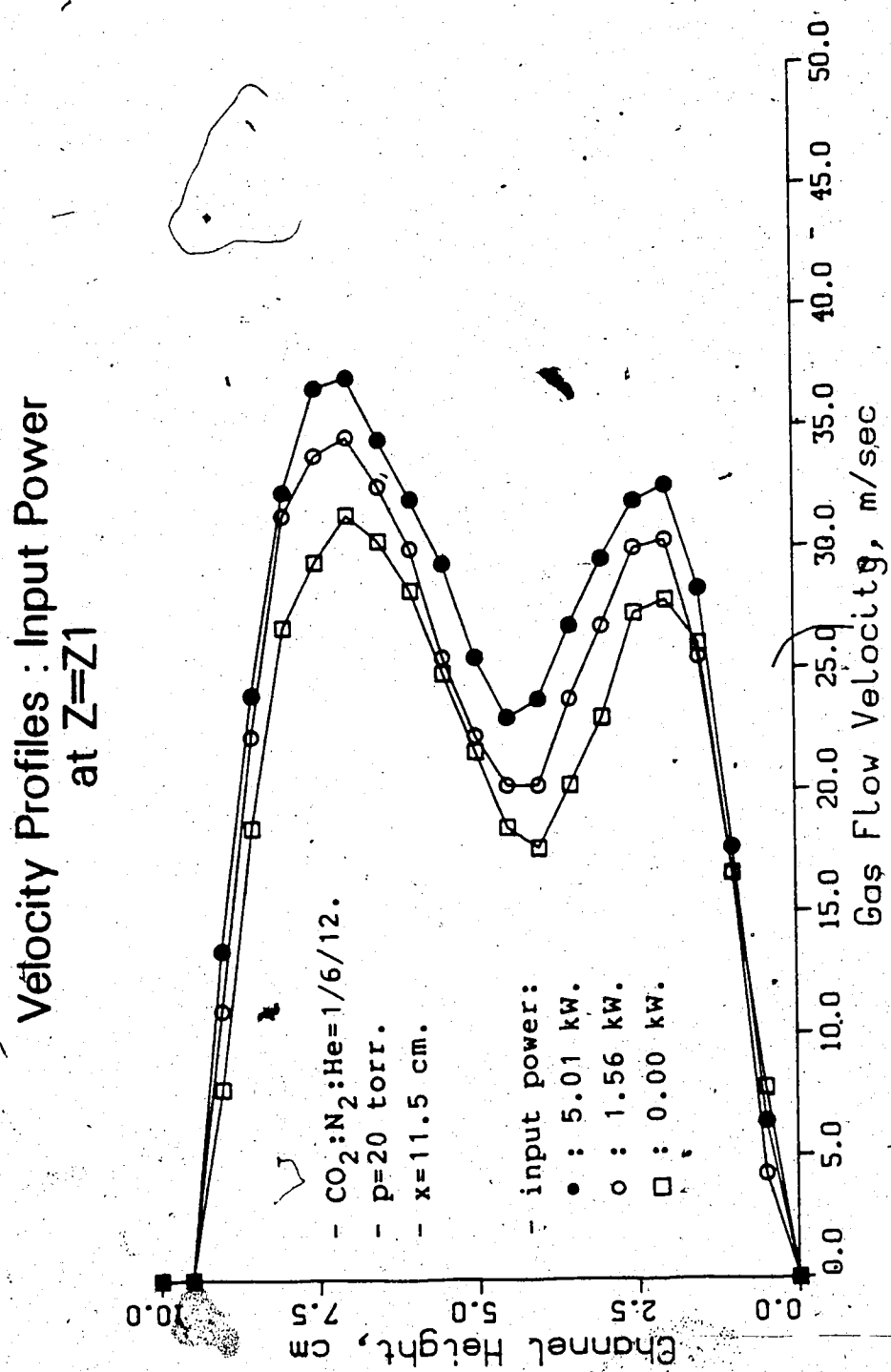


Fig. 7.29 Velocity profile dependence on the input power at $z=z_1$ and $x=11.5$ cm.

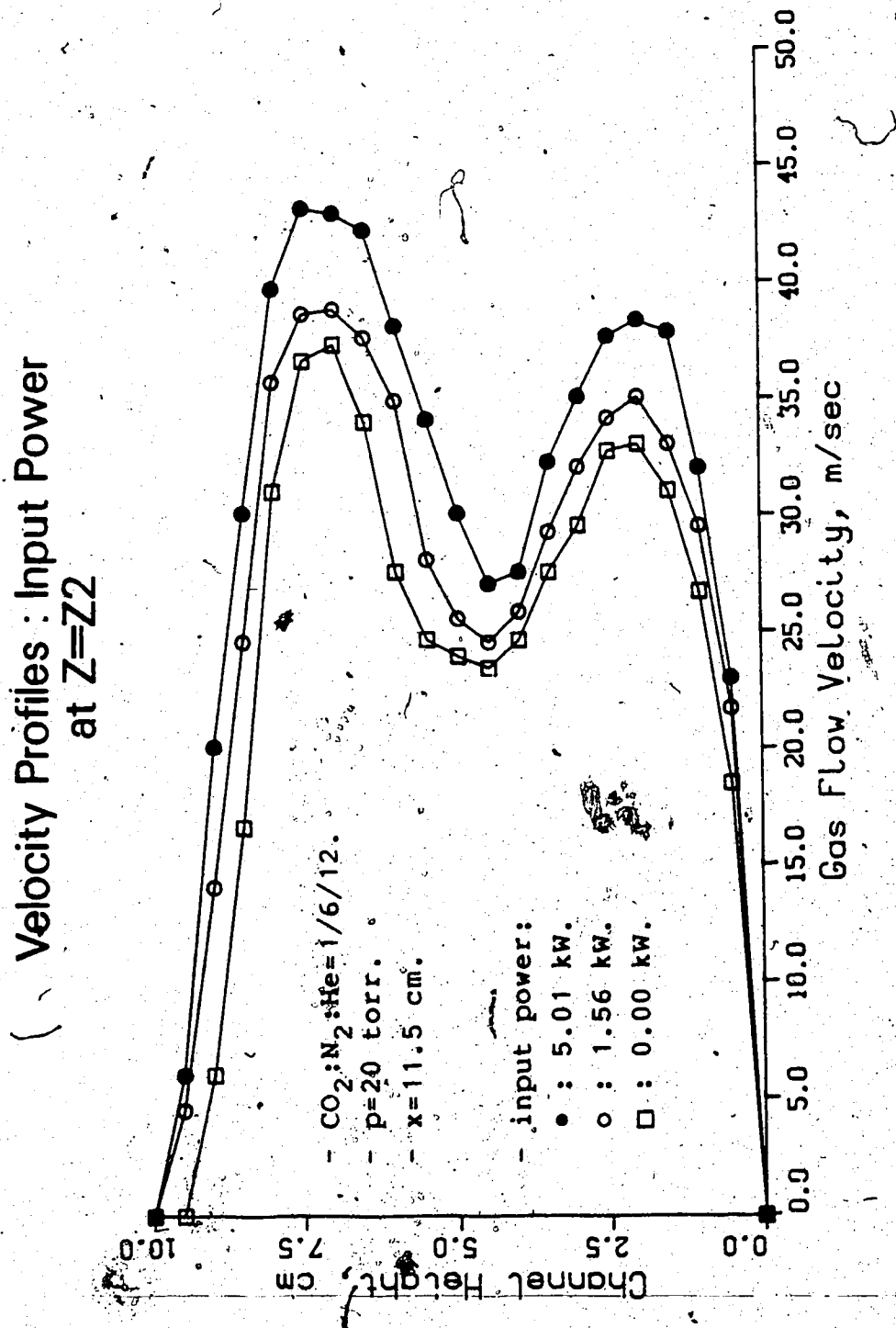


Fig. 7.30 Velocity profile dependence on the input power at $z=z_2$ and $x=11.5 \text{ cm}$.

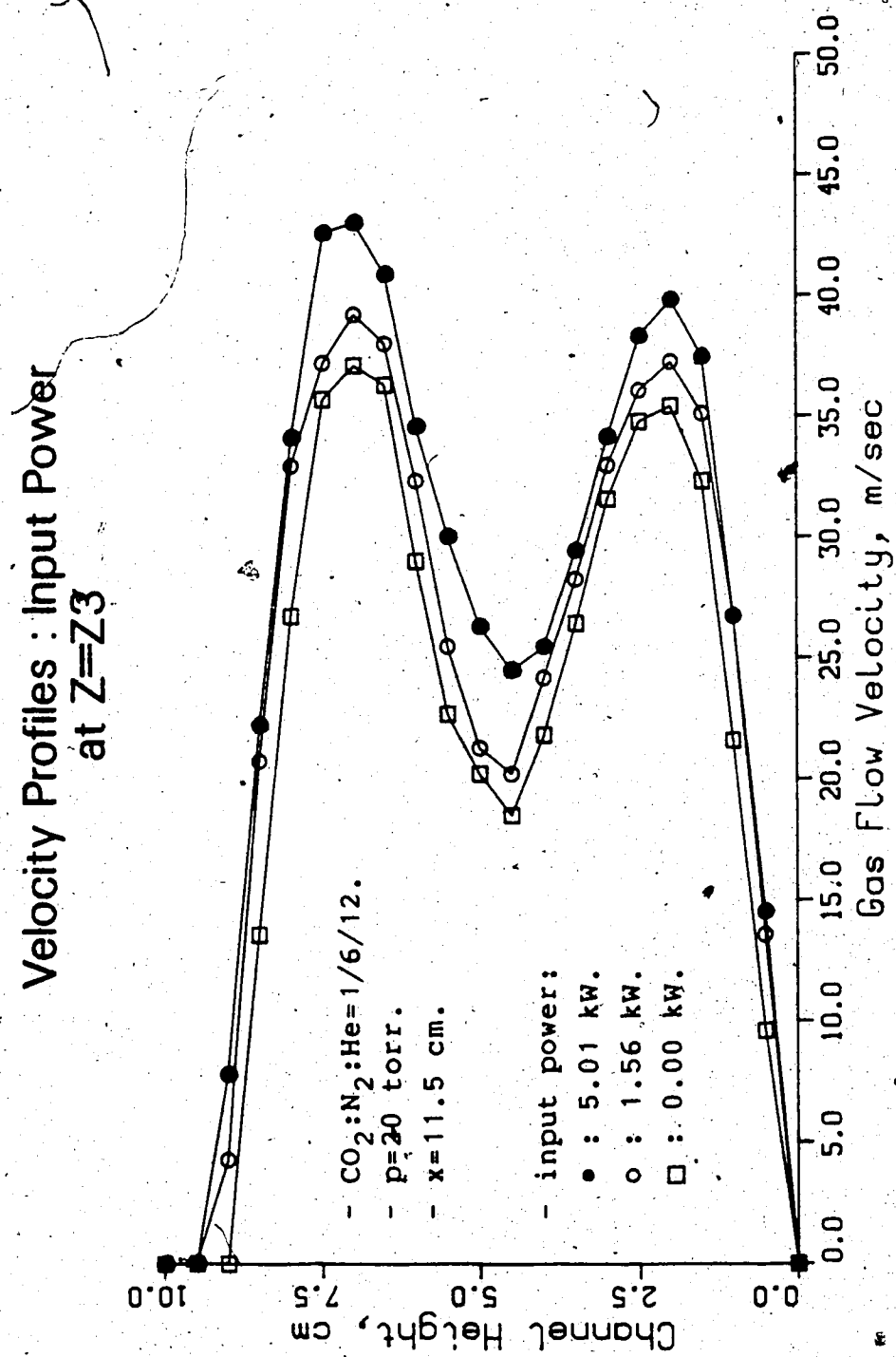


Fig. 7.31 Velocity profile dependence on the input power at $z=z_3$ and $x=11.5 \text{ cm}$.

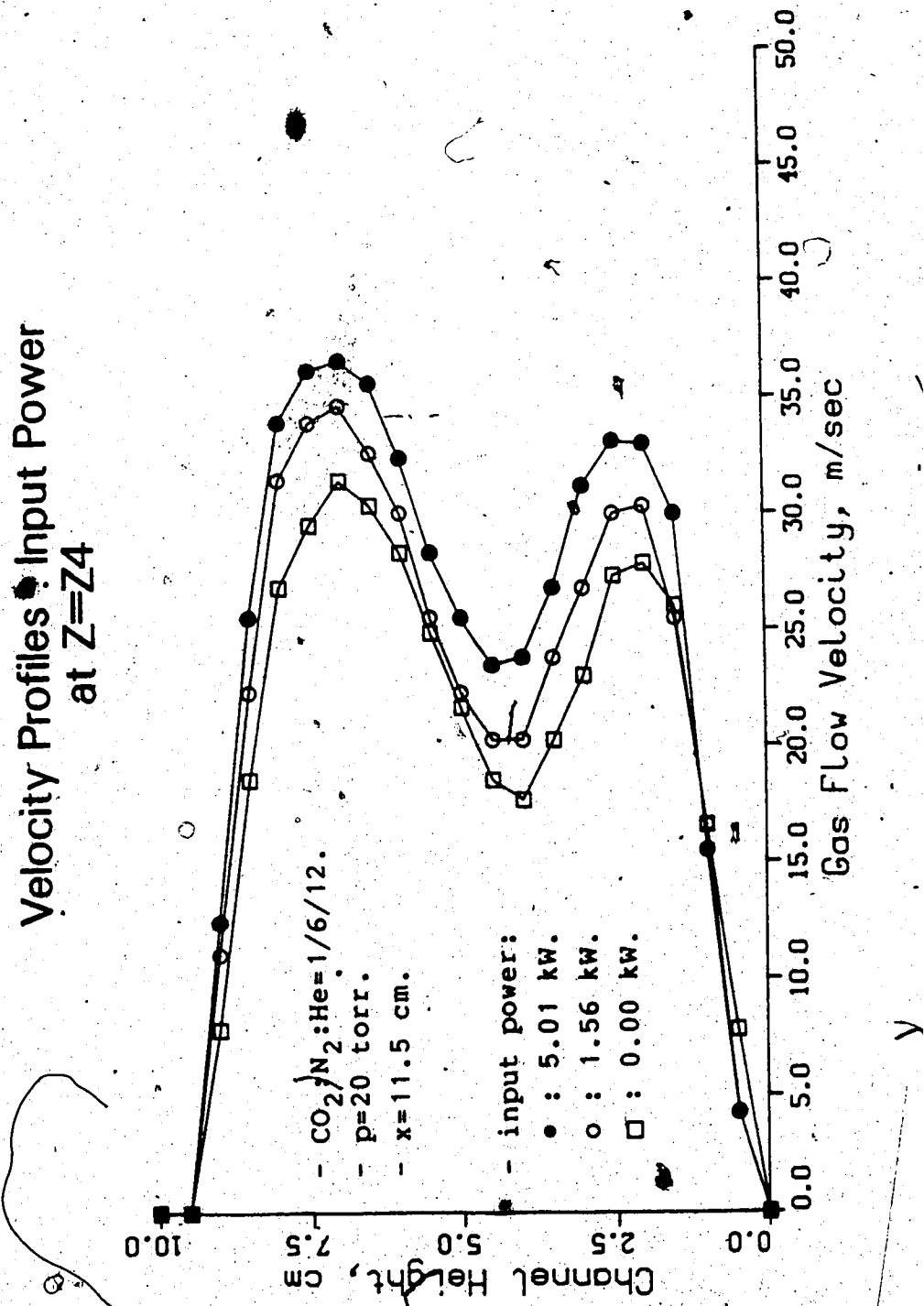


Fig. 7.32 Velocity profile dependence on the input power at $Z=Z_4$ and $x=11.5$ cm.

Velocity Profiles along the Flow Direction
Input Power=1.56 kW

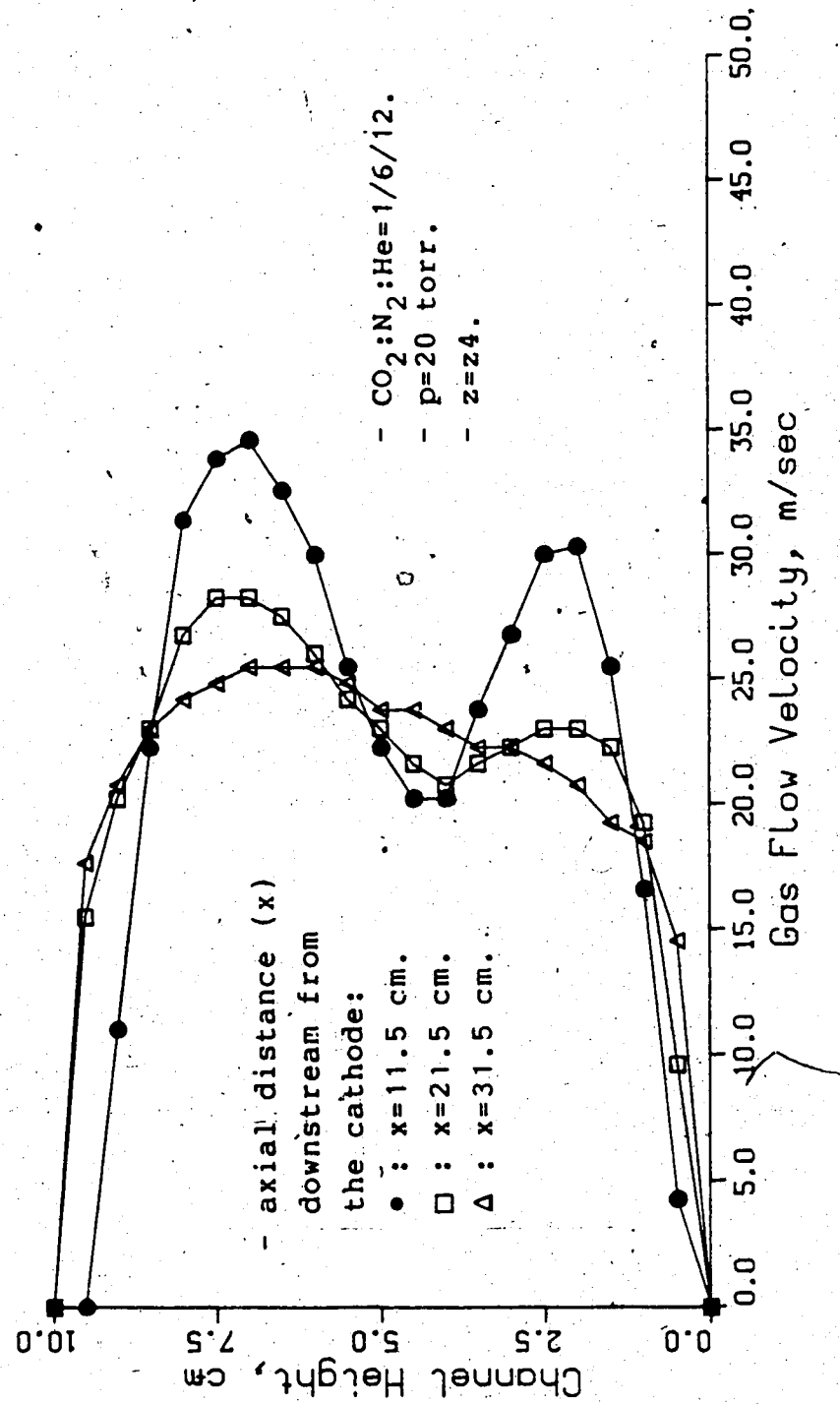


Fig. 7.33 Velocity profile dependence on axial distance (x),
for $P_{\text{inp}} = 1.56$ kW.

is in good agreement with the computer simulation results presented earlier. Also, this result is in good agreement with the measurements of Kovasznay [143] who investigated the flow around a circular cylinder.

Similar profiles were measured for different input power settings. Figure 7.34 shows the velocity at three locations downstream of the cathode for $P_{inp} = 3.16$ kW. The gas velocity increases with increasing input power. Further increases in the input power to the system results in a further increase in the gas velocity as can be seen in Fig. 7.35. In this case, an approximately 17% increase in the gas velocity was achieved with 5.01 kW input power.

The dependence of the velocity profiles on the input power was investigated in greater detail and comparison made with the isothermal results. The velocity profiles were measured at six different points downstream of the cathode.

The laser gas mixture used was $\text{CO}_2/\text{N}_2/\text{He}$ in the proportion 1:6:12 at a pressure of 20 torr. The input power was set at 0.0, 1.56, 3.16 and 5.01 kW respectively. The velocity profiles which were taken across the channel (along the y-direction) were measured at $z=z_4$ and at $x=7.5, 11.5, 16.5, 21.5, 26.5$ and 31.5 cm respectively.

Figure 7.36 illustrates the velocity profiles at $x=31.5$ cm downstream of the cathode, which is the farthest point of measurement along the x-axis in our measurements. The profiles are approximately flat and uniform as can be

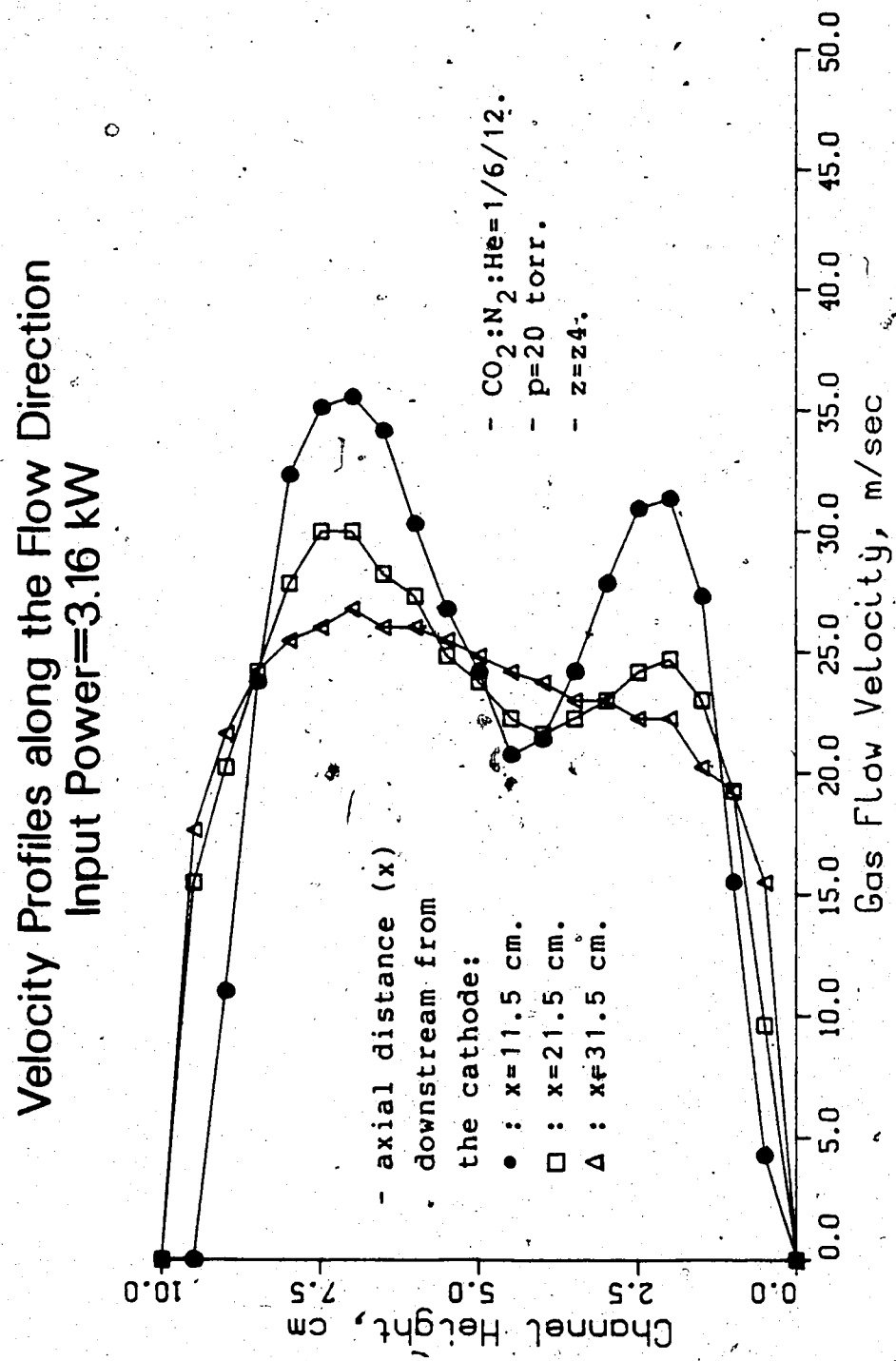


Fig. 7.34 Velocity profile dependence on axial distance (x),
for $P_{\text{inp}} = 3.16$ kW.

Velocity Profiles along the Flow Direction
Input Power=5.01 kW

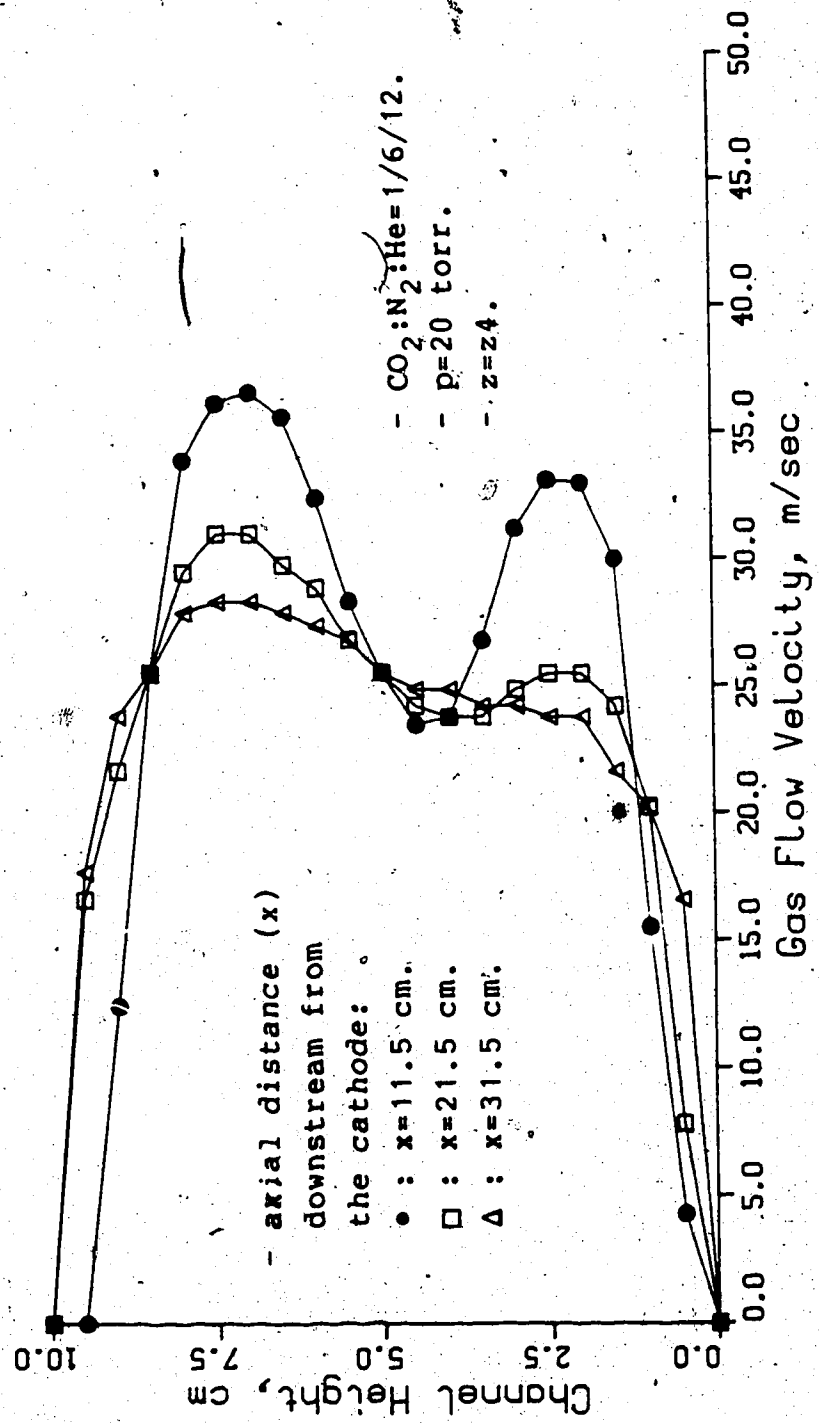


Fig. 7.35 Velocity profile dependence on axial distance (x),
for $P_{\text{inp}} = 5.01 \text{ kW}$.

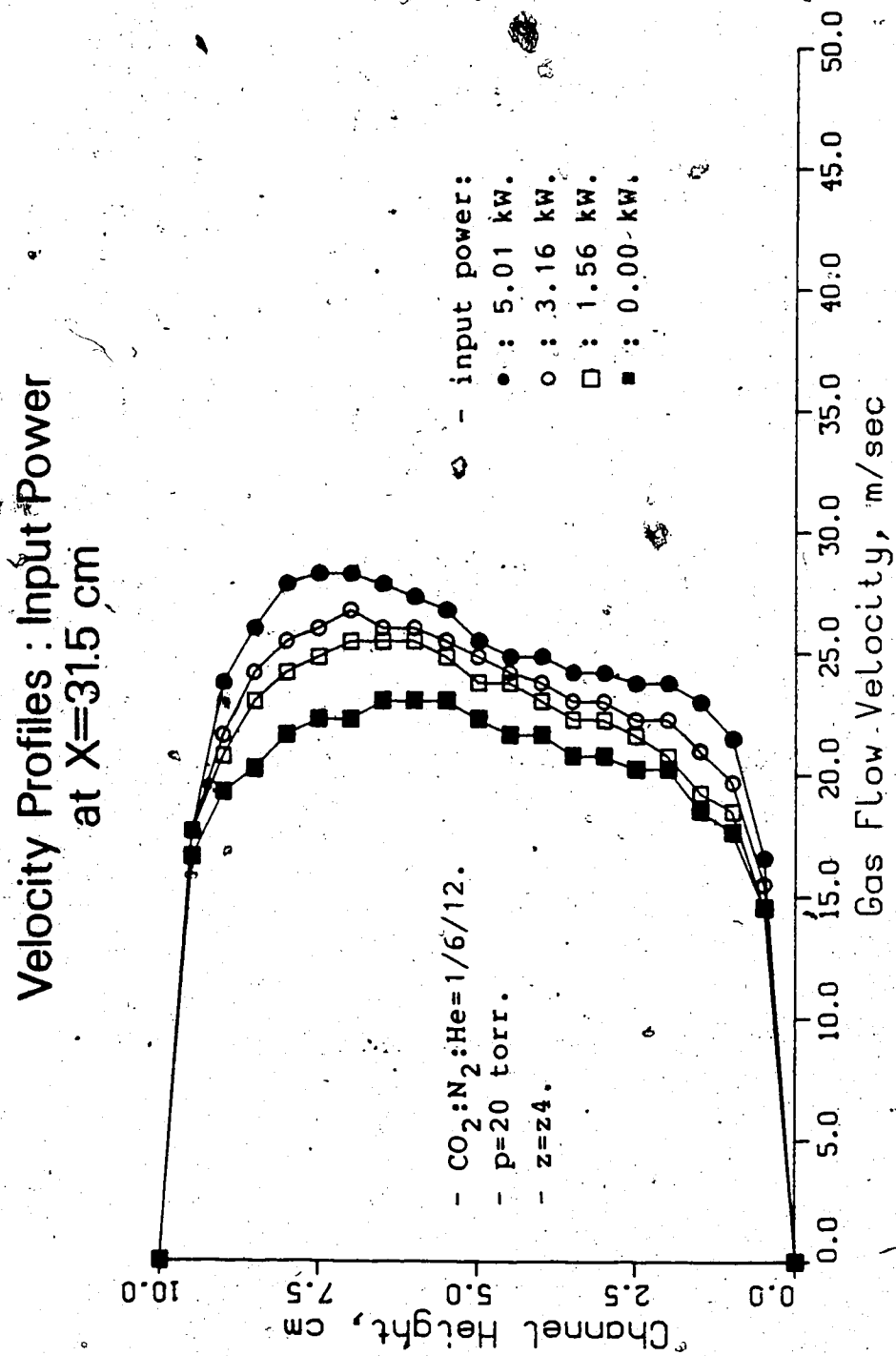


Fig. 7.36 Velocity profile dependence on the input power at $x=31.5$ cm and $z=z_4$.

determined, where the effect of the stagnation point is minimal. The increase in the input power results in an increase in the gas velocity, which is evident from these plots. Comparison with the isothermal case indicates an average increase of 17% in the gas velocity with the increased input power.

Figure 7.37 shows the velocity profiles at $x=26.5$ cm downstream of the cathode. The shape of the profiles changes slightly. The gas velocity increases in the mid region between the centerline (A-A) (Fig. 5.3) and the anodes. This occurs for all power settings. The effect of the stagnation point on the velocity pattern is more pronounced as we come closer to the cathode as shown in Figs. 7.38,39. The velocity profiles are measured at $x=21.5$ and 16.5 cm downstream of the cathode. A 17% average increase in the gas velocity is maintained by increasing the input power up to 5.01 kW.

The velocity profiles are measured also close to the cathode, at $x=11.5$ cm from the downstream surface. The results are shown in Fig. 7.40 where the gas velocity drops to 60% of its maximum value at the middle of the channel. This reduction is due to the stagnation point caused by the cathode (obstacle). The effect of the input power is similar to that described earlier, where up to 17% increase in the gas velocity is obtained. Finally, Fig. 7.41 shows the velocity profiles very close to the cathode, where $x=7.5$ cm

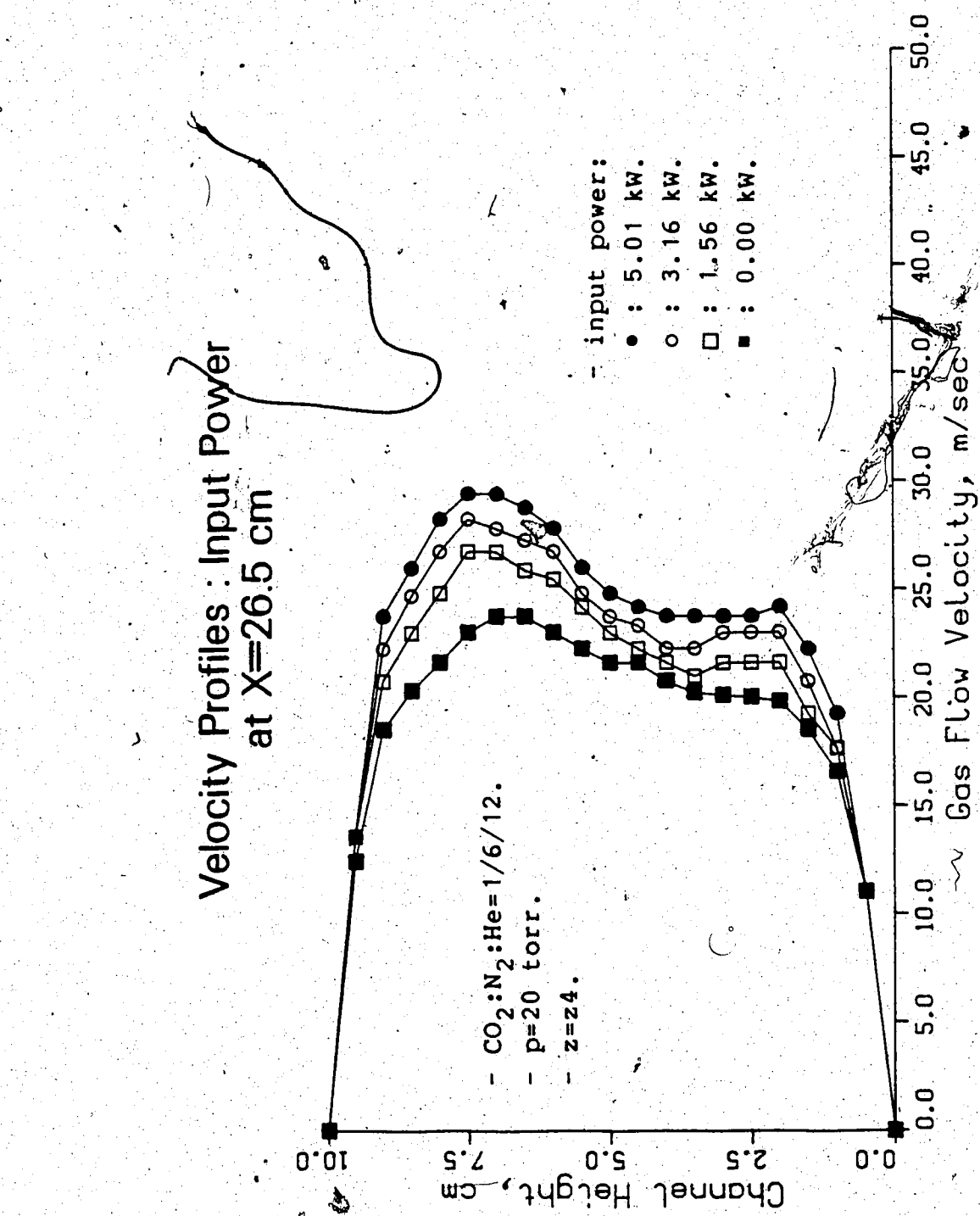


Fig. 7.37 Velocity profile dependence on the input power at $x=26.5$ cm and $z=z_4$.

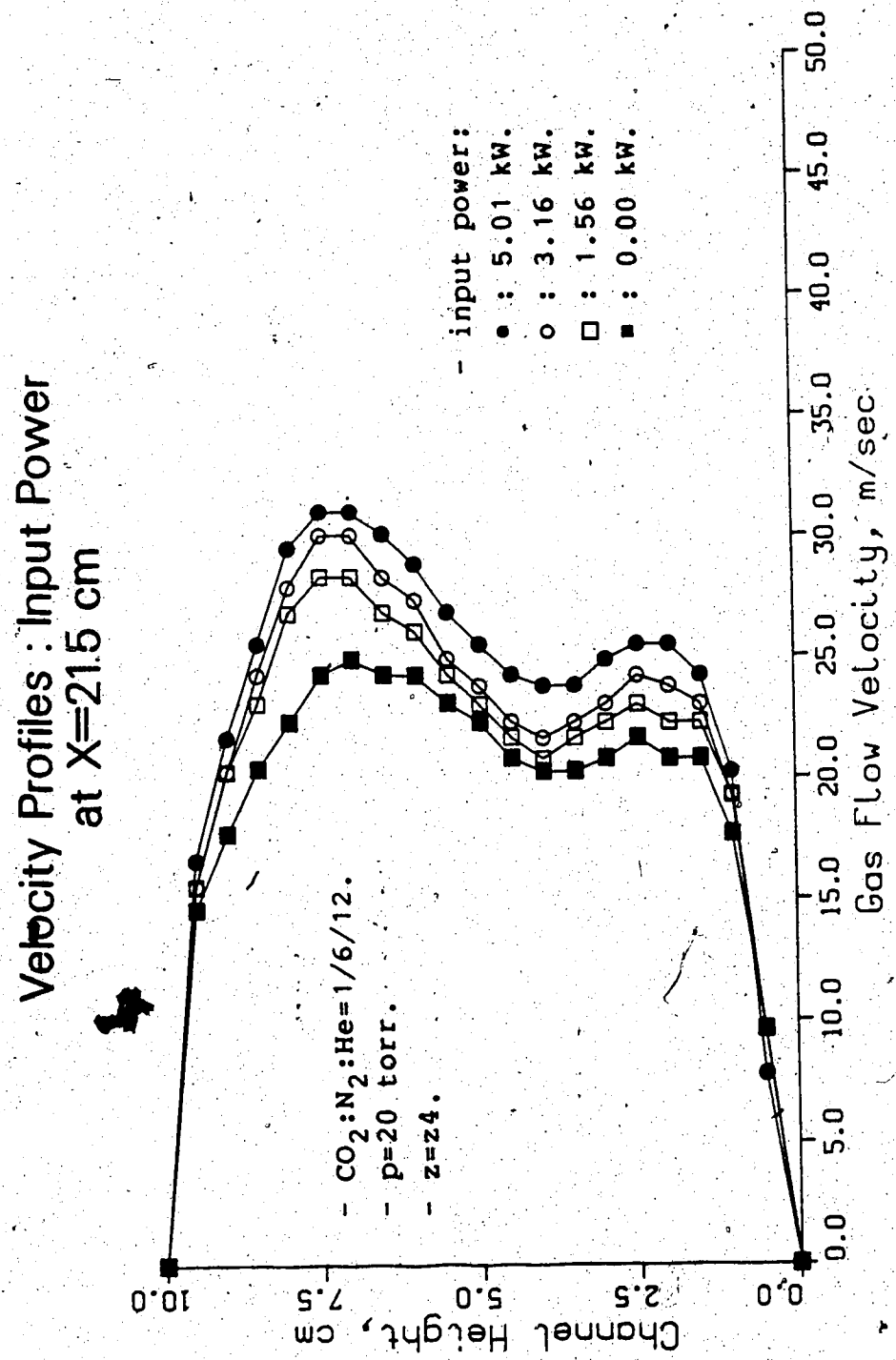


Fig. 7.38 Velocity profile dependence on the input power at $x=21.5$ cm and $z=z4$.

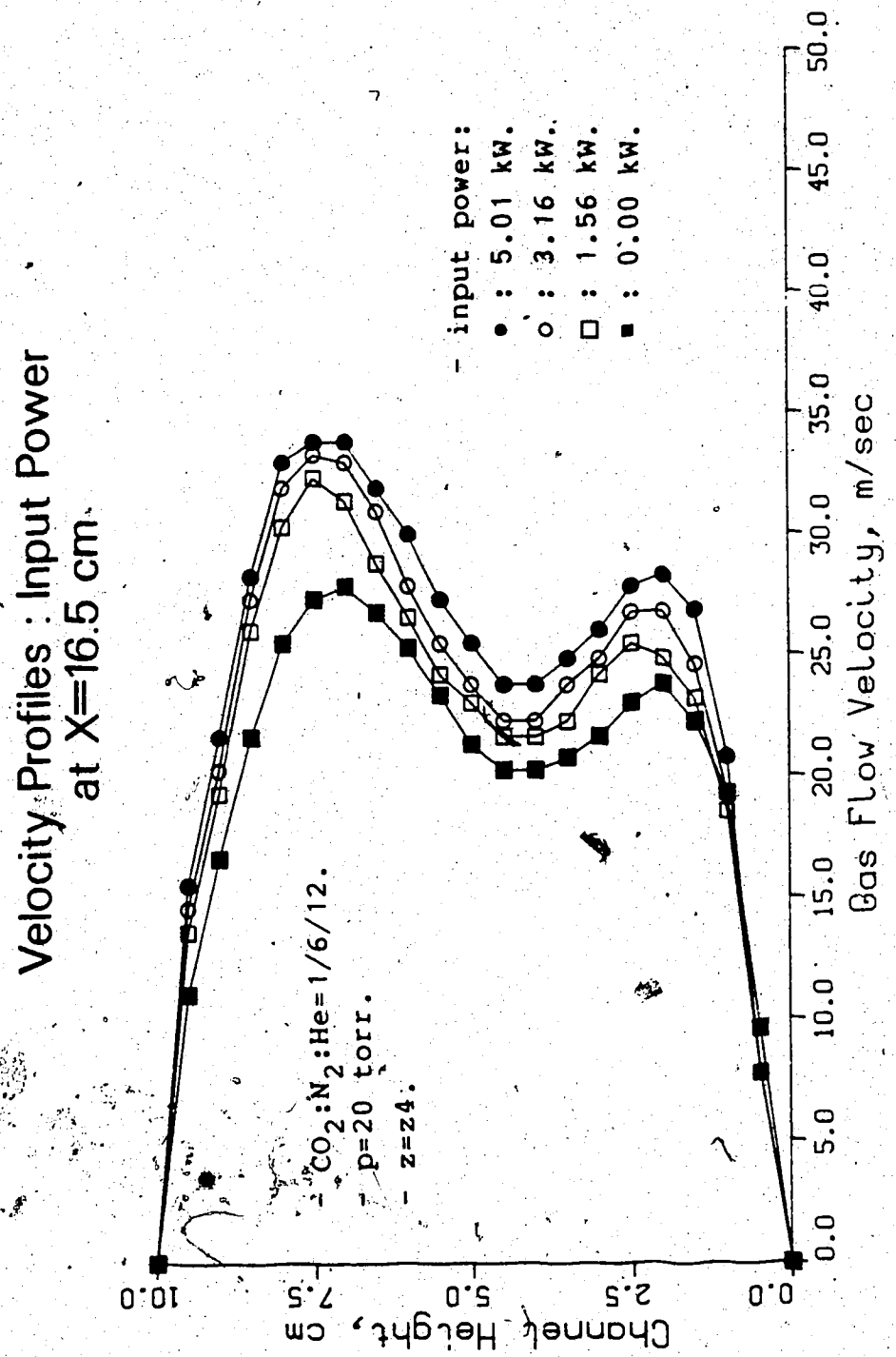


Fig. 7.39 Velocity profile dependence on the input power at $x=16.5$ cm and $z=z_4$.

Velocity Profiles : Input Power
at $X=11.5$ cm

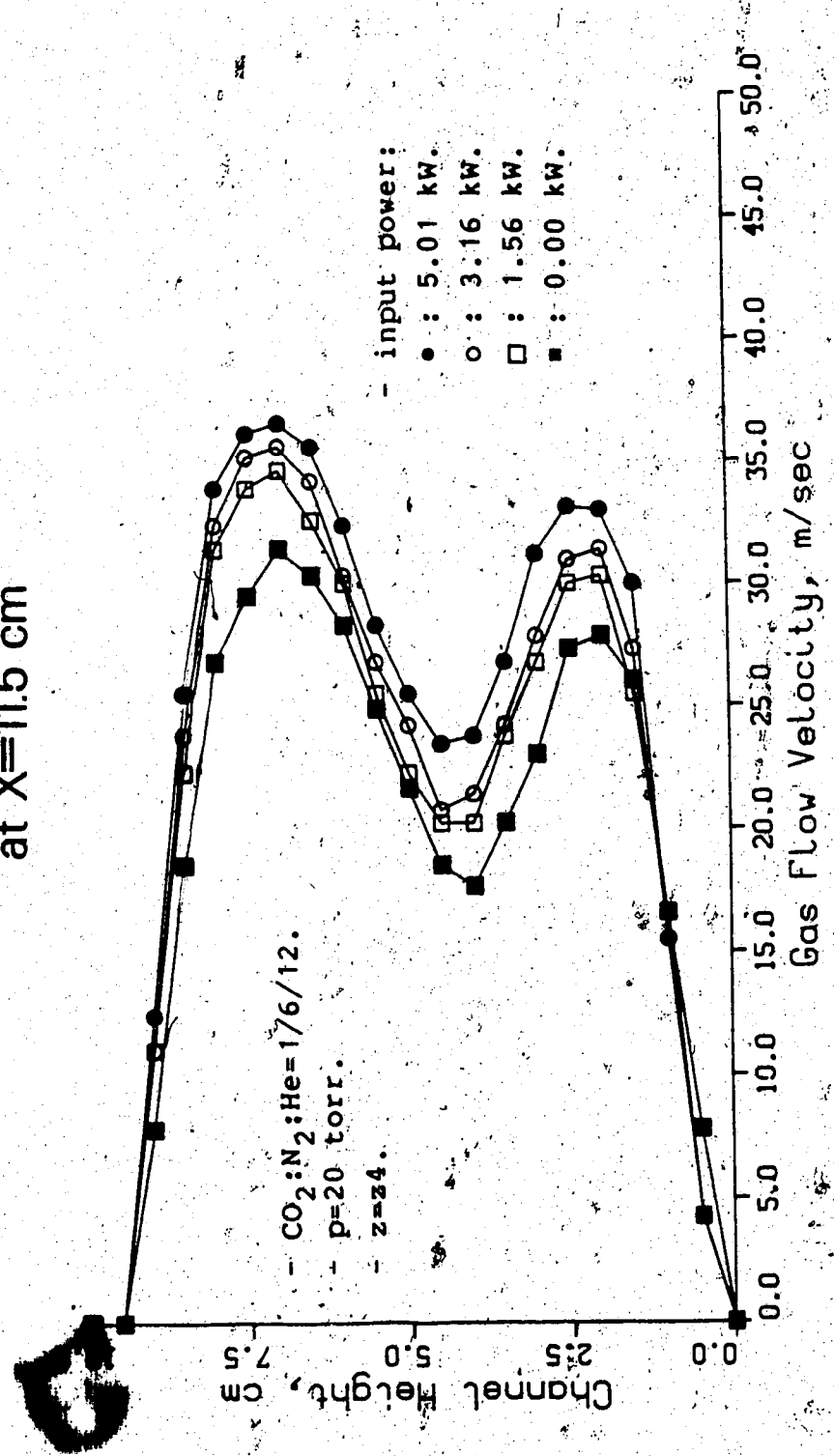


Fig. 7.40 Velocity profile dependence on the input power at
 $x=11.5$ cm and $z=z_4$.

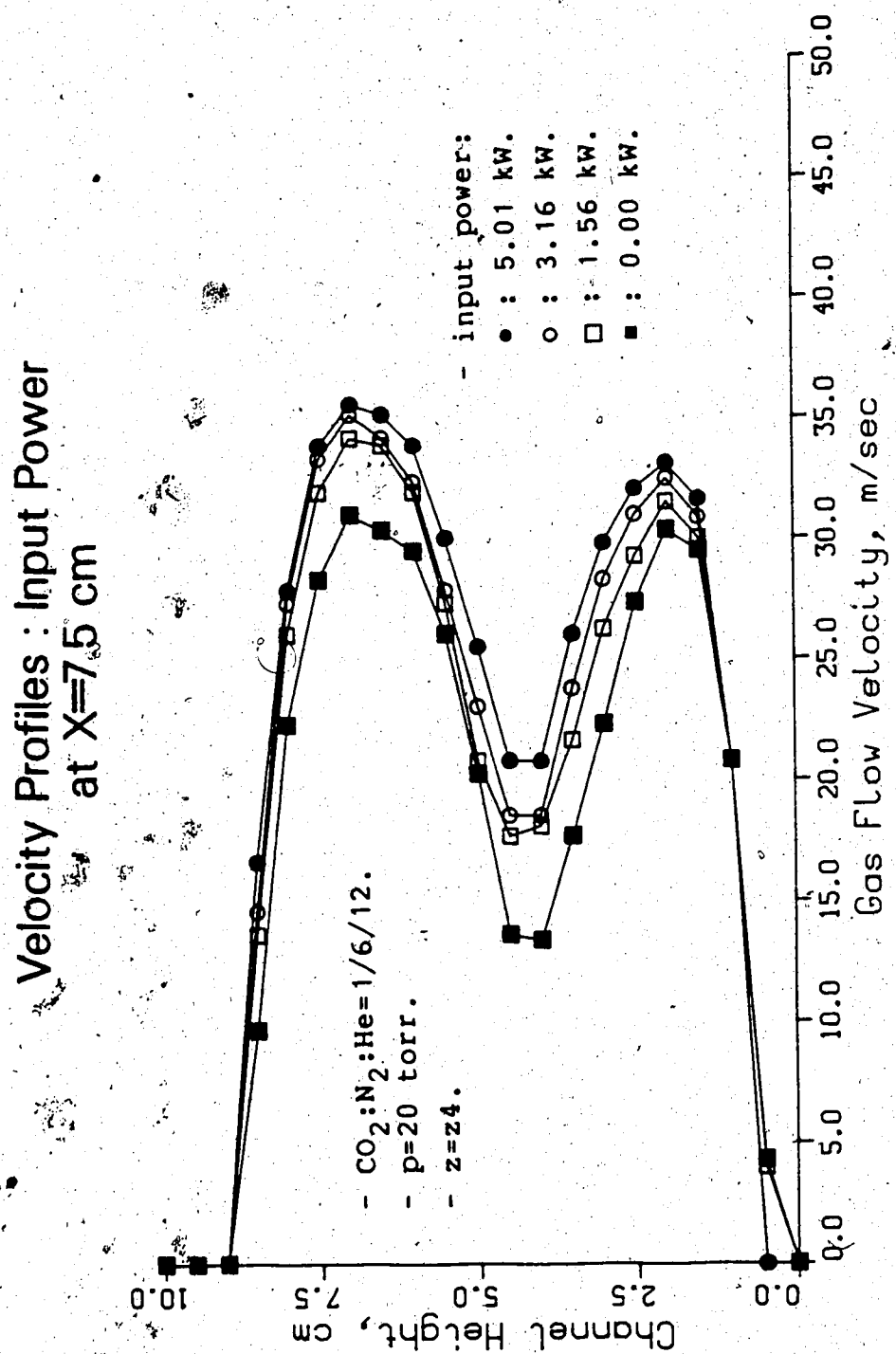


Fig. 7.41 Velocity profile dependence on the input power at $x=7.5$ cm and $z=z_4$.

downstream. The gas velocity drops to about 50% of its maximum value, while the increase in the velocity due to the increase in the input power is maintained.

From the above measurements, it is apparent that the gas velocity decreases as the flow advances downstream. However, at the nearest point to the cathode ($x=7.5$ cm), the velocity shows a little reduction in its amplitude, as can be inferred from the comparison of Figs. 7.40 and 41. Also, the effect of the stagnation point caused by the cathode, results in a reduction in the gas velocity to about 50% of its maximum value at a distance of 7.5 cm downstream.

Finally, regardless of the effect of the stagnation region, increasing the input power results in an increase in the gas velocity, which shifts up the entire profiles by about 17% of its maximum values. These results are in good agreement with our computer simulation results obtained earlier. Comparison of these velocity measurements with the simulation results will be presented in section 7.4.

E. VELOCITY MEASUREMENTS ALONG THE X-AXIS

An interesting result was obtained when the gas velocity was measured along the axis (A-A) (Fig. 5.3). The measurements were made as close as 2.5 cm downstream of the cathode surface by using a metal pitot tube. It may be noted that the metal pitot tube was well isolated from the system during these measurements. Figure 7.42 shows the results

Velocity Distribution along the
Centerline a-a : Input Power

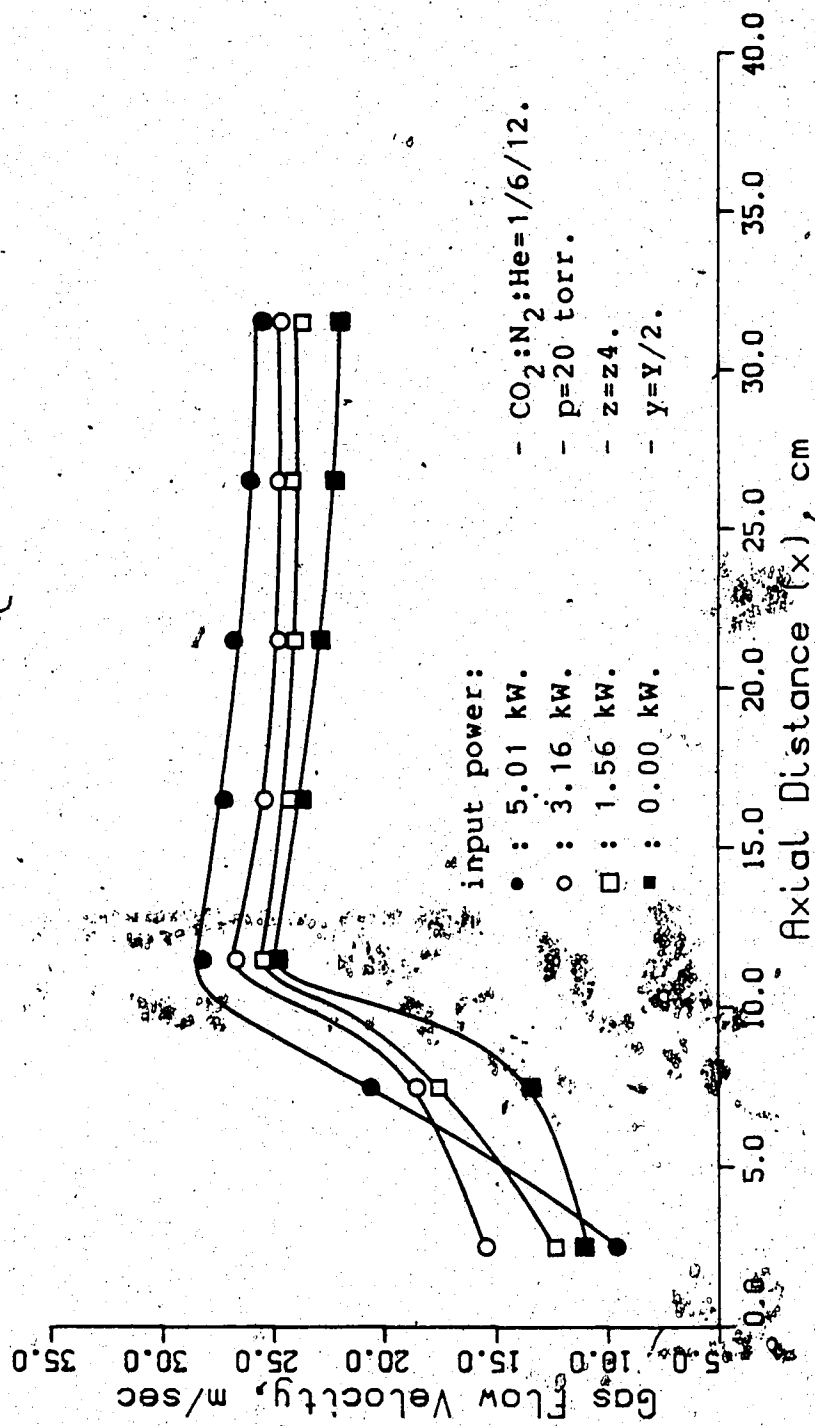


Fig. 7.42 Gas velocity distribution along the centerline
(A-A), as a function of the input power.

obtained. The lower curve is for the isothermal case ($P_{inp} = 0.0$ kW) where only the gas flow was considered. With the discharge on, and for 1.56 kW input power, an increased velocity is observed for all x-values.

An increase in the input power to 3.16 kW results in further increase in the axial flow velocity. When the input power increased to 5.01 kW, a similar behavior was observed as shown by the upper curve, except at the point close to the cathode ($x=2.5$ cm). At this point the gas velocity dropped even below the isothermal value as can be seen in Fig. 7.43. This is an interesting result which may be explained as due to the formation of swirls or wakes downstream of the cathode. Fortunately, this explanation is supported by our computer simulation results, evident by the velocity vector distribution obtained earlier. This velocity vector distribution indicated that a flow separation occurred downstream of the cathode. Further investigation is required in order to determine the flow structure in this region in more detail.

7.3.3 TEMPERATURE DISTRIBUTION MEASUREMENTS

As was mentioned in section 4.1, the gas temperature in the discharge chamber must remain below about 600 °k, if this device is to serve as a laser. At higher gas temperatures the lower laser level becomes populated and consequently the population inversion is destroyed [88]. It

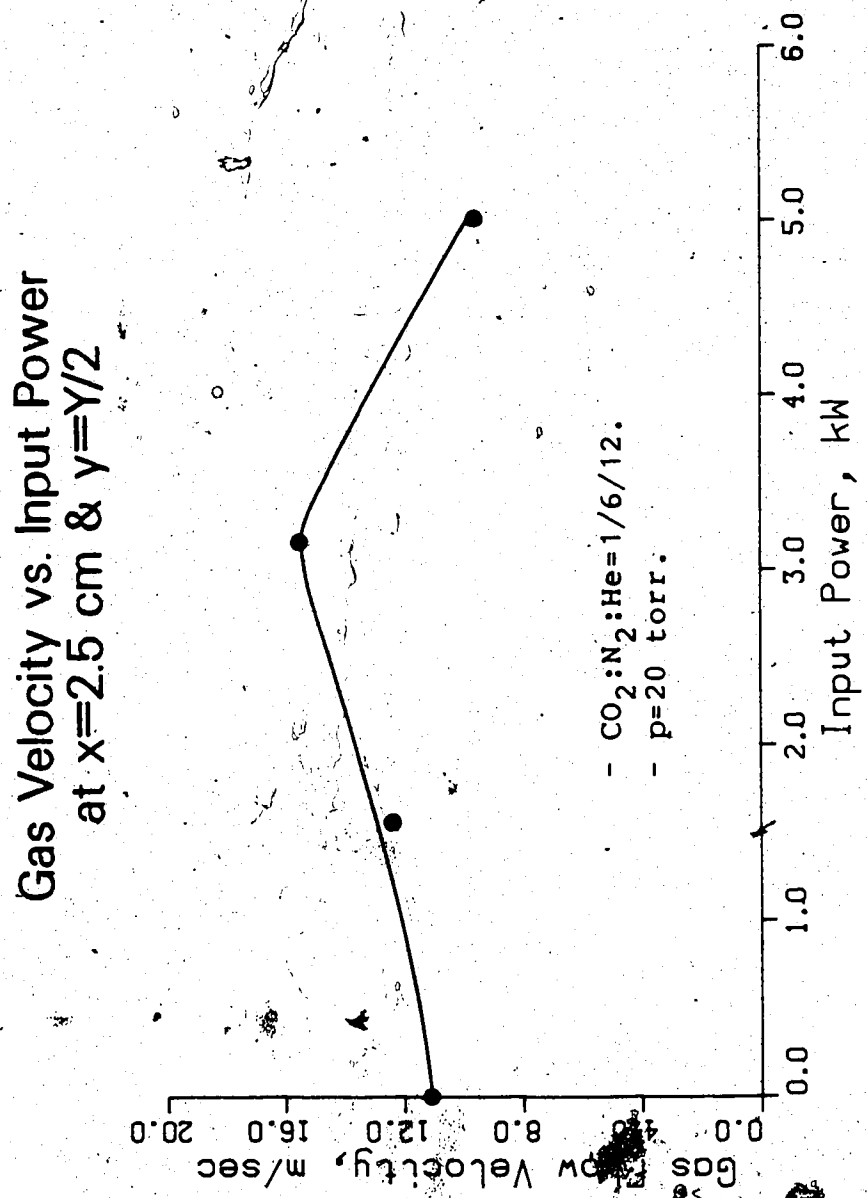


Fig. 7.43 Gas velocity dependence on input power at $x=2.5$ cm
and $y=y/2$.

was mentioned also that disposing of the waste heat by convecting it out of the discharge region is the best way to meet the above constraint [6,7,9]. Therefore, one of the most important tasks in the present work is to study heat transport in our device. Investigation of the temperature distributions in the discharge region, and its dependence on the various parameters were conducted.

The temperature measurements were performed using an iron-constantan (type J) thermocouple. The thermocouple terminals were connected to a floating digital voltmeter to measure the thermoelectric potential. Calibration tables were then used to obtain the corresponding temperature values. The temperature was measured at different points along the x-axis, downstream of the cathode. Another set of measurements was obtained at different points on the z-axis, along the discharge length. At each of those points the temperature distribution (profile) across the channel height (y-direction) was obtained. The temperature profile dependence upon gas pressure, laser gas mixture and the input power will be discussed. Also, the temperature profiles along the discharge length and along the flow direction will be presented and discussed.

To be able to discuss the nature of these profiles which are far from being linear, we consider first the simple case of convective heat transfer described by Newton's law of cooling [157] and is given by:

$$q = A h \Delta T , \quad (7.1)$$

where q is the rate of convective heat transfer, A is the cross sectional area, h is the convective heat transfer coefficient, and ΔT is the temperature difference.

Then we consider the convective heat transfer in a unit volume dV rather than in a surface area A . Therefore Eqn. 7.1 can be modified to describe the volumetric convective heat transfer in the x -direction as:

$$Q_h dV = A \rho v c_p dT , \quad (7.2)$$

where Q_h is the convective heat transfer per unit volume, dV is a unit volume, ρv is the mass flow rate, ρ is the gas density, v is the gas velocity, c_p is the specific heat, and dT is the temperature change across the volume element. In Eqn. 7.2, dV and ρ are given by:

$$dV = A dx \quad (7.3)$$

and

$$\rho = pm/K_B T \quad (7.4)$$

where p is the gas pressure, m is the average molecular mass of the gas mixture, K_B is Boltzmann constant, and T is the gas temperature.

Substitution of Eqns. 7.3 and 7.4 into Eqn. 7.2 gives:

$$Q_h A dx = (pm/K_B T) v A c_p dT , \quad (7.5)$$

$$Q_h dx = \left(\frac{pmvc_p}{K_B T} \right) dT ,$$

which can be arranged as:

$$dT/T = \left(\frac{Q_h K_B}{pmvc_p} \right) dx . \quad (7.6)$$

Equation 7.6 can be integrated between T_0 and T_x along a distance X to give:

$$\ln(T_x/T_0) = Q_h K_B X / pmvc_p \quad (7.7)$$

or

$$T_x = T_0 \exp(Q_h K_B X / pmvc_p) \quad (7.8)$$

where T_x is the gas temperature at a distance X along the direction of flow in the discharge region, and T_0 is the inlet temperature.

Equation 7.8 can further be arranged as:

$$T_x - T_0 = T_0 [\exp(Q_h K_B X / pmvc_p) - 1] \quad (7.9)$$

which gives the temperature difference across a distance X .

Equation 7.9 shows that the temperature T is an exponentially varying function. It shows also that T increases with increasing the input power (the convective heat transfer Q_h is a representative of the input power). Also, increasing the gas pressure or the gas velocity results in an exponentially decreasing temperature. These results are the basis upon which the temperature distributions will be discussed in the following subsections.

A. TEMPERATURE DEPENDENCE ON PRESSURE,

LASER GAS MIXTURE AND INPUT POWER

The temperature profiles were obtained for three different gas pressure values of 20, 30 and 40 torr. The measurements were taken across the channel (along the y-axis) at $x=11.5$ cm downstream of the cathode, and at $z=z_4$. The laser gas mixture used was $\text{CO}_2/\text{N}_2/\text{He}$ in the proportion of 1:6:12 and the input power was 3.16 kW. Figure 7.44 shows the profiles obtained from these measurements. The profiles have almost the same shape for each pressure setting as can be seen in this figure.

For simplicity of explanation, the plot may be divided into three distinguished regions I, II and III. Region II corresponds to a stagnation region where the mass flow is minimum, and consequently the temperature is high and reaches its maximum. Away from the cathode region, regions I and III correspond to regions of maximum flow rate, and consequently convective cooling is stronger. Therefore, the temperature in regions I and III is low and decreases towards the anodes as can be seen in Fig. 7.44.

Figure 7.45 illustrates the dependence of the gas temperature on gas pressure and input power. For a given gas pressure, the temperature increases exponentially as the input power is increased. This result may be explained by the exponential relation of Eqn. 7.9, which was obtained

Temperature Profiles : Gas Pressure

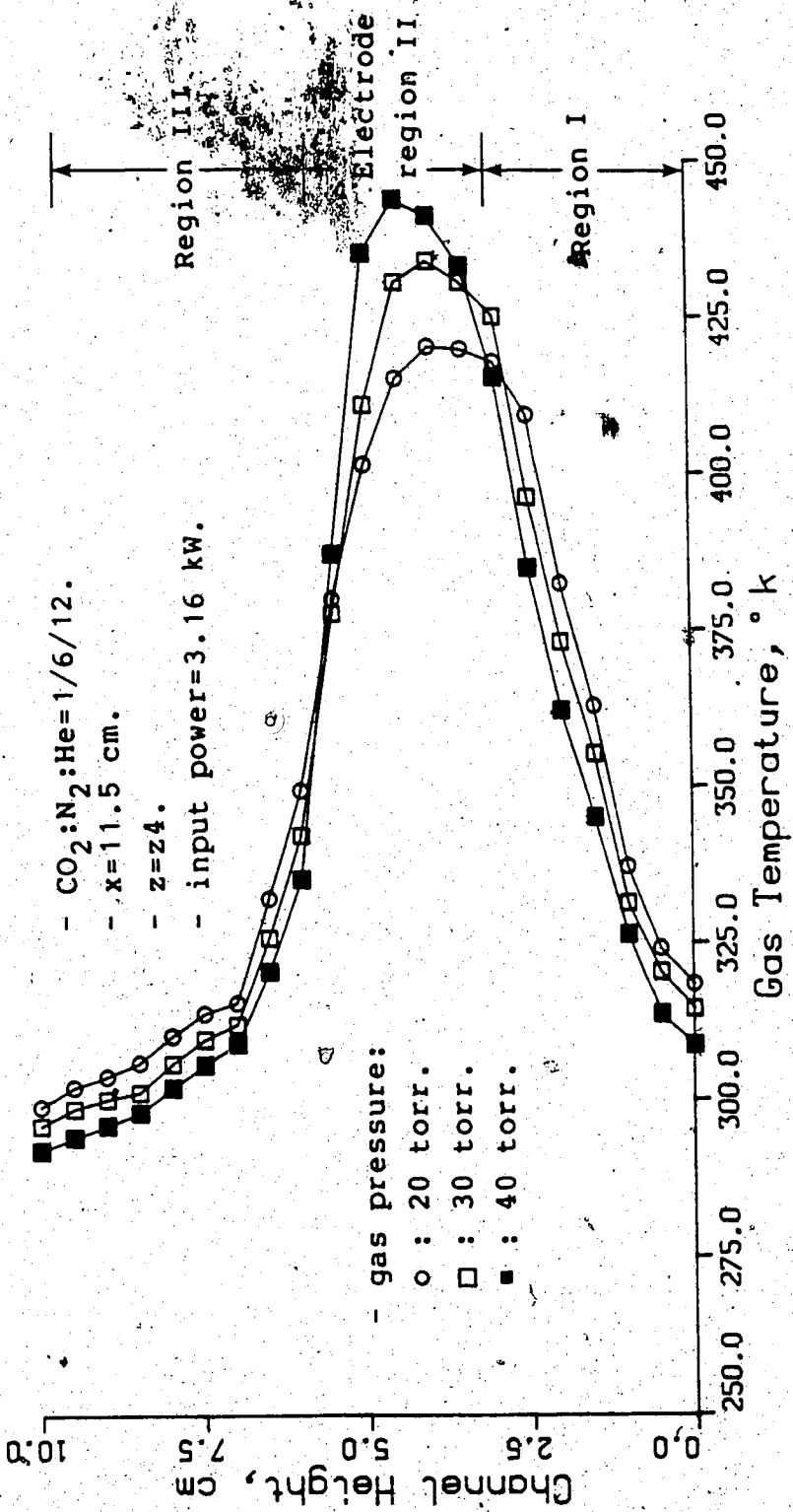


Fig. 7.44 Temperature profile dependence on gas pressure at
x=11.5 cm and z=z₄.

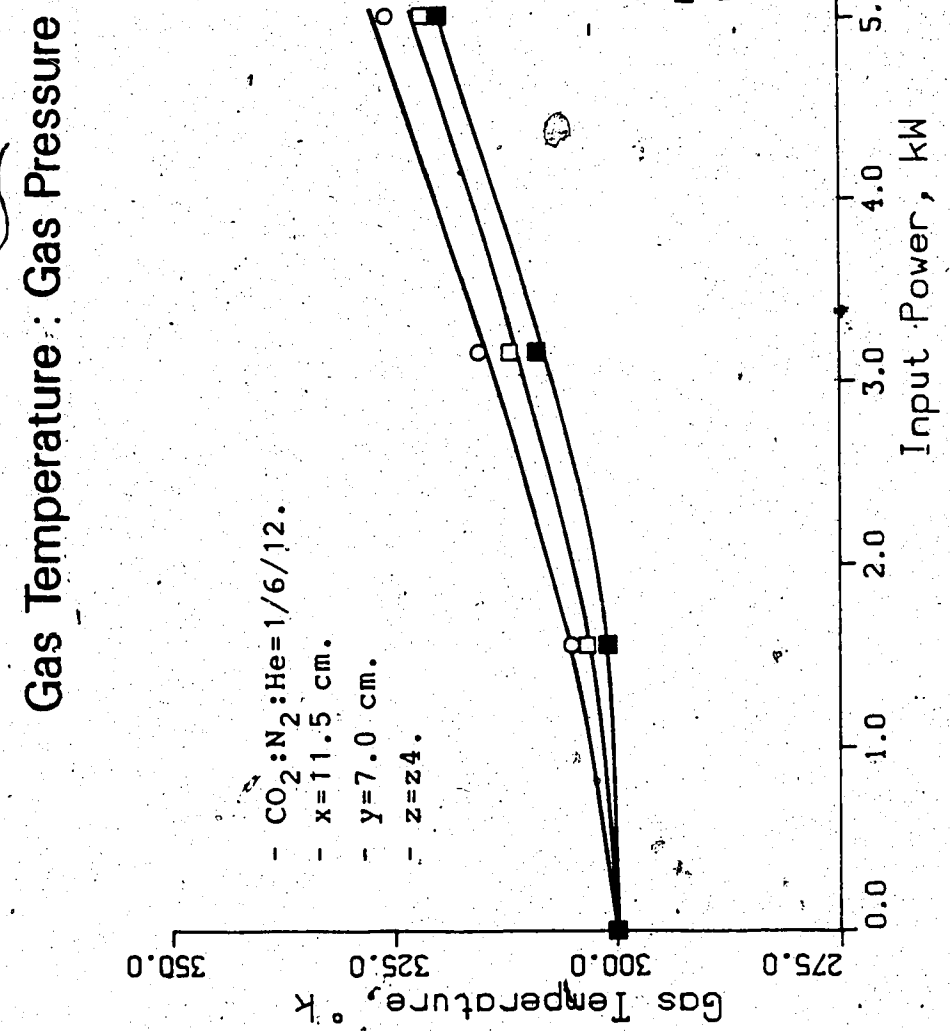


Fig. 7.45 Gas temperature dependence on input power for different gas pressures.

earlier. This result is also in good agreement with the computer simulation results presented earlier. As the gas pressure is increased, the temperature decreases and the temperature-input power curve shifts down as can be seen from Fig. 7.45. These measurements were obtained at $y=7.0$ cm.

The dependence of gas temperature on laser gas mixture and input power was also investigated. Figure 7.46 shows the temperature profiles for different laser gas mixtures, while Fig. 7.47 illustrates the gas temperature as a function of the input power for the same laser gas mixtures. It was found that the laser gas mixture which contains more He yields a profile which has the lowest temperature as shown by profiles (1) and (2). This result is expected, since the helium (He) plays the role of a cooling agent in the laser gas mixture.

However, when using another laser gas mixture which contains large amount of nitrogen (N_2), the temperature profile (3) behaves differently, where higher temperature values were observed in the middle section and even lower temperatures in the regions with high mass flow. Also with increasing the input power, the exponentially varying temperature curve shifts to lower temperatures when using a laser gas mixture with higher He ratio. As observed, all the curves have exponential dependence on the input power, a result which is in good agreement with Eqn. 7.9, where the

Temperature Profiles : Laser Gas Mixture

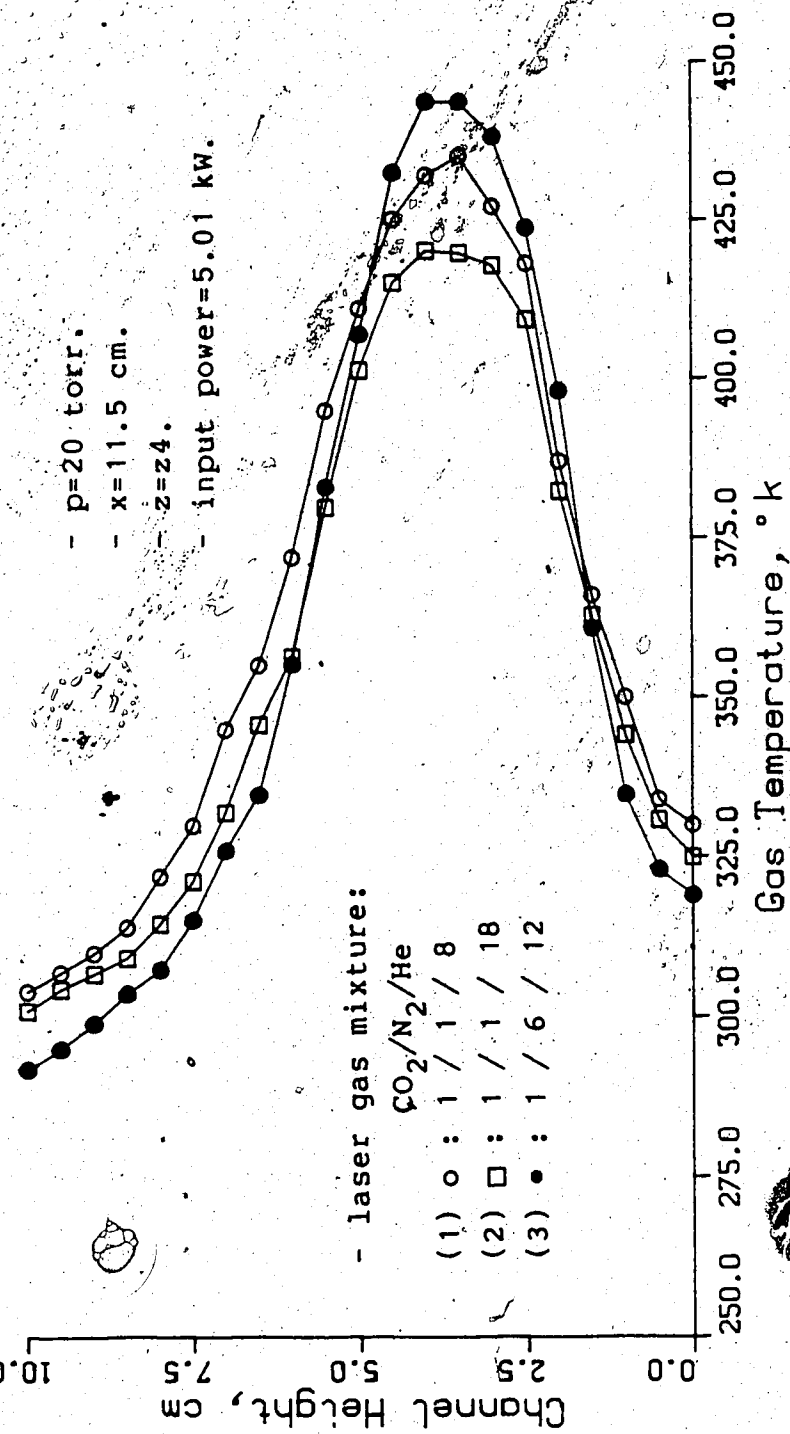


Fig. 7.46 Temperature profile dependence on laser gas mixture at $x=11.5 \text{ cm}$ and $z=z4$.

Gas Temperature : Laser Gas Mixture

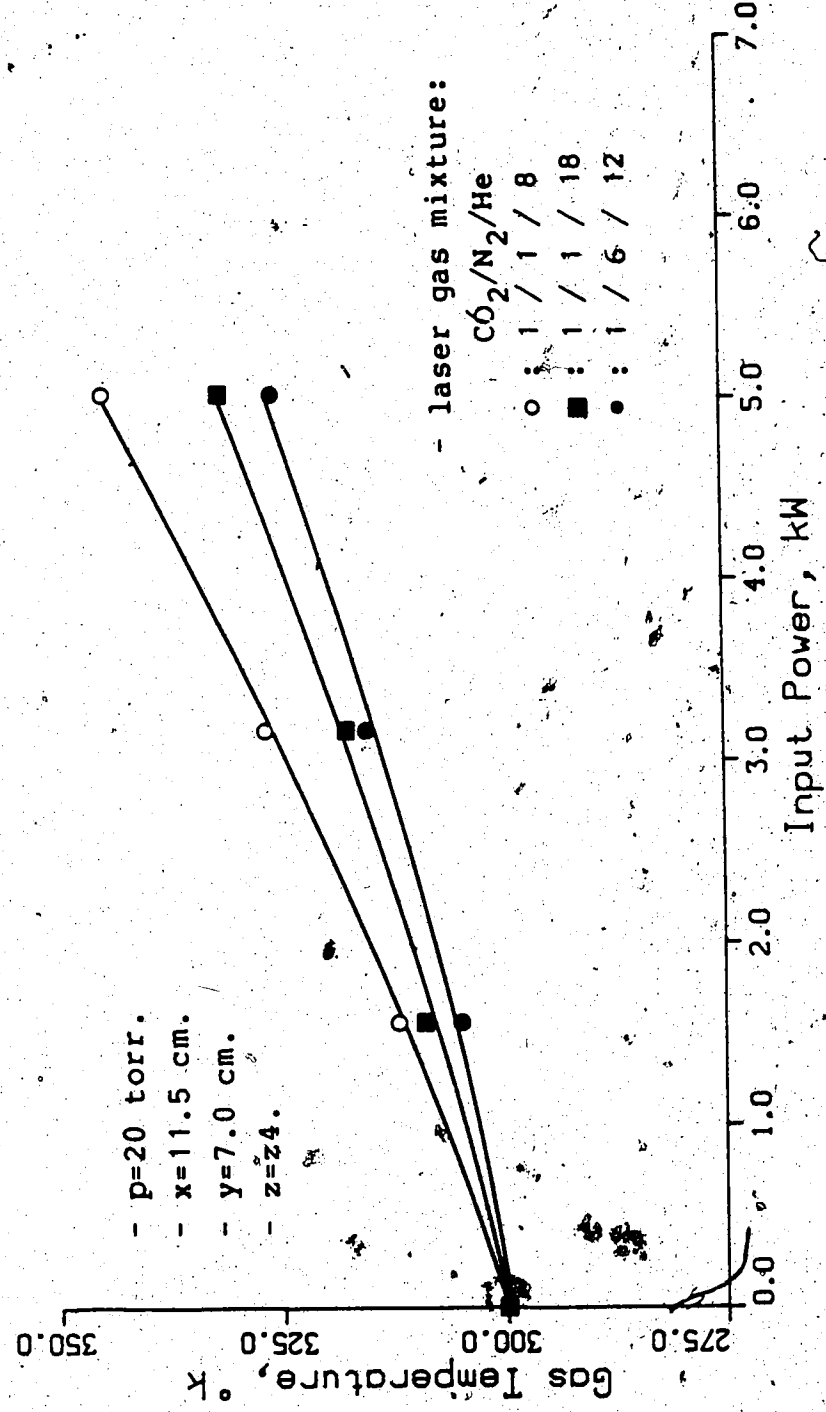


Fig. 7.47 Gas temperature dependence on input power for different laser gas mixtures.

temperature is an exponentially varying function in the input power.

The temperature profiles were measured at two locations downstream of the cathode for different input power values. The laser gas mixture was $\text{CO}_2/\text{N}_2/\text{He}$ in the proportion 1:6:12, at a total pressure of 20 torr. The profile measurements were taken across the channel height (along the y-axis) at $z=z_4$. Figure 7.48 shows the temperature profiles at $x=16.5$ cm downstream of the cathode, while Fig. 7.49 illustrates the temperature profiles at $x=31.5$ cm downstream. It can be seen from these figures that by increasing the input power, the gas temperature increases. This increase in temperature with the input power has an exponential nature as was discussed earlier.

At the far point downstream ($x=31.5$ cm), the profiles show a decrease in temperature particularly in the mid section (stagnation region II), while at the outer regions I and III the temperature shows a little increase. This is an indication of a convective heat transfer occurring in the discharge region. For this reason, investigation of the temperature profiles along the flow direction will be conducted in more detail in the next subsection.

Temperature Profiles : Input Power
at $X=16.5$ cm

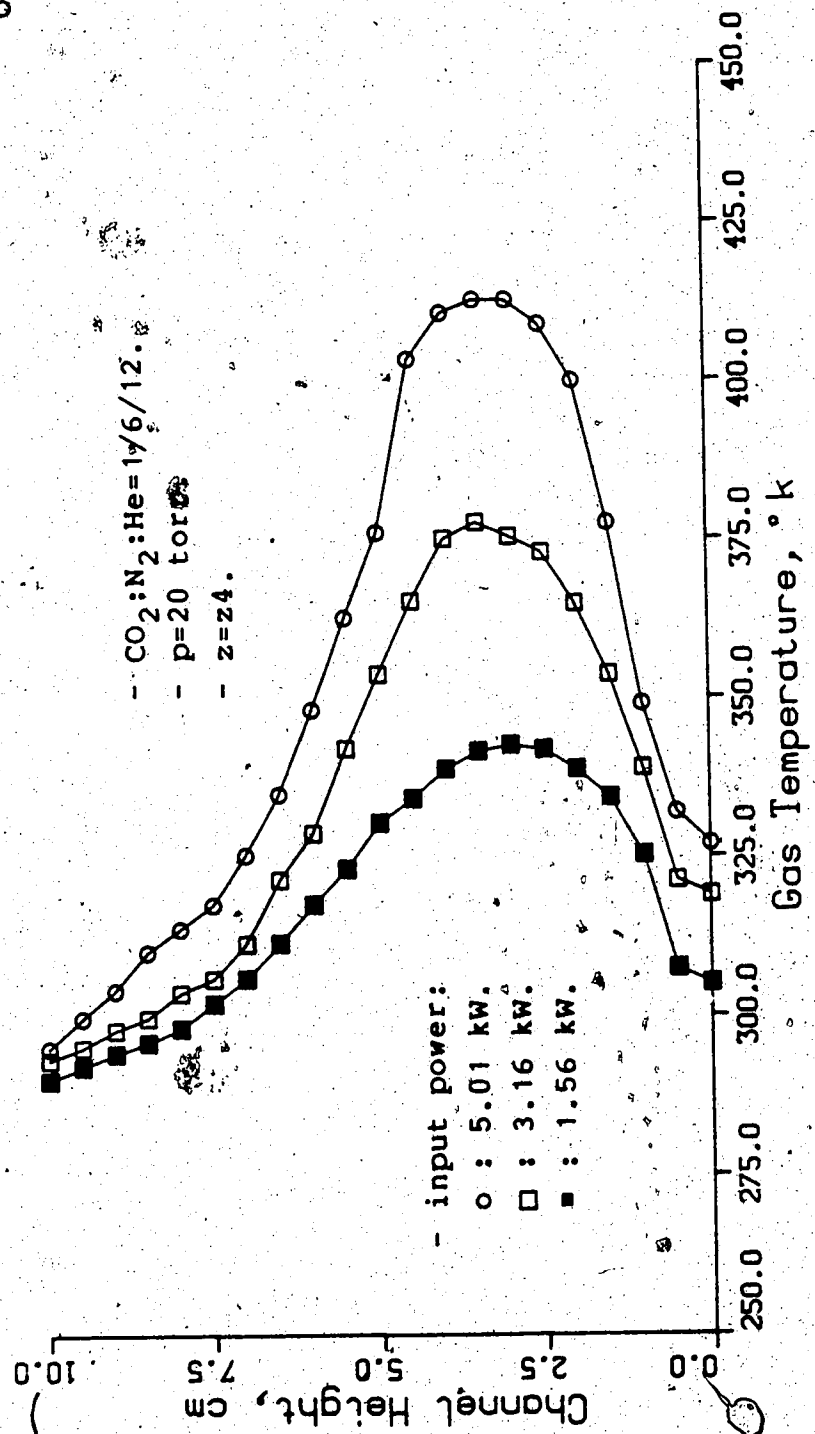


Fig. 7.48. Temperature profile dependence on input power at $x=16.5$ cm and $z=z_4$.

Temperature Profiles : Input Power
at $X=34.5$ cm

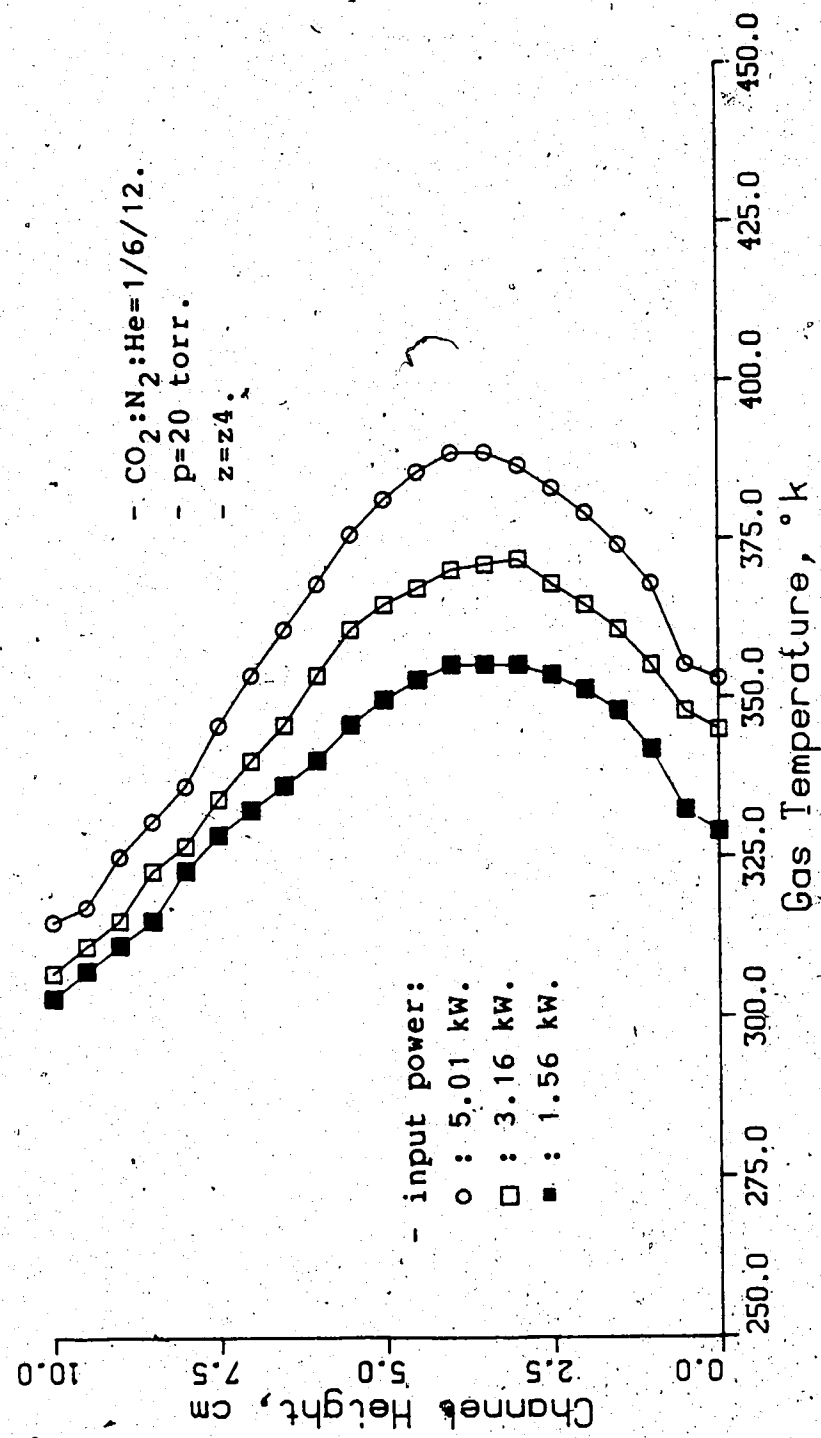


Fig. 7.49 Temperature profile dependence on input power at $x=34.5$ cm and $z=z_4$.

B. TEMPERATURE PROFILES ALONG THE DIRECTION OF FLOW AND ALONG THE DISCHARGE LENGTH

Figure 7.50 shows the temperature profiles at five different locations downstream of the cathode along the direction of flow. The measurements were taken across the channel (along the y -axis) at $z=z_4$. The input power was fixed at 5.01 kW. The laser gas mixture used contained $\text{CO}_2/\text{N}_2/\text{He}$ in the proportion 1:6:12 at a total pressure $p=20$ torr. It is clear from Fig. 7.50 that, as the flow advances downstream, the temperature in the hot region II decreases considerably. While in regions I and III the temperature actually increases. This means that convective heat transfer is really occurring, and the heat is transported downstream away from the discharge region. This convective cooling is very important in our device, since it is the best way to dispose the excess heat from the discharge region [6,7,9].

Finally, the temperature profiles were obtained at different locations along the discharge length (z -axis). The locations of measurement points z_1 , z_2 , z_3 and z_4 were illustrated in Fig. 3.6. Figures 7.51 and 7.52 show the temperature profiles at z_1 and z_4 respectively. The temperature reaches its maximum values at the stagnation region (the mid section) and decreases towards the anodes. Figure 7.53 show the temperature profiles at z_2 for different input power values. Again, the temperature increases exponentially with the increase in the input power.

Temperature Profiles : Axial Distance X

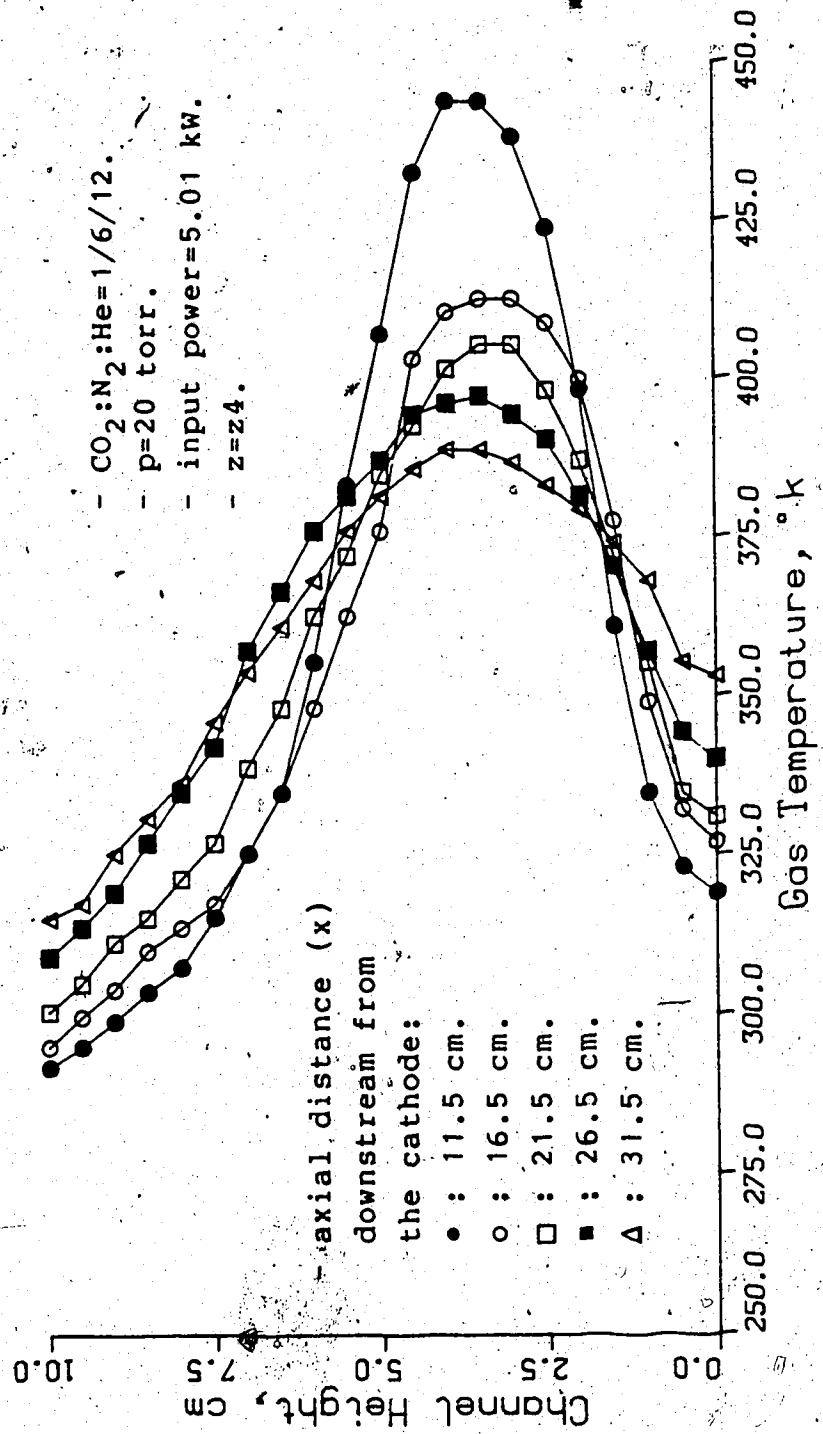


Fig. 7.50 Temperature profiles along the direction of flow (x) at $z=z4$.

Temperature Profile, $Z=z_1$

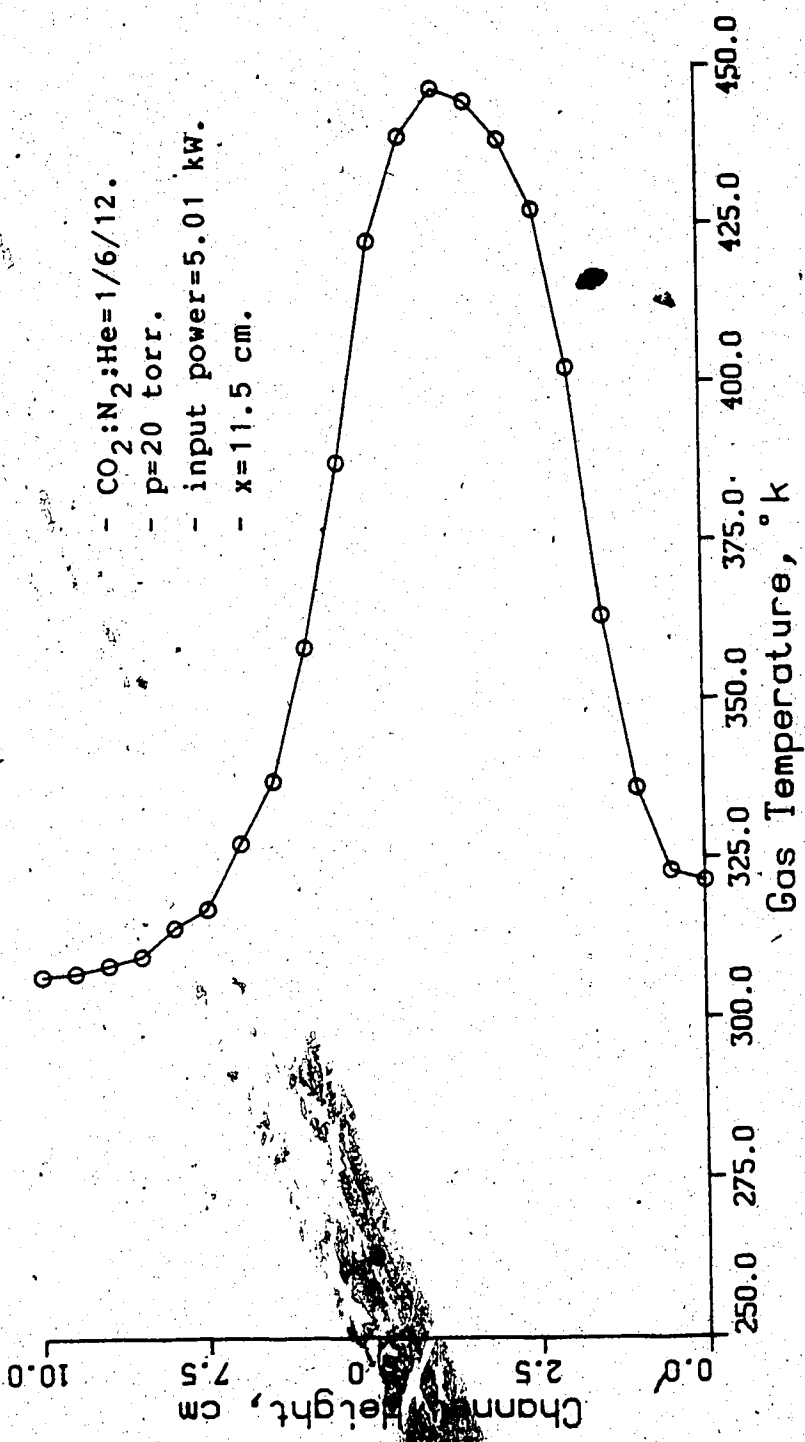


Fig. 7.51 Temperature profile at $z=z_1$ for input power of 5.01 kW.

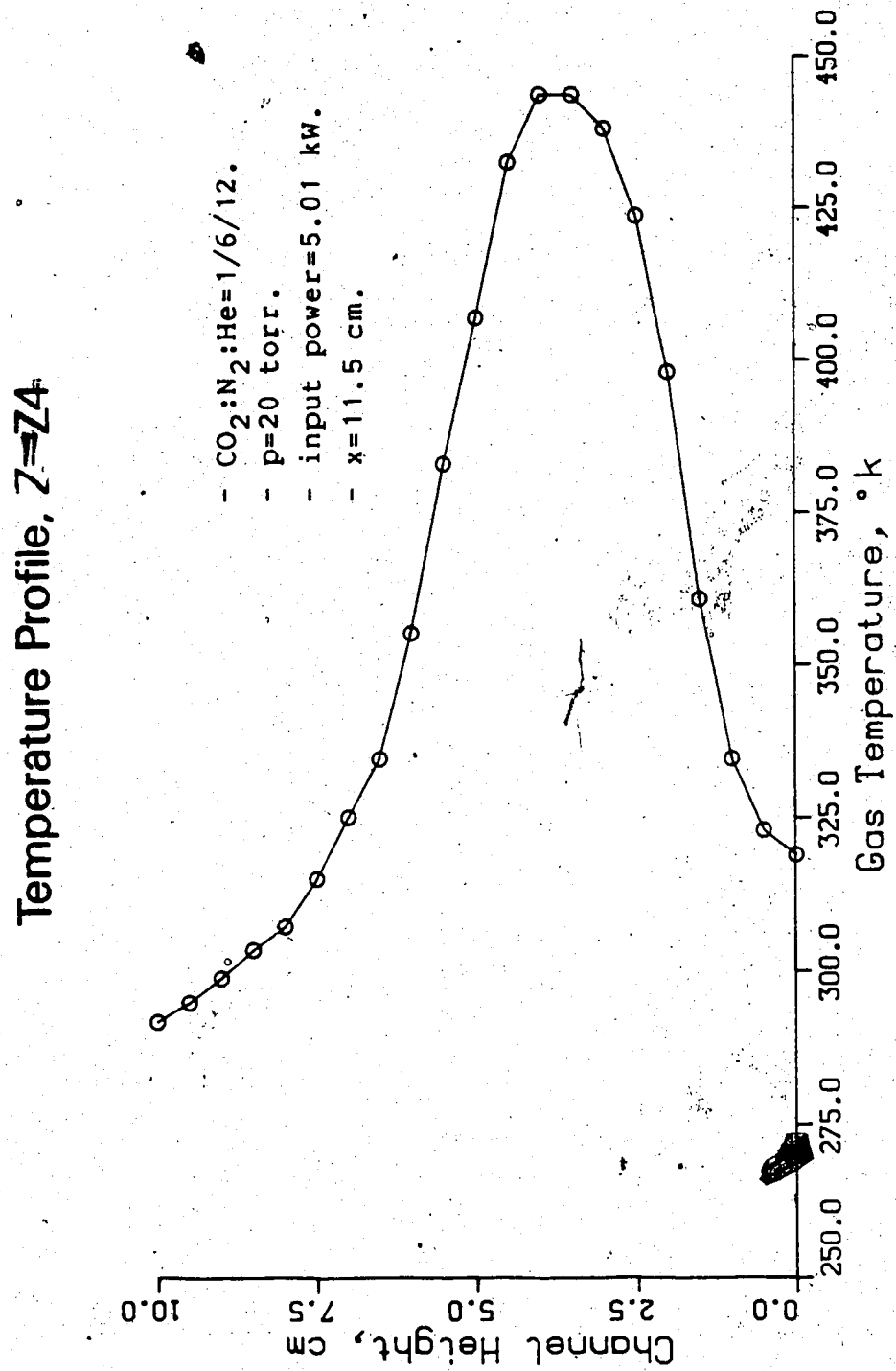


Fig. 7.52 Temperature profile at $z=z_4$ for input power of 5.01 kW.

Temperature Profiles : Input Power
at $Z=Z_2$

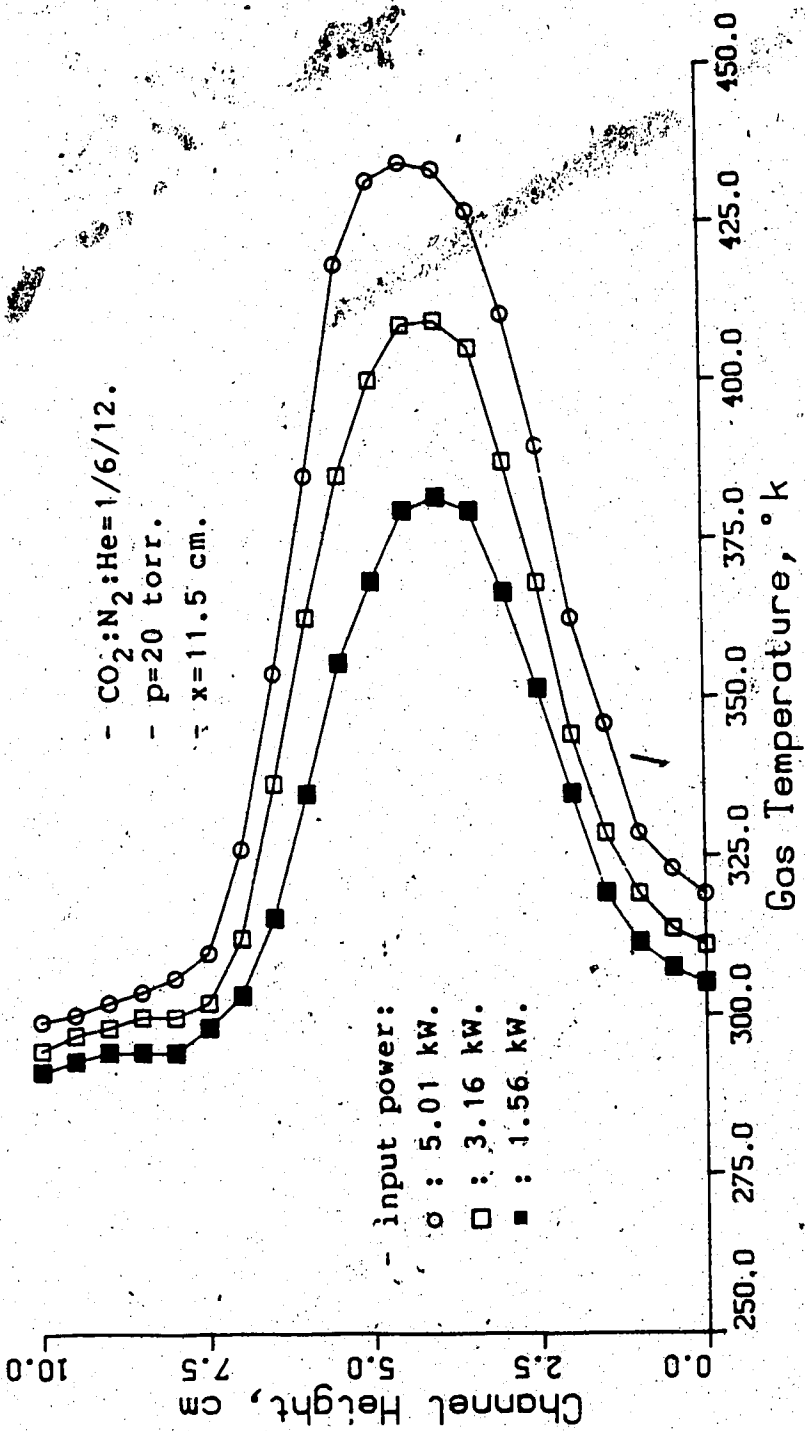


Fig. 7.53 Temperature profile dependence on the input power
at $z=z_2$.

as can be seen from Fig. 7.54. Similar results were obtained at z_3 and are shown in Figs. 7.55 and 7.56.

From these results, it can be concluded that the temperature behavior is identical along the length of the discharge which is relatively long (135 cm). It may be noted also that the temperature in the mid section (at z_2 and z_3) is lower than that at the edges (at z_1 and z_4). This is because of the stronger convective cooling in the mid region of the discharge length, where the gas velocity exceeds 40 m/sec. Figure 7.57 shows the maximum and minimum temperature distribution along the discharge length (in the z -direction). This was obtained at $x=11.5$ cm for 5.01 kW input power. The temperature is relatively low in the mid section and higher at the edges as can be seen in this figure.

7.4 COMPARISON OF EXPERIMENTAL AND SIMULATION RESULTS

In this section, the experimental results obtained for the TE CW CO₂ laser gas discharge system will be compared to the simulation results obtained from the IGCP code. It was mentioned earlier that matching the input power, cathode temperature, mass flow rate, gas composition, dimensions of the discharge region, and gas viscosity fulfil the requirements to match the simulation results to the experimental one. In this comparison, a sample of the experimental and simulation results will be presented,

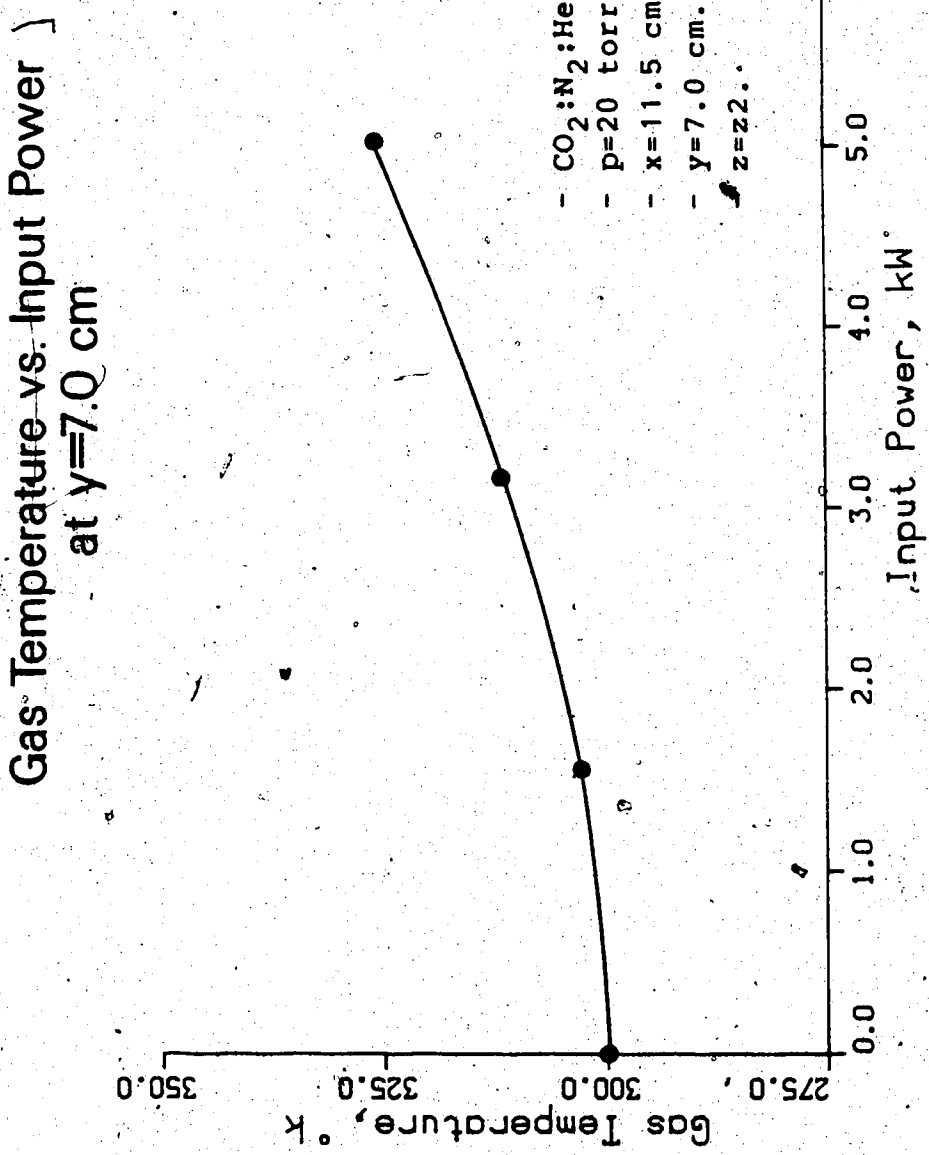


Fig. 7.54 Gas temperature dependence on the input power at $z=z_2$ and $y=7.0$ cm.

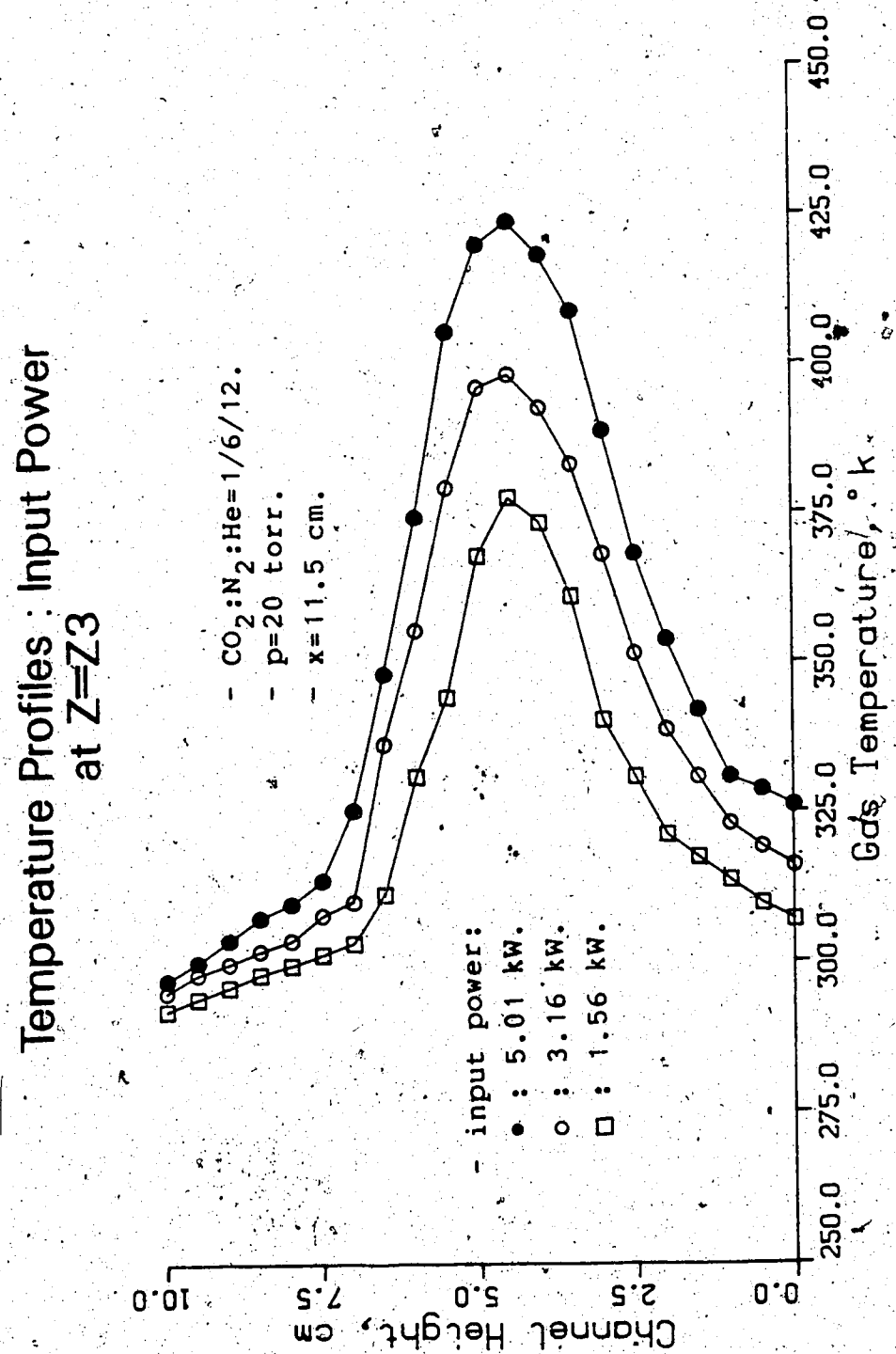


Fig. 7.55 Temperature profile dependence on the input power
at z=z3.

Gas Temperature : Input Power
at $y=7.0$ cm

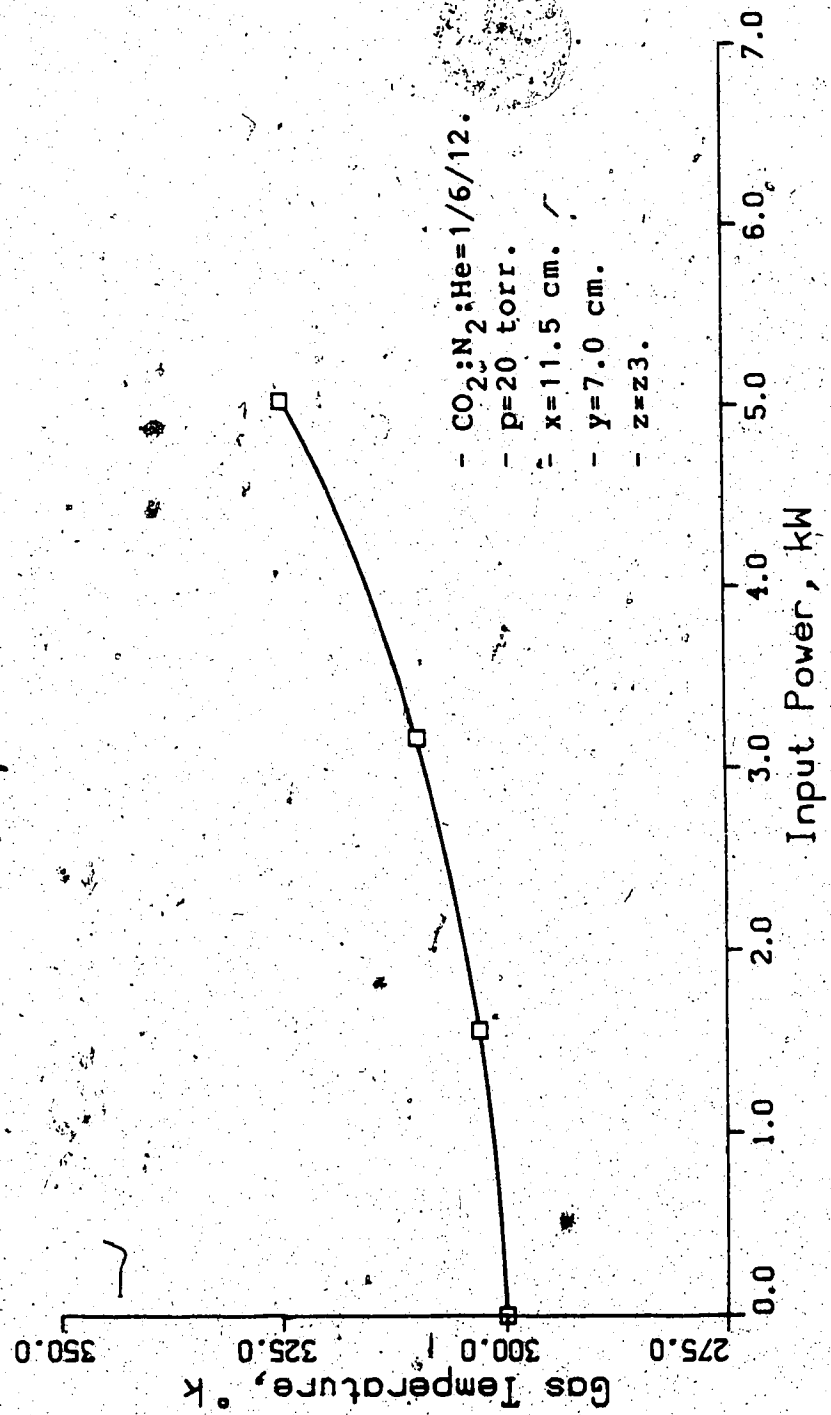


Fig. 7.56 Gas temperature dependence on the input power at $z=z_3$ and $y=7.0$ cm.

**Maximum and Minimum Temperatures
along the Discharge Length**

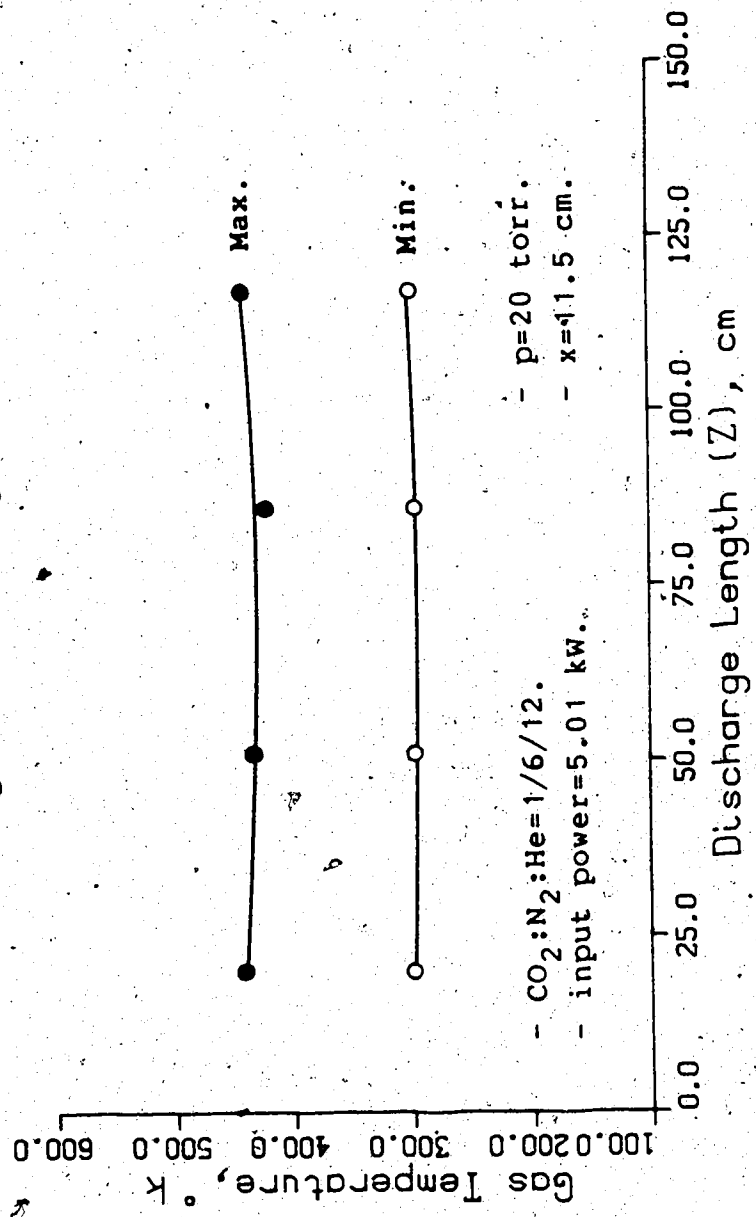


Fig. 7.57 Maximum and minimum temperatures along the z-axis,
at $x=11.5 \text{ cm}$.

particularly the gas flow velocity and the gas temperature.

Figure 7.58 illustrates the gas velocity profiles obtained from both the experimental measurements and the simulations. The experimental profile was measured at 11.5 cm downstream from the cathode surface and across the y-direction. During the measurements, a laser gas mixture of $\text{CO}_2/\text{N}_2/\text{He}$ in the proportion 1:6:12 and at a total pressure of 20 torr was used. The input power used in this case was set to 5.01 kW which corresponds to an estimated cathode temperature of 600 °k. The simulation profile was predicted at the same distance (x) downstream from the cathode and for the same conditions as mentioned above. As can be seen from Fig. 7.58, the experimental and simulation results are in good agreement.

Figure 7.59 shows a comparison between the gas temperature distributions obtained from both the experimental measurements and the computer simulations. The temperature measurements and simulations were made or predicted at the same location downstream from the cathode and for the same conditions as indicated above. From this figure we can see that the profile obtained from measurements agree well with that obtained from simulation. It may be noted that the temperature values obtained from simulations are slightly higher than the measured values - this is probably due to the overestimated cathode temperature (600 °k in this case). The temperature was

**Computed and Measured Velocity Profiles
Input Power=5.01 kW**

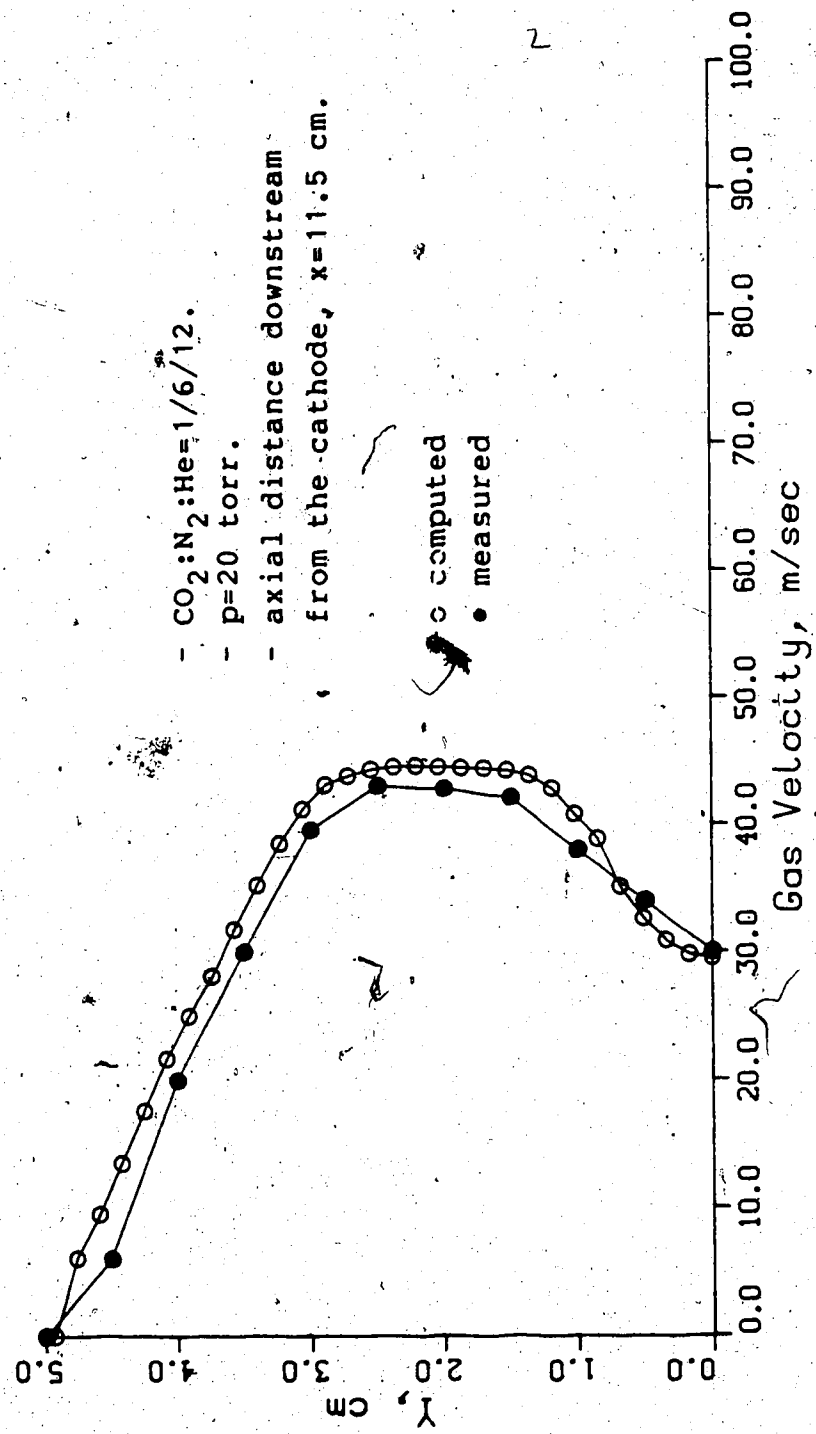


Fig. 7.58 Comparison of computed and measured velocity profiles for the TE CW CO_2 laser.

**Computed and Measured Gas Temperature Profiles
Input Power=5.01 kW**

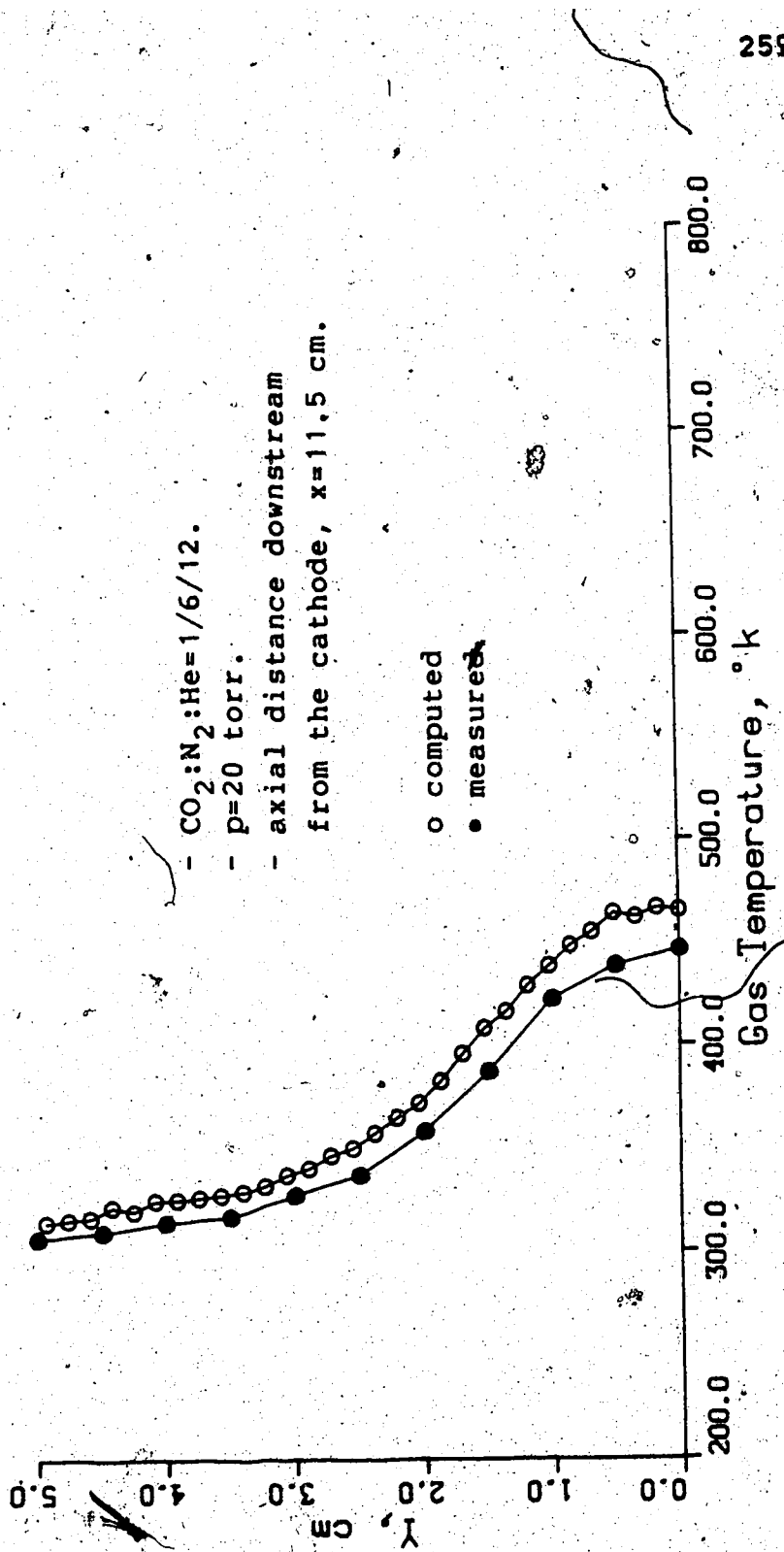


Fig. 7.59 Comparison of computed and measured gas temperature profiles for the TE CW CO₂ laser.

measured very close to the cathode ($x=2.5$ cm) at 551°k , therefore a 600°k cathode temperature was estimated. The actual value may be lower than 600°k . In any case, the results appear to match and good agreement between experimental and simulation results is obvious.

In conclusion, this chapter presents the results of the computer simulation and experimental measurements for the TE CW CO₂ laser gas discharge system. In the simulations, a flow separation phenomenon was observed from the velocity vector distributions. This was confirmed by predicted velocity profiles near the cathode. The results of gas velocity, pressure and temperature behavior in the discharge region indicate the essence of convective mass and heat transport in an open channel flow system.

In the experimental measurements, the flow velocity profiles indicated the effect of a stagnation region (due to the cathode) on the flow structure along the flow direction. Also, when increasing the input power to a large value, the measured velocity on the x-axis near the cathode indicates a sudden drop, which is believed to be due to the formation of swirls behind the cathode.

The behavior of the velocity profiles and gas temperature along the flow direction, indicate that mass and heat convection take place in our device. Consequently, discharge heat is transported out of the discharge region via convective cooling, which is important in our laser

system.

The experimental measurements and computer simulation results validate and support each other in measuring and predicting the effect of cathode (obstacle) on the flow structure in our device. Also, both results validate each other in evaluating the heat transport in our open channel flow system.

In the next chapter, a final conclusion of the research work presented in this thesis will be reported. A recommendation for future research will be presented as well.

CHAPTER 8

CONCLUDING REMARKS

8.1 CONCLUSIONS

The main objective of this thesis has been to advance the understanding of the behavior of open channel flow laser gas discharges. The flow structure and heat flow in a TE CW CO₂ laser gas discharge system has been studied in detail, both theoretically and experimentally, in order to advance the state-of-the-art for these devices.

In chapter 1, a review of CO₂ lasers and the associated problems, including the different kinds of instabilities which usually occur in these lasers, was presented. In chapter 2, some of the efforts which have been made to enhance the understanding of the basic discharge processes and to stabilize the glow discharge in high power CO₂ lasers were reviewed.

A detailed description of the TE CW CO₂ laser gas discharge system constructed for this thesis is presented in chapter 3. A system employing a Mo spiral wire cathode and graphite anodes has been built and successfully operated. A stable glow discharge was obtained in this system under self-sustained conditions.

In chapters 4 and 5, the development of computer code IGCP is described. This computer program provides a detailed simulation of the transient and steady state flows in an open channel laser gas discharge. The time-dependent Navier-Stokes equations were solved numerically in two-dimensional cartesian coordinates. These included the equations of conservation of mass, momentum and energy. The algorithm used is based upon an iterative, alternating direction implicit (ADI) temporal advancement technique.

By using a single-fluid gasdynamic model, the IGCP code was able to predict the flow pattern and heat transport in an open channel flow laser gas discharge system. The numerical results were presented in chapters 6 and 7. The flow separation phenomenon was observed downstream of the cathode (obstacle). This is in good agreement with previous results of fluid flow over an obstacle, which have been obtained by previous authors [109, 134, 148-151].

The addition of the energy equation to our computer code was of great importance, since it allowed us to predict the gas temperature within the discharge region. For the particular structure of the discharge section in our device, the prediction of gas temperature and velocity profiles downstream of the cathode emphasized the process of convective cooling in this system.

The experimental results which are presented in chapters 6 and 7 are intended to validate the computer

algorithm. The velocity profile measurements also, indicate that the placement of the cathode in the middle of the channel creates a stagnation point downstream. The gas velocity is reduced to its minimum value in this region. A maximum velocity occurs in the mid regions between the centerline of the cathode and the anodes.

It was also found that the effect of the stagnation point on the gas velocity decreases as the flow advances downstream. In this case, the velocity profile tends to flatten as the flow proceeds downstream, where the stagnation point effect is minimal. This result is in good agreement with the computer simulation results, and also in good agreement with the measurements of Kovasznay [143] who investigated the flow around a circular cylinder.

A further effect of the stagnation point caused by the cathode, is a reduction in the gas velocity to about 50% of its maximum value at a distance of 7.5 cm downstream from the cathode. It may be noted that regardless of the effect of this stagnation region, increasing the input power to the discharge results in an overall increase in the gas velocity by about 17%. These results are in good agreement with our computer simulation results.

An interesting result was obtained when the gas velocity was measured along the horizontal axis (which passes through the cathode centerline) downstream from the cathode surface. Increasing the input power to the discharge

causes an increase in the gas velocity along the axis. However, when increasing the input power to a high value (5.01 kW) a similar behavior was observed except at the point close to the cathode ($x=2.5$ cm). At this point the gas velocity dropped even below the isothermal value (where the input power = 0.0 kW). This is an interesting result which may be explained as due to the formation of swirls or wakes downstream of the cathode. Fortunately, this explanation is supported by our computer simulation results, as is evident by the velocity vector distribution. This velocity distribution indicates that a flow separation occurred downstream of the cathode.

The dependence of the measured gas temperature on gas pressure, gas mixture and input power was also investigated. For all these parameters, it was found that the gas temperature is an exponentially varying function with the input power. It was also found that the gas temperature reaches a maximum in the stagnation region of the cathode. However, it decreases in the region between the cathode and the anode, where a maximum flow exists and consequently convective cooling is stronger. These results are in good agreement with our computer simulation results.

The temperature profile measurements, particularly along the direction of flow, indicates that convective heat transfer is really occurring, and the heat is transported downstream away from the discharge region. This convective

cooling is very important in our device, since it is the best way to dispose of the excess heat from the discharge region [6,7,9].

8.2 FUTURE CONSIDERATIONS

The experimental measurements outlined in this thesis proved valuable in exploring the flow structure and heat transport in the TE CW CO₂ laser gas discharge system. However, further experimental work is required to investigate in more detail the phenomenon of flow separation downstream of the cathode (obstacle). The placement of the cathode in the middle of the discharge channel formed a stagnation region downstream of the cathode. This reduces the flow velocity and causes the temperature to rise in this region, which in turn affects the convective cooling process.

The sudden decrease in axial gas velocity (measured very close to the cathode) when increasing the input power suggested the formation of swirls or wakes downstream of the cathode. The exact role of swirl formation and its relation to the input power is not well known. Further investigation, which may include different high input power levels and various gas flow velocities above 40 m/sec, is needed.

The experimental study of the TE CW CO₂ laser gas discharge system can be extended further by introducing a

turbulence source (grid or baffles) just upstream of the discharge section. The combination of turbulent flow (produced by the turbulence source) and the swirls or wakes (caused probably by the presence of the cathode in the middle of the channel) form an interesting problem to investigate. This would be beneficial for understanding the role of turbulence in enhancing the convective cooling and discharge stabilization in this system.

Finally, the IGCP computer code proved a very useful tool to predict the gas flow structure and heat transport in the discharge region of the TE CW CO₂ laser gas discharge system. This code can be modified to handle a variety of discharge configurations. Thus the behavior of gas laser systems with complicated electrode structures are now amenable to a numerical simulation.

REFERENCES

- [1] C.K.N. Patel, "Interpretation of CO₂ optical maser experiments", Phys. Rev. Lett., Vol. 12, No. 21, pp. 588-590 (1964).
- [2] C.K.N. Patel, "Continuous-wave laser action on vibrational-rotational transitions of CO₂", Phys. Rev., Vol. 136, No. 5A, pp. A1187-A1193 (1964).
- [3] C.K.N. Patel, "Selective excitation through vibrational energy transfer and optical maser action in N₂-CO₂", Phys. Rev. Lett., Vol. 13, No. 21, pp. 617-619 (1964).
- [4] G. Moeller and J. Dane Rigden, "High-power laser action in CO₂-He mixtures", Appl. Phys. Lett., Vol. 7, No. 10, pp. 274-279 (1965).
- [5] C.K.N. Patel, P.k. Tien, and J.H. McFee, "CW High-power CO₂-N₂-He laser", Appl. Phys. Lett., Vol. 7, No. 11, pp. 290-292 (1965).
- [6] T.F. Deutsh, F.A. Harrigan, and R.I. Rudko, "CW Operation of High-Pressure Flowing CO₂ Lasers", Appl. Phys. Lett., Vol. 15, p. 88 (1969).
- [7] W.B. Tiffany, R. Tang, and J.D. Foster, "Kilowatt CO₂ Gas-Transport Laser", Appl. Phys. Lett., Vol. 15, p. 91 (1969).

- [8] R. Targ and W.B. Tiffany, "Gain and saturation in transverse flowing $\text{CO}_2\text{-N}_2\text{-He}$ mixtures", *Appl. Phys. Lett.*, Vol. 15, No. 9, pp. 302-304 (1969).
- [9] A.E. Hill, "Uniform Electrical Excitation of Large-Volume High-Pressure Near-Sonic $\text{CO}_2\text{-N}_2\text{-He}$ Flow System", *Appl. Phys. Lett.*, Vol. 18, p. 194 (1971).
- [10] P.A. Miles and J.W. Lotus, "A high-power CO_2 laser radar transmitter", *IEEE J. Quantum Electron.*, Vol. QE-4, p. 811 (1968).
- [11] H. Seguin and J. Tulip, "Photoinitiated and photosustained lasers", *Appl. Phys. Lett.*, Vol. 21, p. 414 (1972).
- [12] C.A. Fenstermacher, M.J. Nutter, W.T. Leland, and K. Boyer, "Electron-beam-controlled electrical discharge as a method of pumping large volumes of CO_2 laser media at high pressure", *Appl. Phys. Lett.*, Vol. 20, No. 2, p. 56 (1972).
- [13] L. Pekarek, "Ionization waves (striations) in a discharge plasma", *Sov. Phys. USP*, Vol. 11, No. 2, p. 188 (1968).
- [14] G. Ecker, W. Kröll, and O. Zöller, "Thermal instability of the plasma column", *Phys. Fluids*, Vol. 7, No. 12, p. 2001 (1964).

- [15] A. Garscadden and D.A. Lee, "Forward and backward-wave moving striations in the constricted discharge", Int. J. Electron., Vol. 20, No. 6, p. 567 (1966).
- [16] K.W. Gentle, "Moving striations in the argon positive column. I. Theory", Phys. Fluids, Vol. 9, No. 11, p. 2203 (1966).
- [17] W.L. Nighan, W.J. Weigand, and R.A. Haas, "Ionization Instability in CO₂ Laser Discharges", Appl. Phys. Lett., Vol. 22, No. 11, p. 579 (1973).
- [18] D.H. Douglas-Hamilton and S.A. Mani, "An electron attachment plasma instability", Appl. Phys. Lett., Vol. 23, No. 9, p. 508 (1973).
- [19] D.H. Douglas-Hamilton and S.A. Mani, "Attachment instability in an externally ionized discharge", J. Appl. Phys., Vol. 45, No. 10, p. 4456 (1974).
- [20] A.F. Vitshes and K.N. UI'yanov, "Ionizational instability of a non-self-maintained glow discharge in a molecular gas", Sov. Phys. Tech. Phys., Vol. 21, No. 4, p. 523 (1976).
- [21] A.T. Rakhimov and F.R. Ulinich, "Contraction of a cylindrical gas discharge", Sov. Phys. Dokl., Vol. 14, No. 7, p. 655 (1970).
- [22] J.H. Jacob and S.A. Mani, "Thermal instability in

- high-power laser "discharges", *Appl. Phys. Lett.*, Vol. 26, No. 2, p. 53 (1975).
- [23] E.F. Jaeger, L. Öster, and A.V. Phelps, "Growth of thermal constrictions in a weakly ionized gas discharge in helium", *Phys. Fluids*, Vol. 19, No. 6, p. 819 (1976).

- [24] A.V. Eletskii and V.A. Kutvitskii, "A thermal instability in a glow discharge in a molecular gas", *Sov. J. Plasma Phys.*, Vol. 3, No. 4, p. 496 (1977).

- [25] A.V. Bondarenko, V.S. Golubev, E.V. Dan'shchikov, F.V. Lebedev, and A.V. Ryazanov, "Thermal Instability of a self-sustained gas discharge", *Sov. J. Plasma Phys.*, Vol. 5, No. 2, p. 237 (1979).

- [26] G.G. Gladyshev and A.A. Samokhin, "Thermal discharge contraction in a fast-flow CO₂ laser", *Sov. J. Plasma Phys.*, Vol. 5, No. 3, p. 384 (1979).

- [27] W.L. Nighan and W.J. Wiegand, "Influence of negative-ion processes on steady-state properties and striations in molecular gas discharges", *Phys. Rev. A*, Vol. 10, No. 3, p. 922 (1974).

- [28] V.N. Oraevskii, O.I. Fisun, and E.I. Yurchenko, "Instability of dissociative attachment of a molecular-gas plasma", *Sov. J. Plasma Phys.*, Vol. 1, No. 5, p. 446 (1975).

- [29] G.D. Myl'nikov and A.P. Napartovich, "Domain instability of a glow discharge", Sov. J. Plasma Phys., Vol. 1, No. 6, p. 486 (1975).
- [30] Yu. S. Akishev, A.P. Napartovich, and S.V. Pashkin, "Attachment instability in a glow discharge in flowing air", Sov. J. Plasma Phys., Vol. 4, No. 1, p. 86 (1978).
- [31] I.I. Galaktionov and V.A. Pivovar, "Effect of negative ions on a CO₂ discharge", Sov. Phys. Tech. Phys., Vol. 24, No. 2, p. 165 (1979).
- [32] N.L. Aleksandrov, "Three-body electron attachment to O₂ in a discharge in a CO₂-N₂-He-O₂ mixture", Sov. Phys. Tech. Phys., Vol. 24, No. 8, p. 917 (1979).
- [33] W.L. Nighan, "Causes of thermal instability in externally sustained molecular discharges", Phys. Rev. A., Vol. 15, No. 4, p. 1701 (1977).
- [34] K.N. Ul'yanov and L.P. Menakhin, "Current instability in a gas at medium pressures", Sov. Phys. Tech. Phys., Vol. 16, No. 12, p. 2020 (1972).
- [35] R.A. Haas, "plasma stability of electric discharges in molecular gases", Phys. Rev. A, Vol. 8, No. 2, p. 1017 (1973).

- [36] W.L. Nighan and W.J. Wiegand, "Causes of arcing in CW CO₂ convection laser discharges", *Appl. Phys. Lett.*, Vol. 25, No. 11, p. 633 (1974).
- [37] A.V. Eletskii and B.M. Smirnov, "Contraction of the positive column of a glow discharge", *Sov. Phys. Tech. Phys.*, Vol. 15, No. 8, p. 1308 (1971).
- [38] A.V. Eletskii and A.N. Starostin, "Thermal instability of the nonequilibrium state of a molecular gas", *Sov. J. Plasma Phys.*, Vol. 1, No. 4, p. 377 (1975).
- [39] A.V. Eletskii and A.N. Starostin, "Contraction of discharges in molecular gases", *Sov. J. Plasma Phys.*, Vol. 2, No. 5, p. 466 (1976).
- [40] A.M. Soroka and G.I. Shapiro, "Ionization-thermal instability in a glow-discharge plasma", *Sov. J. Plasma Phys.*, Vol. 1, No. 6, p. 479 (1975).
- [41] W.L. Nighan, "Progress in high pressure electric lasers", Invited paper, Eleventh International Conference on Phenomena in Ionized Gases, Prague, Czechoslovakia, Sept. 10-14 (1973).
- [42] W.J. Wiegand and W.L. Nighan, "plasma chemistry of CO₂-N₂-He discharges", *Appl. Phys. Lett.*, Vol. 22, No. 11, p. 583 (1973).
- [43] W.L. Nighan, "Electron energy distribution and

- collision rates in electrically excited N₂, CO and CO₂", Phys. Rev. A, Vol. 2, No. 5, p. 1989 (1970).
- [44] W.J. Wiegand, M.C. Fowler, and J.A. Benda, "Influence of discharge properties on CO₂ laser gain", Appl. Phys. Lett., Vol. 18, No. 9, p. 365 (1971).
- [45] K.N. Ul'yanov, "Contraction of the positive column by dissociative recombination", Sov. Phys. Tech. Phys., Vol. 18, No. 3, p. 360 (1973).
- [46] A.M. Orishich, A.G. Ponomarenko, and R.I. Soloukhin, "Power characteristics and stability of a double transverse discharge", Sov. Phys. Dokl., Vol. 18, No. 10, p. 671 (1974).
- [47] W.P. Allis, "Review of glow discharge instabilities", Proc. of the Twelfth International Conference on Phenomena in Ionized Gases, Eindhoven, The Netherlands, August 18-22 (1975).
- [48] A.J.T. Holmes, "The glow-discharge-to-arc transition instability", J. Phys. D : Appl. Phys., Vol. 8, p. 690 (1975).
- [49] V. Yu. Zaleskii, "Homogeneity of an infinite glow discharge in a dense gas", Sov. Phys. Tech. Phys., Vol. 21, No. 8, p. 960 (1976).
- [50] E.H. Velikhov, S.A. Golubev, Yu. K. Zemtsov, A.F.

- Pal', I.G. Persiantsev, V.D. Pis'mennyi, and A.T. Rakhimov, "Non-self-sustaining stationary gas discharge induced by electron-beam ionization in N_2 -CO₂ mixtures at atmospheric pressure", Sov. Phys. JETP, Vol. 38, No. 2, p. 267 (1974).
- [51] R.K. Garnsworthy, L.E.S. MatRias, and C.H.H. Carmichael, "Atmospheric-pressure pulsed CO₂ laser utilizing preionization by high-energy electrons", Appl. Phys. Lett., Vol. 19, No. 12, p. 506 (1971).
- [52] E.P. Velikhov, I.V. Novobrantsev, V.D. Pis'mennyi, A.T. Rakhimov, and A.N. Starostin, "Combined pumping of gas lasers", Sov. Phys. Dokl., Vol. 17, No. 8, p. 772 (1973).
- [53] E.P. Velikhov, S.D. Pis'mennyi, A.T. Rakhimov, and T.V. Rakhimova, "Steady-state nonself-sustained gas discharge in high-pressure molecular mixtures", Sov. J. Plasma Phys., Vol. 1, No. 5, p. 463 (1975).
- [54] A.P. Napartovich and A.N. Starostin, "Stability of a glow discharge with external ionization", Sov. J. Plasma Phys., Vol. 2, No. 5, p. 469 (1976).
- [55] O.P. Judd, "An Efficient Electrical CO₂ Laser Using Preionization by Ultraviolet Radiation", Appl. Phys. Lett., Vol. 22, No. 3, p. 95 (1973).
- [56] L.E. Kline and L.J. Denes, "Investigation of glow

- discharge formation with volume preionization", J. Appl. Phys., Vol. 46, No. 4, p. 1567 (1975).
- [57] Y. Sakai, M. Takahashi, S. Sakamoto, and H. Tagashira, "CO₂ TEA laser discharge development - A high-speed-camera investigation"; J. Appl. Phys., Vol. 50, No. 2, p. 647 (1979).
- [58] A.C. Eckbreth and P.R. Blaszuk, "Closed-cycle CO₂ laser discharge investigations", AIAA 5th Fluid and Plasma Dynamics Conference, Boston, Massachusetts, June 26-28 (1972).
- [59] A.C. Eckbreth and J.W. Davis, "RF augmentation in CO₂ closed-cycle dc electric-discharge convection lasers", J. Appl. Phys. Lett., Vol. 21, No. 1, p. 25 (1972).
- [60] B.V. Kuteev, A.S. Smirnov, and A.P. Zhilinsky, "Application of r.f. discharge with rotating electric field for excitation of CO₂-laser", 14th International Conference on Phenomena in Ionized Gases, July (1979).
- [61] R. Mcheary, P.J. Beckwith, and W.E.K. Gibbs, "Uniform continuous discharges and CO₂-laser action at atmospheric pressure by plasma injection", IEEE J. Quantum Electron., Vol. QE-10, p. 649 (1974).
- [62] J.P. Reilly, "Pulser/sustainer electric-discharge laser", J. Appl. Phys., Vol. 43, No. 8, p. 3411 (1972).

- [63] Z. Bauman, F. Dothan, and S. Yatsiv, "Glow discharge stabilisation in a transverse flow CO₂ laser", J. Phys. E : Sci. Instrum., Vol. 11, p. 189 (1978).
- [64] K-H. Wu, "Operational characteristics of a TE CW CO₂ laser with a DC auxiliary discharge", IEEE J. Quantum Electron., Vol. QE-23, No. 11, p. 1981 (1987).
- [65] G.A. Garosi, G. Bekefi, and M. Schulz, "Anomalous diffusion and resistivity of a turbulent, weakly ionized plasma", Appl. Phys. Lett., Vol. 15, No. 10, p. 334 (1969).
- [66] G.A. Garosi, G. Bekefi, and M. Schulz, "Response of a weakly ionized plasma to turbulent gas flow", Phys. Fluids, Vol. 13, No. 11, p. 2795 (1970).
- [67] C.O. Brown and J.W. Davis, "Closed-cycle performance of a high-power electric-discharge laser", Appl. Phys. Lett., Vol. 21, No. 10, p. 480 (1972).
- [68] H. Shirahata and A. Fujisawa, "Aerodynamically mixed electric discharge CO₂ laser", Appl. Phys. Lett., Vol. 23, No. 2, p. 80 (1973).
- [69] O. Biblarz and R.E. Nelson, "Turbulence effects on an ambient pressure discharge", J. Appl. Phys., Vol. 45, No. 2, p. 80 (1974).
- [70] O. Biblarz, J.L. Barto, and H.A. Post, "Gas dynamic

effects on diffuse electrical discharges in air", Israel J. of Technology, Vol. 15, p. 59 (1977).

[71] J. Shwartz and Y. Lavie, "Effects of Turbulence on a Weakly Ionized Plasma Column", AIAA J., Vol. 13, No. 5, p. 647 (1975).

[72] J. Shwartz and E. Wasserstrom, "The role of gas flow and turbulence in electric discharge lasers", Israel J. of Technology, Vol. 13, p. 122 (1975).

[73] A.C. Eckbreth and J.W. Davis, "Cross-beam electric-discharge convection laser", Appl. Phys. Lett., Vol. 19, No. 4, p. 101 (1971).

[74] A.C. Eckbreth and F.S. Owen, "Flow conditioning in electric discharge convection lasers", Rev. Sci. Instrum., Vol. 43, No. 7, p. 995 (1972).

[75] W.J. Wiegand and W.B. Nighan, "Influence of fluid-dynamic phenomena on the occurrence of constriction in cw convection laser discharges", Appl. Phys. Lett., Vol. 26, No. 10, p. 554 (1975).

[76] E. Wasserstrom, Y. Crispin, J. Rom, and J. Shwartz, "The interaction between electrical discharges and gas flow", J. Appl. Phys., Vol. 49, No. 1, p. 81 (1978).

[77] V.I. Myshenkov and G.M. Makhviladze, "Suppression of the ionization instability in a glow discharge by

- turbulent transport", Sov. J. Plasma Phys., Vol. 4, No. 2, p. 231 (1978).
- [78] A.V. Bondarenko, V.S. Golubev, E.V. Dan'shchikov, E.V. Lebedev, and A.V. Ryazanov, "Effect of turbulence on the stability of a self-sustained discharge in an air flow", Sov. J. Plasma Phys., Vol. 5, No. 3, p. 386 (1979).
- [79] C.J. Buczak, R.J. Wayne, P. Chenausky, and R.J. Freiberg, "Magnetically stabilized cross-field CO₂ laser", Appl. Phys. Lett., Vol. 16, No. 8, p. 321 (1970).
- [80] C.J. Buczak, R.J. Freiberg, P.P. Chenausky, and R.J. Wayne, "Magnetic stabilization of the plasma column in flowing molecular lasers", Proc. IEEE, Vol. 59, No. 4, p. 659 (1971).
- [81] H.J.J. Seguin, C.E. Capjack, D. Antoniuk, and K.A. Nam, "High-power laser discharge stabilization with magnetic fields", Appl. Phys. Lett., Vol. 37, No. 2, p. 130 (1980).
- [82] C.E. Capjack, D.M. Antoniuk, and H.J.J. Seguin, "Dynamics of Magnetically Stabilized Laser Discharge", J. Appl. Phys., Vol. 52, No. 7, p. 4517 (1981).
- [83] H.J.J. Seguin, C.E. Capjack, D. Antoniuk, and V.A. Seguin, "A magnetically stabilized radial discharge for

- a high powered laser", Appl. Phys. Lett., Vol. 39, No. 3, p. 203 (1981).
- [84] V.A. Seguin, A MAGPIE Coaxial CO₂ Laser System, Ph.D. Thesis, University of Alberta 1986.
- [85] W. Zheen, S. Baorong, H. Shaoyi, C. Kexin, W. Donglai, X. Quanxin, C. Jinsi, Y. Zhijiang, and C. Zhaogu, "A 2.5-kW transverse-flow CO₂ laser", Beijing/Shanghai Proceedings of an International Conference on Lasers, May 1980, J.W.
- [86] M. Kasamatau, K. Tsukamoto, S. Shiratori, A. Obara, and F. Uchiyama, and M. Ikeda, "High-Power TE CO₂ laser with graphite electrodes", Conference on Lasers and Electrophysics, 10-12 June 1981, IEEE/OSA, Washington, D.C., Digest of Technical papers.
- [87] M. Kasamatau, K. Tsukamoto, S. Shiratori, A. Obara, and F. Uchiyama, "High-Power TE CO₂ laser with graphite electrodes", IEEE Journal of Quantum Electronics, Vol. QE-18, No. 2, February 1982.
- [88] A.J. DeMaria, "Review of CW High-Power CO₂ Lasers", Proc. IEEE, Vol. 61, No. 6, p. 731 (1973).
- [89] K.R. Manes and H.J. Seguin, "Analysis of the CO₂ TEA laser", J. Appl. Phys., Vol. 43, No. 12, p. 5073 (1972).

- [90] J. Tulip and H. Seguin, "Gas-dynamic CO₂ laser pumped by combination of hydrocarbons", *J. Appl. Phys.*, Vol. 42, No. 9, p. 3393 (1971).
- [91] M.J. Yoder, H.H. Legner, J.H. Jacob, and D.R. Ahouse, "Theoretical and experimental performance of a high-power cw electron-beam-sustained electric laser", *J. Appl. Phys.*, Vol. 49, No. 6, p. 3171 (1978).
- [92] E. Armandillo and A.S. Kaye, "Modelling of transverse-flow cw CO₂ lasers : theory and experiment", *J. Phys. D : Appl. Phys.*, Vol. 13, p. 321 (1980).
- [93] S. Martellucci, J. Quartieri, G. Mastrocicque, and S. Solimeno, "High-power electron beam preionized CO₂ CW laser modeling. I: Description of the investigated device and numerical calculations on e-beam ionization", *NUOVO CIMENTO*, Vol. 54B, No. 1, p. 99 (1979).
- [94] E. Botti, S. Martellucci, J. Quartieri, G.L. Braglia, and S. Solimeno, "High-power electron beam preionized CO₂ laser modelling. II. Analysis of plasma characteristics", *NUOVO CIMENTO*, Vol. 69B, No. 1, p. 47 (1982).
- [95] J. Quartieri, G. Mastrocicque, and R. Bruzzese, "High-power electron beam preionized CO₂ CW laser

- modelling. III. Kinetic and fluid-dynamic model", NUOVO CIMENTO, Vol. 78B, No. 1, p. 21 (1983).
- [96] T. Ngoc An, E. Marode, and P.C. Johnson, "Monte Carlo simulation of electrons within the cathode fall of a glow discharge in helium", J. Phys. D : Appl. Phys., Vol. 10, p. 2317 (1977).
- [97] R. Razdan, C.E. Capjack, and H.J.J. Seguin, "Influence of a Magnetic Field on the Growth of Instabilities in a Helium Glow Discharge Using Monte Carlo Simulation of the Cathode Fall Region", J. Appl. Phys., Vol. 57, No. 11, p. 4954 (1985).
- [98] R. Razdan, C.E. Capjack, and H.J.J. Seguin, "A Monte Carlo Simulation of the Cathode Fall Region of a CO₂ Laser Glow Discharge for Studying the Influence of Magnetic Fields on Instability Growth", Appl. Opt. (USA), Vol. 25, No. 17, p. 2915 (1986).
- [99] D.M. Antoniuk, C.E. Capjack, and H.J.J. Seguin, "Computer simulation of gas transport in a magnetically stabilized glow discharge", J. Appl. Phys., Vol. 55, No. 3, p. 708 (1984).
- [100] Axial Flow fan blades "Multiwing", manufactured by F.S. Anderson, Staktofen, 16-TRO, ROD 2950, Vedvaek, Denmark. Distributed in the US by J. Crowley Co. Ltd, P.O. Box 97, New Bury, Ohio.

- [101] Private Communications, Dr. D.J. Marsden Department of Mechanical Engineering, University of Alberta.
- [102] E. Ower and R.C. Pankhurst, The measurement of Air Flow, Pergamon Press (1977).
- [103] R.G. Folsom, "Review of the Pitot Tube", Transactions of the ASME, Vol. 78, pp. 1447-1460, October (1956).
- [104] F.M. White, Viscous Fluid Flow, McGraw-Hill (1974).
- [105] J.R. Wetty, C.E. Wicks, and R.E. Wilson, Fundamentals of Momentum, Heat and Mass Transfer, John Wiley, N.Y. (1969).
- [106] R.H. Bullis, W.L. Nighan, M.C. Fowler, W.J. Wiengand, "Physics of CO₂ Electric Discharge Lasers", AIAA J., Vol. 10, p. 407 (1972).
- [107] J. Shwartz and E. Margalith, J. Appl. Phys., Vol. 45, p. 4469 (1974).
- [108] G. Francis, Encyclopedia of Physics, edited by S. Flügge (Springer-Verlag, Berlin, 1956), Vol. XXII, p.53.
- [109] N. Takemitsu, "Finite Difference Method to Solve Incompressible Fluid Flow", J. Comp. Phys., Vol. 61, p.499-518 (1985).
- [110] P.J. Roache, Computational Fluid Dynamics, Hermosa

- Publishers (1972).
- [111] J.D. Verdeyen, Laser Electronics, Prentice-Hall, Inc., (1981), p. 280.
- [112] B. Carnahan, H.A. Luther, and J.O. Wilkes, Applied Numerical Methods, John Wiley, N.Y. (1969), p. 429.
- [113] G.K. Batchelor, An Introduction to Fluid Dynamics, Cambridge University Press (1967).
- [114] A.K. Agrawal and R.S. Peckover, "A Co-ordinate Transformation Method for Thermohydraulics in Arbitrary Geometries", UKAEA, Culham Laboratory, CLM-R209 (1980).
- [115] M. Mitchner and C.H. Kruger Jr., Partially Ionized Gases, John Wiley, N.Y. (1973), p. 182.
- [116] L.D. Landau and E.M. Lifshitz, Fluid Mechanics, Pergamon Press (1959).
- [117] Ref. 104, p. 89.
- [118] D. Schnack and J. Killeen, "Nonlinear Two-Dimensional Magnetohydrodynamic Calculations", J. Comp. Phys., Vol. 35, p. 110-145 (1980).
- [119] P.L. Pritchett, C.C. Wu and J.M. Dawson, "Interchange instabilities in a Compressible Plasma", Phys. Fluids, Vol. 21, p. 1543 (1978).

- [120] A. Sykes and J.A. Wesson, "Relaxation instability in tokamaks". Phys. Rev. Lett., Vol. 37, p. 140 (1976).
- [121] D. Potter, Computational Physics, John Wiley (1973).
- [122] R.H. Pennington, Introductory Computer Methods and Numerical Analysis, Macmillan (1965).
- [123] H.C. Lui and C.K. Chan, "Two-dimensional magnetohydrodynamic simulation of toroidal pinches", Phys. Fluids, Vol. 18, No 10, p. 1277 (1975).
- [124] C.H. Finan III, Ph.D Thesis, University of California, Davis. Department of Applied Science, (1980).
- [125] I. Lindemuth and J. Killeen, "Alternating Direction Implicit Techniques for Two-Dimensional Magnetohydrodynamic Calculations", J. Comp. Phys., Vol. 13, p. 181 (1973).
- [126] H.C. Lui and C.K. Chan, "Two-dimensional magnetohydrodynamic simulation of toroidal pinches II: Belt Pinches", Phys. Fluids, Vol. 19, No 12, p. 1947 (1976).
- [127] D. Schnack and J. Killeen, "Non-linear Saturation of the tearing mode in a reversed field pinch", Nucl. Fusion, Vol. 19, p. 877 (1979).
- [128] C.H. Finan III and J. Killeen, "Solution of the

- time-dependent three-dimensional resistive magnetohydrodynamic equations", Comp. Phys. Commun., Vol. 24, p. 441 (1981).
- [129] D.W. Peaceman and H.H. Rachford Jr., "The Numerical Solution of Parabolic and Elliptical Differential Equations", J. Soc. Indust. Appl. Math., Vol. 3, p. 28 (1955).
- [130] D.M. Antoniuk, Ph.D. Thesis, University of Alberta, 1983.
- [131] P.M. Morse and H. Feshbach, Methods of Theoretical Physics, McGraw Hill (1953).
- [132] R.D. Richtmyer and K.W. Morton, Difference Methods for Initial Value Problem, Interscience, New York (1967).
- [133] I.R. Lindemuth, Ph.D. Thesis, University of California, Davis, Department of Applied Science (1971).
- [134] M. Kawaguti, "Numerical Solution of the Navier-Stokes Equations for the flow Around a Circular Cylinder at Reynolds Number 40", J. Physical Society of Japan, Vol. 8, No. 6, pp.747-757 (1953).
- [135] Ref. 110, p. 272.
- [136] A. Thom and C.J. Apelt, Fluid Computations in Engineering and Physics, C. Van Nostrand Company

(1961).

[137] Ref. 110, p. 275.

[138] Ref. 104, p. 7.

[139] S. Eskinazi, Principles of Fluid Mechanics, Allyn and Bacon, Inc., Boston (1962) p. 354.

[140] N. Takemitsu, J. Comp. Phys., Vol. 61, p. 499 (1985).

[141] D. Thoman and A.A. Szewczyk, "Time Dependent Viscous Flow Over a Circular Cylinder", The Physics of Fluids Supplement II, p. 76 (1969).

[142] P.J. Roache and T.J. Mueller, "Numerical solutions of compressible and incompressible laminar separated flow", AIAA paper No. 68-741, AIAA Fluid and Plasma Dynamics Conference, Los Angles, California, June 24-26 (1968).

[143] L.S.G. Kovasznay, "Hot-wire investigation of the wake behind cylinders at low Reynolds numbers", Proceedings of the Royal Society of London, Ser. A, Vol. 198, p. 174 (1949).

[144] C.R. Wilke, "A Viscosity Equation for Gas Mixtures", J. Chem. Phys., Vol. 18, No. 4, p. 517 (1950).

[145] R.C. Reid and T.K. Sherwood, The Properties of Gases and Liquids, Their Estimation and Correlation,

- McGraw-Hill, N.Y., 1958) p. 182.
- [146] M. Cloutier, "Computed Physical and Thermodynamic Properties of Various He-CO₂-N₂ Mixtures", DREV Technical Notes, Quebec, Canada, (1970).
- [147] Ref. 104, p. 6.
- [148] D. Thoman and A.A. Szewczyk, "Time Dependent Viscous Flow Over a Circular Cylinder", The Physics of Fluids Supplement II, pp. 76-87 (1969).
- [149] P.J. Roache and T.J. Mueller, "Numerical Solutions of Compressible and Incompressible Laminar Separated Flows", AIAA Paper No. 68-741, AIAA Fluid and Plasma Dynamics Conference, Los Angles, California, June 24-26 (1968).
- [150] D.N. deG. Allen and R.V. Southwell, "Relaxation Methods Applied to Determine the Motion, in Two Dimensions, of Viscous Fluid Past a Fixed Cylinder", Quarterly J. of Mechanics and Applied Mathematics, Vol. 8, Pt. 2, pp. 129-145 (1955).
- [151] A. Thom, "The Flow Past Circular Cylinders at Low Speeds", Proceedings of the Royal Society of London, Ser. A, Vol. 141, pp. 651-669 (1933).
- [152] I. Imai, "Discontinuous Potential Flow as the Limiting Form of the Viscous Flow for Vanishing Viscosity", J.

- Phys. Soc. Japan, Vol. 8, No. 3, pp. 399-402 (1953).
- [153] M. Kawaguti, "Discontinuous Flow Past a Circular Cylinder", J. Phys. Soc. Japan, Vol. 8, No. 3, pp. 403-406 (1953).
- [154] W.H. Finlay, M.Sc. Thesis, University of Alberta (1984).
- [155] A. Von Engle, Ionized Gases, Oxford University Press (1965).
- [156] F. Llewellyn-Jones, The Glow Discharge and an Introduction to Plasma Physics, John Wiley (1966).
- [157] Ref. 105, p. 220.

APPENDIX A

ORTHOGONAL CURVILINEAR COORDINATES

The set of equations 4.15 is valid in any coordinate system. Computationally, a coordinate system must be selected and then the indicated vector operations expanded in order to obtain a set of differential equations to which finite-difference techniques may be applied. In this appendix, these equations are kept as general as possible by expanding Eqns. 4.15 in orthogonal curvilinear coordinates [118]. This has the advantage of allowing the computer model to be applicable for different electrode geometries and different coordinate systems to be considered. The equations will then be reduced to the appropriate coordinate system, which is the cartesian system in our case.

In orthogonal curvilinear coordinates, the differential arc length is given by:

$$ds^2 = h_1^2 dx_1^2 + h_2^2 dx_2^2 + h_3^2 dx_3^2 \quad (A.1)$$

where x_1 , x_2 and x_3 are orthogonal curvilinear coordinates with scale factors h_i . The terms $h_i dx_i$ measure the differential arc length in the e_i direction. In this system, the metric g is described by:

$$g = (h_1 h_2 h_3)^2. \quad (A.2)$$

The dot and cross products of the unit vector \vec{e}_i , which are required in the generalized coordinate system are given by:

$$\vec{e}_i \cdot \vec{e}_j = \delta_{ij} = \begin{cases} 1, & \text{for } i=j \\ 0, & \text{for } i \neq j \end{cases} \quad (\text{A.3})$$

where δ_{ij} is the Kronecker delta and

$$\vec{e}_i \times \vec{e}_j = \epsilon_{ijk} \vec{e}_k \quad (\text{A.4})$$

where ϵ_{ijk} is the Levi-Civita permutation symbol and is defined as:

$$\epsilon_{ijk} = \begin{cases} +1 & \text{if } (ijk) = \text{even permutation of } (ijk) \\ -1 & \text{if } (ijk) = \text{odd permutation of } (ijk) \\ 0 & \text{otherwise} \end{cases}$$

In this generalized system, special forms for the gradient of a scalar ψ or the divergence and curl of a vector \vec{v} are needed. The gradient operator becomes:

$$\nabla = \frac{\vec{e}_1}{h_1} \frac{\partial}{\partial x_1} + \frac{\vec{e}_2}{h_2} \frac{\partial}{\partial x_2} + \frac{\vec{e}_3}{h_3} \frac{\partial}{\partial x_3} = \sum_i \frac{\vec{e}_i}{h_i} \frac{\partial}{\partial x_i} \quad (\text{A.5})$$

where the summation runs for $i=1,2,3$. In this respect, the gradient of a scalar ψ is:

$$\nabla \psi = \sum_i \frac{1}{h_i} \frac{\partial \psi}{\partial x_i} \vec{e}_i \quad (\text{A.6})$$

The divergence of a vector \vec{v} is:

$$\nabla \cdot \vec{v} = \sum_i \frac{1}{\sqrt{g}} \frac{\partial}{\partial x_i} \left(\sqrt{g} \frac{\vec{v}_i}{h_i} \right) \quad (\text{A.7})$$

The curl of a vector \vec{v} is given by:

$$\nabla \times \vec{v} = \sum_i \frac{\vec{h}_i \cdot \vec{e}_i}{\sqrt{g}} - \sum_{i,m} \epsilon_{ilm} \frac{\partial h^m}{\partial x^l} \quad (A.8)$$

The divergence of a tensor T is expressed as:

$$(\nabla \cdot \hat{T})_j = \sum_i \vec{h}_j \cdot \vec{e}_j \hat{T}^{ij} \quad (A.9)$$

where \hat{T}^{ij} is the covariant derivative of T . Now, using the concept of covariant and contravariant [131], Eqn. A.9 can be arranged in the form:

$$(\nabla \cdot \hat{T})_j = \sum_i \vec{h}_j \cdot \vec{e}_j \left[\frac{1}{\sqrt{g}} \frac{\partial}{\partial x^i} (\sqrt{g} T^{ij}) + \sum_k T^{ik} [i^j]_k \right] \quad (A.10)$$

where $T^{ij} = T_{ij}/h_i h_j$ is the contravariant form of the Tensor T_{ij} and $[i^j]_k$ is a Christoffel symbol whose properties are

$$[i^i]_i = \frac{1}{h_i} \frac{\partial h_i}{\partial x^i}, \quad [i^j]_j = [j^i]_i = \frac{1}{h_i} \frac{\partial h_i}{\partial x^j},$$

$$[j^i]_i = - \frac{h_i}{(h_j)^2} \frac{\partial h_i}{\partial x^j},$$

$$[j^i]_k = 0 \quad \text{for } i, j, k \text{ all different.} \quad (A.11)$$

The Christoffel symbols represent the change in directions of the unit vectors as one moves in space. For clarity, and to show the actual form of the $\nabla \cdot \hat{T}$ terms, we expand the first component as:

$$(\nabla \cdot \vec{T})_1 = \frac{1}{h_1 h_2 h_3} \left[\frac{\partial}{\partial x_1} (h_2 h_3 T_{11}) + \frac{\partial}{\partial x_2} (h_2 h_3 T_{21}) + \frac{\partial}{\partial x_3} (h_1 h_2 T_{31}) \right. \\ \left. + h_3 \frac{\partial h_1}{\partial x_2} T_{12} + h_2 \frac{\partial h_1}{\partial x_3} T_{13} - \left[h_3 \frac{\partial h_2}{\partial x_1} T_{22} + h_2 \frac{\partial h_3}{\partial x_1} T_{33} \right] \right]. \quad (A.12)$$

Equation A.12 contains terms which resemble normal vector divergence terms plus a set of extra terms known as Coriolis terms. The Coriolis terms arise due to the change in direction of the unit vectors with changes in position.

Finally, the gradient of a vector as expressed by the dyadic form [131] is given by:

$$A_{nm} = \left(\frac{1}{h_m h_n} \right) f_{m,n} = \left(\frac{1}{h_m h_n} \right) (h_m F_{m,n})$$

which can be written in the form:

$$A_{nm} = \frac{1}{h_n} \frac{\partial F_m}{\partial x_n} - \frac{F_n}{h_m h_n} \frac{\partial h_m}{\partial x_n} \quad \text{for } m \neq n$$

and

$$A_{mm} = \frac{\partial}{\partial x_m} \left(\frac{F_m}{h_m} \right) + \frac{1}{h_m} \sum_n \frac{F_n}{h_n} \frac{\partial h_m}{\partial x_n}.$$

For $F = \vec{v}$ we have:

$$\nabla \vec{v} = \begin{cases} A_{nm} = \frac{1}{h_n} \frac{\partial v_m}{\partial x_n} - \frac{v_n}{h_m h_n} \frac{\partial h_m}{\partial x_n} & \text{for } m \neq n \\ A_{mm} = \frac{\partial}{\partial x_m} \left(\frac{v_m}{h_m} \right) + \frac{1}{h_m} \sum_n \frac{v_n}{h_n} \frac{\partial h_m}{\partial x_n} & \end{cases}. \quad (A.13)$$

Using the above definitions, we may now write Eqns. 4.15 in component form as:

$$\frac{\partial \rho}{\partial t} + \frac{1}{h_1 h_2 h_3} \left[\frac{\partial}{\partial x_1} (h_2 h_3 \rho v_1) + \frac{\partial}{\partial x_2} (h_1 h_3 \rho v_2) + \frac{\partial}{\partial x_3} (h_1 h_2 \rho v_3) \right] = 0.$$

(A.14a)

$$\frac{\partial}{\partial t} (h_1 h_2 h_3) + \frac{1}{h_1 h_2 h_3} \left[\frac{\partial}{\partial x_1} (h_2 h_3 \rho v_1^2) + \frac{\partial}{\partial x_2} (h_1 h_3 \rho v_1 v_2) + \frac{\partial}{\partial x_3} (h_1 h_2 \rho v_1 v_3) \right]$$

$$+ [h_3 \rho v_1 v_2 \frac{\partial h_1}{\partial x_2} + h_2 \rho v_1 v_3 \frac{\partial h_1}{\partial x_3} - [h_3 \rho v_2^2 \frac{\partial h_2}{\partial x_1} + h_2 \rho v_3^2 \frac{\partial h_3}{\partial x_1}]]$$

$$- \frac{\eta}{h_1 h_2 h_3} \left[\frac{\partial}{\partial x_1} (h_2 h_3 A_{11}) + \frac{\partial}{\partial x_2} (h_1 h_3 A_{21}) + \frac{\partial}{\partial x_3} (h_1 h_2 A_{31}) + h_3 \frac{\partial h}{\partial x_2} A_{12} \right]$$

$$+ [h_2 \frac{\partial h_1}{\partial x_3} A_{13} - [h_3 \frac{\partial h_2}{\partial x_1} A_{22} + h_2 \frac{\partial h_3}{\partial x_1} A_{33}]] - [\xi + \frac{1}{3}\eta] \frac{1}{h_1} \frac{\partial}{\partial x_1} \left[\frac{1}{h_1 h_2 h_3} \right]$$

$$\left[\frac{\partial}{\partial x_1} (h_2 h_3 v_1) + \frac{\partial}{\partial x_2} (h_1 h_3 v_2) + \frac{\partial}{\partial x_3} (h_1 h_2 v_3) \right] + \frac{KT}{m} \frac{1}{h_1} \frac{\partial \rho}{\partial x_1} = 0.$$

(A.14b)

$$\frac{\partial}{\partial t} (\rho v_2) + \frac{1}{h_1 h_2 h_3} \left[\frac{\partial}{\partial x_1} (h_2 h_3 \rho v_1 v_2) + \frac{\partial}{\partial x_2} (h_1 h_3 \rho v_2^2) + \frac{\partial}{\partial x_3} (h_1 h_2 \rho v_2 v_3) \right]$$

$$+ [h_3 \rho v_1 v_2 \frac{\partial h_2}{\partial x_1} + h_1 \rho v_2 v_3 \frac{\partial h_2}{\partial x_3} - [h_3 \rho v_1^2 \frac{\partial h_1}{\partial x_2} + h_1 \rho v_3^2 \frac{\partial h_3}{\partial x_2}]]$$

$$- \frac{\eta}{h_1 h_2 h_3} \left[\frac{\partial}{\partial x_1} (h_2 h_3 A_{12}) + \frac{\partial}{\partial x_2} (h_1 h_3 A_{22}) + \frac{\partial}{\partial x_3} (h_1 h_2 A_{32}) + h_3 \frac{\partial h_2}{\partial x_1} A_{12} \right]$$

$$+ [h_1 \frac{\partial h_2}{\partial x_3} A_{32} - [h_3 \frac{\partial h_1}{\partial x_2} A_{11} + h_1 \frac{\partial h_3}{\partial x_2} A_{33}]] - [\xi + \frac{1}{3}\eta] \frac{1}{h_2} \frac{\partial}{\partial x_2} \left[\frac{1}{h_1 h_2 h_3} \right]$$

$$\left[\frac{\partial}{\partial x_1} (h_2 h_3 v_1) + \frac{\partial}{\partial x_2} (h_1 h_3 v_2) + \frac{\partial}{\partial x_3} (h_1 h_2 v_3) \right] + \frac{KT}{m} \frac{1}{h_2} \frac{\partial \rho}{\partial x_2} = 0.$$

(A.14c)

$$\begin{aligned}
 & \frac{\partial}{\partial t} (\rho v_3) + \frac{1}{h_1 h_2 h_3} \left[\frac{\partial}{\partial x_1} (h_2 h_3 \rho v_1 v_3) + \frac{\partial}{\partial x_2} (h_1 h_3 \rho v_2 v_3) + \frac{\partial}{\partial x_3} (h_1 h_2 \rho v_3^2) \right. \\
 & \quad \left. + h_2 \rho v_1 v_3 \frac{\partial h_3}{\partial x_1} + h_1 \rho v_2 v_3 \frac{\partial h_3}{\partial x_2} - \left[h_2 \rho v_1^2 \frac{\partial h_1}{\partial x_3} + h_1 \rho v_2^2 \frac{\partial h_2}{\partial x_3} \right] \right] \\
 & = \frac{\eta}{h_1 h_2 h_3} \left[\frac{\partial}{\partial x_1} (h_2 h_3 A_{13}) + \frac{\partial}{\partial x_2} (h_1 h_3 A_{23}) + \frac{\partial}{\partial x_3} (h_1 h_2 A_{33}) + h_2 \frac{\partial h_3}{\partial x_1} A_{13} \right. \\
 & \quad \left. + h_1 \frac{\partial h_3}{\partial x_2} A_{23} - \left[h_2 \frac{\partial h_1}{\partial x_3} A_{11} + h_1 \frac{\partial h_2}{\partial x_3} A_{22} \right] \right] - \left[\zeta + \frac{1}{3} \eta \right] \frac{1}{h_3} \frac{\partial}{\partial x_3} \left[\frac{1}{h_1 h_2 h_3} \right] \\
 & \quad - \left[\frac{\partial}{\partial x_1} (h_2 h_3 v_1) + \frac{\partial}{\partial x_2} (h_1 h_3 v_2) + \frac{\partial}{\partial x_3} (h_1 h_2 v_3) \right] + \frac{K T}{m} \frac{1}{h_3} \frac{\partial \rho}{\partial x_3} = 0
 \end{aligned} \tag{A.14d}$$

$$\begin{aligned}
 & \frac{\partial T}{\partial t} + \frac{1}{h_1 h_2 h_3} \left[\frac{\partial}{\partial x_1} (h_2 h_3 v_1 T) + \frac{\partial}{\partial x_2} (h_1 h_3 v_2 T) + \frac{\partial}{\partial x_3} (h_1 h_2 v_3 T) \right] \\
 & = \frac{2 \tilde{\eta}}{\rho C_p} \left[\frac{1}{h_1} \frac{\partial v_1}{\partial x_1} + \frac{1}{h_2} \frac{\partial v_2}{\partial x_2} + \frac{1}{h_3} \frac{\partial v_3}{\partial x_3} \right]^2 + \frac{2 \eta}{3 \rho C_p} \left[\frac{1}{h_1 h_2 h_3} \frac{\partial}{\partial x_1} (h_2 h_3 v_1) \right. \\
 & \quad \left. + \frac{\partial}{\partial x_2} (h_1 h_3 v_2) + \frac{\partial}{\partial x_3} (h_1 h_2 v_3) \right]^2 - \frac{K}{\rho C_p} \frac{1}{h_1 h_2 h_3} \left[\frac{\partial}{\partial x_1} \left(\frac{h_2 h_3}{h_1} \frac{\partial T}{\partial x_1} \right) \right. \\
 & \quad \left. + \frac{\partial}{\partial x_2} \left(\frac{h_1 h_3}{h_2} \frac{\partial T}{\partial x_2} \right) + \frac{\partial}{\partial x_3} \left(\frac{h_1 h_2}{h_3} \frac{\partial T}{\partial x_3} \right) \right] - Q'' = 0
 \end{aligned} \tag{A.14e}$$

Equations A.14 can be expressed in vector form as:

$$\frac{\partial}{\partial t} \vec{M}(\vec{u}) + \vec{F}(\vec{u}) + \vec{G}(\vec{u}) + \vec{H}(\vec{u}) = 0 \tag{A.15}$$

where the functions $\vec{F}(\vec{u})$, $\vec{G}(\vec{u})$ and $\vec{H}(\vec{u})$ contain all terms in Eqns. A.14 that have leading derivatives with respect to x_1 , x_2 and x_3 . These leading derivatives can take any of the

forms of Eqns. 4.17. \vec{M} and \vec{u} are defined in section 4.3. The terms \vec{F} , \vec{G} and \vec{H} can be inferred from comparison of Eqns. A.14 and A.15.

In our case, Eqns. A.14 are reduced to a set of equations in two dimensional cartesian coordinates. This is given by:

$$\frac{\partial \rho}{\partial t} + \frac{\partial}{\partial x_1} (\rho v_1) + \frac{\partial}{\partial x_2} (\rho v_2) = 0 \quad (A.16a)$$

$$\begin{aligned} \frac{\partial}{\partial t} (\rho v_1) + \frac{\partial}{\partial x_1} (\rho v_1^2) + \frac{\partial}{\partial x_2} (\rho v_1 v_2) - \eta \left[\frac{\partial}{\partial x_1} (A_{11}) + \frac{\partial}{\partial x_2} (A_{21}) \right] \\ - \left[\xi + \frac{1}{3} \eta \right] \frac{\partial}{\partial x_1} \left[\frac{\partial}{\partial x_1} (v_1) + \frac{\partial}{\partial x_2} (v_2) \right] + \frac{KT}{m} \cdot \frac{\partial \rho}{\partial x_1} = 0 \end{aligned} \quad (A.16b)$$

$$\begin{aligned} \frac{\partial}{\partial t} (\rho v_2) + \frac{\partial}{\partial x_1} (\rho v_1 v_2) + \frac{\partial}{\partial x_2} (\rho v_2^2) - \eta \left[\frac{\partial}{\partial x_1} (A_{12}) + \frac{\partial}{\partial x_2} (A_{22}) \right] \\ - \left[\xi + \frac{1}{3} \eta \right] \frac{\partial}{\partial x_2} \left[\frac{\partial}{\partial x_1} (v_1) + \frac{\partial}{\partial x_2} (v_2) \right] + \frac{KT}{m} \cdot \frac{\partial \rho}{\partial x_2} = 0 \end{aligned} \quad (A.16c)$$

$$\begin{aligned} \frac{\partial T}{\partial t} + \frac{\partial}{\partial x_1} (v_1 T) + \frac{\partial}{\partial x_2} (v_2 T) - \frac{4\eta}{3\rho c_p} \left[\frac{\partial v_1}{\partial x_1} + \frac{\partial v_2}{\partial x_2} \right]^2 \\ - \frac{K}{\rho c_p} \cdot \left[\frac{\partial}{\partial x_1} \left(\frac{\partial T}{\partial x_1} \right) + \frac{\partial}{\partial x_2} \left(\frac{\partial T}{\partial x_2} \right) \right] - Q'' = 0 \end{aligned} \quad (A.16d)$$

In Eqns. A.16, the dyatic terms A_{nm} are described by Eqn. A.13. Equations A.16 are the equations that IGCP uses to

simulate the open channel flow. These equations are then expressed in the vector form of Eqn. 4.16 and the terms F and G can be inferred from comparison of the similar terms.

APPENDIX B

BOUNDARY CONDITIONS FOR CODE VERIFICATION

B1. BOUNDARY CONDITIONS OF THE TWO-ELECTRODE SYSTEM

In this case, the boundary conditions were obtained in a way similar to that described in section 5.4. The simulation mesh used is shown in Fig. 5.1. The appropriate boundary conditions that are applied at the upper and lower solid electrodes for the velocity components v and u are as follows:

$$v(x, y=0) = v(x, y=Y) = 0 \quad (\text{no-slip condition}), \quad (B.1)$$

$$u(x, y=0) = u(x, y=Y) = 0 \quad (\text{zero normal flow}), \quad (B.2)$$

At the electrode surfaces, a homogeneous Neumann condition is imposed on the neutral mass density ρ :

$$\left(\frac{\partial \rho}{\partial y}\right)_{x,0} = \left(\frac{\partial \rho}{\partial y}\right)_{x,Y} = 0 \quad (B.3)$$

The boundary conditions at the entrance and the exit are exactly similar to that considered in subsections 2 and 3 in section 5.4.2, without the temperature (T) term.

Applying the finite difference technique as described in section 5.4.1 to the boundary condition's equations and comparing with Eqn. 5.32, we obtain the submatrix elements which can be used in the block tridiagonal scheme. At the boundaries $j = 1$ and $j = M$ we have:

$$[\hat{G}_B] = [\hat{G}_T] = \begin{bmatrix} 1 & 0 & 0 \\ 0 & 1 & 0 \\ 0 & 0 & 1 \end{bmatrix}, \quad (B.4)$$

$$[\hat{H}_B] = [\hat{H}_T] = \begin{bmatrix} -1 & 0 & 0 \\ 0 & -1 & 0 \\ 0 & 0 & 1 \end{bmatrix} \quad (B.5)$$

and

$$\vec{I}_B = \vec{I}_T = \begin{bmatrix} 0 \\ 0 \\ 0 \end{bmatrix}, \quad (B.6)$$

where the subscript B refers to the bottom boundary wall and the subscript T refers to the top boundary wall.

In a similar manner we can write the boundaries for $i = 1$ as:

$$[\hat{G}_L] = \begin{bmatrix} 1 & 0 & 0 \\ 0 & 1 & 0 \\ 0 & 0 & 1 \end{bmatrix}, \quad (B.7)$$

$$[\hat{H}_L] = \begin{bmatrix} -1 & 0 & 0 \\ 0 & -1 & 0 \\ 0 & 0 & -1 \end{bmatrix}, \quad (B.8)$$

and

$$\vec{I}_L = \begin{bmatrix} 2v_i \\ 0 \\ 2\rho_i(T_{en}, P_i) \end{bmatrix} \quad (B.9)$$

where L refers to the entrance.

Finally, for $i=N$ we can write:

$$[\hat{G}_R] = \begin{bmatrix} 1 & 0 & 0 \\ 0 & 1 & 0 \\ 0 & 0 & 1 \end{bmatrix}, \quad (B.10)$$

$$[\hat{H}_R] = \begin{bmatrix} 1 & 0 & 0 \\ 0 & -1 & 0 \\ 0 & 0 & 1 \end{bmatrix}, \quad (B.11)$$

and

$$\vec{I}_R = \begin{bmatrix} 0 \\ 0 \\ 0 \end{bmatrix}, \quad (B.12)$$

where R refers to the exit.

B2. BOUNDARY CONDITIONS OF THE THREE-ELECTRODE SYSTEM

In both cases of single and double step electrode structures, the boundary conditions are obtained in the same fashion as described in section 5.4.2 without the temperature (T) term.

VITA

NAME : MOHAMED SALEM ELGWAILY

PLACE OF BIRTH : DAMANHOUR, EGYPT

YEAR OF BIRTH : 1944

POST-SECONDARY EDUCATION:

- 1967: B.Sc. in Electrical Engineering,
Alexandria University.
- 1972: M.Sc. in Electrical Engineering,
Cairo University.
- 1978: M.A.Sc. in Electrical Engineering,
University of Waterloo.
- 1988: Ph.D. in Electrical Engineering,
University of Alberta.

HONORS AND AWARDS:

- Egyptian Scholarship 1965-1967.

RELATED WORK EXPERIENCE:

- Dec 86/ : Technologist, Department of Physics,
April 87 University of Alberta.
- May 79/ : Research in CO₂ lasers, Department of
July 81 Electrical Engineering,
Univeristy of Alberta.
- 1980/1985: Teaching Assistant,
Univeristy of Alberta.

1976/1978: Teaching Assistant,

University of Waterloo.

1967/1975: Research Engineer,

Atomic Energy Center, Cairo, Egypt.

Publications:

1. Elgwaily M.S., Capjack C.E. and Tulip J. "Computer Simulation of an Open Channel Flow Laser Gas Discharge", in preparation.
2. Elgwaily M.S., Capjack C.E. and Tulip J. "Application of Large Time Step ADI Technique for Modeling Open Channel Flow", in preparation.
3. Roulsten D.J., Elgwaily M.S., et. al. "Comments on Current and Base Transit Time Relations in Normal and Inverted (I^2L) Bipolar Transistors". IEEE Trans. Electron Devices, Vol. ED-25, No. 9, September 1978, p. 1172.
4. Elgwaily M.S. "On the Performance of Ion Implanted Integrated Injection Logic I^2L ". M.A.Sc. Research Project, University of Waterloo, Department of Electrical Engineering, 1978.
5. El-Khalafawy T., Elgwaily M.S., et. al. "Propagation of Switch-on Shock in Magnetized Collisionless Plasma". 6th European Conference on Controlled Fusion and Plasma Physics, Moscow (1973) 569.
6. Mahmoud H.M., Elgwaily M.S. and El-Khalafawy T. "Shock Waves Generated from Conical Electrode Source". A. Journal of Nuclear Sciences and Applications Vol. 6, No. 1, P. 13 (1973).
7. Masoud M.M., Elgwaily M.S. and El-Khalafawy T. "Conical Electrode Discharge". A.R.E. A.E.E. Report 155 (1972).
8. Elgwaily M.S. and Mahmoud H.M. "Construction and Operation of Conical Electrode Discharge System for Shock Waves Generation". A.R.E. A.E.E. Report 149

(1972).

9. Elgwaily M.S. and El-Khalafawy T. "Generation of Shock Waves in Water". A.R.E. A.E.E. Report 143 (1972).
10. Elgwaily M.S. "Experimental Study of Shock Waves Interactions". M.Sc. Research Thesis, Cairo University, Department of Electrical Engineering 1971.
11. Elgwaily M.S., Mahmoud H.M. and El-Khalafawy T. Shock waves Generated from Conical Electrode Source". 2nd Physics Conference, Cairo, Egypt (1971).
12. El-Khalafawy T., Elgwaily M.S., et. al. "Dense Plasma Flow from an Electrode Conic Source". 4th European Conference on Controlled Fusion and Plasma Physics, Rome (1970) 110.
13. Elgwaily M.S. and El-Khalafawy T. "Experimental Studies on Shock Waves Propagated Through a Longitudinal Magnetic Field in Electrodeless Discharge Tubes". U.A.R. A.E.E. Report 101 (1970).
14. El-Khalafawy T., Elgwaily M.S. et. al. "Experimental Studies on Shock Waves Propagated Through a Longitudinal Magnetic Field". 9th International Conference on Phenomena in Ionized Gases, Bucharest (1969).

MSGW
864501 University of Alberta Computing Service (System EC107)
Job number 864501 17:21:46 MDT Thu Apr 21/88

University of Alberta Computing Service (System EC107)

Job Number 864501

User: MSGW
Project no: THEL

*****	Obtained at	17-21-46	THU APR 21/88
*****	Released at	17-23-03	Thu Apr 21/88
*****	Lines printed	29170	
*****	Images printed	325	
*****	Pages printed	325	